Integration of Optical Components and Magnetic Field Sources in Atom Chips

Fernando Ramirez-Martinez

Thesis submitted in partial fulfilment of the requirements for the degree of Doctor of Philosophy of the University of London and the Diploma of Membership of Imperial College.

Imperial College London

University of London

July, 2008

Abstract

Integration of Optical Components and Magnetic Field Sources in Atom Chips

Fernando Ramirez-Martinez

This thesis reports on the integration of optical components and magnetic field sources on the surface of an atom chip. Pyramidal hollow mirrors with an angle of 70.5° between its opposing faces have been fabricated on the surface of an atom chip to generate miniature magneto-optic traps. This work demonstrates that magneto optic traps can be created in these pyramids. An experimental determination of the scaling laws that govern the capture and loss rates of the 70.5° pyramid MOTs indicates that the capture rate follows a power law dependence on the position on the pyramid apex, with a characteristic exponent of 3.4(4). The loss rate has shown to be much less sensitive to this distance down to 600 μm, position below which it increases rapidly. Based on these measurements, it is estimated that as many as 10^4 can be collected in a pyramid with a 1.2 mm side length, while as few as some tenths of atoms would be trapped in a 200 μm side length pyramid. The first pyramid atom chip is presented in this thesis. This device includes pyramids sizes which range between 200 μm and 1.2 mm in steps of 200 μm. The quadrupole magnetic fields for creating the pyramid MOTs are generated by micro-fabricated current carrying wires circling around the pyramid apertures. This thesis also demonstrates that Co/Pt magneto-optic thin films are particularly suitable for creating tight magnetic traps. These MO films present an out-of-plane and strong remanent magnetisation, as well as a large room temperature coercivity. A thermo-magnetic writing apparatus is described. Two examples of the magnetic patterns written in these MO films are an array of parallel lines and a set of Z-trap patterns. A numerical calculation demonstrates that with the apposite bias fields, trapping potentials can be created at a height of 0.75 μm from the film surface.

Acknowledgements

In the first place I would like to thank my supervisor Ed Hinds. His vast experience and passion for Physics have been an example and an inspiration for me.

I will continue by acknowledging the support of the government of México, which through its institutions, Consejo Nacional de Ciencia y Tecnología (CONACYT), Banco de México (BANXICO) and the Secretaría de Educación Pública (SEP), has provided the economical support that allowed me to study this PhD.

During the realisation of my PhD, I was fortunate of working with a long list of postdocs and I would like to thank each one of them for their help and friendship. They are Stefan Eriksson, Anne Curtis, Jonathan Ashmore, Jonathan Goldwin, Gabriel Dutier, Athanasios Laolitis. In addition, other members of the Centre for Cold Matter with whom I did not have the luck to work directly but that have also played a role in this PhD are Benoit Darquie, Jos Dingjan, Jony Hudson, Ben Sauer, Mike Tarbutt, and Robert Nyman.

Next, I want to thank my office mates and friends Chris, Paul, Richard, Isabel and Henry. To Daniel and Oliva I have to thank them for maintaining a little piece of our University years close to me here in London. I would like to thank Michael, with whom I shared a desk, an optics table, a lot of coffee and a good friendship, for his contribution to this research project. A particular mention has to go to Sam Pollock, who brought a great deal of much needed freshness to the project.

Sanja Maricic has been an interminable source of help and encouragement during the most difficult stages of this process and because of this, I am in great debt with her.

Most of the components fabricated in the CCM for this project went through the hands of Jon Dyne or David William, or both. Their extraordinary disposition and ability is well recognised within the group and I have to thank for their advice and hard work.

To Gareth Lewis, Dr. Zakaria Moktadir, and Dr. Michael Kraf, members of the School of Electronics and Computer Science, University of Southampton, that worked very hard on the development and fabrication of the pyramid atom chips.

To Nacho and Jordi for being our guides in our first few weeks in London. As well, I would also like to thank Cristina, Gaby, Dani and Emma for your friendship and company throughout these years.

I want to thank my parents, Lala and Fernando, as well as to Ricardo and Aurora. The great support and affection you have given to us in these years is invaluable and I can not express how grateful I am.

At last but definitely not least, I want to thank Julia because this thesis is also her achievement.

Contents

List of Figures

List of Tables

Chapter 1

Introduction

This chapter explains the motivations behind this research project. Firstly, a brief overview of the field of atom optics will be provided, including its most recent advances. In particular, I will centre my attention in explaining how atom optics experiments are combined with state-of-the-art microfabrication techniques to create atom chips. Both electromagnets and optical components integrated at a microscopic scale on the surface of these devices provide a level of simplicity not achievable in any other way. Consequently, this chapter concludes by describing the contributions that this work provides to the advance of the field.

1.1 Atom optics

Atom optics is a field of physics in which the motion of atoms is controlled by means of electric, magnetic and optical fields. The development of techniques for cooling, trapping and manipulating atoms has been a common task of a growing number of research groups around the world. The large impact these developments have had in atomic and molecular physics was recognised with the Nobel prize in 1997. The Nobel lectures given by the laureates Will Phillips, Steven Chu, and Claude Cohen-Tannoudji are extraordinary introductions to the research field; they provide not only a broad overview of the field but also an exciting recount of the first few years of what is now one of the most fruitful research fields in physics [1, 2, 3]. Since the first demonstration of laser cooling and trapping of neutral atoms, these techniques have been refined and several new methods and devices for trapping and guiding atoms have been proposed and demonstrated. As a result of these advances, a few millions of atoms are routinely collected in tight traps and cooled down to a few millionths of a degree above the absolute zero.

Laser cooling of atoms consists of a reduction in kinetic energy of moving atoms by the mechanical action of laser radiation at a frequency near an atomic resonance. The idea of laser cooling was first introduced in 1975 by Hansch and Schawlow at Stanford University and Wineland and Dehmelt at the University of Washington. In particular, Hansch and Schawlow envisaged an experiment in which a gas of atoms is irradiated from

all sides by six laser beams along each of the six Cartesian coordinate directions. With the laser frequency tuned below the atomic resonance, the atoms in the gas experience a viscous force. The motion of the atoms in the resulting viscous fluid of photons has been called an optical molasses [4, 5]. The Doppler effect plays a crucial role in this kind of laser cooling, which is therefore often called Doppler cooling. Various aspects of this cooling mechanism were studied theoretically by David Wineland [6], including its characteristic rates and its cooling limit, the Doppler cooling limit [5, 7].

Atoms in optical molasses were first observed by Steven Chu's research group in Bell Laboratories [4]. Nearly ten years after Wineland *et al.* estimated the Doppler cooling limit, which was widely accepted by the laser cooling community, strong disagreements between the experimental results and the two-level atom theories were observed. Atoms laser cooled below the Doppler limit were reported for the first time by Will Phillips' group at NIST [8], and later confirmed by Steven Chu and his group. To understand the low temperatures found in these experiments, the Doppler cooling theory had to be extended to multiple level atoms. The groups of Steven Chu at Bell Laboratories and Claude Cohen-Tannoudji at the ENS in Paris proposed similar theories based on the idea of nonadiabatic motion of a multilevel atom through the polarisation gradient in optical molasses. The new theories of sub-Doppler cooling and polarisation gradient cooling are the result of these efforts [9, 7].

In parallel with these advances, the group of Steven Chu in collaboration with Jean Dalibard devised a method for not only cooling but also trapping neutral atoms with the radiation force. The magneto-optical trap (MOT) was first reported by Raab *et al.* in [10] and soon after various groups were already utilising this technique for producing large collections of cold atoms. Nowadays, laser cooled atoms trapped in magneto-optical traps provide the starting point for a still increasing number of exciting atomic and molecular physics experiments. For its simplicity, the implementation reported in [11, 12, 13] has received particular attention and is now a fundamental element of most cooling and trapping systems.

Magnetostatic trapping of the laser cooled neutral atom clouds was the next natural step taken by these pioneer research groups [14]. Magnetic field configurations for trapping neutrons had been developed previously by Wolfgang Paul [15]. Following this example, Harold Metcalf and his colleges identified and characterised field configurations that could be useful for magnetically confining neutral atom clouds [16, 17]. The atomic magnetic dipole moment interacts with an inhomogeneous magnetic field creating a potential energy minimum around which sufficiently cold atoms can be confined. The typical trap depth of a magnetostatic trap for neutral atoms is of just 1 K. Consequently, owing to the new laser cooling techniques, it was now relatively simple to collect atom clouds with temperatures of a few microkelvin above the absolute zero.

In these traps, the interatomic distances become of the order of the de Broglie wavelength of the atomic matter waves. Consequently, the wave properties of matter are manifested in experiments where atoms are reflected, refracted and diffracted. Moreover, atom clouds can be cooled down even further and compressed at the point of placing all of its atoms in the state of minimum energy of the trap, leading to the Bose-Einstein condensation of the cloud. The groups leadered by Carl Wieman, Eric Cornell and Wolfgang Ketterle were the first in creating a Bose-Einstein condensate (BEC) [18, 19, 20]. The long range of the coherence effects of a Bose-Einstein condensate has led to the development of coherent atom optics devices. This achievement has paved the way for an incredible number of exciting experiments. Owing to the enormous impact that these

experiments have had on the field of atom optics in particular, and on physics research in general, the Nobel prize was awarded in 2001 to the leaders of these three groups. The Nobel lectures of the three laureates provide interesting overviews of the road to the BEC [21, 22], and more in depth descriptions of these experimental techniques are provided in [23, 24].

The advances mentioned so far and many more have opened the door to a long list of applications. Metrology [25, 26], measurement of fundamental physics constants, high precision spectroscopy, interferometry, quantum information and computation [27] are just some few examples of these applications.

1.2 Atom chips

A new approach to research in atom optics has been adopted by several research groups (see for example [28, 29, 30, 31, 32, 33]). This approach consists of the development of miniaturised and integrated atom optical systems based on microfabricated structures. Compact and reliable atom optical devices promise to expand the applicability of atom optics in fundamental research and technological implementations. Robust and highly controllable atom manipulation requires of steep traps or guides to be created with high precision. This can be achieved by means of standard micro-fabrication techniques. For instance, tight confining magnetic potentials can be realized, in principle, by miniaturising the elements which generate the magnetic field. Weinstein and Libbrecht [34] proposed microscopic traps based on combinations of current conductors which can be made extremely small by standard microfabrication techniques. These authors described the first loading of a miniaturised wire trap of this type by means of adiabatic transport and compression.

State-of-the-art lithographic manufacturing techniques adapted from semiconductor processing enable to fabricate high resolution structures with dimensions in the micrometer range and submicrometer features. As a result of the small scale of these structures, atoms held a few microns away from a device experience strong trapping gradients and large trap curvatures. The manufacturing techniques developed by the semiconductor industry can therefore create very robust, efficient and highly scalable resources for the manipulation of cold atom samples. In conclusion, these fabrication techniques can create steep traps and guides with high precision and in a highly scalable fashion.

The techniques of nano-fabrication, micro-electronics and micro optics are being exploited by several groups in order to built integrated mesoscopic matter wave surface devices. The name of *Atom Chip* has been given to devices that combine the unique features of techniques based on the quantum mechanical behaviour of atomic matter waves with the potential of micro- and nanofabrication technology. Among the new and exciting quantum devices that can be created with integrated atom optics are miniature atom interferometers, ultra-sensitive measuring devices, and quantum information processors. These micro-fabricated devices may integrate sources of electric, magnetic or optical fields with the aim of confining, controlling and manipulating cold atoms. According to Folman *et al.* [30]: "A final integrated atom chip should contain a reliable source of cold atoms, with an efficient loading mechanism, single mode guides for coherent transportation of atoms, nanoscale traps, movable potentials allowing controlled collisions for the creation of entanglement between atoms, extremely high resolution light fields for the manipulation of individual atoms, and internal state sensitive detection to read out the result of the processes that have occurred. All of these, including the

bias fields and probably even the light sources, could be on the board of a self-contained chip."

1.3 Integrated optical components in atom chips

Atom optics and laser cooling techniques are based on the optical manipulation of atoms [35, 36]. In an atom chip, the quantum states of a few atoms in very tight traps only a few micrometers away from the chip surface need to be detected and manipulated. Most experiments to date deliver the light required for these operations by means of external mirrors and lenses. This makes difficult to detect and manipulate atoms, as well as to address individual atoms on the chip. Lithographic manufacturing techniques allow for the creation of structures with dimensions in the micrometer scale and features in the sub-micron scale. The flexibility of these manufacturing processes can give rise to complex optical elements which would create light fields not achievable with standard optical components. Additionally, these structures can be reproduced in a scalable fashion in such a way that many identical elements could be fabricated in parallel in the same substrate. In conclusion, the application of microfabricated optical elements for manipulating atoms and atomic matter waves with laser light is a natural route in the development of atom chips.

Integrated atom optical devices can be created in a compact fashion, therefore allowing one to scale, parallelise, and miniaturise atom optics devices. New compact sources of ultracold atoms, compact sensors based on matter wave interference, and new approaches towards quantum computing with neutral atoms are all examples of the possibilities that can be realised by integrating optical components in atom chips. In particular, the steps required for quantum information processing with neutral atoms in atom chips, as identified by Birkl *et al.* [36], include preparation, manipulation and storage of qubits, entanglement, and efficient read-out of quantum information. All these tasks can in principle be performed using microfabricated optical elements integrated on the surface of an atom chip.

An important step towards fully integrated atom optical systems is the development of miniaturised sources of cold atoms. The efficient operation of these devices would benefit greatly from the development of new compact sources of ultracold atoms. Preparation techniques for cold atomic samples are based on optical manipulation. Therefore, microoptical components can be used to achieve this goal. Among the microoptical elements that can be used for atom optical applications are micro mirrors. In addition, these microoptical components can also be complemented with miniturised magnetic trapping structures to generate the initial cooling and trapping stages of these integrated cold atom sources.

1.4 Magnetic trapping in atom chips

There are two main methods for creating magnetic trapping potentials in atom chips: mesoscopic designs of current carrying wires and permanently magnetized surfaces. In the next two sections I will give a short introduction to the principles of trapping atoms with microfabricated electromagnets and permanently magnetised recording media.

1.4.1 Current carrying wires

The research in miniaturised atom optics has evolved rapidly and there are plenty of examples of this in the literature. In the following lines I give some few examples of this evolution. An atom chip consisting of surface mounted current carrying wires was presented in [30]. Atoms trapped and manipulated close to the surface of this atom chip are shown in the paper. Similarly, Muller *et al.* [28] report that laser cooled neutral atoms from a low-intensity atomic source have been guided via magnetic fields generated between two parallel wires on a glass substrate. The guiding of neutral atoms by the magnetic field due to microfabricated current-carrying wires on a chip is demonstrated in [37]. Two guide configurations are used in this work: the first one consists of two wires with an external magnetic field, and the second consists of four wires without an external field. It is pointed out that atom based splitters for interferometry are extensions of these chip-based guides. A simple splitter for guided atoms has been designed and experimentally studied in [38]. This splitter was realized with a current carrying Y-shaped wire nanofabricated on a surface. This splitter design ensures symmetry under a wide range of experimental parameters. Atom chips with these and more sophisticated designs can be integrated into surface mounted atom optical devices at the mesoscopic scale. Single mode propagation (12 mm) of Bose-Einstein condensates has been produced by [39]. Using optical tweezers, these condensates are first loaded into a microfabricated magnetic trap, and then released along homogeneous segments of the waveguide. It was observed that, due to geometric deformations of the microfabricated wires, inhomogeneities appear in the guiding potential which cause strong transverse excitations.

The possibility of creating a miniature de Broglie wave guide formed by two parallel current-carrying wires and a uniform bias field is presented in [40]. This waveguide can be split in a highly controlled way and manipulated on the submicron scale. Hinds *et al.* derive analytical expressions to describe this guide, together with a quantum theory to show the range of possibilities of atom manipulation on the submicron scale [40]. Cooling and trapping atoms, controlled splitting of the wave function, and exceedingly sensitive microscopic atom interferometry are examples of the possibilities proposed in this letter.

A microstructure which consists of microfabricated linear copper conductor of widths ranging from 3 μm to 4 μm is used in [41] for generating a strongly anisotropic potential. Bose-Einstein condensation has been achieved in this magnetic surface microtrap. An overview of atom chip magnetic micro traps is given in [42], where particular emphasis is given to the discussion of the use of microscopic lithographic conductors for the generation of Bose-Einstein condensates.

The formation of a BEC in surface micro traps was soon achieved by several groups [41, 43, 44, 45]. Furthermore, in [43] it is shown that the formation of a condensate can be greatly simplified using a microscopic magnetic trap on a chip. Hansel *et al.* have achieved Bose-Einstein condensation inside the single vapour cell of a magneto-optical trap in as little as 700 ms. This is more than a factor of ten faster than typical BEC experiments. A review of the use of microchip traps for Bose-Einstein condensation is provided by Jakob Reichel in [42]. Various publications since the first BECs were produced in atom chips have confirmed the suitability of these microfabricated devices for atom optics research [41, 46, 47]. Moreover, the atom chip BEC tool box keeps growing. Examples of new improvements on the manipulation of BECs on atom chips include magnetic waveguides [48], single-atom detection schemes [49], and long distance

magnetic conveyor belts [50].

The creation of Bose-Einstein condensates on atom chips and the highly controlled manipulation of atomic motion in these devices opened the door to a series of promising applications. The creation of quantum gates, quantum information processing devices, highly precise interferometric measurement devices, magnetometers, and accelerometers are some of the applications that have been identified. Treutlein *et al.* [51] have demonstrated the coherent manipulation of internal atomic states in a magnetic microchip trap. These authors have shown that a portable atom chip clock with a relative stability in the range 10^{-13} is a realistic goal. In addition, for applications in quantum information processing, this paper authors propose to use microwave near fields in the proximity of chip wires to create potentials that depend on the internal state of the atoms.

Undesired effects

In order to benefit from quantum mechanical effects manifested in atom optic experiments, the coherence of the matter waves and of their internal degrees of freedom must be maintained as long as possible. However, when quantum-degenerate gases are prepared in electromagnetic solid-state hybrid surface traps, such as atom chips, the maintenance of this coherence is highly non-trivial. The coupling of an atomic sample at a temperature of a few micro-Kelvin with a room temperature surface located a few micrometers away leads to heating of the sample, splitting of the clouds, and losses induced by thermal fluctuations on the surface.

A theoretical study of the lifetime and loss rate for a trapped particle coupled to fluctuating fields in the vicinity of a room temperature metallic surface is provided in [52]. This paper shows how the Zeeman coupling of the atomic magnetic moment to a fluctuating magnetic field leads to an enhancement of the trap loss rate at distances of a few tens of microns from a room temperature surface. Firstly, this investigation considers the atom-surface coupling leading to heating of the trapped atom; secondly, transitions to untrapped atomic internal states are also considered. These authors conclude that the effect of the near-field fluctuations is much stronger than that of the blackbody radiation.

A transport theory for atomic matter waves in low-dimensional waveguides is outlined in [53]. This study leads to an estimation of the thermal spectrum of magnetic near fields leaking out of metallic microstructures. Henkel *et al.* show that the coherence of cold atom clouds is limited by the scattering from thermal magnetic near fields generated by metallic microstructures at room temperature. These results imply that decoherence may be reduced by working with smaller metallic structures, reducing their temperature and their specific conductivity.

Bose-Einstein condensates and cold atom clouds held by a microscopic magnetic trap near a room temperature metal wire 500 µm in diameter were experimentally studied in [54]. Three surface-related decoherence effects are identified by the authors of this paper. Firstly, atom clouds break into fragments as a result of small spatially alternating magnetic fields parallel to the wire. This is presumably due to a small transverse component of the current. Secondly, the atom clouds are heated by audio frequency technical noise present in the currents that form the microtrap. In the third place, atoms trapped some tens of micrometres above a metal interact with the thermally fluctuating near field of the surface. In accordance with [52], the surface near-field induces spin-flips in the trapped atoms. These spin flips are induced by radio-frequency

thermal fluctuations of the magnetic field near the surface. The loss of atoms from the microtrap due to these spin flips was observed over a range of distances down to 27 μm from the surface [54]. However, atoms trapped in a chip should approach much more closely to the surface than ~ 10 μm. Consequently, the observed coupling between the atoms and the substrate represents a technical difficulty for the development of atom chips.

The limitations of coherent manipulations of neutral atoms with wire-based magnetic traps on atom chips are investigated in [55]. The magnetic noise originating from the surface of the chip is identified as the dominant decoherence mechanism. The contribution of fluctuations in the chip wires at the shot noise level is not negligible. Then, the coherence times are estimated and ways to increase them are discussed. It is shown that the spatial correlation length of magnetic fields due to shot noise is fixed by the distance between the micro-trap and the chip wire. In this paper is suggested that substrates with a permanent magnetization may provide the required low-noise environment.

Similarly, the behavior of Bose-Einstein condensates and ultracold atoms were investigated in the vicinity of a surface magnetic microtrap by Fortagh *et al.* in [56]. They report that the lifetime of cold atoms prepared near copper conductors shows a linear dependence on the distance from the surface. Additionally, a periodic fragmentation of the condensate and thermal clouds was detected above the surface. These same authors reported a characterisation of the magnetic field near the surface of room temperature copper conductors using ultracold atoms [57]. Kraft *et al.* have also found a longitudinal field $10^3 - 10^4$ times smaller than the usual circular field around the conductor. The presence of the anomalous longitudinal magnetic field produced near the conductor is manifested as fragmentation of the atom clouds when the distance from the conductor is $\lesssim 100$ μm. The atomic samples for these experiments have been prepared both above and below the critical temperature for Bose-Einstein condensation, and the fragmentation of the atomic distribution has been observed in both cases. The potential responsible for this fragmentation is shown to be of a magnetic nature and caused by a longitudinal field component, which in turn is caused by the current in the wire rather than by permanent magnetic inhomogeneities of the conductor. In addition, the results presented in this letter suggest that the field is generated at the surface rather than inside the conductor. This work represents an example of how ultracold atoms can be used as a sensitive probe for magnetic fields.

The weak magnetic field component previously observed in [54] has been probed with a cold atom cloud in the Centre for Cold Matter [58]. In agreement with Kraft *et al.* results, Jones *et al.* have found that the anomalous magnetic field has an average period along the wire of $\lambda = 230$ μm. Over the range of distances investigated in this work ($y = 250 - 350$ μm), the decrease of this field with the distance from the centre of the wire is well described by the modified Bessel function $K_1(2\pi y/\lambda)$. Jones *et al.* explain, in accordance with [56, 57], that the current follows an oscillatory or helical path along the wire with wavelength λ.

In conclusion, the coherent manipulation of cold atom clouds with surface mounted micro-fabricated current carrying wires is limited by two fundamental processes. In the first place, the trajectories of the charges flowing through the conductor seem to oscillate in the direction perpendicular to the main current flow. This current component is responsible for the fragmentation of the atom clouds when the distance to the surface is of the order of a few tens of micrometres. The second decoherence effect is a consequence

of the thermal fluctuation of charges in the room temperature surface. The near field generated by this fluctuation can drive spin flip transitions in the trapped atoms, causing atom losses and limiting the life times of these traps. For a review of the progress regarding the manipulation of atoms using microscopic atom-optical elements using current-carrying wires refer to Folman *et al.* [59]. Groth *et al.* have created a set of guidelines for minimising losses and related decoherence in atom chips [60]. Similarly, a study of the reduction of magnetic noise in atom chips by material optimization is provided in [61].

1.4.2 Permanently magnetised media

Three alternatives have been proposed to overcome the limitations that the experiments performed with current carrying wires had shown. First, Scheel *et al.* [62] have explored the possibility of reducing the spin decoherence due to surface fields by making metallic surfaces thin; second, Hohenester *et al.* [63] state that superconducting surfaces can be used to achieve low spin-flip rates in an atom chip; finally, it has been proposed to use instead permanently magnetised surfaces.

An extensive characterisation of the interaction between cold atom clouds and the field of periodically magnetised data storage media has been developed by our group. The interaction of cold rubidium atoms with media such as the audio-tape, the flexible computer disk ('floppy disk') and the video tape has been extensively studied [64, 65, 29]. For instance, these works have permitted the demonstration of an efficient magnetic reflector above the surface of a periodically magnetised piece of video tape. This is a particularly interesting and representative result of the work that has been developed by our research group.

A method for creating traps for neutral atoms above magnetic surfaces was presented in [66]. This method relies on the shift of the hyperfine sublevels that a paramagnetic atom experiences due to an external magnetic field. The magnetic field produced by the magnetisation of the surface can be optimised for trapping paramagnetic atoms with hyperfine structure. Very strong confinement and high vibrational frequencies perpendicular to the surface can be achieved. The *Zeeman effect surface trap* (ZEST) presented in [66] can be used to create a 2D waveguide. Due to the large mode spacing, the propagation of de Broglie waves in a single-mode is feasible.

Jones *et al.* [54] recommend to avoid the use of current-carrying wires on the surface of the chip. As an alternative for cooling the chip, permanent magnets, such as the surface of magnetic recording media, are suggested as substitutes for current carrying wires. The videotape and magneto-optical (MO) thin films are suggested for this applications. Atoms clouds have already been loaded into microtraps formed above a sinusoidally magnetised piece of videotape [67]. The characteristic length of the structures recorded in the videotape is $\sim 5\,\mu\text{m}$. MO films are proposed in [54] for reaching an even smaller length scale and then producing deep traps a few microns away from the surface.

Sinclair *et al.* [67] describe the array of micro-traps formed by a pattern of magnetisation on a piece of videotape. A magnetic sine wave with a period of 106 µm creates highly anisotropic (aspect ratio as large as $40\,\text{kHz} \times 4\,\text{Hz}$) micro-traps in which cold atom clouds have been successfully loaded. A measurement of the dependence of the atom-surface distance on the applied bias field allowed for the determination of the magnetic field present at the surface of the videotape, which is found to be of $11 \pm 1\,\text{mT}$. This is half of the field expected by the saturated magnetisation of the magnetic me-

dia, reported to be of 2.3 kG. When maintained at a distance of 100 μm, where the trap radial frequency f_r is ≤ 1 kHz, the traps are smooth and the atom clouds do not show signs of undesirable structure. Nevertheless, microscopic wells of order 1 μK deep are revealed at a distance of 50 μm from the video tape surface, where $f_r \leq 10$ kHz. These wells cause the atom cloud to break into pieces when it approaches the video tape surface.

A Bose-Einstein condensate containing 8×10^4 atoms has been produced in the videotape micro-traps [68]. The longitudinal and radial frequencies of the trap were 15 Hz and 320 Hz respectively. Measurements of lifetimes for the loss of atoms trapped above the videotape atom chip show that the spin flip rate should be due entirely to the 400 nm gold film on the surface. The videotape does not contribute appreciably to the loss rate, showing that permanent magnets may be preferable to metal atom chips in applications where the decoherence caused by magnetic field fluctuations needs to be avoided.

1.5 Overview of the project

In this project we have developed two new tools that can be integrated on an atom chip. Firstly, I have explored the possibility of integrating pyramidal hollow mirrors on the surface of a silicon based atom chip. Secondly, I have demonstrated how the remarkable properties of high density magnetic recording media can be utilised for creating a new kind of atom chip based on permanently magnetised media.

1.5.1 Pyramidal hollow mirrors in silicon

In this project we have explored the possibility of integrating optical components in atoms chips with the aim of overcoming the difficulties and disadvantages of the methods that are usually followed for loading cold atom clouds in the chip trapping potentials. In a typical atom chip experiment, an atom cloud is initially collected in a mirror magneto-optic trap. In this mirror MOT, cloud-surface distances are usually on the order of two or three millimetres and the temperature of the cloud is approximately 100 μK. Next, the collection of atoms is compressed down into a cylindrical cloud in what is called a compressed MOT [69]. For this purpose, the magnetic field utilised for creating the mirror MOT is replaced by a two dimensional quadrupole field. The 2D quadrupole is generated by a single current carrying wire and a bias field which creates a line of zero magnetic field parallel to the chip surface. In order to keep the loss of atoms as low as possible, the new 2D quadrupole has to be closely matched to the original MOT 3D quadrupole field. The temperature of the cloud in this stage is nearly 50 μK and the cloud-surface distance has been shifted down to around 800 μm.

After the compression stage, the cloud is transferred to a purely magnetic trap. The atomic population in the compressed MOT is distributed over a set of magnetic sublevels. In order to maximize the number of atoms confined in the magnetic trap, the atoms are optically pumped into a *low-field seeking* state. The magnetic trapping potential is obtained by combining the centre wire and bias fields, with the field of two auxiliary current carrying wires which close the ends of the 2D guide. The magnetically trapped atom cloud is then taken closer to the chip surface by increasing the bias field and reducing the current running through the centre wire. When the distance between the cloud and the chip surface becomes less than 100 μm, the collection of atoms begins to interact with the chip trapping potentials.

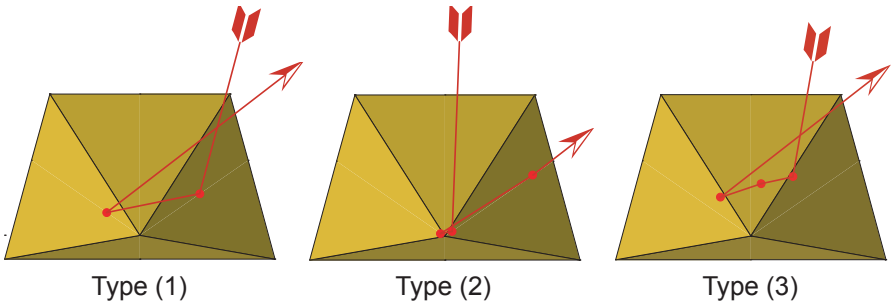

Figure 1.1: Examples of the three ray types generated in a 70.5° pyramid. In these images, a top view of a hollow 70.5° pyramid is presented with the paths that light incident parallel to the pyramid axis can follow as it is reflected from the hollow surface. Type (1) and type (2) rays are only reflected by two opposing faces of the pyramid, while type (3) rays suffer reflections on three of the four pyramid faces.

As both the loss of atoms and the heating of the cloud are desired to be kept as low as possible, properly matching the different stages of the loading process turns out to be a very meticulous, tedious, and time consuming task. As the atom chip fabrication techniques have been refined, it has been possible to attain atom-surface distances on the order of a few micrometers. This also means that tighter traps are created and consequently, fewer number of atoms are held in these traps. In order to detect, manipulate and controllably modify the internal states of atoms in these tiny clouds it is necessary to make them interact with light. In the experimental sequence outlined before, the laser light is delivered to the chip by means of external mirrors and lenses. As the atom-surface distance becomes small and fewer numbers of atoms are confined in these traps, detection and further manipulation tasks become very difficult. In response to these complications, the necessity of integrating, not only the sources of the trapping potentials, but also optical components into the atom chip has been pointed out in various publications [35, 36, 59].

Arrays of pyramidal pits have been fabricated in silicon wafers. A gold coating was laid on these pyramids to create an array of pyramidal hollow mirrors. We believe that these pyramids can be the main building block of an efficient mechanism for loading cold atom clouds right at the surface of an atom chip. We have studied in detail the optical properties of the pyramids fabricated in silicon wafers. Firstly, the angle between opposite faces in these pyramids is of 70.5°, instead of 90° as in the usual pyramid MOT arrangement [70, 71]. This has consequences on the light force balance produced inside the micro-fabricated mirrors. To begin with, a ray tracing analysis of this pyramidal geometry allowed us to identify three different types of pyramid reflections. An example of these ray types is given in figure 1.1. Type (1) and type (2) rays, those which are reflected exclusively by opposing faces of the pyramid, create a force balance along the pyramid axis and can therefore generate magneto-optical traps. In contrast, the third reflection type is reflected by three of the four pyramid faces. This type of ray is severely affected both in its propagation direction and in its polarisation state along its path inside the pyramid. The reflected intensity pattern generated when a laser beam is shone parallel to the pyramid axis shows contributions from the three ray types, as anticipated by the ray tracing analysis.

We have studied both theoretically and experimentally the appropriateness of the 70.5° pyramidal geometry for the generation of magneto-optical traps [72]. For this, we fabricated a large scale glass replica of the geometry generated in the silicon micro-mirrors. In addition, for comparison purposes, we also fabricated a pyramid with a 90° angle between its faces. We have proved that in order to create magneto-optical traps in silicon pyramids, it is necessary to eliminate or reduce the third type of rays. The first method that we proposed for this is to lay a low reflectivity coating on the surface of these pyramids. The third ray type is reflected three times by the pyramid faces before crossing through the pyramid axis, where the MOT is supposed to be generated. On the other hand, the first two ray types cross twice through the trapping region, the first time after just one reflection and the second after being reflected twice. Consequently, if a low reflectivity coating is utilised, the intensity of the third ray type, in comparison with the other two ray types, is severely reduced before reaching the trapping region. In our large scale replica of the silicon pyramid we tested various reflectivity coatings and found that an $\sim 80\%$ reflectivity gives the best results.

The second method that we proposed for taking care of these undesired light components consists of completely eliminating the areas of the light which give rise to these reflections. We first demonstrated the efficacy of this approach by placing a mask on the trapping beam utilised for creating the MOT in the large pyramid replica. In this experiment we found that a high reflectivity gold coating, which does not generate a MOT in the 70.5° when the full beam is shone into it, can be made to work if the type three ray areas of the beam are masked. We confirmed this result both by placing a mask on the trapping beam and by masking the pyramid surface at the moment of laying down the metallic coating.

We have also estimated the number of atoms that can be collected in a miniature silicon pyramid. We modelled numerically the scattering forces generated in the volume of these pyramidal hollow mirrors when circularly polarised light is shone perpendicularly to the chip surface and a quadrupole magnetic field is generated in the pyramid region. To confirm these estimations, we have mimicked experimentally the tiny pyramids using the large scale pyramid replica. Taking advantage of the pyramidal symmetry, we have placed the centre of the MOT magnetic quadrupole a few millimetres away from the pyramid apex. Then, scaling laws for the number of atoms collected in pyramids of different sizes have been determined by displacing the quadrupole centre positions along the pyramid axis. These experiments have allowed us to establish an empirical scaling law for the number of atoms that can be collected in a 70.5° pyramidal MOT. In addition, we have studied in detail the capture and loss rates as a function of the pyramid size, for pyramids which side length goes from 16 mm and down to about 3 mm. With this scaling law we anticipate that these traps can in principle collect as many as a few hundred atoms and as few as a single atom.

The first prototype of an atom chip with pyramids integrated on its surface has been designed and fabricated. Together with these micro-fabricated pyramids, this atom chip integrates also micro-fabricated current carrying wires circling the pyramid square openings. We show that the field generated by these wires is equivalent to square closed loops running along the edge of the pyramid apertures. Therefore, a bias field perpendicular to the chip surface can be utilised together with these wires to generate an spherical quadrupole field inside the pyramid. This configuration creates two points of zero magnetic field. Both points are located on the pyramid axis, one inside of the pyramid and the second one outside of the pyramid. This extra feature can in principle

Table 1.1: Magnetic Specifications of Recording Media [29, 75, 67].

Recording Medium	Remanent Field (G)	Magnetic Layer Thikness (μm)	Room Temperature Coercivity (Oe)
Audio tape Denon HD-M	3500	4.0	1200
5 1/4 inch floppy disk Sony MD-2D	700	2.5	290
Video Tape Ampex 398 Betacam SP	2300	3.5	1500
MO Multi Layer Film $15 \times$ (4 Å Co/10 Å Pt)	23000	0.021	1600

be utilised for controllably extracting the atoms from the hollow pyramid volume. This atom chip has been mounted and wire bonded to an electronics industry standard ceramic pin grid array chip carrier.

1.5.2 Magneto-optic multilayer thin films

The second part of this research project is related to the testing of new magnetic materials suitable for using in atom chip applications. New materials with high room-temperature coercivity, strong remanent magnetisation and small domains are developed for the production of high density magnetic recording media [73, 74]. Curiously, the requirements of this later application are very much the same as those for applications in atom optics. An example of these novel magnetic media is the Co/Pt multilayer thin film.

The properties of high density magnetic recording media seem to be ideal for the creation of atom chips. Well defined microscopic patterns of magnetisation can be created with sub-micron resolution on the surface of these media. In addition, long term stability and robustness of a signal recorded in these media, as in the storage of information, results particularly interesting for atom optical applications. The magnetic field produced above the surface of a patterned Co/Pt multi-layer thin film, together with suitable external fields, has been proposed for trapping Rb atoms [54]. The properties of Co/Pt MO films represent clear advantages over other magnetic media that, nevertheless, have already shown their suitability for reflecting, guiding, and trapping neutral atoms. In table 1.1, these MO films properties are compared with those of other magnetic media that our group has previously used. Co/Pt MO films present perpendicular magnetic anisotropy. Therefore, arbitrary two-dimensional patterns can be created in the plane of the film. To continue, the strong remanent magnetisation together with the small scale of the structures imply that large magnetic field gradients of the order of 10^4 T/m can be produced above the surface of these films. The high room-temperature coercivity of these films guarantees the stability of the magnetic patterns even in the presence of the magnetic fields utilised in a typical atom chip experiment.

We have built an apparatus for writing magnetic patterns in these films [73]. The patterns are determined by areas of opposite magnetisation within the film surface. We have shown that patterns with features in the micrometre scale can be written. These

patterns can be scaled up to millimetre dimensions. Two different patterns have been created. The first consists of a large array of parallel lines such as the signal recorded in the video tape atom chip. However, the features recorded in the Co/Pt film are much smaller than those present in the video tape and the high remanent magnetisation of the MO film promise higher trap frequencies. The second pattern that we have created is an array of Z-like patterns, which result in Ioffe-Pritchard type traps above the film surface. We have performed numerical estimations of the atom traps that can be generated above these magnetic patterns.

We demonstrated that magnetic micro-traps can be generated above the surface of magneto-optical Co/Pt thin films [76]. In this thesis, I will describe the apparatus used for writing the magnetisation patterns on the surface to these MO films. These patterns have features of a few microns and numerical calculations of the steep trapping potentials that can be generated above them has been developed. At a distance of 750 nm from the chip surface, these traps can be as deep as 3 mK and have harmonic frequencies of up to 1.1 MHz. The domain structure of these magnetic films seems to be the limiting factor of the patterns quality. We show that the borders between regions of opposite magnetisation present transverse oscillations which dimensions are comparable to the domain structure observed in a demagnetised sample.

1.6 Organization of this thesis

In the following paragraphs I describe the contents of this thesis.

To begin with, the theory of laser cooling and trapping of neutral atoms is given in chapter 2. The scattering force is the starting point for explaining the concept of Doppler cooling. Next, the processes involved in subDoppler cooling are briefly described. To continue, the magneto-optic trap (MOT) operation principles are introduced. Particularly, the filling dynamics of the MOT are studied in some detail. Finally, some relevant concepts regarding magnetic trapping of neutral atoms are studied with the aim of setting the basic requirements utilised in the design of atom chips.

Chapter 3 contains a description of the experimental resources that have been built as part of my research project. This begins with the design and construction of both the vacuum and the laser systems; next, the procedure for making glass pyramids is described together with the analysis of the resulting hollow mirrors; in the third place, I present the various magnetic field sources utilised in our experiments and how they were used for achieving the required field configurations; this chapter concludes with a description of the methodology used for imaging of cold atom clouds.

Chapter 4 reports the experiments performed to determine the suitability of the silicon hollow pyramidal mirrors for applications in atom optics. In this chapter I first demonstrate that cold rubidium clouds can be magneto-optically trapped in a 70.5° pyramid. Then, I also present the results obtained by coating both the 70.5° and the 90° pyramids with different metallic coatings. Here, it is also shown under which circumstances the MOT works in a 70.5° pyramid covered with a highly reflective gold coating. Next, the chapter continues with an experimental determination of the scaling laws for the number of atoms versus the size of the pyramids. Capture and loss rates measurements are then provided and these results are used to estimate the number of atoms that can be trapped in an atom chip pyramid.

Chapter 5 begins with a brief description of the fabrication of pyramids in silicon wafers. Then, the chapter continuous analysing both the geometrical and optical prop-

erties of the resulting pyramids, as well as these properties implications on the MOT performance. The first prototype of a pyramid atom chip, which integrates microfabricated pyramids and wires, is shown next. This is accompanied with a detail description and characterisation of the resources utilised for incorporating the atom chip into our vacuum system.

An introduction to the physics of magneto-optic thin films is provided at the beginning of chapter 6. After this, the focus of the chapter is narrowed around the characteristics of the Co/Pt multilayer films that we have fabricated. The thermo-magnetic recording technique utilised for writing magnetisation patterns in these MO films occupies a separate section of the chapter. Then, I present the two different patterns that we have created. A detailed analysis of the magnetic trapping potentials that can be generated above these patterns is provided.

To conclude, chapter 7 summarizes the most important results of this research project. Here, I discuss the place that these achievements occupy in atom optics research, and particularly in the development of atom chips. In addition, this chapter identifies the future directions of this research and the challenges that this particular project faces.

Chapter 2

Cooling, trapping and manipulating atoms

In this chapter, I describe the basic theory involved in atom optics. Firstly, the two-level atom laser cooling model is used for introducing the concepts of Doppler cooling and optical molasses. Then this model is extended to multilevel atoms for explaining the sub-Doppler cooling mechanisms. Next, I explain how a magnetic field can work together with the optical field for trapping atom clouds in a magneto-optical trap (MOT). Then, the MOT filling dynamics are analysed. In addition, I also provide an introduction to the Physics of magnetostatic trapping neutral atoms. Finally, I conclude this chapter by discussing the miniaturization of MOTs and magnetic traps.

2.1 The scattering force

The scattering force that a laser light field exerts on an atom is the basis of a method for cooling atoms. As Metcalf and Van der Straten explain in [77], when an atom absorbs a photon, it gains a momentum $\hbar\mathbf{k}$ in the direction of the laser beam, where $\mathbf{k} = \frac{2\pi}{\lambda}\hat{\mathbf{k}}$ is the wave vector of light with wavelength λ. Over many absorption cycles, the time-averaged force exerted on an atom by a laser beam is equal to the momentum kick $\hbar\mathbf{k}$ each photon exerts on the atom times the rate at which the absorption and emission process takes place. This force is then $\vec{F} = \hbar\mathbf{k}\Gamma$, where Γ is the total scattering rate. In sponataneous emission however, the time-average momentum gain experienced by this atom is zero because photons are emitted symmetrically in all directions. The total scattering rate Γ can be expressed in terms of both the laser intensity I and the detuning from the atomic transition Δ as measured in the atom frame of reference:

$$\Gamma(I, \Delta) = \frac{\gamma}{2} \frac{I/I_{sat}}{1 + I/I_{sat} + (2\Delta/\gamma)^2} \tag{2.1}$$

In this equation, γ is the spontaneous emission rate ($\tau = 1/\gamma$ is the excited state lifetime) and I_{sat} is the saturation intensity of the atomic transition, which is defined

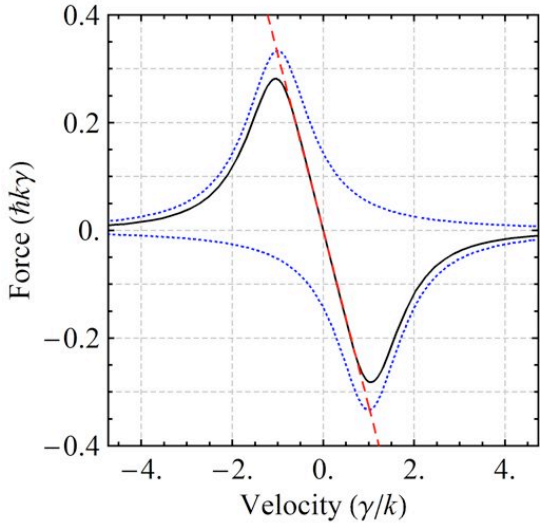

Figure 2.1: The time-averaged force on a two-level atom in a 1D optical molasses. The forces exerted by each light beam individually are shown as blue dotted lines and the solid line corresponds to the total force given by equation 2.4. The linear approximation (equation 2.5) is represented as a dashed straight line.

as the laser intensity value which generates an excited state population fraction of $^1/_4$ at zero detuning. For a two level atom, I_{sat} is given by

$$I_{sat} = \frac{\pi h c \gamma}{3\lambda^3}. \tag{2.2}$$

In conclusion, the scattering force experienced by an atom at rest turns out to be

$$\mathbf{F} = \frac{\hbar \mathbf{k} \gamma}{2} \frac{s_0}{1 + s_0 + (2\Delta/\gamma)^2} \tag{2.3}$$

where the on-resonance saturation parameter is $s_0 = I/I_{sat}$.

2.1.1 Doppler cooling and optical molasses

The scattering force depends on the Doppler shift ω_D of the laser frequency as experienced in the reference frame of a moving atom. The wavelength of the light measured in the reference frame of an atom moving away from the source of the light is longer than the actual wavelength measured in a reference frame at rest. Similarly, an atom moving towards the light source witnesses the opposite shift of the wavelength of the light. As a result of this shifts, the scattering rate depends on the velocity of the atom and on the detuning of the laser frequency from the atomic transition. The laser frequency in the reference frame of the moving atom is Doppler shifted, which results in a detuning $\Delta_D = (\omega_\ell - \omega_a) - \mathbf{k} \cdot \mathbf{v}$ with ω_ℓ as the laser frequency, ω_a as the atomic transition frequency in the absence of a magnetic field, and $\mathbf{k} \cdot \mathbf{v}$ as the first order Doppler shift. For red detuned light ($\omega_\ell < \omega_a$) the atom is more likely to absorb photons from the beam whose propagation direction opposes the motion of the atom. Therefore, a detuning of the laser frequency around the atomic transition can be used to selectively reduce the velocity of those atoms moving against the light. This method for reducing the kinetic energy of a sample of atoms is known as *Doppler Cooling* [77].

Let $\delta = \omega_\ell - \omega_a$ be the detuning of the laser frequency from the atomic transitions as measured on a reference frame at rest. Then, the one-dimensional time-averaged force on a two-level atom due to a counter-propagating pair of beams can be written as

$$F_x = \frac{\hbar k_x \gamma}{2} \left(\frac{s_0}{1 + s_0 + \frac{4(\delta - k_x v_x)^2}{\gamma^2}} - \frac{s_0}{1 + s_0 + \frac{4(\delta + k_x v_x)^2}{\gamma^2}} \right). \tag{2.4}$$

This force can be expanded as a Taylor series in v_x around $v_x = 0$. Retaining only the linear term of this expansion gives

$$F_x = -\frac{8\hbar\delta k_x^2}{\gamma}\frac{s_0}{\left(1+s_0+\frac{4\delta^2}{\gamma^2}\right)^2}v_x = -\beta v_x \tag{2.5}$$

This shows that the average force tends to damp the motion of atoms in the direction of the laser field, where we have defined β as the damping constant. The total force expressed in equation 2.4 is plotted in figure 2.1 as a solid curve, together with the contributions from each one of the two laser beams that are shown as dotted curves. The dashed straight line is the first order Taylor expansion (equation 2.5) which shows the restoring nature of this force.

If the laser field consists of three pairs of counter propagating beams, each pair aligned orthogonal to others, the force acts on each of the three spatial degrees of freedom of these atoms. The analysis presented previously can be easily extended to three dimensions. This creates a region, the intersection of the six laser beams, where the motion of the atoms experiences a viscous damping. This is known as an *optical molasses* [5]. A cold atom cloud forms in the optical molasses having a velocity distribution which is generally Maxwellian. A temperature T can be assigned to the velocity distribution, which for an n-dimensional trap is

$$\frac{n}{2}k_B T = \sum_{i=1}^{n}\frac{m}{2}v_i^2 \tag{2.6}$$

Here, the thermal energy per degree of freedom is $\frac{1}{2}k_B T$ and v_i is the r.m.s. velocity in the ith direction.

The minimum temperature achievable with Doppler cooling is reached when the rate of removal of kinetic energy by the damping force is balanced by the heating rate due to the random nature of the absorption and emission of photons. Due to the discrete nature of atom-photon interaction, the cycles of absorption and emission of photons are seen by the atom as two steps of a random walk in momentum space [77]. The size of these steps is given by the momentum kick $\hbar k$ induced in the atoms. After N such kicks, the atom r.m.s. momentum grows as $\sqrt{N}\hbar k$. Therefore, the condition of balance between the damping force and the heating rate leads to the *Doppler Temperature* [77]

$$T_D = \frac{\hbar\gamma}{4k_B}\frac{1+I/I_{Sat}+(2\delta/\gamma)^2}{2|\delta|/\gamma} \tag{2.7}$$

In the low intensity limit and for $\delta = -\gamma/2$, the Doppler temperature is minimal and is reduced to $T_D = \hbar\gamma/2k_B$. For example, the $5P_{3/2}$ state of ^{85}Rb and ^{87}Rb are characterised by spontaneous decay rates equal to $\gamma = 5.98$ MHz and $\gamma = 6.07$ MHz respectively. Correspondingly, the minimal Doppler temperature associated to the D2 line of these two rubidium isotopes is $T_D = 143$ µK and $T_D = 145$ µK respectively.

2.2 Sub-Doppler cooling

The variety of processes taking place in optical molasses is much richer than this two level atom model. In a real atom, energy shifts in the hyperfine sublevels can be induced by perturbing fields, such as light or an external magnetic field. The multilevel atom picture is then more adequate for distinguishing the more subtle details of these experiments.

2.2.1 Polarization gradient cooling

When considering the multilevel atom, temperatures below T_D can be achieved through the interaction between the atom hyperfine structure and the spatial variation of the light polarisation in optical molasses. This mechanism, called *Polarization Gradient Cooling*, operates in low magnetic fields ($\mid B \mid < 100\,\mathrm{mG}$) and with an optimum detuning greater than that for Doppler cooling. Polarisation gradient cooling can lower the minimum temperature by a large factor compared to that predicted by Doppler cooling theory [7, 77].

The variation of the light intensity in optical molasses induces AC Stark shifts in the atomic energy sublevels. Due to these shifts, atoms experience an exchange of kinetic for internal potential energy as they move through the light field. As the atoms move across the polarisation gradients of the light field, the shift tunes the atomic energy levels to the frequency of the light and, at the point of maximum potential energy, these atoms are optically pumped into a state of lower energy. The energy stored in the internal structure of the atom has now been liberated and its initial kinetic energy is lost. As the atom moves trough the changing polarisation of the light field, it continues losing energy in successive cycles of shifts and optically pumped transitions. A detailed description of this cooling mechanism is given in [7]. The recoil of one photon then corresponds to the lowest theoretically achievable temperature by sub-Doppler cooling:

$$T_{recoil} = \frac{\hbar^2 k^2}{k_B m} \tag{2.8}$$

For ^{87}Rb $T_{recoil} = 361\,\mathrm{nK}$ and for ^{85}Rb $T_{recoil} = 370\,\mathrm{nK}$. Note that this new limit is four hundred times lower than the one given by the Doppler temperature.

2.3 The magneto-optic trap (MOT)

In a magneto-optic trap (MOT), the exchange of momentum is produced in a wide range of distances and velocities. The change in the Doppler shift of the decelerated atoms is compensated by introducing a Zeeman shift [77]. A spherical quadrupole magnetic field is in general utilised for generating this compensation. This field consists of a point of zero magnetic field located in the centre of the quadrupole, with the field increasing linearly with position as one moves radially from the centre. Consequently, the Zeeman shift is induced by the movement of the atoms in the inhomogeneous magnetic field. The Zeeman interaction energy is given by $-\boldsymbol{\mu} \cdot \mathbf{B}$, where $\mathbf{B}$ is the spatially varying magnetic field and $\boldsymbol{\mu}$ is the atomic magnetic dipole moment. Therefore, the effective detuning between the atomic cooling transition and the laser field in this situation is given by

$$\Delta_Z = \delta - \mathbf{k} \cdot \mathbf{v} - \boldsymbol{\mu} \cdot \mathbf{B} \tag{2.9}$$

Substituting this detuning in equation 2.3 results in a force that depends on both the velocity and the position of the atoms.

Provided that the magnetic field magnitude B is $\lesssim 300\,\mathrm{Gauss}$, the interaction of a moving atom with the magnetic field can be approximated by the first-order Zeeman shift. The splitting between a pair of magnetic sublevels can be written as $\omega_Z = -\mu' B/\hbar$, where $\mu' \equiv (m_e g_e - m_g g_g)\mu_B$ is the effective magnetic moment of the transition. Here, $m_{g,e}$ and $g_{g,e}$ are the magnetic quantum numbers and the Landé factors of the ground g and the excited e states respectively.

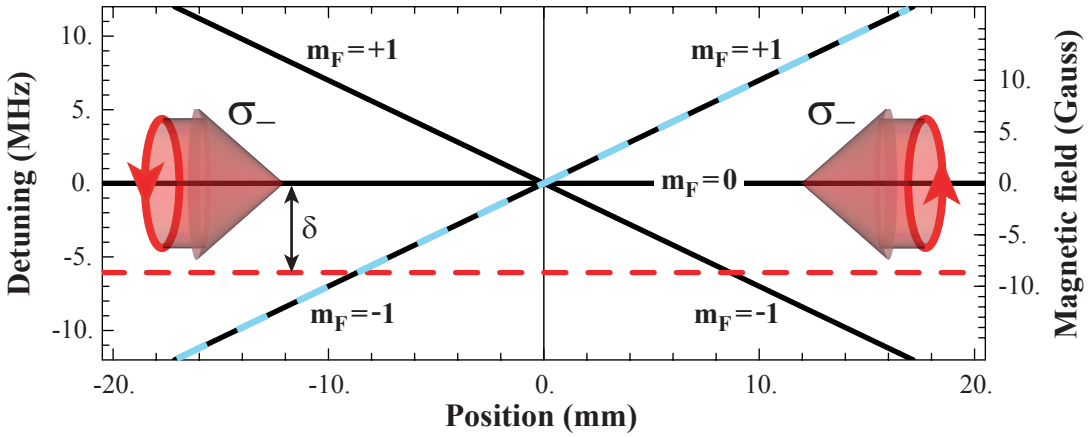

Figure 2.2: The Zeeman splitting tunes the atomic transition energy as the atom moves across the inhomogeneous magnetic field. In this graph, the right hand side scale indicates the magnetic field (dashed light blue line) that increases linearly with position having a gradient of 10 G/cm. The left hand side scale shows the corresponding splitting of the $m_F = \pm 1$ magnetic sublevels (solid black lines). Finally, the red dashed horizontal line denotes the trapping light frequency, which is tuned below the resonance with the unshifted transition $m_F = 0$

A scheme of transitions between hyperfine levels for magneto-optic trapping can be summarised as follows: $|F, m_F\rangle \longrightarrow |F', m'_F\rangle = |F', m_F\rangle, |F', m_F \pm 1\rangle$, where m_F and m'_F are respectively the ground and excited states projections of the total atomic angular momentum, F, onto the quantization axis defined by the magnetic field direction. In the one-dimensional case, in which the field B can be written in terms of a constant gradient $\partial_x B = \frac{\partial B}{\partial x}$, the energy shifts grow linearly with the field magnitude and the Zeeman induced tuning of the atomic transition is

$$\omega_Z = -\frac{\mu' B}{\hbar} = -\frac{\mu' \partial_x B}{\hbar} x$$

This tunes the atomic transition around the laser frequency as the atom moves away from the trap centre. The blue dashed line superimposed in figure 2.2 represents a linearly increasing magnetic field, whose magnitude is given by the right hand axis of the graph. The left hand axis on this graph represents the Zeeman tuning of the magnetic sublevels $m_F = \pm 1$ with respect to the unshifted $|0, 0\rangle \longrightarrow |1, 0\rangle$ transition.

Each photon carries an angular momentum $\hbar$. The projection of this angular momentum on the quantisation axis defined by the magnetic field direction can be 0, or ± 1. In the MOT diagram given in figure 2.2 we have assumed that the quantisation axis is defined locally by the magnetic field direction $\mathbf{B}$. In this basis, σ_+ denotes light for which the projection of its angular momentum along the magnetic field direction is positive (right hand circularly polarised light with respect to $\mathbf{B}$), σ_- corresponds to light for which this projection is negative (left hand circularly polarised light with respect to $\mathbf{B}$), and π refers to linearly polarised light with angular momentum equal to zero.

The conservation of angular momentum establishes that the absorption of a photon must be accompanied by the corresponding change of the projection of the atomic angular momentum. This imposes a set of selection rules on transitions driven by circularly

and linearly polarised light. Firstly, σ_+ light drives $\Delta m_F = +1$ transitions; next, σ_- light drives $\Delta m_F = -1$ transitions; and finally, for π light $\Delta m_F = 0$. The dashed horizontal line included in figure 2.2 represents light that is red detuned (detuning δ) from the $|0,0\rangle \longrightarrow |1,0\rangle$ transition. Then, if an atom moves away from the trap centre in the positive direction it preferentially absorbs σ_- photons from the beam travelling towards the left. Likewise, if the atom moves away from the trap centre along the negative direction it will preferentially absorb σ_- photons from the beam that travels towards the right.

2.3.1 The one-dimensional analysis of the MOT

The one-dimensional treatment of the optical molasses introduced in section 2.1.1 can be extended to take into account the Zeeman shift generated in the presence of an inhomogeneous magnetic field. The linearly increasing field strength creates a spatial dependence in the detuning term of the scattering rate given in equation 2.1. This produces a confining force that points towards the centre of the trap and makes it possible to cool and trap atoms simultaneously. Including the first-order Zeeman shift, the detuning term becomes

$$\Delta_\pm = \delta \mp kv \pm \mu' B/\hbar$$

where the + and − subindexes refer to the right going and the left going beams respectively. Equation 2.3 can be used to write down the force exerted by each beam on the atoms

$$\mathbf{F}_\pm = \pm \frac{\hbar k \gamma}{2} \frac{s_0}{1 + s_0 + (2\Delta_\pm/\gamma)^2}, \tag{2.10}$$

and the total force would be

$$\mathbf{F} = F_+ + F_-$$

A first order series expansion in v around $v = 0$ of this force results in a velocity independent term that can be identified with a restoring force characterised by a spring constant

$$\kappa = \mu' \partial_x B \frac{8 k s_0 \delta}{\gamma \left(1 + s_0 + \frac{4\delta^2}{\gamma^2}\right)^2}, \tag{2.11}$$

Similarly, as found in the analysis of the optical molasses (see equation 2.5), the velocity dependent term is identified with a damping coefficient

$$\beta = \frac{8 k^2 s_0 \delta \hbar}{\gamma \left(1 + s_0 + \frac{4\delta^2}{\gamma^2}\right)^2} \tag{2.12}$$

The force around the MOT centre is therefore approximated by

$$\mathbf{F} \approx -\beta v - \kappa x, \tag{2.13}$$

which leads to damped harmonic motion of the atoms. For ^{85}Rb atoms with $s_0 = 1$, a detuning $\delta = \gamma/2$ and a field gradient $\partial_x B = 10\,\mathrm{G/cm}$, the damping rate of this motion ($\Gamma_{MOT} = \beta/M$) is 21 kHz and the oscillation frequency ($\omega_{MOT} = \sqrt{\kappa/M}$) is less than 5 kHz. This corresponds to overdamped motion with a restoring time to the trap centre $2k/\mu' \partial_x B = 1.8$ ms. In addition, under this simplified model of the MOT we can conclude that a trap of radius R has a depth $U_0 = \frac{1}{2}\kappa R^2$ and a capture velocity $v_c = \frac{\beta R}{M}$.

2.3.2 Extension to three dimensions and multiple level atoms

A complete treatment of the MOT has to consider the spatial variation of the light intensity, the angle between the light propagation direction and the local magnetic field direction, as well as optical pumping processes between multiple atomic levels. Lindquist *et al.* [78] have derived an extension to the MOT force for the two-dimensional case. A further extension to three dimensions and N_{Beams} laser beams can be written as

$$\mathbf{F} = \sum_{i=1}^{N_{Beams}} \frac{\hbar \mathbf{k}_i \gamma}{2} \sum_{\Delta m=-1}^{\Delta m=+1} \sum_{m_F=-F}^{m_F=+F} P^{\sigma^\pm}_{\Delta m=0,\pm1} |C^{\Delta m}_{m_F}|^2 \frac{I(\mathbf{r})}{I_{sat}(\Delta m, m_F)} \times \left(\frac{1}{1 + \frac{I(\mathbf{r})}{I_{sat}(\Delta m, m_F)} + \frac{4\Delta^2}{\gamma^2}} \right) \tag{2.14}$$

The dependence of the light intensity $I(\mathbf{r})$ on the three-dimensional position $\mathbf{r} = (x, y, z)$ is now explicitly introduced and the saturation intensity now depends on each individual transition and on the initial m_F level. Similarly, the square of the Clebsch-Gordan coefficients $|C^{\Delta m}_{m_F}|^2$ provides the probability for each m_F to $m_{F'}$ transition. Finally, to account for the different orientations of the light propagation direction and the local magnetic field, in [79, 80, 81] it is shown that the fraction of light $P^{\sigma^\pm}_{\Delta m=0,\pm1}$ that drives $\Delta m = -1, 0$, or $+1$ transitions is given by

$$P^{\sigma^\pm}_{\Delta m=+1} = \frac{1}{4}(1 \pm \cos\theta)^2, \qquad P^{\sigma^\pm}_{\Delta m=-1} = \frac{1}{4}(1 \mp \cos\theta)^2, \qquad P^{\sigma^\pm}_{\Delta m=0} = \frac{1}{2}\sin^2\theta \tag{2.15}$$

where θ represents the angle between the local magnetic field and the propagation direction of each laser beam. The effective detuning Δ needs to be computed in accordance with equation 2.9.

2.3.3 The Rubidium MOT

Because of the large number of absorption and spontaneous emission cycles that are required for laser cooling, a closed transition between atomic states needs to be selected. The large hyperfine energy splitting of alkali atoms allows large laser detuning from a given transition, while transitions to unwanted energy levels are minimised. The D2 transition (see figure 2.3) is used for cooling and trapping either of the two most abundant isotopes of rubidium, ^{87}Rb and ^{85}Rb.

Two laser sources are required to magneto-optically trap rubidium atoms. Firstly, a closed atomic transition that can be excited repeatedly needs to be selected. For the most abundant Rubidium isotopes, ^{87}Rb and ^{85}Rb, $5^2S_{1/2}; F = 2 \rightarrow 5^2P_{3/2}; F = 3$ and $5^2S_{1/2}; F = 3 \rightarrow 5^2P_{3/2}; F = 4$ are, respectively, cycling transitions. The light used for generating this excitation can also drive off-resonant transitions to the $5^2P_{3/2}; F = 2$ state in ^{87}Rb, or to the $5^2P_{3/2}; F = 3$ state in ^{85}Rb. Atoms in these states can decay to the complementary F states of the $5^2S_{1/2}$ level. Once in this state, these atoms can not be excited by the cooling laser and therefore, a second laser, the repumper, is required for pumping them back into the cycling transition.

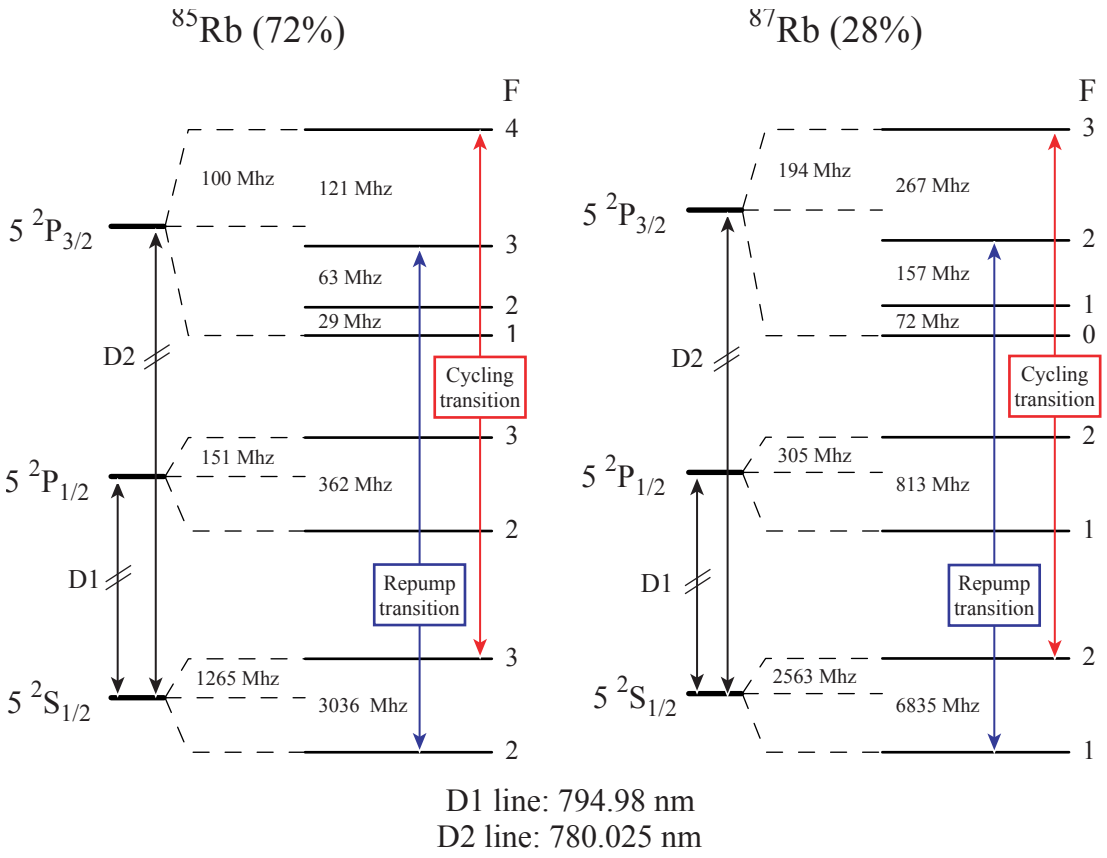

Figure 2.3: The rubidium energy levels [82].

2.4 The MOT filling rate equation

The change in the number of atoms N collected in a MOT is equal to the difference between the rate at which atoms are captured and the rate at which atoms are lost. The MOT filling rate equation can be expressed [79, 83] as

$$\frac{dN}{dt} = R - \frac{N}{\tau} - \eta\frac{N^2}{V} \tag{2.16}$$

The capture rate and the trap lifetime are represented as R and τ respectively. The third term in eq. 2.16 corresponds to the losses resulting from two-body collisions between atoms in the trap, where V is the volume occupied by the atom cloud. Steane *et al.* [79] explain that this term is significant at high densities of trapped atoms. In contrast, when $\eta\frac{N^2}{V}$ is insignificant compared with the first two terms in eq. 2.16, the loss rate is independent of the number of atoms contained in the trap. Under these circumstances, the capture rate R and the trap life time τ determine the MOT filling dynamics. Neglecting the third term in the rate equation, the solution to eq. 2.16 is

$$N(t) = N_s(1 - e^{-t/\tau}) \tag{2.17}$$

where $N_s = R\tau$ is the steady state number of atoms in the MOT.

2.4.1 The capture rate

To estimate the capture rate of a MOT we first consider that the rubidium vapour is in thermal equilibrium with the vacuum chamber walls. This gas can therefore be described by a Maxwell Boltzmann distribution and the flux of atoms entering into the MOT capture region can be easily calculated. We begin by defining the capture velocity v_c as the maximum velocity an atom entering into the capture region can have in order to be trapped. The capture rate is then estimated by determining the number of atoms with velocities lower than or equal to v_c crossing through the surface that delimits the trapping volume. Hence, the summation which makes up the atom flux entering into the capture region is limited to the interval $0 \leq v \leq v_c$.

For a gas at a temperature T, the mean number of atoms per unit volume $n(\boldsymbol{v})$ with a speed $v \equiv |\boldsymbol{v}|$ in the range between v and $v + dv$ is given by the Maxwell Boltzmann distribution of speeds [84]

$$n(\boldsymbol{v})\, dv = 4\pi n \left(\frac{m}{2\pi k_B T}\right)^{3/2} e^{-\frac{m\boldsymbol{v}^2}{2k_B T}}\, dv$$

where the atom mass is denoted by m and n is the gas density. The number of atoms Φ_c with velocities lower than or equal to v_c entering the trapping region per unit area and per unit time is

$$\Phi_c = \frac{1}{4}\int_0^{v_c} n(v) v\, dv = n\sqrt{\frac{m}{2\pi k_B T}}\left[\frac{k_B T}{m} - e^{-\frac{m v_c^2}{2k_B T}}\left(\frac{k_B T}{m} + \frac{1}{2}v_c^2\right)\right] \tag{2.18}$$

Only the slowest atoms are collected in the trap. Consequently, equation 2.18 can be simplified by expanding it into a power series in v_c around $v_c = 0$. Truncating the series at the fourth term yields

$$\Phi_c \simeq \frac{n}{8\sqrt{2\pi}}\left(\frac{m}{k_B T}\right)^{3/2} v_c^4 \tag{2.19}$$

The MOT capture rate R can then be obtained by multiplying the flux Φ_c by the area A that bounds the trapping region. In the case of the six beam MOT this region would be defined by the intersection of the six laser beams. Consider for example that the trapping region is a sphere of radius r, in which case the capture rate is

$$R = \Phi_c A \simeq \frac{n}{8\sqrt{2\pi}}\left(\frac{m}{k_B T}\right)^{3/2} v_c^4 (4\pi r^2) \tag{2.20}$$

The capture velocity

As an initial estimate of the capture velocity, let us consider the point where the Doppler shift takes the atom out of resonance with the trapping beams [11]. If laser light of wavelength λ is detuned by one natural linewidth from the atomic resonance, this estimate would correspond to $v_c \approx \gamma\lambda$. Here, $\gamma\lambda$ is the velocity at which the Doppler shift is equal to the natural linewidth γ of the transition. In the case of ^{85}Rb atoms, for which $\gamma = 2\pi\ 5.98\,\text{MHz}$, $v_c \approx 9\,\text{m/s}$.

However, Steane *et al.* [79] pointed out that the force is still significant at velocities above a few Doppler widths. Instead, these authors suggest that a typical value of v_c can be estimated by considering a force equal to half the maximum scattering force, which would correspond to a deceleration $a = \hbar k\gamma/4m$. Then, the capture velocity is

identified with the velocity of an atom that is stopped in a distance equal to the radius r of the trap, $v_c = (2ar)^{1/2}$. For a ^{85}Rb atom and considering a trap radius of 4 mm, this estimation results in $v_c = 21$ m/s.

We can take now this estimate of v_c to express the capture rate derived before (equation 4.2) in terms of the spherical trapping region radius

$$R = \sqrt{2\pi}\left(\frac{m}{k_B T}\right)^{3/2}\left(\frac{\hbar k\gamma}{4m}\right)^2 n\, r^4 \tag{2.21}$$

If we consider again a 4 mm in radius spherical trapping region for ^{85}Rb atoms, a capture rate of 4×10^7 s^{-1} for a rubidium partial pressure of 4×10^{-9} mbar ($n \sim 10^{14}$ m^{-3}) is obtained by this relation.

2.4.2 The loss rate

The loss mechanisms that normally determine the value of τ are due to collisions with Rb and non-Rb background atoms. Equation 2.16 with no loading term and neglecting the two body loss term reduces to

$$\frac{dN}{dt} = -\frac{N}{\tau} \tag{2.22}$$

This indicates that the number of atoms in the trap decays exponentially with time after the loading is switched off

$$N(t) = N_0 e^{-t/\tau}$$

where N_0 is the initial number of atoms in the trap.

Losses from a trapped atom cloud occur due to collisions with room-temperature background atoms. The losses caused by collisions with background Rb atoms can be expressed in terms of the rubidium atom density,

$$\frac{1}{\tau_{Rb}} = n_{Rb}\,\sigma_{Rb}\,v_{th} = n_{Rb}\,\sigma_{Rb}\left(\frac{3\,k_B\,T}{m_{Rb}}\right)^{1/2} \tag{2.23}$$

where σ_{Rb} is the cross section for collisions between a cold trapped atom and a fast background rubidium atom. In addition, this equation makes use of the definition of the mean velocity of thermal atoms $v_{th} = \sqrt{3\,k_B\,T/m_{Rb}}$. Similarly, other species contributing to the background pressure can eject atoms out of the MOT. The characteristic time of these processes is such that

$$\frac{1}{\tau_b} = n_b\,\sigma_b\left(\frac{3\,k_B\,T}{m_b}\right)^{1/2}. \tag{2.24}$$

Consequently, the total amount of losses caused by collisions with all varieties of hot background atoms is characterised by the $^1/_e$ time in which atoms are ejected from the MOT:

$$\frac{1}{\tau} = \frac{1}{\tau_{Rb}} + \frac{1}{\tau_b} \tag{2.25}$$

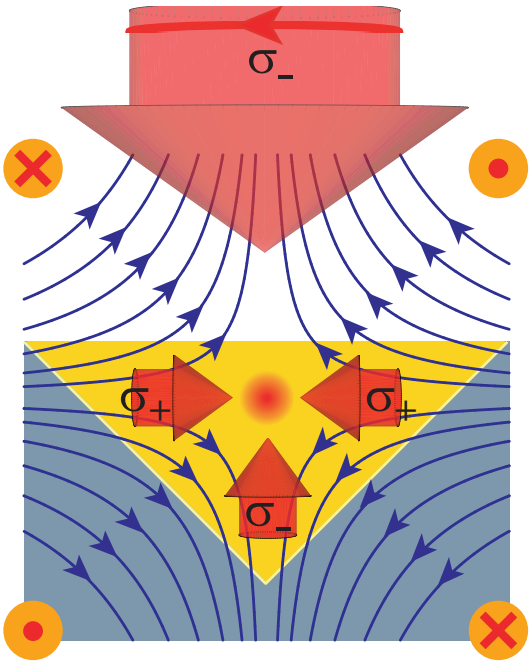

Figure 2.4: The longitudinal cross section of the 90° pyramid MOT shows that the light polarisation configuration is equivalent to the six beam MOT. Therefore, to create a MOT inside of a 90° pyramidal mirror it is only necessary to use a single circularly polarised beam and to generate a quadrupolar magnetic field with its centre inside the hollow volume of the pyramid.

2.4.3 The steady state number of atoms

Since the pressure of background vapour is much less than the rubidium pressure when loading the MOT, let us assume that $\tau_b \gg \tau_{Rb}$. Then, the combination of the results obtained in the previous two sections (equations 2.21 and 2.23) can be used to estimate the steady number of atoms that are collected in the MOT

$$N_s = R\tau = \sqrt{\frac{2\pi}{3}}\frac{1}{\sigma}\left(\frac{m}{k_B T}\right)^2\left(\frac{\hbar k\gamma}{4m}\right)^2 r^4 \tag{2.26}$$

This equation demonstrates the strong dependence of the steady state number of atoms on the size of the trap, which is usually determined by the size of the laser beams. In addition, note that on the approximation $\tau_b \gg \tau_{Rb}$ the number of atoms collected in the MOT is independent of the gas density.

To conclude, we can use this last result to estimate the steady state number of ^{85}Rb atoms that could be trapped in a MOT characterised by a 4 mm in radius spherical region. For this purpose, we take that the Rb-Rb collision cross section is 3.2×10^{-13} cm^2, which is the value measured by Rapol *et al.* [85] in a ^{87}Rb MOT. This way, we find that 4×10^7 atoms could be trapped in this MOT.

2.5 The Pyramid MOT

Hollow optical systems provide a very simple way to generate the correct MOT light configuration [71, 80, 86, 87, 88]. As shown in figure 2.4, a single circularly polarised laser beam shone with its direction of propagation parallel to the axis of any of these hollow systems generates automatically all the 3D MOT light components. The functioning of these hollow optics MOTs relies on the fact that a circularly polarised light beam changes helicity upon reflection from a mirror. Consequently, the reflections from the various faces automatically prepare the three orthogonal pairs of counter propagating laser beams having opposite angular momentum, hence preparing the light polarisations required for laser cooling and trapping atoms.

Figure 2.4 also shows the field lines of the quadrupolar magnetic potential generated by two circular coils running current in opposite directions. The coils are coaxial with the pyramid axis and are located at opposite sides of the hollow pyramid. This creates a point of zero magnetic field inside the hollow pyramid and the magnetic field strength grows linearly with position as one moves away from that point. In order to create a MOT, it is only necessary to ensure that the direction in which these coils current runs, as shown in the scheme, opposes the helicity of the light component that travels towards the point of zero magnetic field.

This arrangement represents a great simplification of the MOT system. While in the usual six beam configuration it is necessary not only to align the six light components but also to prepare properly the polarisation of each one of the six beams, in the pyramid MOT it is sufficient with aligning and preparing the circular polarisation of a single beam. As a result of the inherent simplicity and robustness of these MOTs, 90° pyramidal hollow mirrors are used in several atom optics research groups as highly reliable and extremely robust sources of cold atoms [89], and even in laser cooling and trapping apparatus for undergraduate laboratories as valuable teaching resources [90].

2.6 Magnetic trapping

Magnetic trapping of neutral atoms depends on the interaction between an inhomogeneous magnetic field and the atomic magnetic dipole moment. The potential associated with this interaction is given by the projection of the atomic magnetic dipole moment $\boldsymbol{\mu}$ along the direction of the field $\mathbf{B}$:

$$U = -\boldsymbol{\mu} \cdot \mathbf{B} \tag{2.27}$$

There are two important consequences of magnetically trapping neutral atoms: first, the atomic energy levels will necessarily shift as the atoms move on the trap; second, practical traps for ground-state neutral atoms are necessarily very shallow compared with thermal energy because energy levels shifts are considerable smaller than $\kappa_B T$ for $T = 1\ K$ [77]. Therefore, atoms must have been collected in a MOT and prepared in the required state.

The Hamiltonian of the interaction between an atom and a magnetic field consists of two terms. The first term corresponds to the interaction of the nuclear magnetic moment with the magnetic field generated by the electrons, or hyperfine interaction. The second term describes the interaction between the magnetic field $\mathbf{B}$ and the atomic magnetic moment $\boldsymbol{\mu}$, the Zeeman interaction. In the basis of the total electronic angular momentum $\mathbf{J}$ and the nuclear angular momentum $\mathbf{I}$ states $|J, m_J; I, m_I\rangle$, this Hamiltonian is

$$\hat{H} = \frac{A}{I + \frac{1}{2}} \mathbf{I} \cdot \mathbf{J} - \boldsymbol{\mu} \cdot \mathbf{B} \tag{2.28}$$

The hyperfine splitting A/h between the $F = 1$ and $F = 2$ levels of the $5S_{1/2}$ state of ^{87}Rb and ^{85}Rb atoms is 6385 MHz and 3036 MHz respectively. The Zeeman interaction contains electronic and nuclear contributions

$$\begin{aligned} \boldsymbol{\mu} &= -g_J \mu_B \mathbf{J} - g_I \mu_N \mathbf{I} \\ &= -g_J \mu_B \mathbf{J} + g'_I \mu_B \mathbf{I}, \end{aligned} \tag{2.29}$$

where $\mu_B = e\hbar/2m_e$ is the Bohr magneton; $\mu_N = e\hbar/2m_p$ is the nuclear magneton; g_J is the Landé g-factor, which represents the total electronic angular momentum; and

g_I is the nuclear angular momentum g-factor. For ^{87}Rb, $I = 3/2$, $g_I = 2.751$ and $g'_I = 0.995 \times 10^{-3}$; while for ^{85}Rb, $I = 5/2$, $g_I = 1.353$ and $g'_I = 0.293 \times 10^{-3}$ [82, 91].

Taking $g_s \simeq 2$, the Landé g-factor is

$$g_J = 1 + \frac{J(J+1) - L(L+1) + S(S+1)}{2J(J+1)} \tag{2.30}$$

For the $5S_{1/2}$ ground state this results in $g_J = 2$ and for the $5P_{3/2}$ state in $g_J = 4/3$. For $\mathbf{J} = \frac{1}{2}$, the interaction Hamiltonian can be analytically diagonalised and the energies of the magnetic sublevels are given by the Breit-Rabi formula [92]:

$$E_{|J=1/2,m_J;I,m_I\rangle} = -\frac{hA}{2(2I+1)} - g'_I \mu_B B m_F + (-1)^F \frac{hA}{2}\sqrt{1 + \frac{2m_F}{I+\frac{1}{2}}x + x^2} \tag{2.31}$$

where $x = \frac{(g_I+g_s)\mu_B B}{hA}$.

In the limit of low magnetic field ($B < 300\,\mathrm{G}$), the Zeeman interaction lifts the degeneracy in m_F and the resulting energy shift can be approximated to first order to obtain

$$\Delta E_{(J\,I)\,F\,m_F} = \mu_B g_F m_F B \tag{2.32}$$

where

$$g_F = \frac{g_J(F(F+1) + J(J+1) - I(I+1)) + \frac{\mu_N}{\mu_B}(F(F+1) - J(J+1) + I(I+1))}{2F(F+1)} \tag{2.33}$$

Since the ratio $\mu_N/\mu_B \sim 5 \times 10^{-4}$, the second term in this last expression is negligible compared with the first term and this formula can be rewritten as

$$g_F \simeq \frac{g_J(F(F+1) + J(J+1) - I(I+1))}{2F(F+1)} \tag{2.34}$$

An atom polarized in a particular Zeeman sublevel is driven by the Stern-Gerlach force,

$$\mathbf{F} = -\nabla E = -g_F m_F \mu_F \nabla B \tag{2.35}$$

Then, atoms for which $g_F m_F > 0$ are attracted to regions of low magnetic field. These atoms are therefore *low field seekers* and can be trapped in a minimum of the magnetic field. In addition, the highest m_F states are trapped most strongly. For example, ^{87}Rb atoms prepared in the $|F, m_F\rangle = |2, 2\rangle$ state by optical pumping are trapped more strongly in a magnetic field minimum than in any other state. On the other hand, atoms in a state such that $g_F m_F < 0$ are *high field seekers*.

The adiabatic condition

The confining force an atom experiences in a magnetic trap originates from the interaction between the atomic magnetic moment and the nonuniform static field. The confinement depends on the maintenance of a given orientation of the atomic moment with the local field. The energy shift as stated in equation (2.32) is only valid if the projection of the atomic magnetic moment, m_F, on the direction of the field is a constant of the motion. This implies that to keep an atom trapped, it has to remain adiabatically in a given Zeeman sublevel.

When the precession frequency is not large compared with the frequency of orbital motion, the desired orientation is lost. This means that *spin-flipping transitions* between magnetic sublevels do not occur. These transitions are often called *Majorana spin flips* and they cause the particle to escape from the trap [16]. Therefore, the atom should move slowly enough to follow the field adiabatically [93].

Let $\mathbf{v} = (v_x, v_y, v_z)$ be the velocity of the atom. Then, the variation of the magnetic field in the reference frame of the moving atom is given by

$$\frac{d\mathbf{B}}{dt} = \frac{\partial \mathbf{B}}{\partial x} v_x + \frac{\partial \mathbf{B}}{\partial y} v_y + \frac{\partial \mathbf{B}}{\partial z} v_z \tag{2.36}$$

This can be expressed in two components, one parallel and one orthogonal to $\mathbf{B}$:

$$\frac{d\mathbf{B}}{dt} = \omega_1 \mathbf{B} + \boldsymbol{\omega} \times \mathbf{B}, \tag{2.37}$$

where

$$\omega_1 = \frac{\mathbf{B}}{B^2} \cdot \frac{d\mathbf{B}}{dt} \tag{2.38a}$$

and

$$\boldsymbol{\omega} = \frac{\mathbf{B}}{B^2} \times \frac{d\mathbf{B}}{dt}. \tag{2.38b}$$

The atomic magnetic moment, $\boldsymbol{\mu}$, precesses about $\mathbf{B}$ with the instantaneous Larmor frequency $\omega_0 = |g_F m_F \mu_B / \hbar|$. To avoid any transition between spin states, the field direction has to change slowly enough for the magnetic moment of the atom to be able to follow it adiabatically. The adiabatic condition is then

$$|\boldsymbol{\omega}| \ll \omega_0$$

This is,

$$\left| \frac{\mathbf{B}}{B^2} \times \frac{d\mathbf{B}}{dt} \right| \ll \omega_0 \tag{2.39}$$

A general interpretation of ω_0 is that it is the minimum value of the angular frequency of the different allowed transitions between the levels of the quantum systems. The adiabatic condition is generally fulfilled for cold atoms in magnetic traps since the rate of change of the magnetic field that any atom experiences is limited by its low velocity.

2.7 Magnetic traps in atom chips

There are two main methods for creating magnetic trapping potentials in atom chips: current carrying wires and permanently magnetized surfaces.

2.7.1 Microfabricated current carrying wires

The most elementary tool that can be included in an atom chip is a single straight current carrying wire. Provided that the distance r from the centre of the wire is small compared with the wire length, the magnitude of the magnetic field produced by this straight flowing current I is simply $\mu_0 I / 2\pi r$. The direction of the magnetic field vector is determined by the right hand rule. Therefore, a homogeneous bias field pointing in a direction orthogonal to the wire can be used to create a 2D quadrupole field with a

line of zero magnetic field running next to the wire [59]. The bias field, here denoted by B_{bias}, determines the distance of the zero magnetic field line as measured from the centre of the wire

$$r_0 = \left(\frac{\mu_0}{2\pi}\right)\frac{I}{B_{bias}} \tag{2.40}$$

Similarly, the gradient of the magnetic field around this line is

$$\left.\frac{dB}{dr}\right|_{r_0} = \left(\frac{2\pi}{\mu_0}\right)\frac{B_{bias}^2}{I} = \frac{B_{bias}}{r_0} \tag{2.41}$$

The 2D field minimum generated by the wire can be used to guide neutral atoms in a low field seeking state. To avoid Majorana spin flips at the centre of this guide, where the field magnitude is equal to zero, an additional field needs to be included along the wire direction. The new field, which we will denote as B_0, curves the magnetic potential minimum and creates a Ioffe-Pritchard trap. At the field minimum position, the curvature of the field in the direction perpendicular to the wire is given by

$$\left.\frac{d^2B}{dr^2}\right|_{r_0} = \left(\frac{2\pi}{\mu_0}\right)^2\frac{B_{bias}^4}{B_0 I^2} = \frac{B_{bias}^2}{r_0^2 B_0} \tag{2.42}$$

For an atom of mass M in a low field seeking $|F, m_F\rangle$ state, the harmonic oscillation frequency at the centre of this guide is

$$f_r = \frac{\omega_r}{2\pi} = \frac{1}{2\pi}\sqrt{\frac{\mu_B g_F m_F}{M}\left(\frac{d^2B}{dr^2}\right)} = \frac{1}{2\pi}\sqrt{\frac{\mu_B g_F m_F}{M}\left(\frac{B_{bias}^2}{r_0^2 B_0}\right)} \tag{2.43}$$

In consequence, high trap frequencies are achieved when B_{bias} places the guide close to the wire. Additionally, the magnitude of B_0 must be kept as low as possible in order to obtain the highest possible frequencies. The depth of this trap is proportional to the difference in magnitude between the field at the centre of the trap, B_0, and the field far from the wire, B_{bias}. Consequently, the depth of the trap that a low field seeking atom experiences is

$$U_0 = \mu_B g_F m_F \left(B_{bias} - B_0\right) \tag{2.44}$$

The guiding potential can then be transversally closed with the field of two parallel wires running perpendicularly to the direction of the guide. In this way, a new degree of confinement is imposed on the atomic motion. The axial harmonic frequency of the trapping potential is given by

$$f_z = \frac{\omega_z}{2\pi} = \frac{1}{2\pi}\sqrt{\frac{\mu_B g_F m_F}{M}\left(\frac{d^2B}{dz^2}\right)} \tag{2.45}$$

The magnetic field generated by a current carrying wire bent in a Z-like shape is similar to the previous example. In this occasion, a Ioffe-Pritchard type trap is formed on top of the wire when a bias field is added in the direction perpendicular to the central segment. This configuration has the advantage that it is not necessary to apply any further bias fields. The contributions from both extremes of the Z wire provide an axial bias which is high enough for maintaining the atoms in a strongly trapped state.

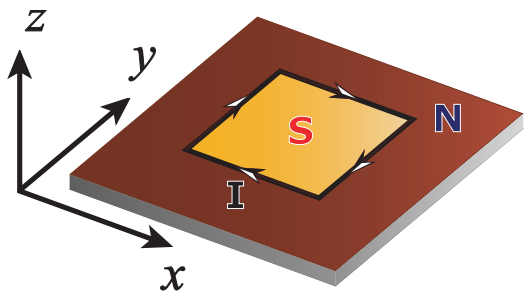

Figure 2.5: Equivalent current I that runs along the boundary of a pattern written on an MO film. The equivalent current along a border between regions of opposite magnetisation is found to be 22 mA.

2.7.2 Permanently magnetised media

As shown by Hinds *et al.* [29], a periodic signal recorded in a piece of video tape produces a magnetic field that can be used as an atomic mirror. The addition of a uniform bias field creates tube-like guides above the surface of the tape. These run parallel to the mirror surface and can be longitudinally closed to produce confinement in that direction too. Similarly, patterns resembling a Z shaped current carrying wires can also be created on magnetic media.

Modelling magnetic traps

Fictitious equivalent currents are utilised for calculating the magnetic field produced above the surface of a patterned MO film, such as the Co/Pt film described in chapter 6. These currents are the result of replacing the magnetisation M by an equivalent current density $\nabla \times M$. The magnetization vector of Co/Pt MO-films is normal to the surface. Figure 2.5 shows an example of a square of downward magnetisation in a background of upward magnetisation. In this case, the fictitious current runs along the edge of the square. The magnitude of the current is obtained by considering the change of magnetisation ΔM across the boundary and the thickness t of the magnetic layer:

$$I = \Delta \mathbf{M} \times \mathrm{t} \tag{2.46}$$

Assuming that the magnetisation at either side of a boundary is $\pm M$, then the change across a boundary is $2M$.

The magnetic field present above the surface of the film can be calculated with the aid of the Biot-Savart law. According to this law, the magnetic field $d\mathbf{B}$ produced of a location $\mathbf{r}$ by a wire segment $d\mathbf{s}$, carrying a current I is given by:

$$d\mathbf{B} = \left(\frac{\mu_0}{4\pi}\right) \frac{I d\mathbf{s} \times \mathbf{r}}{|\mathbf{r}|^3} \tag{2.47}$$

For the calculation of the magnetic field above the surface of the MO film, the patterns are assumed to lie entirely in the xy-plane and the current lines used to model them are either parallel to the x-axis or to the y-axis. Therefore, the field produced by a current carrying wire parallel to the x-axis is:

$$\mathbf{B}_{xwire} = \left(\frac{\mu_0 I}{4\pi}\right) \nabla \times \int_{x_0}^{x_1} \frac{ds}{|\mathbf{r}|} \hat{x} \tag{2.48a}$$

Similarly, the field produced by a wire parallel to the y-axis is:

$$\mathbf{B}_{ywire} = \left(\frac{\mu_0 I}{4\pi}\right) \nabla \times \int_{y_0}^{y_1} \frac{ds}{|\mathbf{r}|}\hat{y} \tag{2.48b}$$

In equations (2.48), (x_0, x_1) and (y_0, y_1) represent the extension of segments of wire along the x-axis or along the y-axis respectively.

Chapter 3

Experimental apparatus

This chapter contains a description of the apparatus that was developed throughout this project. I provide a description of an entirely new vacuum system that was build explicitly for testing atom chips. I also describe the dichroic atomic vapour laser locks as well as polarization and saturation spectroscopy systems that were built for stabilizing the frequencies of the radiation emitted by three extended cavity diode lasers. Magnetic field sources and electronics for controlling and stabilizing the currents supplied to them are also described in this chapter. Additionally, I describe the imaging system that is essential for the operation of our experiments.

3.1 Vacuum system

To evaluate the different elements of the new generation of atom chips and ultimately for testing our atom chip, we built a new vacuum system. A vacuum on the order of a few 10^{-9} mbar had to be easily achieved with the atom chip inside the vacuum chamber.

3.1.1 The vacuum chamber

The main element of the vacuum system (figure 3.1) that has been built is an extended octagon, multi-CFTM fitting (Kimball Physics Inc., MCF800-EO200080.16-A) UHV vacuum chamber. This chamber includes two 8", eight $2\,{}^{3}\!/_{4}$", and sixteen $1\,{}^{1}\!/_{3}$" CF ports. With a large internal volume (7.1" diameter spherical workspace) and wide optical access, this extended octagon is particularly suitable for our application. This vacuum system routinely operates at a base pressure below 10^{-9} mbar and the pumping down procedure followed for achieving this pressure is described in appendix A.

Three aluminium posts support the vacuum chamber, placing its geometrical centre approximately 35 cm above the optics table surface. The two 8" ports of this chamber are parallel to the table surface and a CF anti-reflection coated viewport is attached to the bottom port. Similarly, CF anti-reflection coated viewports cover seven of the $2\,{}^{3}\!/_{4}$" chamber ports, and a combination of CF anti-reflection coated viewports and blank flanges close the sixteen $1\,{}^{1}\!/_{3}$" ports. A four way cross is attached to the remaining $2\,{}^{3}\!/_{4}$" port and the opposite side of this is connected to a $20\,\mathrm{Ls}^{-1}$ ion pump (VacIon Plus 20

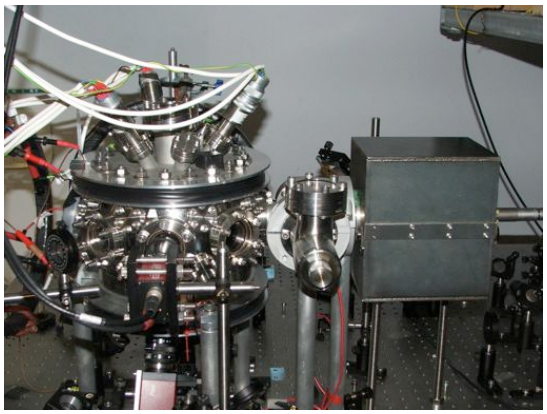

Figure 3.1: The vacuum system. The octagon vacuum chamber rests on three aluminium posts and the ion pump (on right) is attached to one of the chamber ports. The viewports that seal most of the vacuum 2 $^3/_4$" ports provide appropriate view access to our experiments.

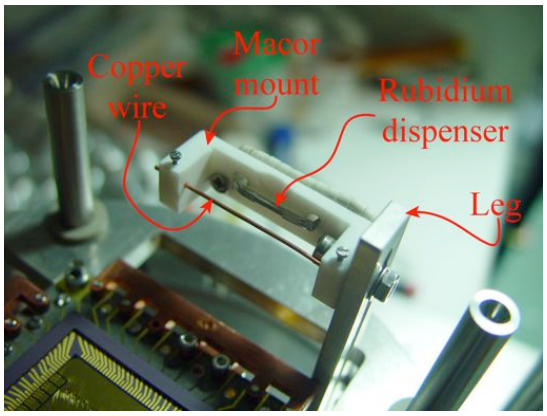

Figure 3.2: The Rubidium dispenser is held on a macor mount, which is in turn attached to a long aluminium leg by a single bolt and screw set. Wires on the back of this holder supply electric current to the dispenser. The dispenser terminals and the wires are sandwiched between copper washers to guarantee good electrical contact. Finally, a thin and straight copper wire in front of the dispenser screens the rubidium effusion.

StarCell). An all-metal CF angle valve and a CF blank flange seal the remaining two 2 $^3/_4$" ports of the four way cross. Finally, the top 8" port is used for loading the atom chip assembly into the vacuum chamber. This assembly is described in section 5.3.1.

The laboratory coordinate system

We defined a left hand coordinate system with respect to the vacuum chamber with its origin at the centre of the octagon. The z axis is vertically upward; the x and y axes are horizontal oriented and the former points towards to the ion pump.

3.1.2 The Rubidium dispenser

We use current heated rubidium dispensers (SAES Getters Rb\NF\4.5\12\FT 10 + 10). This method is suitable for controlling the rubidium partial pressure because the rate of evaporation is reproducible and can be controlled at will. The evaporation process is activated by heat, which in turn is generated by running current through the dispenser body. An insulating macor[1] block, shown in figure 3.2, was designed for holding the rubidium dispenser in the atom chip testing experimental apparatus. This block holds the dispenser and directs the atom effusion. Current carrying wires attached to the back of this block provide electric current to the dispenser, and a wire located in the front of the block screens the atomic flux. A detailed description of the dispenser holder will be given in section 3.1.3.

[1]Macor is a machineable glass-ceramic with good thermal properties and low outgassing rates (www.corning.com).

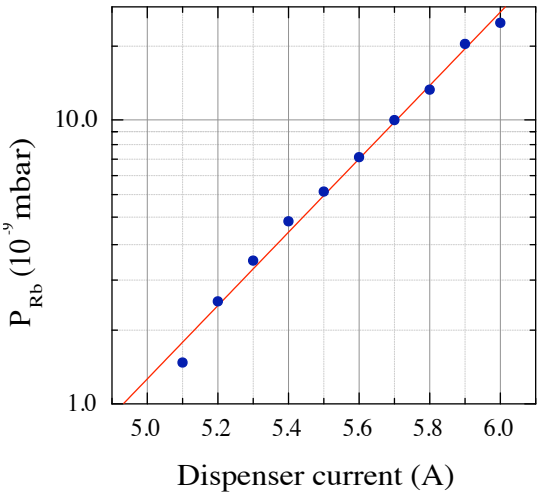

Figure 3.3: The Rubidium partial pressure versus dispenser current calibration curve is shown along with the experimental data used to deduce the dependency. To generate the calibration curve, the data points were fitted to a simple exponential growth formula.

The dependence of rubidium pressure on dispenser current was carefully calibrated by means of an absorption experiment. A laser beam tuned to the $5^2S_{1/2}; F = 3 \rightarrow 5^2P_{3/2}; F = 4$ transition of ^{85}Rb was sent through the vacuum chamber. Then, the fraction of light absorbed by the Rb vapour was recorded as a function of the current supplied to the dispenser.

According to the Beer-Lambert law [94], the fraction of light that is let through a volume filled with an absorbing medium is given by

$$\frac{I}{I_0} = e^{-A} \tag{3.1a}$$

Provided the vapour is optically thin, the absorbance is

$$A = \alpha l n_{Rb} \tag{3.1b}$$

Here, l is the path length that the beam travels through the absorbing medium, n_{Rb} is the rubidium density, and α is the absorption coefficient. Our calibration determines the dependence of the absorbance A on the current supplied to the rubidium dispenser. For this purpose, the laser beam was sent through the 23 cm length of the vacuum chamber and reflected back into it, taking care that the two paths were not overlapped. The laser beam attenuation after crossing twice through the vacuum chamber was determined by means of a photodetector. The voltage V recorded by this photodetector is proportional to the laser intensity and therefore, the ratio I/I_0 is equivalent to the ratio V/V_0.

The absorption coefficient α was independently estimated by repeating the absorption experiment in a 2.5 cm long rubidium cell. The rubidium vapour in the cell is in equilibrium with the solid phase and the experiment was realised at room temperature. Hence, the rubidium pressure in the cell, $P = 3.9 \times 10^{-5}$ Pa [95], corresponds to a rubidium atom density of $n_{Rb} = P/k_BT = 9.6 \times 10^{15}$ m^{-3}. The absorption coefficient determined in this way is $\alpha = 1.94 \times 10^{-16}$ m^2.

The calibration consisted of measuring the light attenuation factor, V/V_0 in this case, for a series of dispenser current values. Then, the rubidium partial pressures in the vacuum chamber corresponding to each one of the measured attenuation factors were calculated by means of equation 3.1 with the aid of the α value determined before. As shown in figure 3.3, the resulting Rb pressure values P_{Rb} (in mbar) were then plotted against the dispenser current I and an exponential curve fitted to them, which resulted

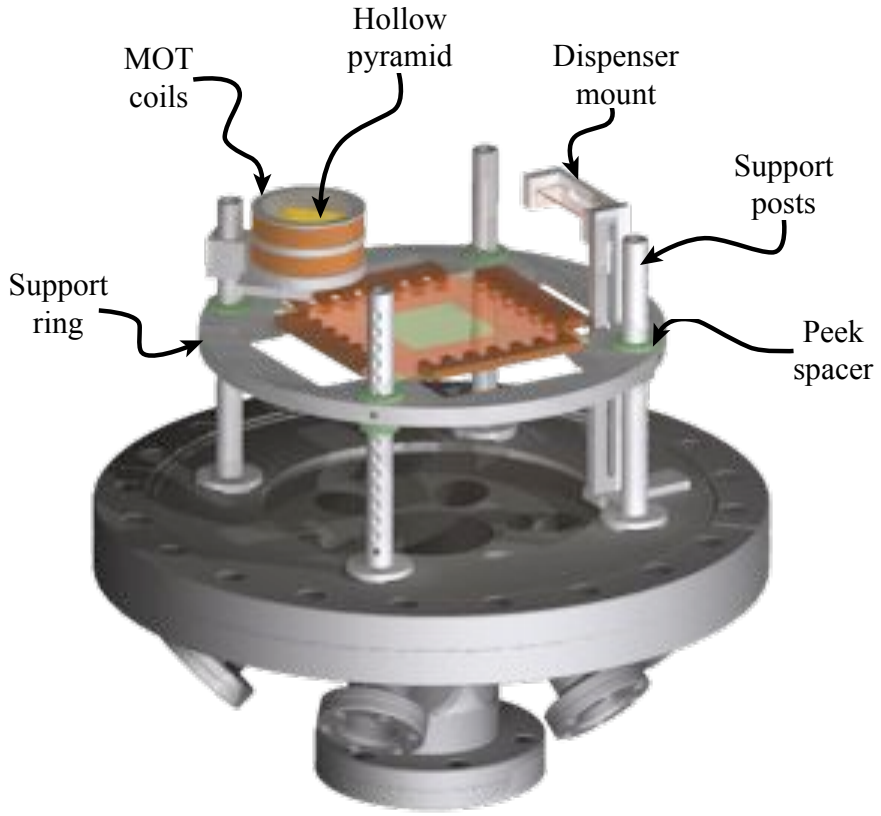

Figure 3.4: The in-vacuum elements of our apparatus are attached to the multiport 8" flange. Four stainless steel posts and an aluminium ring hold the atom chip mounting elements in place. The rubidium dispenser, which is held by its macor mount, can be precisely positioned and oriented with the aim of properly directing the atom effusion. Finally, this image also shows how the large scale pyramid and coils set was included in the atom chip testing system.

in

$$P_{Rb}(I) = 4 \times 10^{-16} e^{2.97(9)\, I} \tag{3.2}$$

where the dispenser current is given in Amperes.

3.1.3 The pyramid assembly

A multiport 8" flange which includes six 1 ⅓" ports equally spaced around a 2 ¾" port (Del-Seal CF Fittings Multiport Angled Flange Part # 409011 by MDC Vacuum products, LLC) is used for supporting the atom chip in the vacuum chamber. In figure 3.4, we show how four stainless steel posts screwed to the flange surface support an aluminium ring. This in turn holds the atom chip and associated components which will be described in section 5.3.1. Four holes on this ring allow us to slide the atom chip arrangement up and down on the posts. Peek[2] spacers between the posts and the ring guarantee smooth sliding of the ring, avoiding the friction between the metallic surfaces of the posts and the ring. Threaded holes on the side of the ring at the posts

[2]Peek stands for Polyaryletheretherketone (www.victrex.com) and is a semi-crystalline thermoplastic with good mechanical and thermal properties.

positions go through not only the ring but also through the peek spacers. Grub screws on these holes fix the location of the ring along the posts, by engaging with a series of dimples. There are 14 of these dimples equally spaced along the full length of the posts, the first being 15 mm away from the flange surface, with 5 mm of separation between consecutive dimples.

The rubidium dispenser is mounted on a macor holder. This can be seen on the right hand side of figure 3.4 and a picture of the holder is provided in figure 3.2. The dispenser terminals go through holes on the macor piece and each one of them is separately sandwiched between a pair of copper washers. As the operation temperature of these dispensers can be as high as 600 °C and currents of up to 8 A are required, a 1 mm cross section diameter wire has been utilised for supplying the current to the dispenser. To avoid undesired electrical connections between these wires and the rest of the components in the vacuum chamber, insulators were threaded along the entire length of these wires. Then, the ends of these wires are sandwiched between copper washers, one of which is in contact with a dispenser terminal. This guaranties good electrical contact between the dispenser terminals and the wire. In addition, the macor holder includes a piece of 0.5 mm in diameter wire located in front of the rubidium dispenser. This wire screens the emission of fast atoms expelled in the direction of the atom chip. A leg attached to the flange is used for holding the macor piece in the vacuum chamber. A slit that runs along the length of the leg is used for setting the height and orientation of the dispenser.

The left hand side of figure 3.4 also shows a glass pyramidal mirror and an anti-Helmholtz coil pair, which are described in sections 3.3 and 3.4.1 respectively. In this case, the pyramid and coil composite system has been attached to one of the steel posts. The support holds these pieces in place taking advantage of the post dimples.

Three ten-pin feedthroughs on the $1^1/_3$" CF ports of the miltiport flange feed current to the atom chip. In the in-vacuum terminal of these pins, beryllium/copper barrels provide the aims for connecting 1 mm in diameter polyimide insulated copper wires. The opposite end of these wires is connected to barrels attached to the atom chip assembly.

3.2 Laser system

The laser system includes three extended cavity diode lasers (ECDL), the tools for stabilising and tuning these lasers, means for preparing and delivering the light to the experiment chamber, and methods for determining the frequency and the stability of the light. A diagram of the laser system and associated optics is given in figure 3.5 and is described in the following sections.

This laser system fulfils a series of basic requirements set by our experiments. First, we needed a trapping laser for driving the cycling transition of either ^{85}Rb or ^{87}Rb atoms. Next, a complementary repump laser had to be incorporated for maintaining the atoms cycling into the cooling transition. In the third place, a laser precisely locked to the centre of the cycling transition was needed to establish a stable frequency reference for measuring the detuning of the trapping laser and for performing various detection tasks. Finally, methods for making fast broad changes of the trapping and the repump frequencies were also necessary in our experiments. These changes could be of just some few tens of megahertz for the production of molasses stages, or as large as hundreds of megahertz for experiments in which it was necessary to take the light as far from resonance as possible, but keeping the lasers locked.

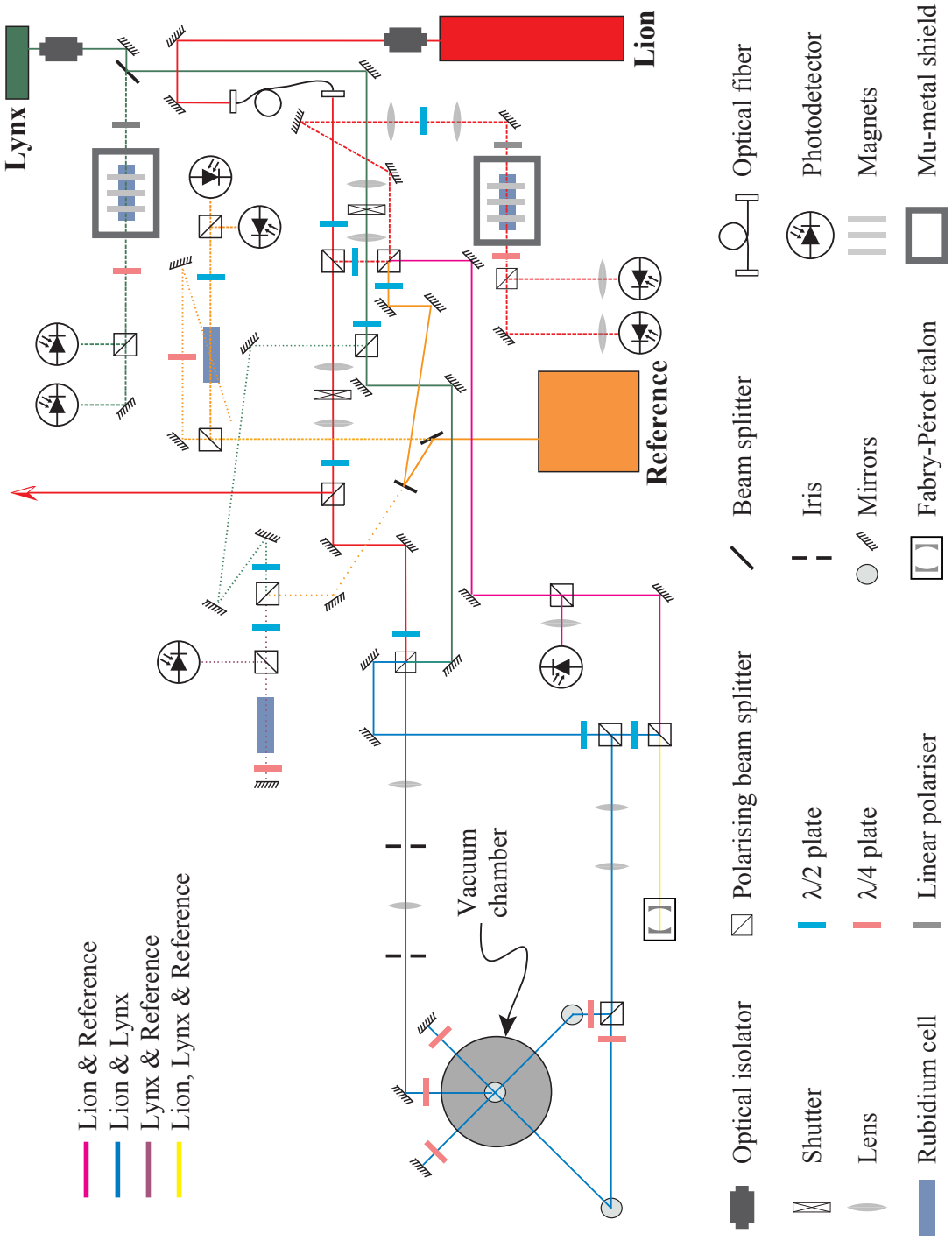

Figure 3.5: The full diagram of the optics table

Figure 3.5 shows three lasers labelled *Reference*, *Lion* and *Lynx*. The Lion and the Lynx drive the trapping and repump transitions of Rb atoms respectively. Means for stabilising and locking these lasers, as well as for controllably varying the frequency of their emissions are mandatory. The Reference laser is used to determine the detuning of the light generated by the Lion with respect to the centre of the cycling transition. This third laser is locked to the centre of the cooling transition and is beaten against the trapping laser. Although there are other methods for determining the frequency difference between two laser, this is a simple and low cost solution which fulfils our experimental requirements. Beside stabilising and locking this third laser, an independent method for precisely identifying the location of the cooling transition centre is also utilised. Finally, we also monitored the stability of the three lasers during the operation of our experiments.

The first of the three lasers, the *Lion* shown in red in figure 3.5, is stabilised around the cycling transition of ^{87}Rb or ^{85}Rb atoms; the second laser, the *Lynx*, is locked to the corresponding repump transition; and finally, with the aim of quantifying the detuning of the *Lion* with respect to centre of the chosen cycling transition, a third light source, the *Reference* laser, is locked to this spectroscopic feature. Locking signals for the trapping and repump lasers are derived from two dichroic-atomic-vapour laser locks (DAVLL). A Doppler free polarisation spectroscopy apparatus is utilised for stabilising the reference laser. The first locking scheme not only stabilises the first couple of lasers, but also allows one to controllably vary their frequencies in the vicinity of the atomic transitions. On the other hand, the polarisation spectroscopy system provides a stable frequency reference. Finally, a saturated absorption spectroscopy system is used for accurately determining the location of the atomic features to which the reference laser has to be locked.

3.2.1 The Reference laser

Let us start with the Reference laser system. A home built extended cavity diode laser in Littrow configuration provides a stable frequency reference for the experiment. This laser is based on the design presented by Arnold *et al.* [96] and a similar system was described in [75]. The back facet of a diode laser has a highly reflective coating and the light emitted from the front facet, which has an anti-reflection coating, is first collimated and then coupled into a diffraction grating. The first-order diffracted light is sent back into the diode and the zeroth-order is coupled out. The wavelength of the output light is tuned by adjusting the external cavity created by the grating and the laser diode. This is done by tilting horizontally the grating either manually or by varying the voltage applied to a piezo-stack between the grating mount and its adjust screw.

Doppler free polarization spectroscopy

The beam generated by the reference laser, shown in orange in figure 3.5, is first divided in two beams by a non-polarising beam splitter. The light transmitted by the splitter goes into a *Doppler free polarisation spectroscopy* apparatus. This has been built for locking the reference laser to the centre of either the $5^2S_{1/2}; F = 2 \rightarrow 5^2P_{3/2}; F = 3$ transition of ^{87}Rb or the $5^2S_{1/2}; F = 3 \rightarrow 5^2P_{3/2}; F = 4$ transition of ^{85}Rb. In this method, an error signal is obtained by detecting a rotation of the polarisation direction in a linearly polarised beam, or probe beam. This rotation of the direction of polarisation is induced by the presence of a more intense beam, the pump beam, when both beams

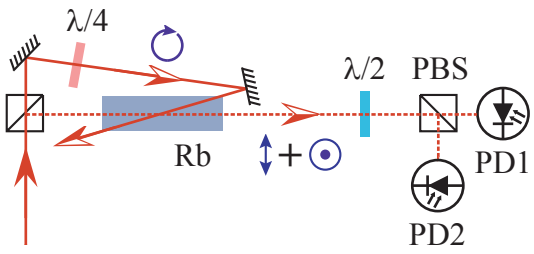

Figure 3.6: The Doppler-free polarisation spectroscopy system used for locking the reference laser to the two cycling transitions in the D_2 line of both Rb isotopes.

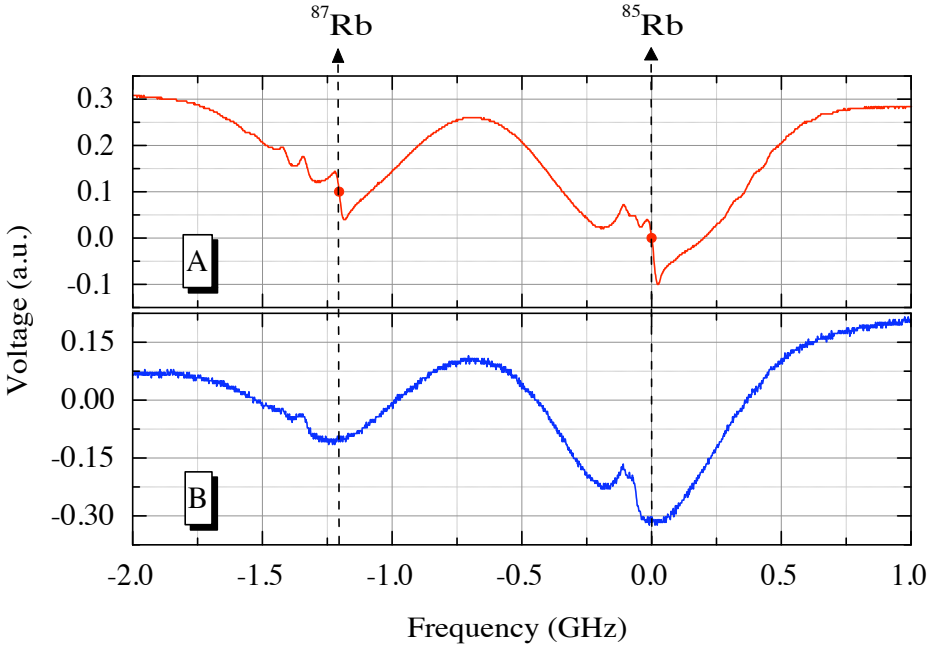

Figure 3.7: The error signal used for locking the reference lasers. Graph **A** shows the error signal obtained from the polarisation spectroscopy system, and graph **B** corresponds to the saturated absorption spectrum. The centre of the trapping transitions in ^{85}Rb and ^{87}Rb are identified on the saturated absorption spectrum and then used to lock the reference laser. These locking points are identified by the vertical lines included in the figure.

are overlapped in an atomic vapour cell.

The principle of polarisation spectroscopy is to induce a birefringence in a medium with a circularly polarised pump beam and to interrogate this with a counterpropagating weak probe beam [97]. Figure 3.6 shows the Doppler-free polarisation spectroscopy system for locking the reference laser. First of all, the input beam is separated into two linearly polarised components by a polarising beam cube. Before this cube, a $\lambda/2$ plate (not shown in the figure) can be used to control the relative power of these two beams.

The beam transmitted by the beam cube is sent through a $\lambda/4$ plate, which prepares the circularly polarisation ◯ of the pump beam. This light beam is then sent through a rubidium cell. The probe beam, which is the beam reflected by the first cube, travels through the rubidium vapour intersecting the pump beam inside the cell with the two beams travelling nearly in opposite directions. Then, the birefringence induced by

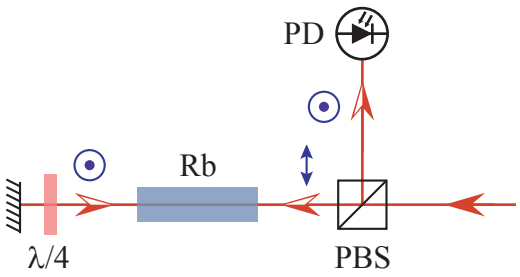

Figure 3.8: The saturated absorption spectroscopy system used to ensure that the locking frequencies of the reference and the repump lasers are located in the centre of the corresponding transitions.

the intense pump beam produces a rotation of the probe beam polarisation (↕+ ⊙). This rotation can be detected by sending the probe beam through a second polarising beam splitter (PBS). The light components transmitted and reflected by the PBS are then sent into separate photodetectors PD1 and PD2. The difference in intensity of the two components, which is proportional to the difference of the signals of the two photodetectors, gives the polarisation spectroscopy signal. Finally, the $\lambda/2$ plate included between the Rb cell and the analyser PBS can be used to carefully tune the zero crossing point along the discriminant slopes shown in figure 3.7, graph A.

In [97] it is demonstrated that for a closed transition, the polarisation spectrum has a derivative lineshape, which is ideal as a signal for actively stabilising the laser frequency. The error signal generated by this polarisation spectroscopy apparatus (see figure 3.7, graph A) is fed into PID servo electronics, which in turn provide the feed back for the laser grating. This slow control of the grating is sufficient for producing a laser linewidth of a few hundred kilohertz.

Graph **A** in figure 3.7 shows the signal generated by the polarisation spectroscopy apparatus when the laser frequency is scanned across the cooling transitions of ^{85}Rb and ^{87}Rb atoms. The error signal generated by this spectroscopic device is fed back into the piezo electric that controls the laser grating. We also add a voltage offset to this error signal to carefully tune the zero crossing position along the discriminant slopes. As shown by the vertical dashed arrows included in figure 3.7, this allows us to lock the reference laser to the cycling transitions of ^{85}Rb or ^{87}Rb atoms.

Saturated absorption spectroscopy

Assuming that the reference laser has been precisely locked to the centre of the cycling transition, the absolute detuning of the trapping beam with respect to this feature can be determined. Nevertheless, the reference laser can be locked to any point over the dispersion slopes shown in figure 3.7, graph A. These dispersion features can be as wide as 90 MHz for ^{85}Rb and 40 MHz for ^{87}Rb. In our experiments, we need to establish detunings on the order of only some few MHz. Therefore, we required an additional method for verifying that the reference laser locking position is located at the centre of the cycling transition.

The light reflected by the first beam splitter is divided a second time, sending one beam into a *saturated absorption spectroscopy* system. We use this system to determine the central frequency of either of the rubidium cycling transitions. Therefore, the saturated absorption apparatus and the polarisation spectroscopy locking system result in a reliable method for measuring the detuning of the MOT light with respect to the centre of the cycling transition.

Figure 3.8 shows the saturated absorption spectroscopy system that we built. To begin with, a light beam is sent into a polarising beam cube (PBS). Then, the beam transmitted by the PBS is sent through both a rubidium vapour cell and a $\lambda/4$ plate. The $\lambda/4$ plate fast axis is set at 45° from the initial direction of light polarisation. Next, this light is reflected back into its path, crossing first through the $\lambda/4$ plate and then through the Rb cell. Therefore, two light beams travelling in opposite directions both linearly polarised in mutual orthogonal directions cross through the rubidium vapour cell. These two beams do not interfere between each other but both interact with the rubidium atoms. The reflected light reaches the PBS and is reflected towards a photodetector (PD), which is used for recording the absorption experienced by this beam. If the laser frequency is swiped across the ^{85}Rb or the ^{87}Rb D_2 lines, and the input beam intensity is high enough for saturating the corresponding hyperfine transitions, the signal recorded in the PD is a profile that shows the saturation features.

The spectrum generated by this system is given in figure 3.7**B**. The signal obtained by means of the saturated absorption spectroscopy system is displayed alongside the Doppler-free polarisation spectroscopy spectrum (graph A). The precise location of the cycling transitions can be spotted in the saturated absorption spectrum and the reference laser can therefore be carefully tuned to this feature centre.

The beam reflected by the second splitter goes through a $\lambda/2$ plate and a polarising beam splitter cube, where it is combined with the MOT light. Then, the combined light beam is sent both into a photodetector and into a Fabry-Perot etalon. The signal given by the photodetector, the *beat note*, is used to determine the difference in frequency between the reference and the MOT beams. This is explained in greater detail in section 3.2.2.

3.2.2 The MOT lasers

The trapping laser

The Lion is an external cavity diode laser in Littman/Metcalf configuration (Sacher Lasertechnik GmbH, TEC 320). This laser is capable of emitting up to 500 mW within a 2.0 GHz bandwidth centred around a 780 nm wavelength. In the Littman/Metcalf lasers produced by Sacher, the front facet emission of the laser diode is collimated and coupled into a diffraction grating. Then, the first order diffraction is sent towards a tuning mirror, which reflects the light back into the diffraction grating. This light is coupled back into the laser diode chip whose rear facet emission, after being collimated, forms the output laser beam. Wavelength tuning of the laser in this configuration can be performed by rotating the tuning mirror. Fine tuning with resolution < 10 MHz is achieved via a piezo actuator. Narrow linewidths (< 300 kHz) can be achieved with this laser [98].

To filter the output beam of the laser and obtain a gaussian beam, figure 3.5 shows that the light emitted by the Lion is first coupled into an optical fibre. Then, the output of the fibre is divided in two beams by a polarising beam splitter cube. The light reflected by this cube is sent into a second beam polarising cube which both combines the MOT and the reference beam, and sends light into the locking system that is described in the following section.

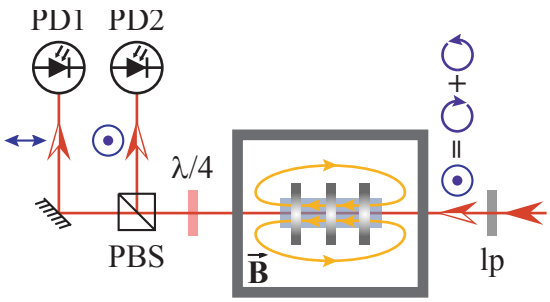

Figure 3.9: A magnetic field induces dichroism in an atomic sample. This dichroism can be detected by sending a linearly polarised beam (⊙) through the sample and then decomposing it into two opposing circular polarisations (↻+↺). An analyser consisting of a $^{\lambda}/_{4}$ plate and a polarising beam cube can then be used to weight the absorption on each of these two circularly polarised components.

The dichroic atomic vapour laser lock (DAVLL)

The Lion is locked to the $5^2S_{1/2}; F = 2 \rightarrow 5^2P_{3/2}; F = 3$ transition of ^{87}Rb or to the $5^2S_{1/2}; F = 3 \rightarrow 5^2P_{3/2}; F = 4$ transition of ^{85}Rb. A *dichroic atomic vapour laser lock*, known as DAVLL, is used for stabilising and locking this laser, which allows for the tuning of its frequency around anyone of the two transitions.

A magnetic field induces dichroism in a rubidium atomic vapour. This dichroism is a result of opposite shifts generated in the absorptions signals of two opposing circular polarizations [99]. To describe this phenomenon, consider first of all that the handedness of the circular polarisation is defined with respect to the quantisation axis, which in turn is determined by the direction of the applied magnetic field. In this basis, right hand circularly polarised light is denoted as σ^+, and σ^- corresponds to left hand circularly polarised light. Then, the selection rules dictated by the conservation of angular momentum establish that σ^+ light drives $\Delta m_F = +1$ transitions; σ^- light drives $\Delta m_F = -1$ transitions; and $\Delta m_F = 0$ transitions are driven by linearly polarised light, denoted as π light. In addition, the applied field induces Zeeman shifts on the atomic magnetic sublevels. In consequence, the resonance frequency for σ^+ light is displaced towards higher frequencies and towards lower frequencies for σ^-.

In the DAVLL technique, a linearly polarised beam is sent through a Rubidium vapour cell and a magnetic field is applied parallel to the light wave vector. A diagram of the DAVLL optical system is provided in figure 3.9. Linearly polarized light (⊙) can be decomposed in two opposing circularly polarised waves of equal amplitude (↻+↺). A quarter wave plate ($^{\lambda}/_{4}$) and a polarising beam cube (PBS) are then placed after the vapour cell. The $^{\lambda}/_{4}$ plate, whose fast axis is set at 45° from the direction of initial polarization, decomposes the light in its two circularly polarised components: the σ^+ component comes out linearly polarised along the initial polarization direction (⊙), while σ^- is transformed into light linearly polarized along the orthogonal direction (↕). In consequence, the polarising beam cube separates these two contributions into two different beams that can be detected independently.

In the absence of a magnetic field, the two circularly polarized components are equally absorbed by the medium. When the magnetic field is applied, the absorption signals corresponding to these two circular polarizations are shifted in opposite directions. An error signal can be generated by subtracting the two absorption signals, which results in a wide dispersion feature. Moreover, a voltage offset can be added to this error signal for shifting the zero crossing position. Consequently, the dichroic-atomic-vapour laser lock (DAVLL) allows one not only to lock the laser frequency to the desired transition, but also to tune the laser over a wide frequency range without using additional

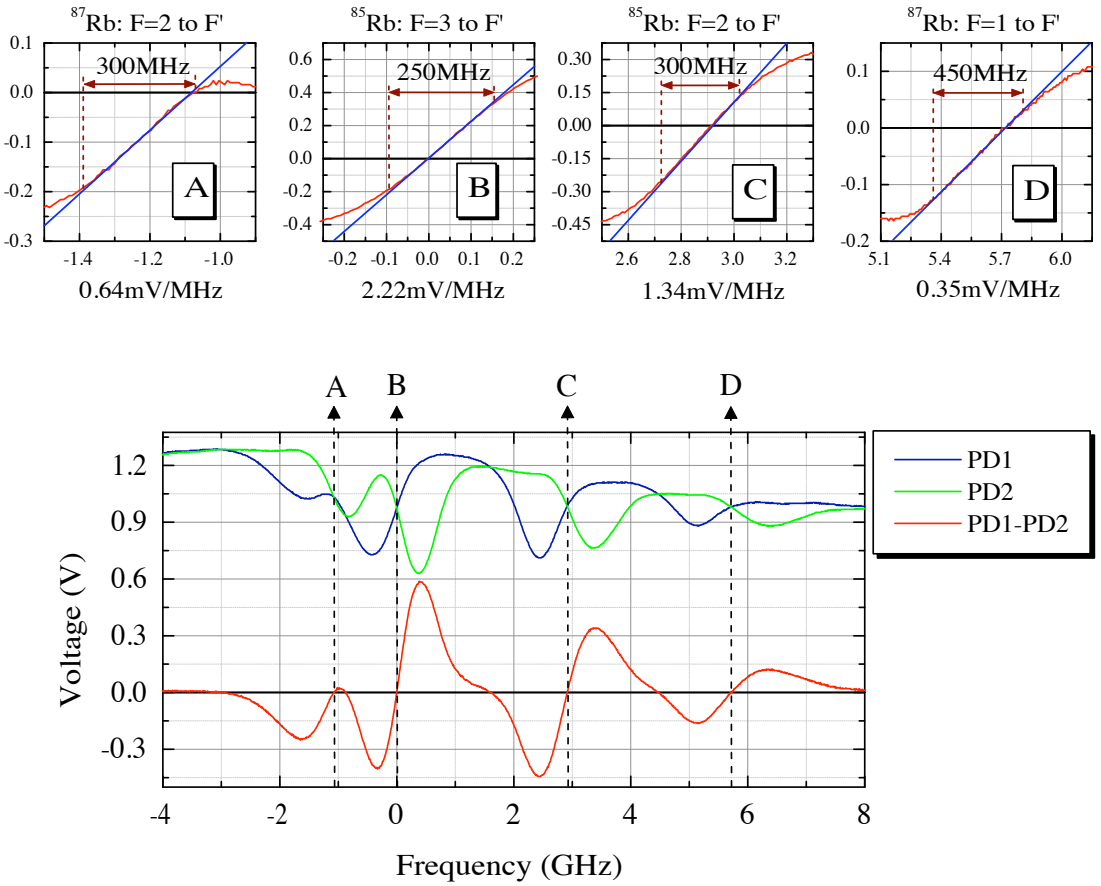

Figure 3.10: The error signal used for locking the trapping and the repump lasers. The blue and green curves shown in the bottom of this figure are the absorption signals measured by the photodiodes in the DAVLL system shown in figure 3.9. The red curve in the graph results from subtracting the two absorption signals, giving rise to the four locking points marked here as A, B, C and D. Each one of these four locking points are shown in detail at the top of the figure, where the tuning ranges have been included for each transition. The axes units in these four graphs are the same as in the bottom graph.

optical elements like acoustic-optic or electro-optic modulators.

The plot shown at the bottom of figure 3.10 is an example of the trace observed when implementing the DAVLL technique. The red line corresponds to the DAVLL dispersion signal obtained when the frequency of the trapping laser is scanned across the D2 line of ^{85}Rb and ^{87}Rb atoms. This signal results from subtracting the signals registered by each one of the two photodiodes, shown as blue and green lines in the plot. The insets on the top of this figure show the width of the linear regions that can be used to lock and tune this laser, in addition to the corresponding slopes of these features. The red curve shown in the bottom graph of figure 3.10 represents the error signal utilised for locking the Lion. This figure also shows the DAVLL locking positions and wide tuning ranges associated to the repump and cooling transitions of rubidium atoms. In particular, graphs **A** and **B** demonstrate that the tuning ranges for locking the Lion to the trapping transitions of ^{87}Rb and ^{85}Rb are 300 MHz and 250 MHz wide

respectively.

The light transmitted by the first polarising cube is the beam that is sent into the experiment vacuum chamber. This goes through a pair of lenses which create a small focus in which a shutter is used for interrupting the trapping light whenever necessary. Then, the trapping light is combined with the repump light (see next section) and send into two paths. The first constitutes the single beam required for trapping atoms into the hollow pyramids and the second has been used to create a 2D molasses below the pyramid atom chip. The beam responsible for trapping atoms in the pyramids is expanded by a pair of lenses. The diameter of the beam after this stage is approximately 2 cm. Then, this beam is sent through a $\lambda/4$ plate whose fast axis is oriented at 45° from the light polarisation direction defined by the polarising beam cube. This prepares the circular polarisation required for creating the MOT light configuration in the pyramid volume.

The repump laser

The *Lynx* (Sacher Lasertechnik GmbH, TEC 100), which is the laser we use for generating the repump light, is an external cavity diode laser in Littrow configuration. The maximum power of this laser is 65 mW and can also be tuned to the D_2 line of the two Rb isotopes. In the lasers produced by Sacher in this configuration, the radiation emitted from the antirreflection coated front facet of a laser diode is first collimated and sent towards a holographic grating. The first order diffraction is reflected back into the diode and this creates the cavity of the laser. The light that is coupled out of the rear facet of this diode constitutes the output light of the laser. Wavelength tuning of the laser in this case is performed by moving the diffraction grating. In addition, high frequency tuning of the laser can be achieved by means of current modulation. The linewidth of this laser is of the order of 1 MHz [98]. The Lynx is also called the *repump* laser and a second DAVLL has been built for locking it to the mentioned transition. Dispersion features similar to those shown in figure 3.10 are used to tune and lock the Lynx around the repump atomic transitions.

The light emitted by the Lynx (the green beam in figure 3.5) goes into a beam splitter that sends a small portion of light towards the DAVLL. This is then used to stabilise and lock the Lynx to the required repump transition. The light reflected by the beam splitter goes through a pair of lenses with a shutter located in the focal point. This has been used in experiments in which we needed to interrupt controllably this light. Then, we use a polarising beam cube for sending some of the Lynx light towards the same saturated absorption apparatus utilised for locating the centre of the cycling transitions. As done with the reference light, we use this spectroscopy tool to determine the centre of the repump transition where the Lynx has to be locked. The reference and repump beams are sent into the same path by a polarising beam cube. Next, a $\lambda/2$ plate selects which of this two light components is analysed in the saturated absorption system.

Finally, some of the Lynx light is combined with the trapping light generated by the Lion to form the single beam used to trap atoms in the glass pyramids and to create a 2D molasses below the pyramid atom chip. This combined Lynx and Lion light is also mixed with the reference laser and monitored in a Fabry-P**é**rot etalon, described in page 55.

The beat note

As we have shown, the reference laser is precisely locked to the trapping transition and can therefore be regarded as a reliable frequency reference. The detuning of the trapping laser from the atomic transition is determined by measuring the frequency difference between this light and the reference laser light.

The difference in frequency between two oscillatory signals can be established by making them interfere. The frequency of the resulting signal, called the beat note signal, is equal to this frequency difference [100]. Consequently, light from the trapping and the reference lasers is carefully overlapped in order to make them interfere. This generates a beat note signal that is used for determining the detuning of the Lion with respect to the reference frequency. After the two beams are combined, the resulting beam is sent into a fast photodetector (Thorlabs DET110). Next, the photodetector output is firstly connected to a high frequency amplifier (Melles Griot, model 13AMP007) and then to a frequency counter (TECSTAR FC 2500). The photodetector capacitance is $C_J = 20\,\text{pF}$ and the amplifier input and output impedance is $R_{Load} = 50\,\Omega$. This results in a photodetector bandwidth $f_{BW} = (2\pi R_{Load} C_J)^{-1} \approx 160\,\text{MHz}$, which allows us to measure the frequency difference between two lasers. The resolution of this system, which is limited by the linewidth of the two laser beams, allows us to obtain sub-MHz frequency difference measurements.

The Fabry Pérot etalon

Light from the three laser sources is combined and sent into a Fabry Pérot etalon (Toptica Photonics. Series DL100, FPI 100 01094). This interferometer has a free spectral range $fsr = 1\,\text{GHz}$ and a finesse $\mathcal{F} \gtrsim 400$. This means that the resolution of this device is $R = fsr/\mathcal{F} \gtrsim 2.5\,\text{MHz}$.

The three light components can be resolved in the interferometer. This provides a method for verifying the trapping light detuning that is initially determined by the frequency counter. The frequency difference between the repump light and the trapping and reference beams can also be measured with this etalon. To determine this last frequency difference, the interferometer free spectral range needs to be taken into consideration. The linewidth of each one of the three laser beams was found to be narrower than the resolution of this resonator.

3.2.3 Laser linewidths and stability

The frequency stability achieved by the DAVLL system has been evaluated by looking at the variation in time of the beat note frequency produced between the trapping and the reference lasers. The results of this measurement are shown in figure 3.11. The beat note frequency measurements were taken in intervals of one second and for a period of up to 2600 seconds. The average value (9.42 MHz) of all these values and the standard deviation (0.69 MHz) of the data set are shown as a dashed horizontal line and as a light red interval respectively.

The stability of the trapping and the reference lasers has been evaluated by calculating the Allan variance [101] of the beat note signal shown in figure 3.11. The Allan variance, which is shown in figure 3.12, allows us to conclude that the best stability of the laser is achieved in a time scale of approximately 3 s, for which we found that the detuning variation of a few hundred kilohertz.

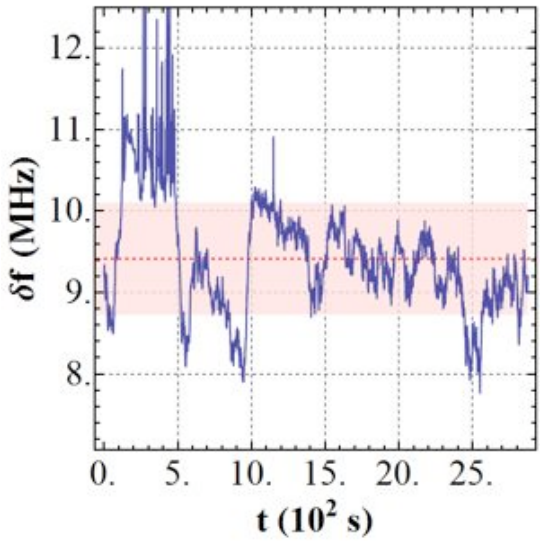

Figure 3.11: The variation in time of the beat note signal generated by mixing the trapping and the reference light beams. The beat note has been measured in intervals of one second and for a period of 2600 seconds. The average value is shown as a dashed horizontal line and the standard deviation of the detuning values is presented as a light red interval around the mean value.

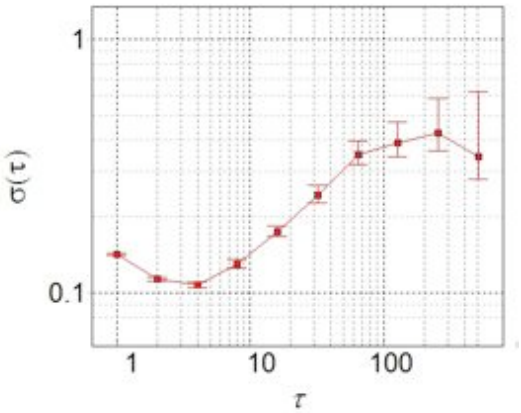

Figure 3.12: The Allan variance of the beat note signal presented in figure 3.11 is presented in this figure. This analysis is a measure of the stability of the two lasers, the Lion and the Reference, and has allowed to identify a random walk of the trapping light frequency as the main source of noise.

Two different methods have been utilised for measuring the linewidth of our lasers. First, in the optics plan given in figure 3.5 it is shown that light from the three lasers is shone into the Fabry Pérot etalon. This way, each one of the three light components can be monitored in real time. The resolution of this etalon has been shown to be limited to ~ 2.5 MHz, and the linewidth of the three lasers has been found to be consistently below this limit. Secondly, the resolution with which we are capable of determining the detuning between the trapping and the reference light components is well below 1 MHz. The linewidth of the beat note signal is the sum of the linewidths of the two oscillatory signals. Assuming that the linewidths of these two lasers are comparable, we can conclude that these lasers are characterised by a linewidth of less than 500 kHz.

3.3 Large scale pyramidal mirrors

Two large-scale glass pyramids were fabricated for performing tests on the particular geometry obtained when pyramidal pits are etched on a silicon surface. The first of

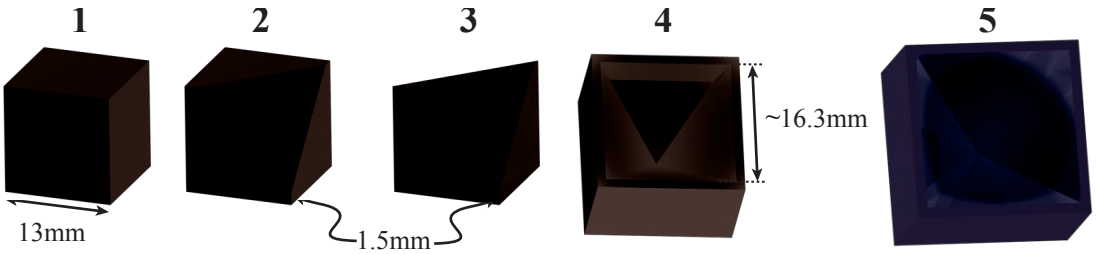

Figure 3.13: The fabrication of the two glass pyramids can be summarised in five steps. **1** The procedure begins with a set of four glass cubes. **2** One corner of each cube is milled off at the desired angle; the resulting surface is polished to produce a mirror quality surface. **3** The machined cubes are cut in half and **4** the resulting pieces are glued together to form the pyramid. **5** Finally, a metallic coating is sputtered over the hollow glass pyramid to create a good quality mirror.

these two pyramids is a replica of the 70.5° silicon geometry, while the second one is a simple 90° pyramidal pit. The initial goal of these experiments was to demonstrate that, in spite of the deviation from the usual 90° geometry, cold atom clouds can still be collected with the pyramidal mirrors fabricated in silicon wafers. We used the two pyramids for comparing the efficiency of the 70.5° pyramid with that of a 90° pyramid of similar dimensions. We also used these pyramids for studying the effect of various metallic coatings with different reflectivities. This was done with the aim of determining which material should be used in the fabrication of atom chips containing chemically etched pyramids. Besides demonstrating that magneto optical traps can be generated with 70.5° pyramidal mirrors and determining which metallic coatings maximise the efficiency of these MOTs, we have also found that blocking the light that is firstly reflected in the vicinity of the pyramid edges greatly improves the trap efficiency. We have used this full replica of the atom chip pyramids to study the effect that reducing the pyramid size has on the resulting trap.

3.3.1 Macroscopic pyramids fabrication

The fabrication of the glass pyramids is schematically represented in figure 3.13. The manufacture of each one of the two large scale pyramids began (**1**) with a set of four glass cubes, each with a side length of 13 mm. In step **2**, the four internal surfaces of the hollow pyramids were obtained by polishing down one of the corners of each cube. The corners were polished to create an optically smooth surface at an angle of either 35.25° or 45° with respect to the chosen edge. The angle that the cutting plane makes with this edge is simply one half of the angle that the opposing pyramid faces are expected to subtend. A lapping machine was used for this purpose and the orientation of the flat pyramidal faces was achieved by maintaining the glass cubes fixed during the polishing process. A strong steel holder kept the orientation of the four glass cubes fixed in the lapping machine and a layer of wax held the four glass cubes firmly attached to the holder during the polishing process. The four glass cubes were polished in this way simultaneously, which guaranteed that the four mirrors share the same orientation. The third step (**3**) of the manufacturing process consisted in milling off one half of the glass cubes. The goal of this step was to keep the resulting pyramid as compact as possible,

allowing the magnetic field coils (see section 3.4.1) to be located close to the pyramid square aperture. The hollow pyramid was then created by gluing together the set of four glass cubes, as shown in the figure step **4**. In this step, the four pieces were also glued to an aluminium disk necessary for integrating the pyramid into the experimental apparatus. Finally, a reflective layer was sputtered onto the four polished surfaces (**5**) and the pyramid was ready for creating MOTs.

3.3.2 The 70.5° pyramid

Once the macroscopic replica of the silicon etched pyramids was fabricated, it was necessary to corroborate that its internal angle was indeed close to 70.5°. For this purpose, a well collimated IR laser beam having a gaussian profile with a radius of 5 mm was shone into the replica with its propagation direction carefully aligned to the pyramid axis. A sheet of graph paper was then placed 54 mm away from and parallel to the plane defined by the pyramid entrance. This paper acted as a screen in which the beam reflections generated by the pyramid faces were imaged.

Three features can be distinguished in the reflection pattern. These features are analysed in detail in section 5.1.3. For the moment it is sufficient to mention that type 1 reflections are the result of the sections of light that are firstly reflected in the middle of the pyramid faces; light in type 2 reflections is initially reflected in the close vicinity of the pyramid apex; and light in type 3 reflections is firstly reflected on the vicinity of the pyramid edges.

As shown in figure 3.14, the pyramid internal angles can be estimated once the distance between the two features originating from type 1 reflections has been measured.

$$\theta = \frac{1}{2}\left[\pi - \tan^{-1}\left(\frac{M-a}{2d}\right)\right] \tag{3.3}$$

The grid on the graph paper allows for the determination of the spot position with millimetre accuracy.

The angles determined in this way have been found to be $68.4 \pm 1.7°$ and $67.9 \pm 1.1°$. The deviations of these angles with respect to the desired value of $\cos^{-1}\left(1/3\right) = 70.5°$ is probably due to the layer of wax used for attaching the glass blocks to the steel holder during the polishing of the mirror faces. Nevertheless, these deviations are small compared to the difference in angles between the usual 90° pyramid and the structure obtained by etching silicon. Therefore, the macroscopic glass pyramid that we fabricated is sufficiently representative of the silicon pyramid geometry.

3.3.3 The 90° pyramid

The first and probably most important step when preparing a pyramid MOT is to verify that the input laser beam is properly aligned to the pyramid axis. Figure 3.15 shows that the laser beam alignment can be done by looking at the images generated on a plane perpendicular to the pyramid axis and ensure that these are symmetrical with respect to the pyramid axis. In the case of a pyramid whose internal angle is exactly 90°, the reflected light forms a beam which travels along the same path of the input beam but in the opposite direction. However, none of our pyramids has an angle of exactly 90° between its opposing faces. In consequence, a well collimated laser beam that is shone into any of these pyramids is decomposed in a number of reflections which then travel in different directions. When the angle is smaller than 90° and the input

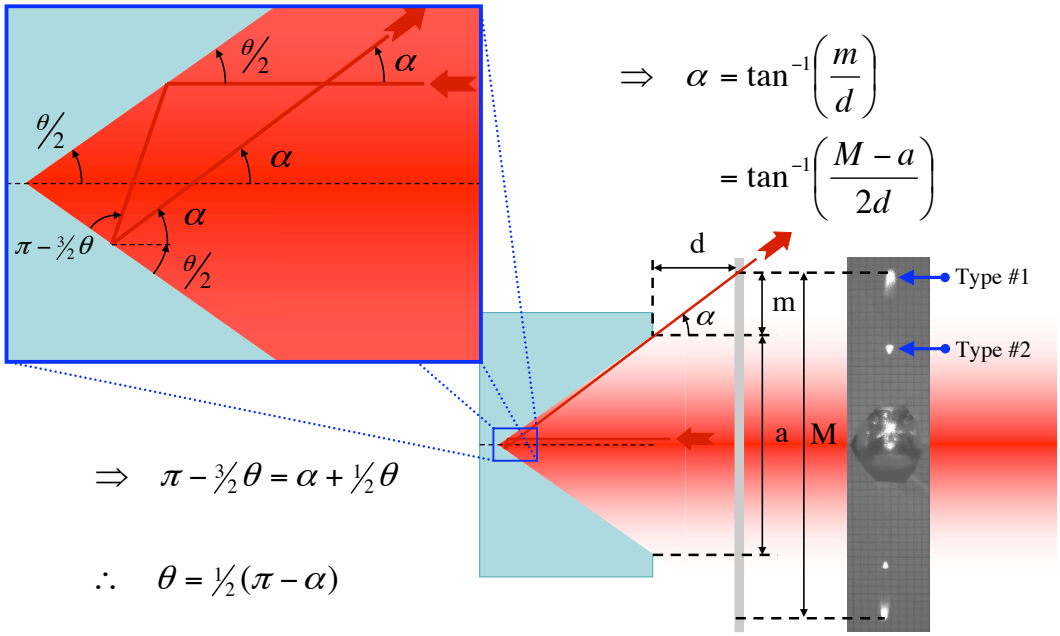

Figure 3.14: The method utilised for measuring the internal angle of the silicon pyramid replica made on glass. A laser beam propagating parallel to the pyramid axis crosses through a hole made on a piece of millimetric paper, which is located at a distance d from the pyramid entrance. The light is reflected by the pyramid faces and creates spots on the paper, which are identified with type 1 and type 2 reflections. The distance between the spots which correspond to type 1 reflections (M), the square aperture side length (a), and the distance d can be used to determine the angle α that the outgoing type 1 ray makes with the pyramid axis. Finally, a zoom into the pyramid apex region allow us to establish the relation between the angle α and the pyramid internal angle θ.

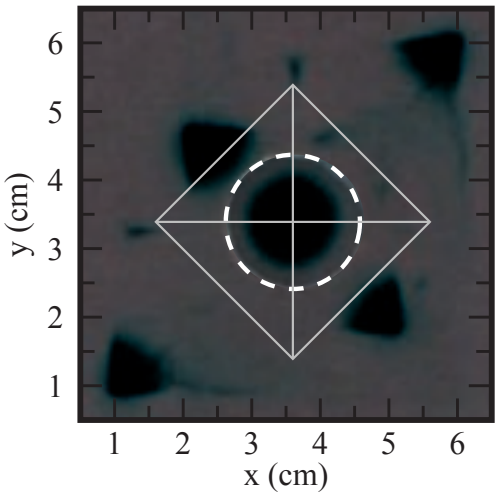

Figure 3.15: A HeNe laser beam was shone into the $\sim 90°$ pyramid and the reflected light was imaged in a white paper screen placed ~ 20 cm away from the pyramid entrance. An image of the input beam has been superimposed over the circular hole (white dashed line) on the screen. A schematic of the pyramid orientation is shown in grey. When the beam propagation direction is aligned to the pyramid axis, the image formed in the screen is symmetric with respect to this axis.

beam is properly aligned to the pyramid axis, the reflections generated by the pyramid surfaces diverge symmetrically from the pyramid axis.

The internal angle of the nominally 90° pyramid was also determined following the procedure described above. In this occasion, a HeNe laser beam was shone into the pyramid and a screen located approximately 20 cm away from the pyramid entrance was used to image the reflection pattern shown in figure 3.15. This pyramid is 10 mm deep and its aperture length is either 20.5 mm or 21.1 mm. The internal angles of this pyramid resulted to be 88.5° and 87.1° respectively.

3.3.4 Reflective coatings

Experiments in this thesis were done with a variety of reflective coatings. In a 70.5° pyramid, the trapping beam sections which are firstly reflected next to the edge of the pyramid faces experience a total of three reflections before crossing through the pyramid axis, where atoms can be trapped. These light components produce an imbalance in the trapping force and unless attenuated or eliminated, the imbalance is sufficient for hindering the MOT functioning. Before crossing through the trapping region, these parasitic rays suffer one more reflection on the pyramid surface than the rest of the trapping beam. Consequently, we proposed that the reflectivity of the mirror surface can be utilised for reducing the undesired effect of the parasitic light sections. In this thesis we have tested four different reflective coatings: aluminium, gold, platinum and chromium.

The information contained in table 3.1 provides the means for estimating the minimum thickness of the metallic layer that should be achieved during the deposition process. The parameter $1/\alpha = \lambda/4\pi k$, with α being the absorption coefficient, is known as the skin depth. This parameter is a measure of how deep an electromagnetic wave with wavelength λ penetrates into a material whose extinction coefficient is k:

$$\frac{1}{\alpha} = \frac{\lambda}{4\pi k} \tag{3.4}$$

The first reflective coating used in both of our pyramids consisted of an aluminium layer covered by a magnesium fluoride (MgF_2) protective layer. The reflectivity of this coating was determined by shining a HeNe laser beam onto each one of the four pyramid mirror faces. The power of the incident beam was compared to the power of

Table 3.1: The real n and imaginary k parts of the complex index of refraction; the normal incidence reflectivity R; and the skin depth $1/\alpha$ exhibited by selected materials for $\lambda = 780\,\text{nm}$ ($\sim 1.6\,\text{eV}$) light [102].

Material	n	k	$R(\phi = 0)$	$1/\alpha$ (nm)
Aluminium	2.625	8.597	0.8794	7.220
Gold	0.08	4.56	0.986	13.61
Platinum	2.76	4.84	0.706	12.82
Palladium	2.08	4.95	0.755	12.54
Chromium	4.097	4.342	0.6351	14.295

the light coming out of the pyramid and, taking into account that this beam suffered two reflections in the pyramid, an average reflectivity of 78% for a single reflection was found. The two pyramids with this aluminium reflective coating were loaded separately in the vacuum chamber and cold atom clouds were trapped in them. These experiments are described in chapter 4.

Next, we decided to investigate the effect that a high reflectivity gold coating has on the trapping performance of the 70.5° pyramid. For this purpose, a thin 5 nm chromium adhesion layer and then a 100 nm thick gold coating were deposited on the surface of both pyramids. We measure that the reflectivity of this coating for infrared light is of 94%. With this new reflective coating the pyramids were once more loaded into the vacuum chamber and used for trapping cold atom clouds.

Metallic coatings which result in intermediate reflectivities, such as chromium and platinum, were also utilised. The reflectivity of the materials that we have considered in our experiments is given in table 3.1. We measure the reflectivities of the chromium and platinum coatings deposited in the two pyramids and the values obtained are consistent with the values reported in the table. The pyramids with these coatings were also loaded in the vacuum chamber and used for trapping rubidium atoms.

3.3.5 The masked coating of the 70.5° glass pyramid

In chapter 4 we demonstrate that in order to create a MOT using a 70.5° pyramid with a highly reflective gold coating, it is necessary to eliminate the light beam sections firstly reflected in the vicinity of the pyramid edges. We first eliminated this parasitic reflections by masking the laser beam shone into the pyramid. However, this method can not be applied easily to each on-chip pyramid. Therefore, instead of masking the trapping beam, the mask was created in the coating laid on the atom chip pyramids. This way, these undesired reflections were practically eliminated. In order to perform further tests on the operation of these MOTs, this masking of the pyramid surface was also incorporated into the 70.5° glass pyramid.

Firstly, the 70.5° macroscopic replica was stripped of all the previous coating layers and, as it was desired to create MOTs as deep into the pyramid as possible, the apex was carefully cleaned. We have already pointed out in section 3.3.1 that during the polishing of the pyramid mirror surfaces, a layer of wax was used for holding the four glass cubes in the lapping machine. Unfortunately, as demonstrated also in section 3.3.1, this wax layer resulted in a slight deviation of the pyramid internal angle with respect to the desired value of 70.5° . This deviation can also be appreciated in the optical microscope

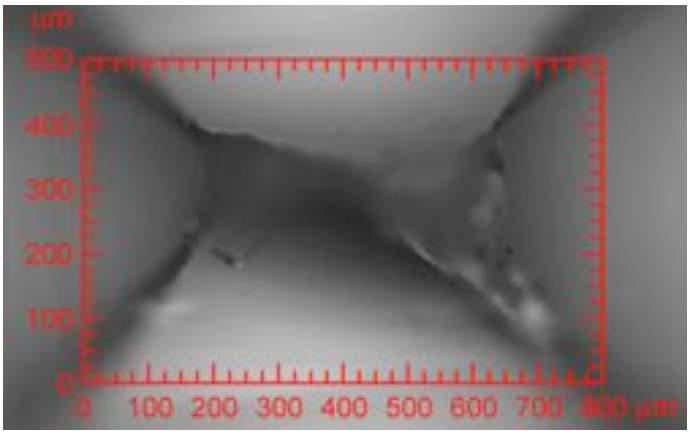

Figure 3.16: The 70.5° pyramid axis has a defect at its apex.

image shown in figure 3.16, which was taken before depositing a reflective coating on the pyramid surface.

The regions of the pyramid internal surface which would give rise to a force imbalance were covered by four small triangular pieces of metal before depositing the new reflective coating. These were made by cutting a 500 μm thick feeler gauge. The four pieces were laid inside the pyramid along each of the edges with their tips touching at the apex. A microscope and a micrometer translator were used to do this. The four isosceles triangle masks were bent at the base so they could be glued to the rim of the pyramid. With the four masks in place, a 5 nm thick adhesion chromium layer and a 100 nm gold reflective layer were sputtered on these pyramid.

The image in figure 3.16 shows not only that the feature at this pyramid apex is not entirely symmetrical but also that there has been some damage inflicted in the apex tip of the four pyramid faces. The small 1.5 mm sections exhibited in figure 3.13 steps **2** and **3** were extremely fragile. These are the sections of glass located in the pyramid apex region of the four pieces. Although the most likely cause of the damage is the unavoidable rubbing of these small corners during the glueing process, these fragile corners might have been broken as early as in the polishing of the faces. The magnification utilised for taking this picture was large and correspondingly the depth of field is evidently short. To measure the dimensions of the apex defect, the focal plane was carefully located at a position where the most damaged of the four mirror surfaces, the right hand side face, is interrupted. This allows us to estimate that along its longest side, the length of this defect is approximately 500 μm, while along the other direction it is 200 μm.

3.4 Magnetic field coils

In this section, I describe the pair of coils that has been attached to either of the two glass pyramids to make the MOT field. Next, I provide the main characteristics of three bias coils and explain how these have been used for controllably displacing the MOT positions. This has been a fundamental tool for measuring the scaling law that determines the number of atoms as a function of the pyramid size.

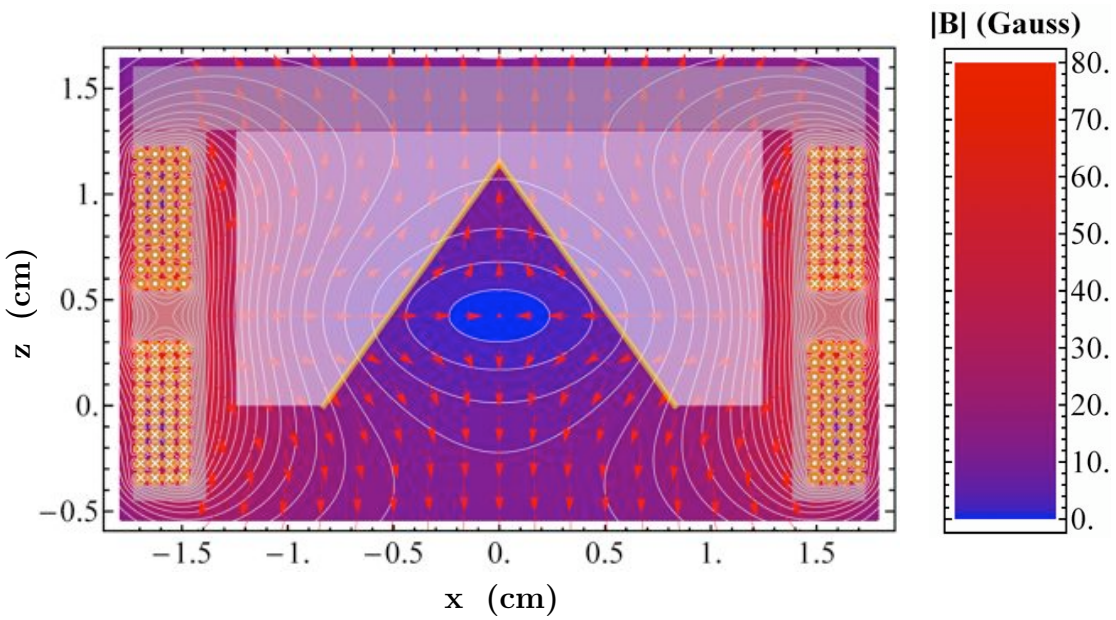

Figure 3.17: A pair of circular coaxial coils generate a quadrupole magnetic field in the hollow pyramidal mirrors. Both coils are supported by a single aluminium former, which is in turn attached to the pyramid base. This not only gives rigidity to the design, but also has allowed us to switch between the two pyramids and still trust in the reproducibility of the field. When operating in the anti-Helmholtz configuration (1.7 A in this case), these coils generate a point of zero magnetic field 4.25 mm away from the pyramid entrance.

3.4.1 Pyramid coils

In order to make a MOT in either of the two glass pyramids, it was necessary to generate a quadrupole field in the pyramids, roughly half the way between the pyramid entrance and its apex. The coil pair used to make the MOT field has already been shown on the left hand side of figure 3.4, and figure 3.17 provides a detailed diagram of these coils and of the quadrupole field generated inside the glass pyramids. In continuous operation a field gradient of up to $20\,\mathrm{G}\cdot\mathrm{cm}^{-1}$ had to be maintained along the pyramid axis. In addition, it was also required to create a design which allowed us to exchange the pyramids while ensuring the reproducibility of the field.

Our initial set of pyramid MOT experiments were performed in a CF $2\,{}^{3}\!/_{4}$" six way cross. Consequently, the pair of coils was originally designed to fit in the $1\,{}^{1}\!/_{2}$" internal diameter of this cross. In view of this space restriction, we decided to use a wire with a cross section diameter of 0.5 mm ($\pm 10\%$) and a 0.06 mm polyimide insulation layer. Although a wire of this diameter can widthstand up to 5 A of current without suffering any damage, in designing these coils it had to be taken into account that the polyimide coating suffers physical damage when it reaches a temperature of approximately 120 °C. The cross sectional cut of these coils provided in figure 3.17 shows that each coil has a total of 40 turns of wire distributed in four layers consisting of ten turns each. The middle point of one of the two coils was positioned slightly above the plane which defines the pyramid entrance. The second coil position was then determined in such a way that the middle point of the coil pair was located 4.25 mm away from the pyramid entrance. The median radius of these coils is 1.6 cm and the distance between their middle points

is 0.9 cm.

A single aluminium former, also shown in figure 3.17, supports both coils, giving rigidity and stability to the design. The coil former can be firmly attached to the aluminium base of either pyramid. Once the pyramid and coil set is loaded into the vacuum chamber, the position of the trap is known accurately and the field characteristics are completely reproducible, regardless of the pyramid under investigation.

Figure 3.17 shows the quadrupole magnetic field generated in either of the two pyramid volumes when a current of 1.7 A is run through the anti-Helmholtz pair. The formulas reported by Bergeman *et al.* [16] for the field of a circular coil were used for creating this plot. The magnetic field from a coil is obtained by integrating the vector potential $\mathbf{A}$ over elements of each loop and then applying $\nabla \times \mathbf{A} = \mathbf{B}$. In cylindrical coordinates $\{\rho, \phi, z\}$, for a single coil of radius R perpendicular to the z axis and centred at $z = A$, $B_\phi = 0$, and

$$B_z = \frac{\mu_0 I}{2\pi} \frac{1}{[(R+\rho)^2 + (z-A)^2]^{1/2}} \times \left(K(k^2) + \frac{R^2 - \rho^2 - (z-A)^2}{(R-\rho)^2 + (z-A)^2} E(k^2) \right) \tag{3.5a}$$

$$B_\rho = \frac{\mu_0 I}{2\pi\rho} \frac{z-A}{[(R+\rho)^2 + (z-A)^2]^{1/2}} \times \left(-K(k^2) + \frac{R^2 + \rho^2 + (z-A)^2}{(R-\rho)^2 + (z-A)^2} E(k^2) \right) \tag{3.5b}$$

where K and E are the complete elliptic integrals of the first and second kind respectively

$$K(k^2) = \int_0^{\pi/2} \frac{d\psi}{\sqrt{1 - k^2 \sin^2 \psi}} \tag{3.5c}$$

$$E(k^2) = \int_0^{\pi/2} \sqrt{1 - k^2 \sin^2 \psi}\, d\psi \tag{3.5d}$$

whose argument k^2 is given by

$$k^2 = \frac{4R\rho}{(r+\rho)^2 + (z-A)^2} \tag{3.5e}$$

In vacuum, this field is given in tesla with $\mu_0 = 4\pi \times 10^{-7}\,\mathrm{NA}^{-}2$. In continuous operation under vacuum conditions, a current of 1.7 A can be run through these coils without increasing the temperature of the wires above 100 °C, and currents of up to 5 A can be run through the coil pair for short periods of time. The image also indicates schematically the position of the glass pyramid (the 70.5° one in this case), the disk to which the pyramid is bonded, the coil former and the coils.

A numerically calculation of the field generated on axis, B_z, when a 1.7 A current is applied is shown in figure 3.18**(a)**. Also, a single wire approximation of this field component is presented in the graph (dashed line). In addition, graph **(b)** in this figure shows that the coil pair can produce an axial gradient of $22\,\mathrm{G \cdot cm^{-1}}$ at the position where $B_z = 0$. This is the position where the MOT is formed and is indicated by a solid red line in the plots. In addition, blue dashed straight vertical lines indicate the position of the pyramid apex to the left, at $z = 1.15$ cm, and the position of the pyramid entrance at $z = 0$.

Section 4.2 describes the experiments we did to measure the scaling laws for the number of atoms that can be trapped in pyramids of different sizes. To do this we placed the MOT position a various positions along the pyramid axis, and particularly

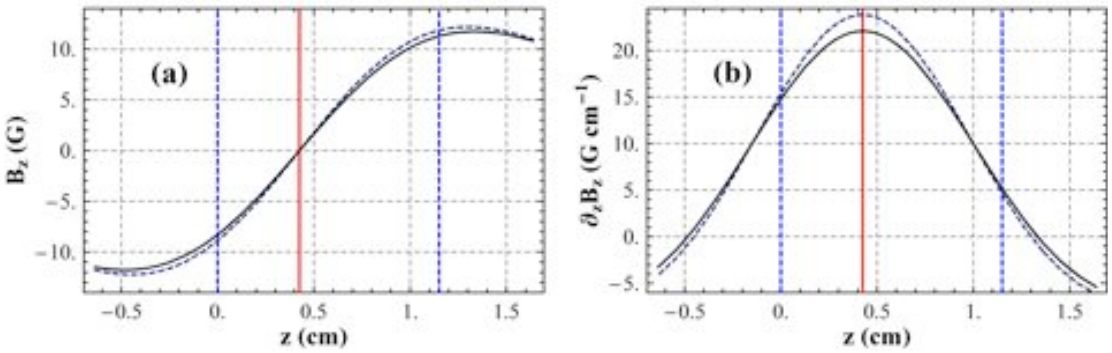

Figure 3.18: The component of the magnetic field that points along the axis of the pyramid and its gradient. These curves were calculated by considering a current of 1.7 A running through the pyramid coils. The solid curve corresponds to calculating the field considering the 40 wire loops that constitute the real coils, and the dashed curve is a single wire loop approximation of the real coils. The vertical red solid line indicates the centre of the coil arrangement and consequently the position where the MOT is normally generated. The vertical dashed lines indicate the position of the pyramid entrance and of its apex.

Table 3.2: Basic parameters of the three large circular coils used for generating bias magnetic fields. These coils axes are aligned to the axes of a left hand coordinate system whose origin is located at the geometrical centre of the vacuum chamber. The coils are labelled in accordance with this alignment.

Coil	**X**	**Y**	**Z**
Radius	22 cm	13.6 cm	13.6 cm
Position	−15.45 cm	14 cm	6.7 cm
Field at origin	325 mG/A	1.72 G/A	2.75 G/A

at short distances from the pyramid apex. With the aim of creating MOTs in the vicinity of the 70.5° pyramid replica apex, we modified the original pyramid and coil arrangement. As pointed out before, the depth of the replica is approximately 11.5 mm and the zero of the magnetic field was originally located 4.25 mm away from the pyramid entrance. With respect to its original configuration, the pyramid position relative to the anti-Helmholtz coils was displaced by 4.25 mm. This displacement was achieved by replacing the aluminium disk to which the 70.5° pyramid is bonded. The new disk has practically the same characteristics as the previous one but includes a step only in the area where the pyramid is glued. This way, the pyramid position was offset with respect to the coil former. Consequently, the magnetic field zero is now located only 3 mm away from the pyramid apex.

For some experiments it was necessary to adjust the position of the MOT either horizontally or vertically. In a MOT, the position where the cold atom cloud is generated is closely linked to the centre of the quadrupole magnetic field, where $|B| = 0$. Once that the pyramid position relative to the anti-Helmholtz coils has been set, the location where $|B| = 0$ can be controllably displaced along the pyramid axis by means of additional magnetic fields. Three coils have been placed outside the vacuum chamber with their axes arranged in such a way that they are mutually orthogonal and all intersect at the

geometric centre of the vacuum chamber. Additionally, these axial directions have been oriented parallel to the directions of the laboratory coordinate system described in 3.1.1. Table 3.2 summarises the basic characteristics of the three bias field coils. The position of each coil plane as measured from the coordinate system origin is given in this table.

The anti-Helmholtz coils utilised for generating the MOT quadrupole field are compact and the magnetic field gradient does not remain constant over the entire pyramid axis. Similarly, the sources of the bias field required for displacing the MOT position introduce a certain amount of gradient. Consequently, it is necessary to calibrate the MOT position with respect to the bias field. The three circular bias coils have been used for controlling the trap position. The pyramid opening faces down and its axis is aligned to the z direction of our coordinate system. Therefore, the MOT vertical displacement was produced by means of the z bias coil. Although the axes of the pyramid and of the z bias coil are parallel, they do not overlap. Consequently, as the current applied to the vertical shim coil increases, the atom cloud position is pushed not only along the pyramid axis direction but also in a direction perpendicular to it. In order to maintain the trap position on the pyramid axis, the horizontal field component generated by the vertical shim coil needs to be compensated. The two additional circular bias field coils, the x and y coils, are used for compensating the off axis field components generated by the z bias coil.

For a given current running through the pyramid anti-Helmholtz coils and at a given position along the pyramid replica axis, setting the three components of the total magnetic field equal to zero results in three simultaneous linear equations in the external coil currents. The solutions to these equations can be used for determining the currents that need to be applied to the bias coils for placing the atom trap at different positions along the pyramid axis. The set of curves shown in figure 3.19**A** correspond to the vertical magnetic field component B_z obtained at various z bias coil currents. The positions at which these curves cross the $B_z = 0$ axis represent the locations where the MOT is formed and demonstrate the vertical displacement of the MOT centre.

Each colour in this graph corresponds to a different set of currents applied to the bias field coils. Also in figure 3.19 and following the same colour code, graph **B** shows the positions along the z direction, i.e. the pyramid axis direction, for which $B_z = 0$. These positions are given as a function of the current applied to the z bias coil. The aim of these calculations is to establish the calibration that has to be used for determining the trap position given the value of the vertical bias coil current. To complement this information, graphs **C** and **D** show the x and y bias coil currents required for compensating the off axis field components and maintaining the cloud over the pyramid axis. The currents supplied to the two horizontal bias coils have been given in terms of the vertical coil current because the later one is the parameter that determines the atom cloud position over the pyramid axis.

The solid lines included in figure 3.19 graphs **B**, **C**, and **D** are polynomial fittings of the coloured point sets. While the fitting in graph **B** was done to second order with the aim of accounting for a slight curvature in the point set, in graphs **C** and **D** a first order fitting was enough for reproducing the trend followed by the set of points. The position where the magnetic field magnitude is equal to zero can therefore be expressed in terms of the current applied to the vertical shim coil:

$$Z_{MOT} = +3.0 + 1.327(5)\ I_z - 7.7(3) \times 10^{-2}\ {I_z}^2 \tag{3.6}$$

Here, Z_{MOT} is the distance in millimetres between the zero magnetic field point and the pyramid apex. Once that the MOT position has been set, I_z can also be used to

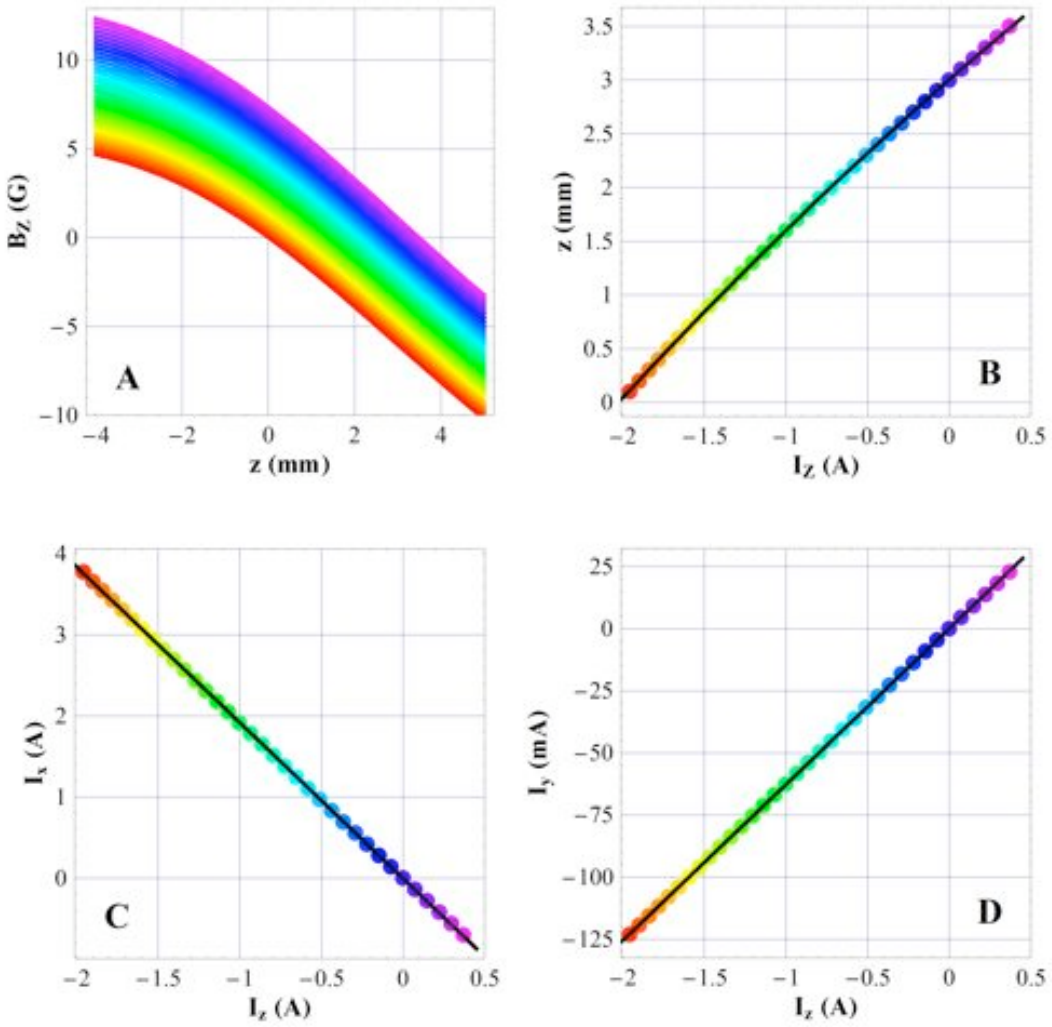

Figure 3.19: The z bias coil current was used for controlling the position of the MOT. The off-axis field components generated by the z coil were compensated for keeping the MOT over the pyramid axis. (**A**) The axial component of the total magnetic field B_z as a function of the position along the pyramid axis. Each curve colour in this graph corresponds to a different set of bias coils currents and shows how the trap position is dragged towards the pyramid apex located at $z = 0$. (**B**) gives the calibration for the position of the MOT in terms of the z bias coil current. The corresponding x and y coils compensation currents are given in (**C**) and (**D**) also as a function of the current applied to the z bias coil.

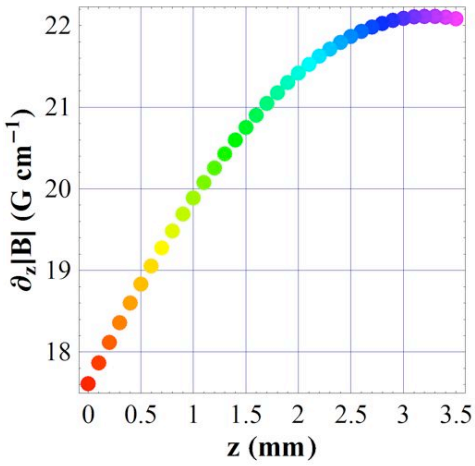

Figure 3.20: The component of the magnetic field gradient that points along the pyramid axis direction is modified as the trapping point is located at different positions along the pyramid axis. A maximum drop of nearly 15% is estimated between the middle point of the anti-Helmholtz configuration ($z = 3\,\text{mm}$) and the point of closest approach achieved in our experiments at $z \sim 500\,\mu\text{m}$.

determine the amount of current that has to be applied through the two additional bias coils. This compensates the horizontal component of the magnetic field and keeps the atom cloud over the pyramid axis:

$$I_x = -1.923(2)\, I_z \tag{3.7a}$$

$$I_y = +62.81(5) \times 10^{-3}\, I_z \tag{3.7b}$$

It is important to ensure that the factors responsible for the generation of the MOT are recreated as closely as possible in all the positions investigated. Therefore, it has to be borne in mind that as the bias field increases, the magnetic field zero not only moves towards the pyramid apex but also towards the upper anti-Helmholtz coil. In consequence, the magnetic field gradient is bound to drop as the point of zero magnetic field is displaced towards the pyramid apex. In addition, although much smaller than the gradient variation just mentioned, the three bias coils also introduce a certain amount of gradient to the total magnetic field. The sets of currents used for obtaining the graphs in figure 3.19 have also been used for tracking the vertical component of the total magnetic field gradient. The graph in figure 3.20 shows the results of this calculation. With a current of 1.7 A running through the pair of anti-Helmholtz coils, the magnetic field gradient generated along the pyramid axis reaches its maximum value of 22.1 G cm^{-1} at the middle point between the coil pair. Based on this calculation, a maximum 14.75% drop in this gradient component is estimated for the relevant range of trap positions.

3.5 Imaging system

We image the atom cloud by focusing its fluorescence in a CCD camera. From this image we deduce the size of the atom cloud and the number of atoms contained on it.

3.5.1 Fluorescence imaging

Consider a cloud of N_A atoms collected in a pyramid MOT. Below saturation ($I_0/I_{sat} < 1$) and averaging over standing waves and polarisation gradients, each atom is being

continuously excited by the trapping light and therefore is emitting photons at a rate

$$R = \frac{\Gamma}{2} \frac{\Pi I_0 / I_{sat}}{1 + \Pi I_0 / I_{sat} + (2\Delta_\nu / \Gamma_\nu)^2}. \tag{3.8}$$

The factor Π accounts for all the different light contributions interacting with the atom. In a MOT formed by six beams of equal intensity, this factor would be equal to 6. In a perfect 90° pyramidal mirror with reflectivity ρ, Π would be equal to $(1 + 4\rho + \rho^2)$. Finally, in a 70.5° pyramid also characterised by a reflectivity ρ, $\Pi = (1 + 4\rho + 4\rho^2)$.

Each radiated photon carries an energy $^{hc}/_{\lambda}$. Hence, the energy radiated per atom per unit time is $R\,^{hc}/_{\lambda}$. Consider a CCD camera located at a distance D from the cloud centre, whose lens defines an aperture diameter d. Then, for $D \ll d$, the solid angle subtended by the camera lens is:

$$d\Omega = \frac{\pi d^2}{4D^2},$$

The detection efficiency η of the camera, in *counts/Joule*, is required for relating the number of atoms N_A collected in the cloud with the total number of counts N_C in a MOT image. Via this efficiency, the energy emitted by the atom cloud in the direction of the solid angle subtended by the camera produces an image with

$$N_C = N_A R \frac{hc}{\lambda} \frac{d\Omega}{4\pi} \eta \tau_e.$$

where τ_e is the exposure time of the camera. In conclusion, if the efficiency of the CCD chip is known, the number of atoms collected in the cloud can be determined by means of the following relation:

$$N_A = N_C \frac{\lambda}{Rhc} \frac{4\pi}{d\Omega} \frac{1}{\eta \tau_e}. \tag{3.9}$$

Camera calibration

Three different cameras have been utilised in our experiments. An AVT Marlin (ALLIED Vision Technologies) is a particularly representative example of these cameras. As this is the camera that we have used in our latest experiments, we will limit ourselves in this section to explaining the calibration method for this camera. Nevertheless, this procedure is completely generic and, with minor modifications, it has been applied for calibrating the other cameras.

The calibration of the CCD camera consists of determining its efficiency η, which is the number of counts stored in a given pixel per unit of energy landing on it. Two parameters influence the operation of the AVT camera, the shutter speed S and the gain G. These two parameters are set by the computer that controls the CCD camera. Although the exposure time is proportional to the shutter speed, $\tau_e \propto S$, the factor of proportionality is determined by the camera electronics and is not known. Because of this, we were not able to determine directly the efficiency η of the camera. Instead, we performed a counts to power calibration. Therefore, if the total number of pixel counts stored in an image is N_C, the calibration of the camera should allow us to determine the corresponding total amount of power detected by our imaging system.

The camera calibration procedure consisted of taking an image of a laser beam of known power that is shone directly into the CCD chip. This is repeated for several combinations of shutter speed, gain, and laser powers. During this process, care must be taken to ensure that the entire laser beam profile fits into the CCD chip area. Next,

we summed the pixel counts contained in each image and plotted them against the corresponding laser powers, as shown in figure 3.21. Provided all the pixels in the image are unsaturated by the light and for each pair of shutter speed and gain values, the total number of pixel counts in the image is proportional to the power of the beam. When the CCD pixels become saturated, the total number of counts drops off the linear tendency and levels down below the maximum number of pixel counts. The solid straight lines included in the figure are linear fits to the data on the unsaturated region of our measurements. The slope of these lines is the calibration factor κ. Then, figure 3.21 shows that the proportionality factor κ relating the number of counts with the power in the laser was found to be proportional to the shutter speed value, but follows a quadratic dependence with the gain values. To simplify the analysis, the power to counts calibration factor was first divided by the corresponding shutter speed value and then a quadratic expression was fitted to the dependence of the resulting values with the gain values.

This procedure resulted in the following camera calibration factor

$$\kappa = (75.93 + 0.1114G + 0.0015G^2)S \tag{3.10}$$

The solid lines in figure 3.21 are the result of plotting equation 3.10 separately for each one of the shutter speed values used in our calibration. The units of κ are pixel counts per nanowatt. In terms of the CCD efficiency, the factor κ is equivalent to the product $(\eta\tau_e)$ in equation 3.9. Consequently, the number of atoms collected in a MOT is found by integrating the pixel counts of the entire image and substituting the result in

$$N_A = \frac{\lambda}{Rhc}\frac{4\pi}{d\Omega}N_C\frac{1}{\kappa} \tag{3.11}$$

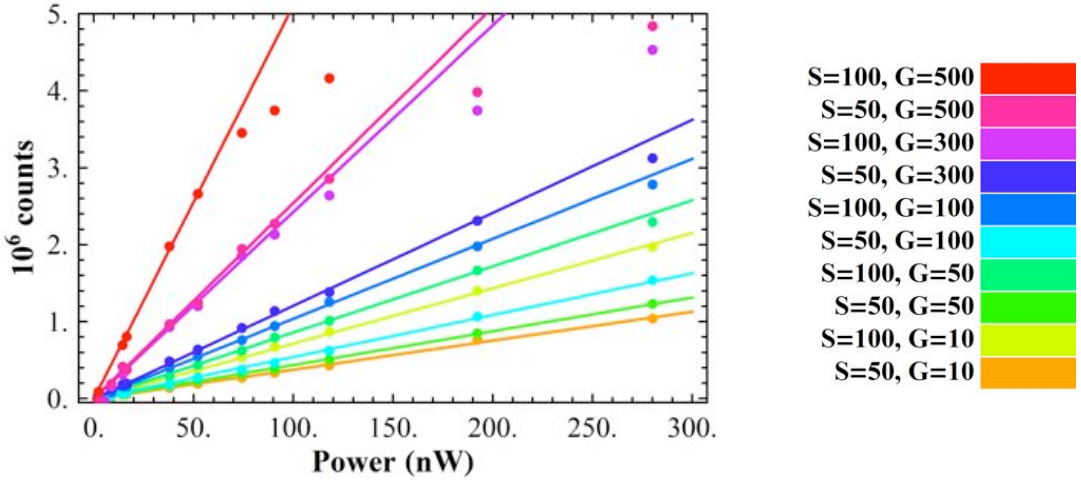

Figure 3.21: For each pair of gain G and shutter speed values S and before saturating the pixels in the image, the total number of pixel counts is proportional to the power of the laser beam. The proportionality factor was obtained by fitting a straight line to the unsaturated region of each one of the data sets. The solid lines included in the graph are the result of this fitting. The slopes of these lines are then plotted in figure 3.22 as a function of gain and shutter speed.

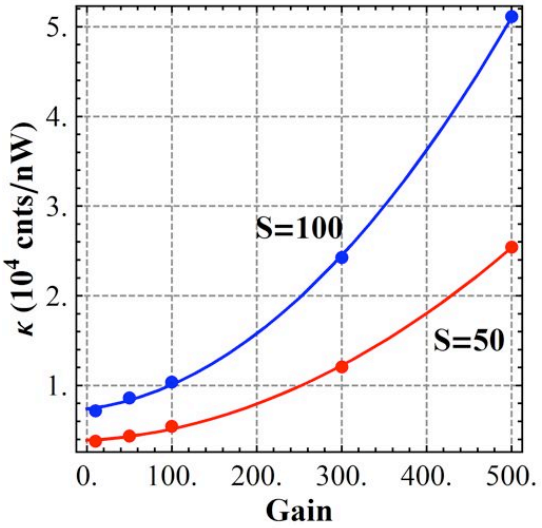

Figure 3.22: We found that the proportionality factor κ follows a quadratic dependence on the gain G, and a linear dependence on the shutter speed S. This graph shows the dependence of this calibration factor on the parameter G for two shutter speeds. The solid lines are the result of evaluating equation 3.10.

Chapter 4

Experiments in glass pyramids

This chapter describes the experiments that we have performed to investigate whether the 70.5° pyramidal geometry generated when etching silicon is suitable for laser cooling and trapping atom clouds. We measured rates for atoms to be captured by and lost from the MOT and we studied how the number of atoms into the MOT depends upon pyramid size.

4.1 Magneto-optic traps in 70.5° pyramids

A 90° pyramid MOT is a simple way to cool and trap neutral atoms, and the six beam MOT has proven to be robust against misalignments of the light beams. On the other hand, the pyramidal geometry created when etching silicon is characterised by an internal angle of 70.5° (see chapter 5). Therefore, it was not clear that this nearly 20° difference in the internal angle of the pyramidal mirror would still generate a laser light configuration useful for cooling and trapping atoms.

We began our experiments by loading in the vacuum chamber the 90° pyramid and the anti-Helmholtz coil pair described in section 3.4.1. This pyramid MOT allowed us to set up and optimise our experiment. After successfully trapping a cloud of atoms in the 90° pyramid, we replaced it with the 70.5° glass pyramid. We kept all the experiment parameters the same as those used for trapping atoms in the 90° pyramid, and found that the 70.5° configuration is also capable of trapping ^{87}Rb atoms.

Figure 4.1 shows a fluorescence image of a cold atom cloud trapped in the glass 70.5° pyramid. The blue solid line in this image delineates the square base of the pyramid and the blue dashed line shows the edge between each pair of pyramid faces. Three images of the cloud can be seen in the pyramid; the one at the centre is the cloud itself and the other two are reflections generated on the pyramid faces. The two lines of scattered light that appear between the three images of the cloud are reflections of the pyramid edges on the mirror faces. The elliptically shaped yellow line indicates the profile of the single trapping laser beam, which can also be seen at the rim of the pyramid where a section of the beam was scattered by the unpolished glass surface.

The clouds formed in either of these two pyramids contained a few 10^7 atoms and no

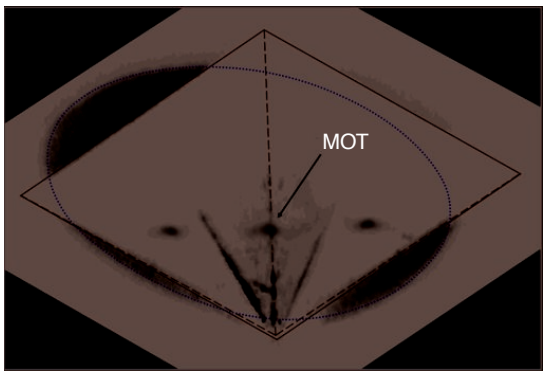

Figure 4.1: A cloud of cold ^{87}Rb atoms collected in a 70.5° pyramid magneto-optical trap. The fluorescence image of the cloud, which was located on the axis of the pyramid, is accompanied by reflections generated on two of the pyramid mirror surfaces. The outline of the single laser beam utilised for creating the trap is superimposed on the image, together with lines that represents the shape of the hollow pyramid.

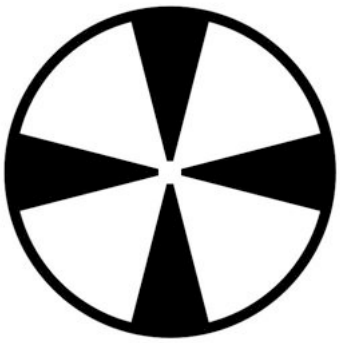

Figure 4.2: Mask used to block the undesired laser beam sections (see sections 1.5.1 and 5.1.3). We found that this mask is required when the 70.5° pyramid has a high reflectivity coating. A rotatable mount was used to hold and position this mask in the path of the trapping beam and with its centre aligned to the pyramid axis. Next, the mask was rotated and a cold atom cloud formed in the pyramid when the unbalancing light sections were covered.

appreciable difference between the MOTs generated in each of these two pyramids was found. In this initial set of experiments, both pyramids had an aluminium reflective coating with a magnesium fluoride over-layer. We measured the reflectivity of the coating of these two pyramids. A small laser beam was sent towards one of the pyramid faces and parallel to the pyramid axis. This beam was reflected twice by the pyramidal mirror before abandoning the pyramid. Hence, to determine the reflectivity of these pyramids, we compared the intensity of the input beam with the intensity of the light that comes out from the pyramid. Taking into account that this light suffered two reflections in the pyramid, a reflectivity of 78% at each reflection was computed, which is low compared with the normal incidence value of 87.9% reported in table 3.1. This difference is mainly due to the protective MgF_2 over-layer, but is also related to the fact that the pyramid reflectivity measurement involved reflections at various incidence angles. The incidence angles of the reflections produced in a 70.5° pyramid are carefully analysed in section 5.1.3.

Next, we recoated both pyramids with gold by sputtering 5 nm of chromium and 100 nm of gold on top of the previous coating. This increased the reflectivity of the pyramid mirror faces to 95%. However, this high-reflectivity coating was unable to produce trapped atoms in the 70.5° pyramid MOT. As I disscus in chapter 5, we had anticipated that this might happen because the unbalancing effect of the light components firstly reflected in the vicinity of the pyramid edges. We therefore made a mask out of black paper in order to block the input light beam sections which would generate these reflections. This mask, shown in figure 4.2, was placed in a rotatable mount. We first ensured

that the centre of this mask coincided with the pyramid axis and next, we rotated the mask around this axis until the pyramid sections responsible for these reflections were entirely covered. The result of this experiment was surprisingly satisfactory. The mask was put in place after the rest of the experimental parameters were ready for making a MOT. Then, the mask was rotated until a cloud of atoms clearly formed in the pyramid, which was only possible once the pyramid corner areas were entirely covered. It was even possible to corroborate that the spots normally seen on the optics table surface as a result of these undesired reflections had entirely disappeared when the atom cloud reached its maximum brightness.

We used the gold coated 70.5° pyramid and mask arrangement for measuring a set of MOT filling curves at various rubidium pressures. As an example of these filling curves, figure 4.3 shows some of the fluorescence images obtained at a pressure of 10^{-8} mbar. These curves (see figure 4.4) were obtained by switching on the current applied to the pyramid anti-Helmholtz coils and then recording a series of fluorescence images as the trap filled with a cold atom cloud. Each image is accompanied by a horizontal profile of the cloud which is taken at the middle of the trap. The vertical scale in these graphs corresponds to the number of pixel counts registered by the CCD camera chip. The number of atoms contained in the trap at any given time was obtained by adding up all the pixel values in the MOT image and then substituting the result in equation 3.9, using the camera calibration given by equation 3.10 in page 70. The shutter speed S utilised in this experiment was equal to 60, the gain G was equal to 200 and the camera was run at 60 frames per second.

For these experiments we trapped ^{87}Rb atoms and then analysed the recorded curves using equation 2.17, which written in terms of the capture rate R and the loss time τ is

$$N(t) = R\tau(1 - e^{-t/\tau}) \tag{4.1}$$

Figure 4.4 shows various examples of the filling curves that we measured. The sets of points are the number of atoms captured in the MOT at each frame recorded by the camera. The solid lines are the result of fitting the filling equation to the data points with R and τ as the fitting parameters. These curves show that as the pressure increases so it does the MOT capture rate R. However, the loss time τ, which is also the loading time in this curves, decreases with increasing the pressure.

An interesting result of this experiment is shown in figure 4.5. In this graph, the capture rate values obtained by means of the filling curve measurements are given as a function of the pressure in the vacuum chamber. As mentioned when discussing the set of filling curves of figure 4.4, the capture rate increases with the rubidium pressure. In section 2.4.1, equation 2.21 expresses the MOT capture rate in terms of a characteristic distance r

$$R = \sqrt{2\pi}\left(\frac{m}{k_B T}\right)^{3/2}\left(\frac{\hbar k\gamma}{4m}\right)^2 n\, r^4 \tag{4.2}$$

The rubidium atom density in this expression is proportional to the rubidium background pressure. Therefore, the slope of the linear fit shown in figure 4.5, which is equal to $5.5(3) \times 10^{15}\,\mathrm{s^{-1}mbar^{-1}}$, can be used to estimate an effective atom stopping distance r in the pyramid MOT. In this particular case, we found that $r = 3.4(1)$ mm.

This result gives us an idea of the limiting factors that determine the MOT functioning in a pyramid. Let us compare this with the scale of the glass pyramid. The full pyramid depth is $D = 11.5$ mm. Since the cloud was located roughly at the middle point of the pyramid depth, the perpendicular distance between the cloud centre and

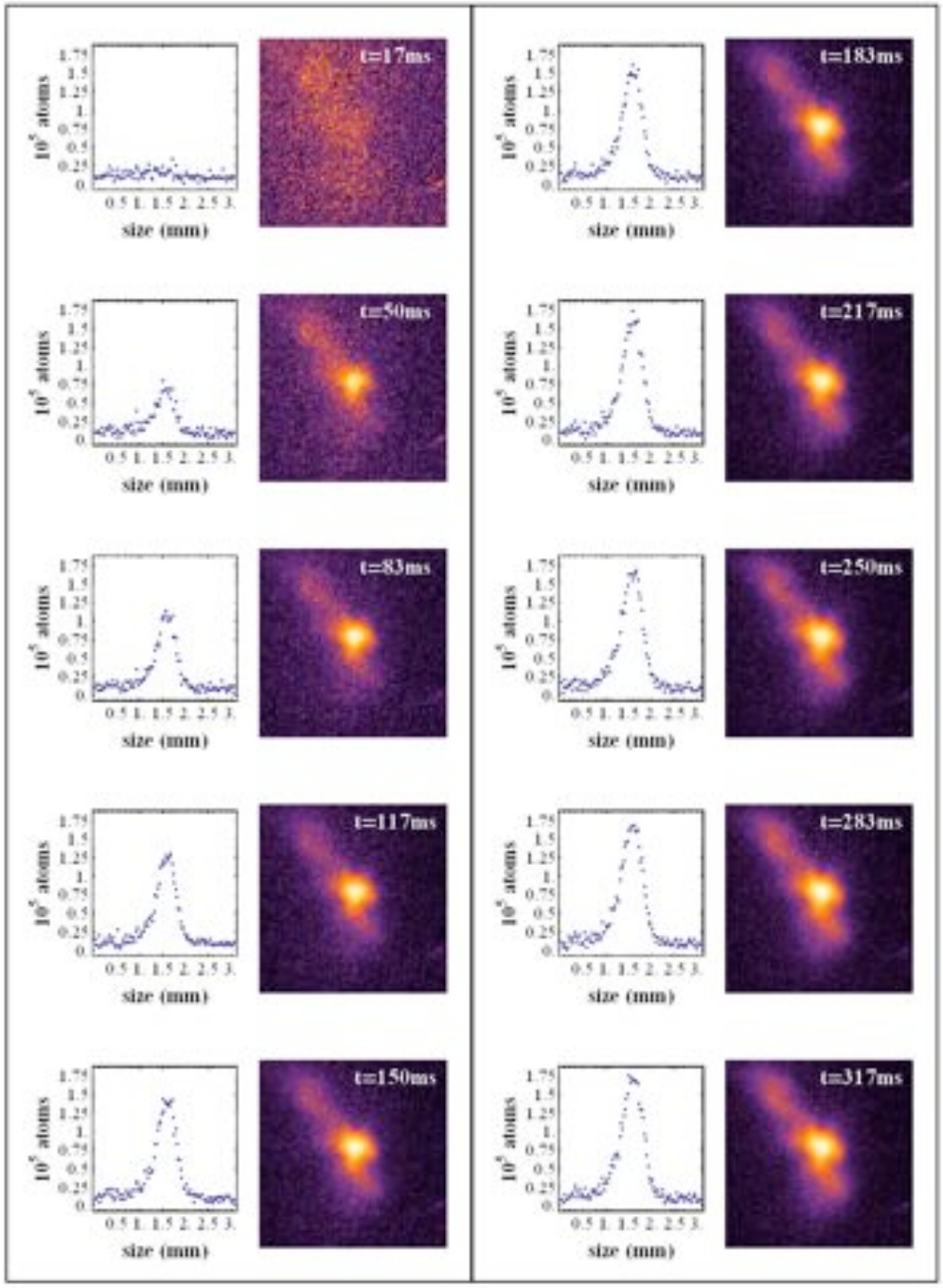

Figure 4.3: A series of fluorescence images of the filling of the MOT in the Au coated 70.5° pyramid and mask arrangement. The time at which each picture was recorded is indicated in the top right corner of each image, where $t = 0$ is defined by moment when the trapping light was let through by a shutter. A horizontal profile taken at the middle of the atom cloud accompanies each frame. The vertical scale on these graphs is the number of pixel counts given by the CCD camera.

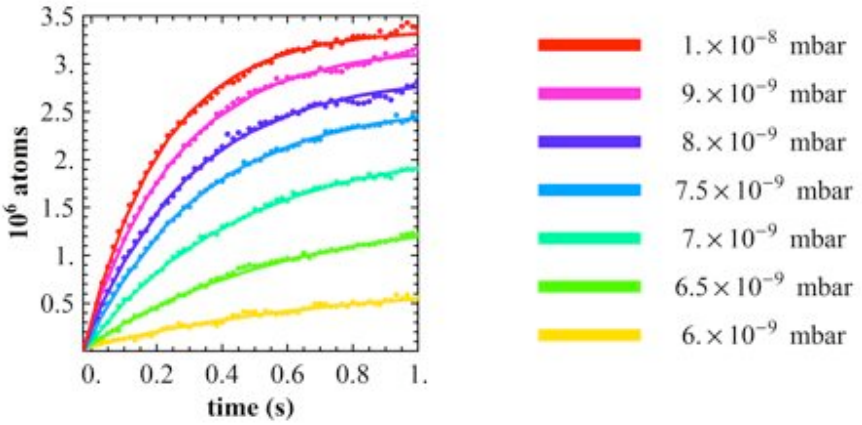

Figure 4.4: The filling curves measured in the gold coated 70.5° pyramid and mask arrangement. The CCD camera recorded 60 frames per second and the number of atoms imaged at each frame in represented by the points in the graph. The solid lines are the result of fitting the MOT filling equation (eq. 4.1) to each data set, each of which corresponds to a different pressure indicated by the colour table included on the right of the figure.

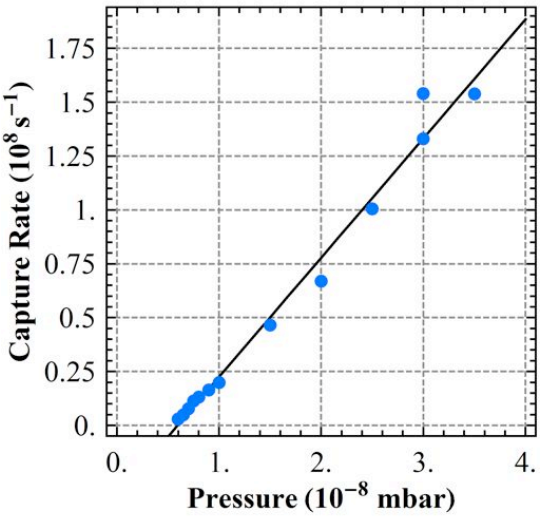

Figure 4.5: A series of filling curves were measured in the gold coated 70.5° pyramid at various rubidium partial pressures. From these measurements, the dependence of the MOT capture rate (see equation 4.2) on the rubidium pressure was established. The slope of the linear fit included in the graph is 5.5×10^{15} $s^{-1}mbar^{-1}$.

the pyramid surfaces is simply

$$\frac{1}{2}D\sin\left(\frac{1}{2}70.5^\circ\right) = 3.3\,\text{mm}.$$

This seems to suggest that the distance to the nearest surface determines the length scale that can be considered for effectively cooling and trapping atoms. This is a very interesting result and we will come back to it when analysing the capture rate dependence on the size of the pyramid in section 4.2.2.

Having looked at pyramids with 78% and then 95% reflectivity, we decided to try a coating with 70% reflectivity. This was motivated in part by our hopes for making

a microfabricated MOT on a chip. The method used for fabricating current carrying wires in an atom chip consists of laying a seed layer of the chosen material and then electroplating more material on top of the seed layer until the desired wire thickness is achieved. This seed layer is laid on top of all the chip surface, including the pyramids, and therefore becomes the reflective layer. The standard options for this seed layer include palladium, which according to table 3.1 has a 70% reflectivity. Although we had no palladium for our coating plant, we did have a platinum source. According to the values given in table 3.1, the reflectivities of platinum and palladium are very similar. For this reason, we decided to evaluate the possibility of utilising a palladium coating on our chip pyramids by laying a platinum coating on the glass 70.5° pyramid. First, a 5 nm thick chromium adhesion layer was sputtered on both pyramids and then 100 nm of platinum were sputtered on top of the chromium layer. We measure a 70.5% reflectivity for the platinum coated pyramid, which is in very good agreement with the value quoted in table 3.1. Figure 4.6 shows a picture of the platinum coated pyramid and the anti-Helmholtz coil pair which constituted the heart of our experiments at that time. Via a couple of posts, the pyramid and coil set is attached to an 8" blank flange, which allowed us to load them into the vacuum chamber.

We demonstrated that a MOT can also be created in the platinum coated 70.5° glass pyramid, both including the mask in the input beam and with the entire beam uncovered. Although the efficiency of the MOT seemed to improve with the inclusion of the beam mask, neither of these two configurations trapped more than 10^6 atoms. We also tested the 90° pyramid with a platinum coating and found that the number of atoms was also low.

Likewise, as we also had the option of sputtering a chromium coating in our atom chip, we later coated both glass pyramids with this material and attempted to make MOTs in both of them. Once more, MOTs were generated in the two pyramids and the effect of masking the beam in the case of the 70.5° pyramid was also tested. These pyramid MOTs trapped even fewer ($\sim 10^5$) atoms than the platinum coated pyramid and masking the input beam when using the 70.5° pyramid once more proved to be slightly more efficient than not masking it.

As a result of the effort invested in testing all these different materials, we concluded that the 70.5° pyramid works more efficiently either when is coated in aluminium (reflectivity $\sim$80%) or when a high reflectivity gold coating and a mask are utilised.

4.2 The scaling laws in the 70.5° pyramid

We turn now to how the size of the pyramidal mirror influences the efficiency of the MOT. Using the gold coated 70.5° glass pyramid with the type 3 ray areas blocked, we made two types of measurements. First, we placed the MOT position at different locations along the pyramid axis and determined how this changes the number of atoms that can be collected in the trap. In these experiments, the laser light illuminated the entire surface of the pyramid. In a second set of experiments, we cropped the cross sectional area of the laser beam with the aim of recreating the situation of having pyramids of various sizes.

4.2.1 Varying the MOT size

Let us begin with describing the trap displacement experiments. The position of the trap was controllably displaced by means of a uniform magnetic field parallel to the

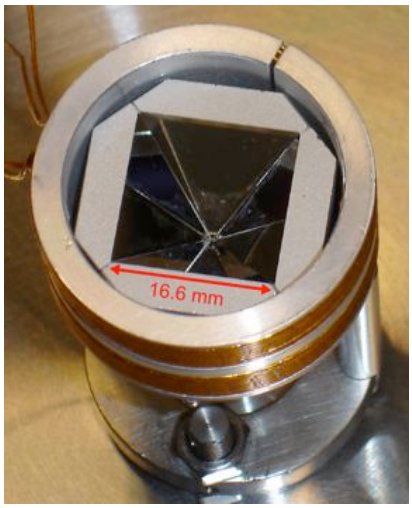

Figure 4.6: This image shows the 70.5° pyramid coated with platinum and mounted inside the coil pair, ready to be loaded into the vacuum chamber. The side length of this pyramidal mirror is shown to be 16.6 mm

pyramid axis. As described in section 3.4.1, this field was generated by the z bias coil and the x and y bias coils were used to compensate any off-axis field components introduced by the z coil. Consequently, the position of the MOT as measured from the pyramid apex was determined by the current I_z supplied to the z bias coil according to graph **B** in figure 3.19 (page 67). Similarly, graphs **C** and **D** in the same figure show the currents required for compensating the off-axis field components at each MOT position.

A set of fluorescence images of cold atom clouds trapped at different positions on the pyramid axis is shown in figure 4.7. The cold atom cloud at the centre of these images is surrounded by a series of its reflections on the pyramid mirror faces. To distinguish between the atom cloud and its reflections, we displaced the position of the MOT perpendicularly to the pyramid axis. We observed the displacement of the cloud and of their images and found that depending on the position of the cloud, some of this reflections disappear while the original image moves accordingly with the field applied to displace the MOT. These images are accompanied by plots of the corresponding magnetic field, which were obtained by calculating the total magnetic field generated by the anti-Helmholtz coil pair and the bias field coils according to the calibrations given in section 3.4.1. The position of the cloud relative to the pyramid apex, which is identified with the point where the magnetic field strength is equal to zero, is given in figure 4.7 for each image in the array. Hence, this figure shows that, as the position of the point of zero magnetic field is displaced by the axial bias field, the location where the cold atom cloud forms is also displaced.

The position calibration given in section 3.4.1 is summarised by equation 3.6

$$Z_{MOT} = +3.0 + 1.327(5)\ I_z - 7.7(3) \times 10^{-2}\ {I_z}^2$$

To verify the validity of this calibration, we measured the MOT to apex distance directly from the set of fluorescence images shown in figure 4.7. This procedure is exemplified in figure 4.8, which corresponds to an estimated distance of 3.0 mm from the apex. We first obtained a pixels to mm calibration by taking a picture of a ruler. Without modifying the CCD camera settings used to image the atom clouds, we placed this ruler at a distance from the camera comparable to the separation between the cold atom cloud and the camera. This resulted in a conversion factor of 0.036 mm/pixel. Next, the position of both the cloud and the pyramid apex was located on each image (red

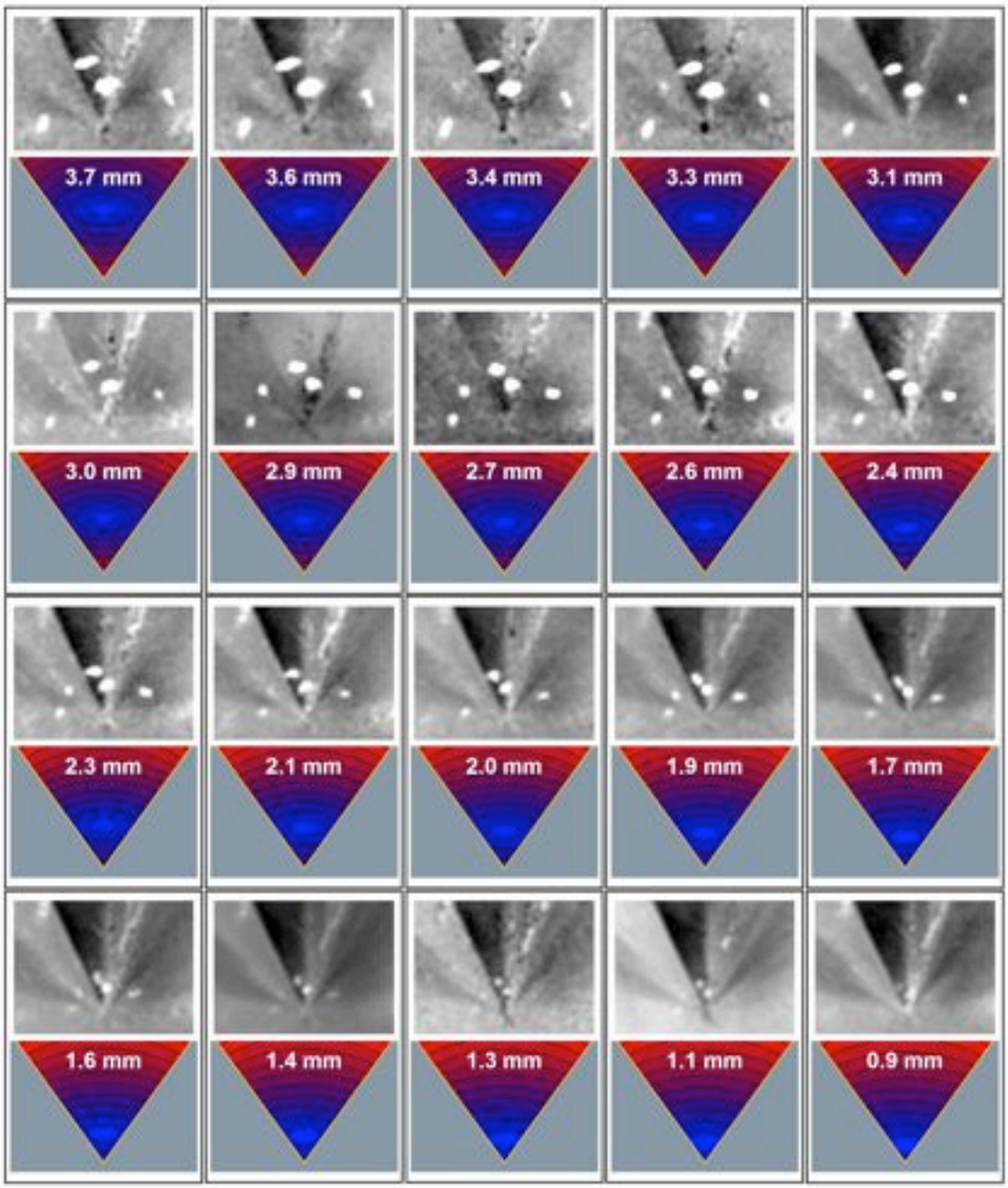

Figure 4.7: The position of an atom cloud can be translated along the 70.5° pyramid axis. A bias magnetic field applied parallel to the pyramid axis can be used to move the position where the field goes to zero. Fluorescence images of trapped atom clouds at different positions over the pyramid axis are shown along with the corresponding magnetic field plots. The distance between the cloud and the pyramid apex is also shown and, as in figure 4.1, the image of the cloud is accompanied by its reflections on the pyramid mirror faces. In the top left image, the real cloud appears at the centre of the image (see figure 4.8) and in the rest of the images, its position gradually moves down towards the pyramid apex.

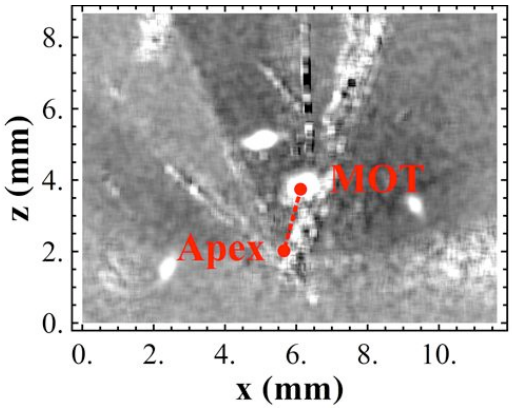

Figure 4.8: The calibration of the distance from the MOT to the pyramid apex was verified by measuring this distance in the MOT fluorescence images. A conversion factor of 0.036 mm/pixel and a camera viewpoint angle of approximately 35° with respect to the pyramid axis are used to calculate the cloud to apex distance in these images. The cold atom cloud, which in the laboratory is identified by moving the cloud position throughout the pyramid, is denoted as MOT in this image.

spots) and the distance between these two points (dashed line) was computed. Then, it was also necessary to consider that the camera was looking straight into the pyramid apex almost at a grazing angle from one of the pyramid faces, which is located at the bottom of the fluorescence images. This implies that, with respect to the pyramid axis, the camera was oriented at an angle of approximately 35°.

The result of repeating this procedure for various MOT positions is shown in figure 4.9 together with a solid line which represents the position calibration based on the current applied to the z-bias coil. This graph demonstrates the good agreement that exists between the two methods used to determine the MOT to apex distance. The differences between these two methods is considerable only at the extremes of the plotted region. Nevertheless, this is due to the difficulty of extracting the position of both the atom cloud and the pyramid apex from the fluorescence images. When far from the apex, the clouds are big and it is not possible to identify the centre of the trap; similarly, the broad feature generated by the light scattered from the pyramid apex makes difficult to identify with precision its position in these images. When the trap is close to the apex, the clouds are small and dim, and their position can not be easily determined. In addition, the pyramid apex can not be located with precision and at such small distances the extent of the apex scatter region becomes comparable to the distance that needs to be determined. In spite of these limitations, the agreement in the middle sector of the investigated range justify using the numerical calculation as a reliable method for determining the MOT to apex distance.

The uncertainty in the determination of the MOT position is estimated by considering the standard deviation associated to the three coefficients on the calibration formula, as well as the uncertainty associated to the current applied to the z bias coil ($\Delta I_Z = 10\,\mathrm{mA}$). This results in uncertainties which are of the order of 0.1 mm. This initial set of experiments established the settings needed to achieve any desired MOT position along the pyramid axis.

The brightness of the fluorescence images displayed in figure 4.7 is a clear indication of the changes in the MOT efficiency. In figure 4.10, the red squares correspond to the number of atoms contained in MOTs generated at various positions over the pyramid axis. The number of atoms contained in the trap was extracted once more from the fluorescence images by means of the camera calibration given in section 3.5.1. Three different regions can be distinguished in the trend followed by the red squares. First, between 0.5 mm and 2.0 mm, the number of atoms in the log-log scale follow a linear tendency. The linear fit shown in the graph indicates that the number of atoms trapped

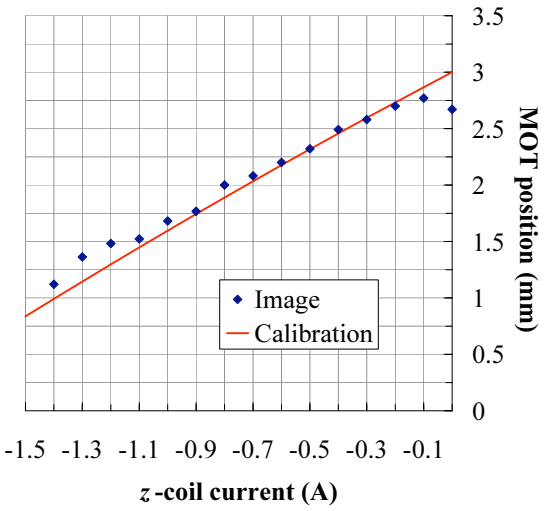

Figure 4.9: The position of the cloud as determined from the fluorescence images shown in figure 4.7 is compared to the calibration given in section 3.4.

in these MOTs obeys a power law. The slope of this line, which is found to be equal to 4.0(1), establishes that the number of atoms in the MOT is proportional to h^4, where h is the distance to the pyramid apex. This result not only suggests that this distance is proportional to the characteristic stopping distance r, but also agrees remarkably well with the dependence given by equation 2.26 (page 35) for the steady state number of atoms on the distance r that was derived in section 2.4.

The second region corresponds to the points above 2.0 mm. In our experiment, the number of atoms that can be trapped at these distances is limited by the size of the gaussian laser beam. The side length of the 70.5° pyramid is 16.3 mm, but the gaussian radius of the trapping light beam was approximately 10 mm. Consequently, in this region of the graph the MOT characteristic length r instead of being determined by the size of the pyramidal mirror, is given by the size of the gaussian profile of the trapping laser beam.

Finally, for distances below 0.5 mm atoms interacting with the trapping light in the vicinity of the MOT begin to explore areas in which the apex defect shadows the light. The capture rate of MOTs generated in this region will necessarily be influenced. We believe that this is the reason why the last point in our graph appears slightly below the linear tendency discussed before. The defect shown in figure 3.16 acts as a region next to the pyramid apex in which light is not reflected. In terms of the light force balance that generates the trap, this means that there is a point along the pyramid axis beyond which it is not possible to create a MOT. Imagine an atom that the light pushes into the trap centre. If this atom explores the region shadowed by the defect, it will experience a force imbalance that will push it away from the trap.

Next, we looked at the effect of limiting the diameter of the MOT laser beam, which is equivalent to varying the size of the pyramid. We placed a circular iris in the beam path with its centre point carefully aligned with the pyramid axis. This way, only the portion of the pyramid that is illuminated by the laser contributes to the MOT. Thus, a variation of the pyramid opening was simulated by changing the iris aperture diameter to limit the diameter of the laser beam. With the aim of finding the optimal MOT operation at each pyramid size (iris aperture diameter), we found the height where the number of atoms collected in the trap was maximum by varying the current of the z-bias

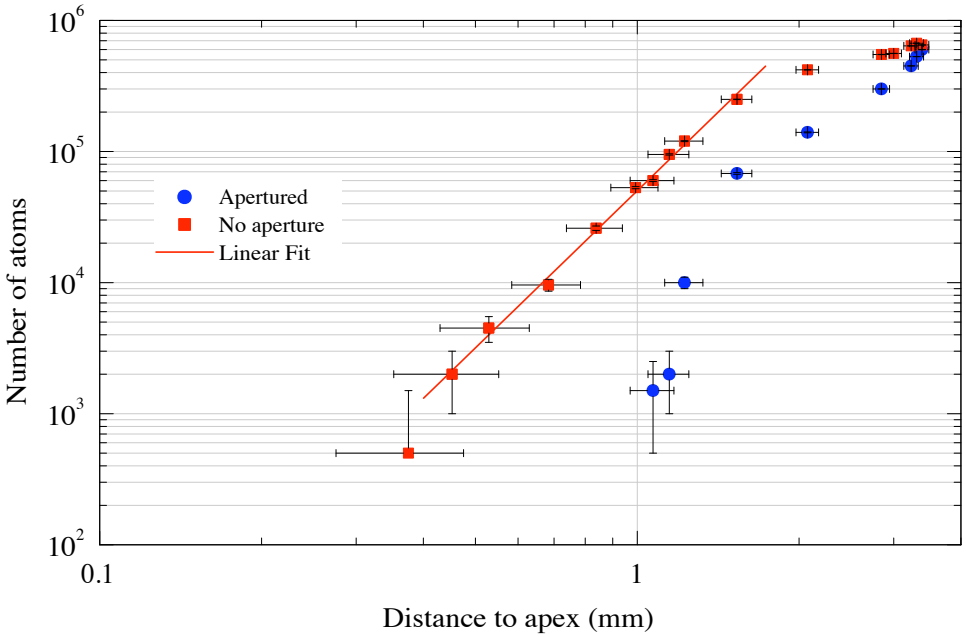

Figure 4.10: Number of atoms trapped versus distance from the pyramid apex. The results obtained when all the pyramid surface was being illuminated by the trapping beam are displayed together with those for which the size of the beam was limited by an iris. This results suggest that the reduction in the number of trapped atoms in the apertured case is mainly due to a change in the capture rate of the MOT.

coil. The smallest iris aperture utilised in these experiments was approximately 5 mm.

The effect the aperture shadow has on the MOT functioning is similar to that of the defect. Consequently, the section of the pyramid axis where the light forces are well balanced is limited. In this situation, the cloud of atoms is located between two regions in which not all the light components required for trapping are present. The section of space in which atoms can be cooled and trapped is severely reduced and therefore, less atoms are collected in the trap. Furthermore, even those atoms that are successfully collected in the trap can leak out as a result of an increase in the possibility of they exploring a not trapping region. This probably results in lower capture rates and higher loss rates, both of which are reflected in a reduction in the number of atoms collected in the trap.

The number of atoms collected in the 70.5° pyramid MOT with the beam diameter clipped by the iris are shown as blue dots in figure 4.10. In both experiment sets, the position of the trap was determined by displacing the point of zero magnetic field along the pyramid axis. Therefore, the magnetic field potentials responsible for the generation of these traps are the same in the two data sets. Similarly, the proximity of the pyramid faces should have the same effect in each data set. The difference between the two sets of data shown in figure 4.10 is just the diameter of the light beam. When an atom enters the pyramid from above, the distance over which it can be decelerated is limited

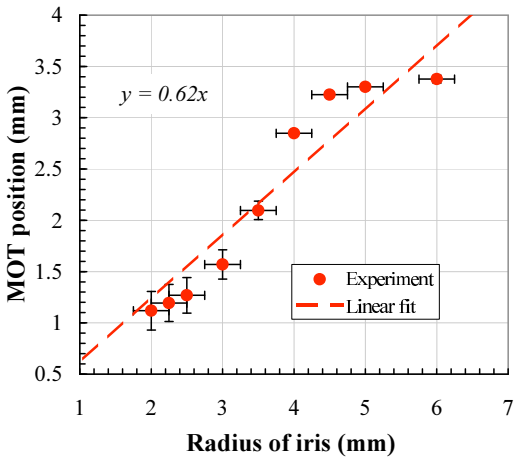

Figure 4.11: The relation between the aperture defined by the circular iris and the MOT optimal position is presented in this graph. A linear fit of this data results in a proportionality factor which indicates that the MOT was located approximately at the middle of the corresponding pyramid depth.

by the size of the beam. As this is clipped by the iris, the distance along which these atoms can interact with the light is reduced. In consequence, the MOT capture velocity is expected to show a dependence on the beam diameter and a reduction in the MOT capture rate can be anticipated.

The results shown in figure 4.11 are the distances above the apex at which the MOT contained the largest number of atoms versus the aperture radius. The linear fit shown in the figure suggests that the optimum MOT height h above the pyramid apex is proportional to the radius A of the laser beam: $h \simeq 0.62A$. This means that the best place for the MOT is roughly half way between the top and bottom of the illuminated section of pyramid. The dispersion of the experimental data around the linear fit can be understood by considering that instead of being a single point, there is a small region in the pyramid volume in which the MOT is optimal. Even if there is indeed a point in which the number of atoms collected in the trap is a global maximum, the sensitivity of our experiment would not allow us to determine this position. Nevertheless, these results are sufficient to identify the approximate location where the MOT is more efficient.

Possible causes for the drop in the number of trapped atoms exhibited by the red squares in figure 4.10 can include a diminution in the flux of atoms reaching the trapping region; a reduction in the distance along which fast atoms can be slowed down and trapped; and loss of atoms from the trap as a result of collisions with the neighbouring pyramid mirror faces. In order to understand the dependence of the number of atoms on the size of the pyramid, we decided to investigate how the capture and loss rates change as the trap position approaches to the pyramid apex.

4.2.2 Capture and loss rates

Consider first of all that the loss rate in equation 2.16 has three components: losses caused by collisions with fast rubidium vapour atoms; losses due to collisions with other species of atoms; and losses due to the proximity of the pyramid walls. The new loss rate is

$$\frac{1}{\tau} = n_{Rb}\beta + \gamma, \tag{4.3a}$$

where

$$\beta = \sigma_{Rb} \left(\frac{3\, k_B\, T_{Rb}}{m_{Rb}} \right)^{1/2} \tag{4.3b}$$

and

$$\gamma = n_b \, \sigma_b \left(\frac{3 \, k_B \, T_b}{m_b} \right)^{1/2} + \frac{1}{\tau_w}. \tag{4.3c}$$

Similarly, the capture rate given in equation 2.16, can be explicitly expressed in terms of the rubidium atom density

$$R = \alpha n_{Rb} \tag{4.3d}$$

With these definitions the MOT filling rate equation is

$$\frac{dN}{dt} = \alpha n_{Rb} - \left[\beta n_{Rb} + \gamma \right] N \tag{4.4}$$

which, with the initial condition $N(0) = 0$, has the solution

$$N(t) = N_s \left(1 - e^{-(\beta n_{Rb} + \gamma) t} \right) \tag{4.5}$$

where, the steady state number of atoms is

$$N_s = \frac{\alpha n_{Rb}}{\beta n_{Rb} + \gamma} \tag{4.6}$$

We have measured the capture and loss rates from MOT loading curves (figures 4.12 and 4.13) taken at different positions along the pyramid axis and at various rubidium pressures. As before, the position of the cloud was controlled by the application of appropriate bias fields. The rubidium pressure was controlled by varying the current supplied to the rubidium dispenser and its value was determined with the calibration given in section 3.1.2

$$P_{Rb}\,(I) = 4 \times 10^{-16} e^{2.97(9)\, I} \tag{4.7}$$

where the current is given in Amperes and the pressure in mbar. The loading curves were obtained by first switching on the anti-Helmholtz coils and then capturing series of fluorescence images as a cold atom cloud was collected in the trap. Firstly, a background light image was taken immediately before feeding current to the coils. Then, the first image of the filling curve was taken immediately after the coils current was switched on and then a new image was captured every 50 ms, until a total of 20 images (950 ms) had been taken. This sequence of images was taken several times for each pair of MOT position and pressure values.

The number of atoms as a function of time was extracted from each sequence of images. First, the background image was subtracted from each image in the filling sequence. In addition, to minimise the noise introduced by variations of the background light between the filling curve images and the background image, a region of interest containing exclusively the section of the image where the MOT is visible was selected. To determine the number of atoms in each frame of the filling, all the pixel values in the subtracted image were summed and the resulting value was substituted in the camera calibration formula deduced in section 3.5.1.

Figures 4.12 and 4.13 contain the MOT filling data sets that we measured. Each colour in these graphs corresponds to a single MOT filling sequence. The solid curves are the result of a least-squares fitting of equation 4.5 to each filling sequence, with the steady state number of atoms N_s and the $1/e$ life-time τ as the fitting parameters. For each MOT filling sequence, the standard deviation associated to the estimate of N_s is typically a 4% of the estimated value. Similarly, a typical standard deviation of 10% is

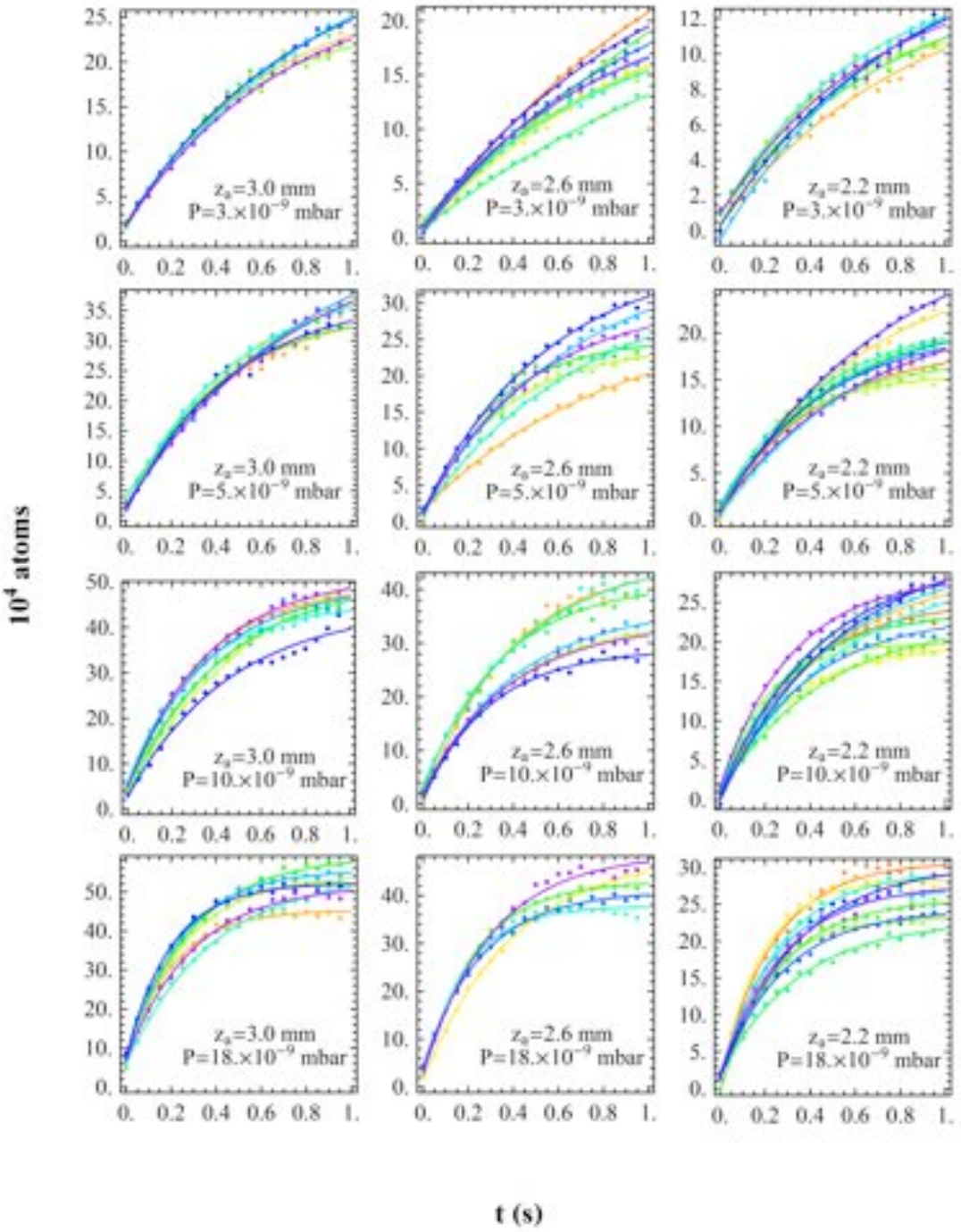

Figure 4.12: The filling curves measurement I. MOT filling curves obtained at various positions over the pyramid apex and at various Rb pressures.

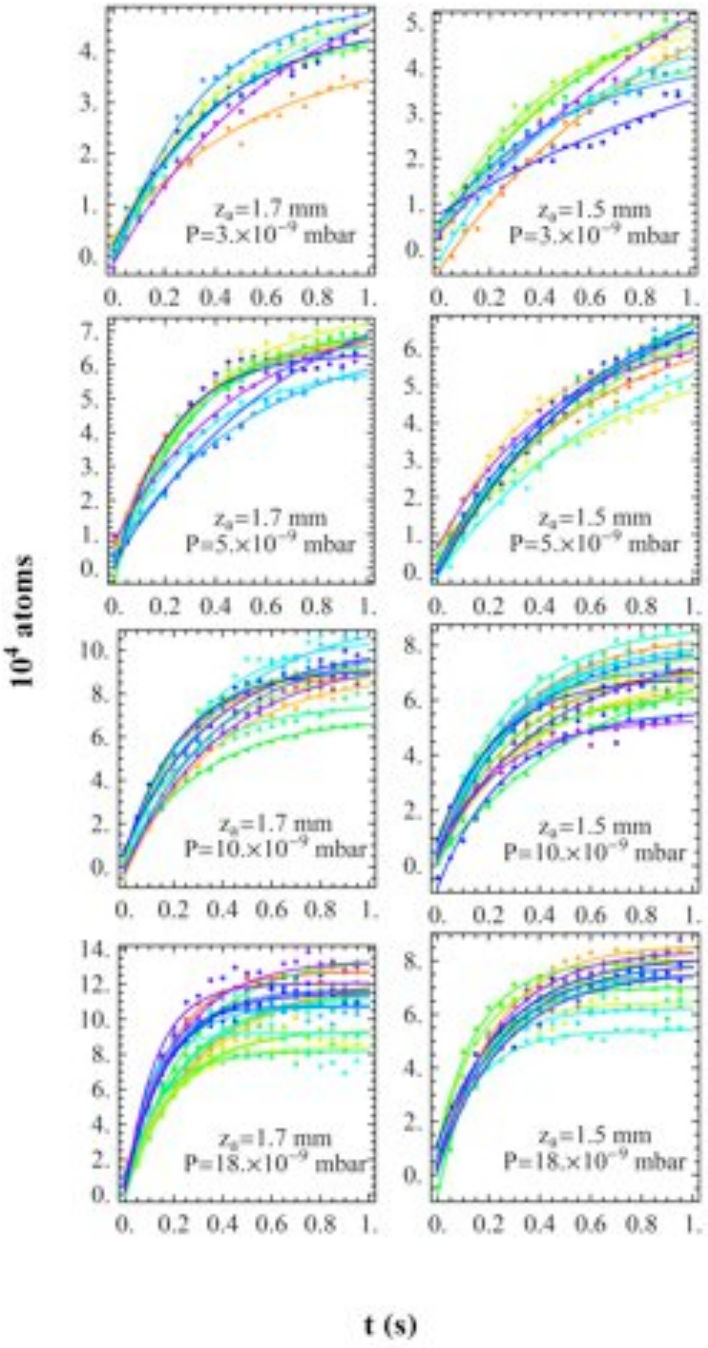

Figure 4.13: The filling curves measurement II.

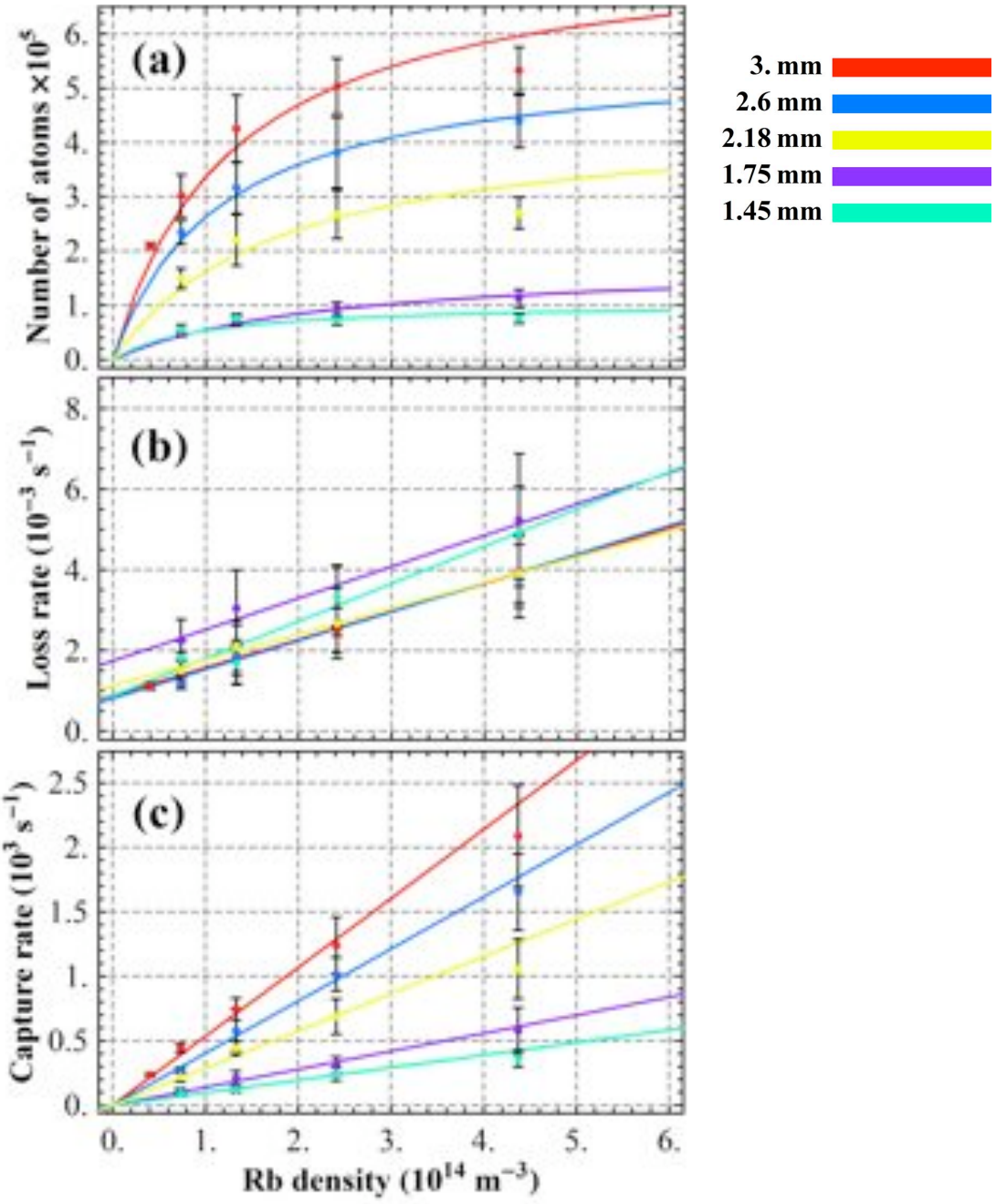

Figure 4.14: The mean values of **(a)** the steady state number of atoms N_S, **(b)** the loss rates $1/\tau$, and **(c)** the capture rates R obtained from the analysis of the MOT filling measurements are shown as a function of the rubidium density n_{Rb} for the series of positions investigated. The capture and loss rate parameters α, β and γ extracted from the linear fits shown as solid lines in graphs **(b)** and **(c)** have been used to evaluate equation 4.6 and generate the solid lines included in graph **(a)**.

associated to the determination of τ. However, the spread of the filling curves shown in the two arrays of graphs represents larger uncertainty intervals than these values. This is a consequence of a build up of the rubidium pressure during the recording of the various filling curves which is not considered in equation 3.2. Consequently, the values of both N_s and τ that have been assigned to each position and pressure are the averages of the results obtained by the various measured sequences, and the corresponding uncertainties are identified with the standard deviations of these values from their averages.

Figure 4.14**(a)** shows the steady state number of atoms N_s collected in the MOT as a function of the rubidium pressure at the various positions measured. These values were obtained by averaging the results of the least-squares fitting of the MOT filling curves at each position and pressure investigated. The uncertainty intervals included in this graph are the standard deviations of the various numbers of atoms from the mean value reported in the graph. These error bars reflect the spread of the various filling curves measured at each pressure and position. The extent of these bars demonstrate that the uncertainty in our determination of N_s is in general dominated by the spread in the various MOT filling sequences and not by the typical 4% value indicated by the curve fitting procedure. This graph clearly shows the strong dependence that the number of atoms has on the position of the MOT, but also gives an indication of to which extent the rubidium partial pressure can be used to feed the trap with atoms. The solid lines included in this graph are the trends predicted by equation 4.6. The values of α, β, and γ utilised for ploting these curves are the results of the rest of this analysis, which is described in the following paragraphs.

The loss rates $1/\tau$ shown in figure 4.14**(b)** as a function of the rubidium pressure for the MOT positions investigated are also the average of the values given by the fitting of the filling curves. Once more, the error bars are the standard deviation of the various loss rates corresponding to each of the filling sequences from the mean value represented by each point in the graph. In accordance with equation 4.3a, the data sets which correspond to each position have a linear dependency on the rubidium density. Therefore, we have utilised these results to determine the dependency of the loss parameters β and γ on the distance to the pyramid apex. The solid lines included in the graph are the linear fits corresponding to each MOT position and the fitting parameters are presented as green points (●) in figures 4.15 and 4.16.

The capture rates $R = N_s/\tau$ were then obtained for each one of the MOT filling sequences shown in figures 4.12 and 4.13. The values of N_s and τ obtained by fitting equation 4.5 to each filling sequence were utilised for calculating these capture rates. Figure 4.14**(c)** presents the average value of R obtained from the various image sequences taken at each position and pressure. In addition, the uncertainty was determined by calculating the standard deviation from the mean value. This graph demonstrates, as proposed in equation 4.3d, that the capture rate R is proportional to the rubidium density and that the proportionality factor α depends on the position of the MOT. The solid lines included in this graph are the result of performing linear regressions on each set of capture rates. This therefore resulted in a single α value for each trap position, which was then displayed as a green point (●) in figure 4.17. The uncertainty assigned to each point in this last graph is the standard error associated to the corresponding linear regression.

Finally, as mentioned before, the solid lines included in figure 4.14**(a)** are the result of substituting in equation 4.6 the values of α, β, and γ that are displayed as green points (●) in figures 4.17, 4.15 and 4.16 respectively. Now that we have described the

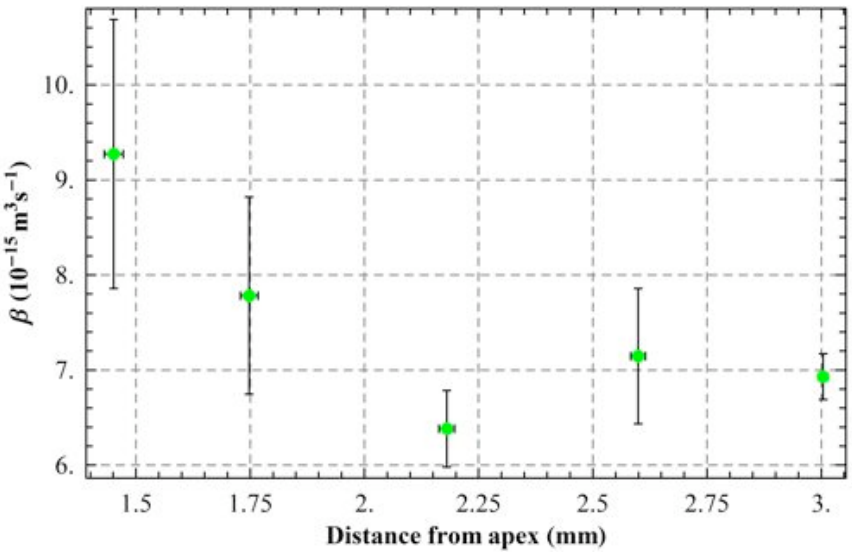

Figure 4.15: The proportionality factor β relating the loss rate and the rubidium vapour density for each of the MOT positions investigated.

methodology followed for obtaining the data contained in these three graphs, in the following paragraphs we will discuss these results.

The factor of proportionality between the MOT loss rate and the rubidium density β is displayed as a function of the distance from the apex in figure 4.15. These points and their error bars, as we have already mentioned, are the slopes obtained from the linear regressions shown in graph 4.14**(b)** and their corresponding standard errors respectively. At the beginning of this section we presented a model in which the dependence of the MOT loss rate on the pyramid walls is absorbed on the term led by the parameter γ. However, the growth on the value of β as the MOT approaches to the pyramid apex suggests that there is a dependence of the rubidium atom density on the distance to the pyramid surfaces. Rubidium atoms in the vapour are continuously being absorbed and desorbed from these surfaces and this could have lead to an enhancement of the loss rate caused by collisions with the desorbed atoms.

The results shown in figure 4.15 can be used to estimate the cross section for collisions between background vapour rubidium atoms and trapped atoms. To keep this simple, we have calculated a single β value by averaging the data points shown in figure 4.15, which results in a value of $(7.9 \pm 1.4) \times 10^{-15}\,\mathrm{m^3 s^{-1}}$. We then obtained the Rb-Rb collision cross section by dividing this average value of β by the mean velocity $\bar{v}$ of the non-trapped, room temperature rubidium atoms, which we assumed to be at a pressure of 10^{-9} mbar. In addition, for simplicity we restricted ourselves to considering collisions between ^{85}Rb atoms. This way, the average of β results in a collision cross section of $2.7(5) \times 10^{-13}\,\mathrm{cm^2}$. This value is in good agreement with the value of $3 \times 10^{-13}\,\mathrm{cm^2}$ reported by Rapol *et al.* [85].

Note that in the range of distances investigated, the parameter that determines the loss rate dependence on the distance from the pyramid apex γ, which is given in figure 4.16 also as green points (●), does not show a significant change. As a result of the limitations imposed by the quality of the pyramid replica, the shortest distance to the apex achieved in our experiments was approximately 1 mm. Let $z = h$ be the position where the cloud sits as measured from the pyramid apex. Then, the perpendicular

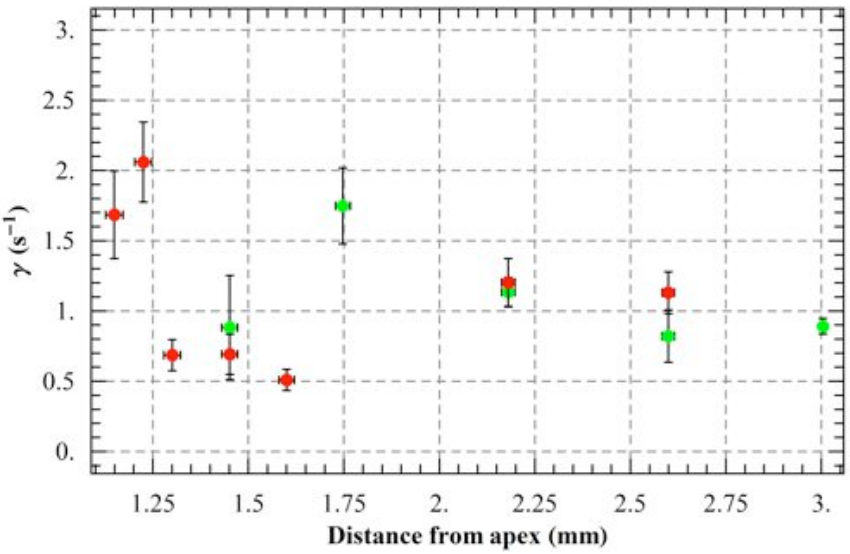

Figure 4.16: The loss rate as a function of the distance from the pyramid apex. This data shows that the loss rate does not exhibit a considerable growth over the range of distances from the pyramid apex that we have studied. As in figure 4.17, the green dots correspond to the measurement of the MOT filling curves (●) and the red dots (●) are the results of the number of atoms versus rubidium pressure experiment.

distance between the pyramid mirror surfaces and the cloud is given by:

$$l_w = h \sin\left[\frac{1}{2}\cos^{-1}\left(\frac{1}{3}\right)\right] \tag{4.8}$$

This implies that in this last set of experiments, the closest the atom cloud got to the pyramid faces is such that $l_w \sim 577\,\mu\text{m}$. Also, for the longest distance from the apex reported in these graphs l_w was 1.73 mm. The radius of the atom clouds collected in both the 90° and the 70.5° pyramids far from the apex was typically 600 µm. Therefore, the minimum distance from the wall that was possible to investigate is comparable to the maximum cloud radius. Furthermore, as a result of the drop in the capture rate, which is presented in figure 4.17, and the corresponding reduction in the number of trapped atoms, the size of the cloud became smaller as the trap position got closer to the pyramid apex. This suggests that in our latest experiments, the size of the cloud was certainly not limited by the proximity of the pyramid walls. This statement is confirmed by the small variation of the loss parameter γ on the range of distances that we have investigated.

The dependence of the capture parameter α on the trap position is reported in figure 4.17. In this graph, it is shown that the parameter that determines the MOT capture rate shows a clear drop in the ~ 2 mm measured range. The tendency of the data in this log-log scale suggest that there is a power law governing the number of atoms trapped at various positions on the pyramid axis. Together with the red points which will be discussed later in this text, a power law has been fitted to these points. This is shown as a blue solid line in the graph. As a result of this, we found that $\alpha \propto h^{3.5(3)}$. This dependence of the capture rate on the distance to the pyramid apex seems to be the most likely cause for the drop in the number of atoms in figure 4.10. In addition, this

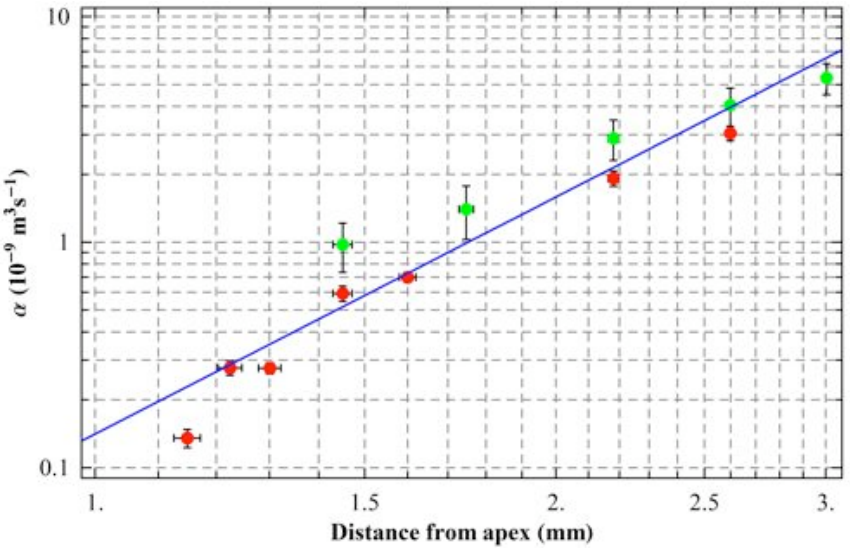

Figure 4.17: The dependence of the capture rate on the distance from the pyramid apex. In contrast to what happens to the loss rate, the capture rate exhibits a drop over the range of distances that were investigated. The MOT filling curves and the number of atoms versus rubidium pressure results are represented by green (●) and red (●) dots respectively. In addition, the blue curve represents a power law fitting of this data, which resulted in an $r^{3.5(3)}$ dependence.

result seems to be consistent with the r^4 dependency anticipated for the capture rate R.

An alternative method has been utilised for studying the capture and loss rates in pyramid MOTs of different sizes. This time, the number of atoms collected in MOTs located at various positions along the pyramid axis were determined as a function of the rubidium pressure in the chamber. In equation 4.6, the steady state number of atoms N_s is equal to the ratio of the capture rate to the loss rate. If the loss of atoms from the MOT is dominated by collisions between atoms in the trap and fast rubidium atoms in the background vapour, N_s is independent of the rubidium pressure. However, this is not always the case as there are other sources of loss in the MOT. For instance, we are interested in determining the dependence of the capture and loss parameters with the distance from the pyramid walls.

Figure 4.18 shows the steady state number of atoms measured as a function of the rubidium atom density for various positions over the pyramid axis. This density is determined from the rubidium partial pressure, which in turn is controlled via the current applied to the rubidium dispenser as given by equation 3.2. The rubidium vapour is assumed to be in equilibrium with the chamber walls at room temperature, $T = 295\,\mathrm{K}$. Hence, the rubidium density is given by

$$n_{Rb} = \frac{10^2 P_{Rb}}{k_B T}$$

where the pressure P_{Rb} is expressed in millibar. With the aim of extracting α and γ from these data sets, it was necessary to use the average value of $\beta = (7.9 \pm 1.4) \times 10^{-15}\ \mathrm{m^3 s^{-1}}$ that was found in our previous experiments. This way, the latest measurements can be

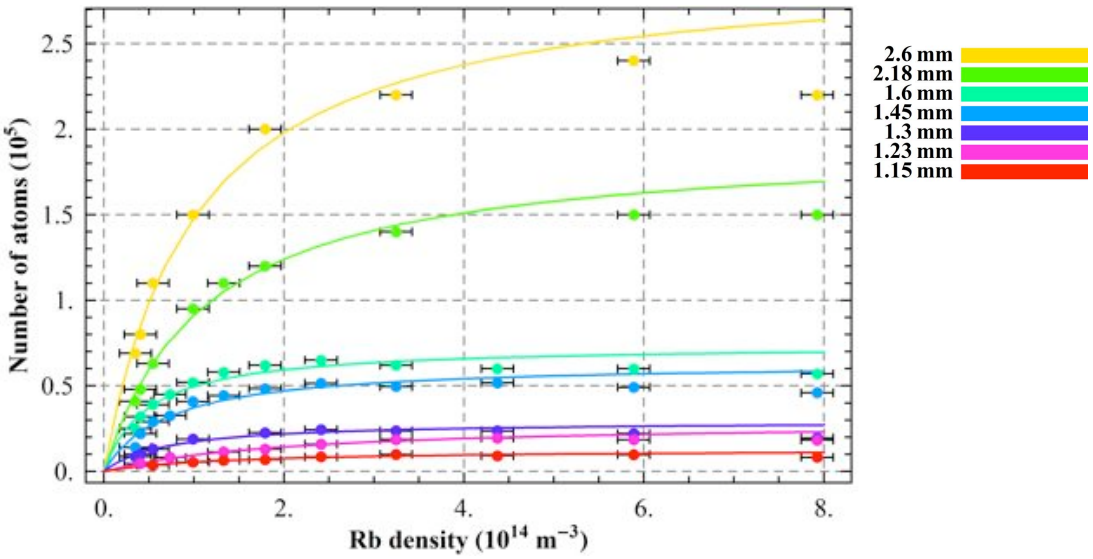

Figure 4.18: The steady state number of atoms was measured as a function of the rubidium density n_{Rb} at various positions along the pyramid axis. These measurements were used together with the value of β ($(7.9 \pm 1.4) \times 10^{-15}$ m^{3}s^{-1}) obtained in our previous experiment to determine the capture α and loss γ parameters. The curves included in the graph are the result of substituting α, β and γ in equation 4.6.

fitted to equation 4.6 and the remaining capture and loss parameters can be determined as functions of the trap position. The solid lines included in the graph are the result of substituting the fitting parameters into equation 4.6. The corresponding values of α and γ are shown as red dots (●) in figures 4.17 and 4.16 respectively. The uncertainty bars of these measurements correspond to the standard errors associated to the fitting represented by the solid curves in figure 4.18.

This second set of measurements are consistent with our previous observations. The loss parameter γ appears to be nearly insensitive to the position along the measured range. It is only when this distance approaches to the minimum values in the range that the proximity of the mirror surfaces might be influencing the values measured for this parameter. This could be the cause of the increase in the dispersion of the two sets of data points included in figure 4.16. The two sets of the capture parameter α measurements, on the other hand, show a clear drop along the range of distances that we measured. The linear fit indicated in the graph includes the two sets of measurements. The red points in the bottom of the scale drop below the linear tendency. This is probably a consequence of the use of an average value of β at the moment of analysing our measurements. At shorter distances from the pyramid apex, the values of β are above the average value utilised in the latest analysis. This higher loss rate value resulted instead in a drop on the capture parameter α.

Losses to a room temperature surface

The defect at the pyramid apex prevented us from creating MOTs closer than 1 mm or so to the pyramid apex. In order to study loss to the wall at shorter ranges, we studied the MOT loss rate independently of the capture rate by displacing the trap position

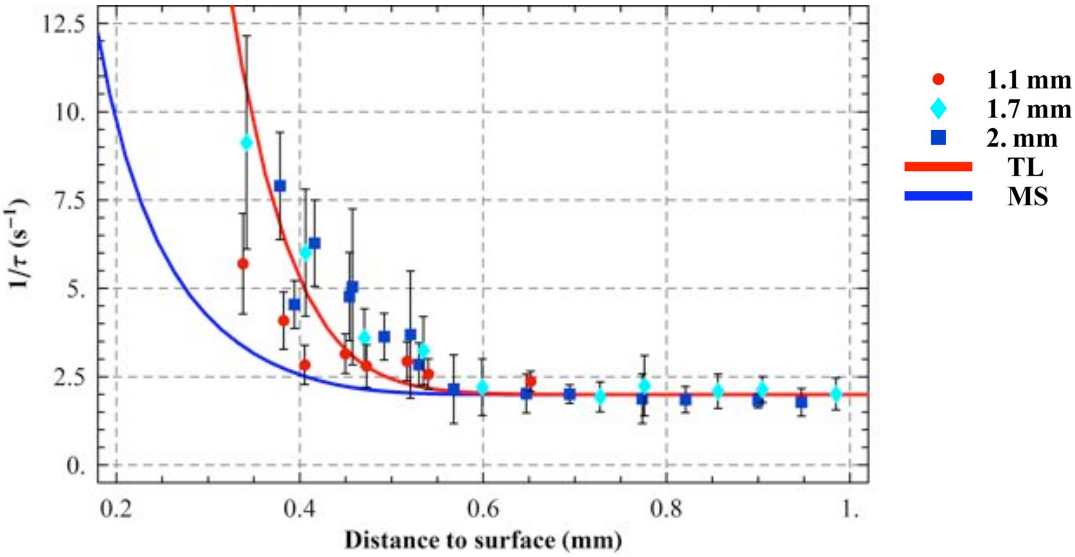

Figure 4.19: The MOT loss rate is as a function of the distance to the pyramid surface. Beginning at three different positions over the pyramid axis, the MOT was displaced towards one of the pyramid walls. This data shows that regardless of the axial position of the MOT, the loss rate increases only when the distance to the surface is $\lesssim 600\,\mu$m. The solid lines represent the result of a theoretical analysis of the problem taking into account that the cold atom cloud is either in the temperature limited regime (TL) or in the multiple scattering regime (MS). The details of this analysis are given in appendix B.

towards only one of the four pyramid faces. New sets of trap filling curves were recorded at different distances from this pyramid mirror face, while the height of the trap position along the pyramid axis was kept constant. This way we aimed at maintaining the MOT capture rate nearly constant while the change in the loss rate due to the proximity of the mirror surface was investigated. We also attempted to maintain the rubidium partial pressure constant so that we could isolate the effect of proximity to the wall. These experiments were repeated at various positions along the pyramid axis.

The MOT displacements ($\lesssim 1\,$mm) were small compared with the anti-Helmholtz coil pair dimensions. Hence, it is reasonable to assume that the shape of the magnetic field potential is the same for each data point and only the position of the zero field point is displaced. In addition, the laser light components responsible for confining the atoms are not modified as the MOT position is displaced. Consequently, the trapping potential is not modified by the displacement. Moreover, the capture volume is not greatly modified by the trap displacement in the y direction. In conclusion, we expected the trap capture rate not to show a significant change with respect to its value at the centre of the pyramid volume.

Once more, the cold atom cloud position was associated with the place where the magnitude of the magnetic field goes to zero. Hence, the MOT horizontal displacement was achieved by applying a bias field pointing along a direction perpendicular to the pyramid axis. This displacement was done along the y direction of our coordinate system. We firstly considered that the z component of the trap position in each experiment was entirely determined by the current applied to the z bias coil. Next, we assumed that the trap did not leave the $x = 0$ plane. Although both the y and the z bias coils gener-

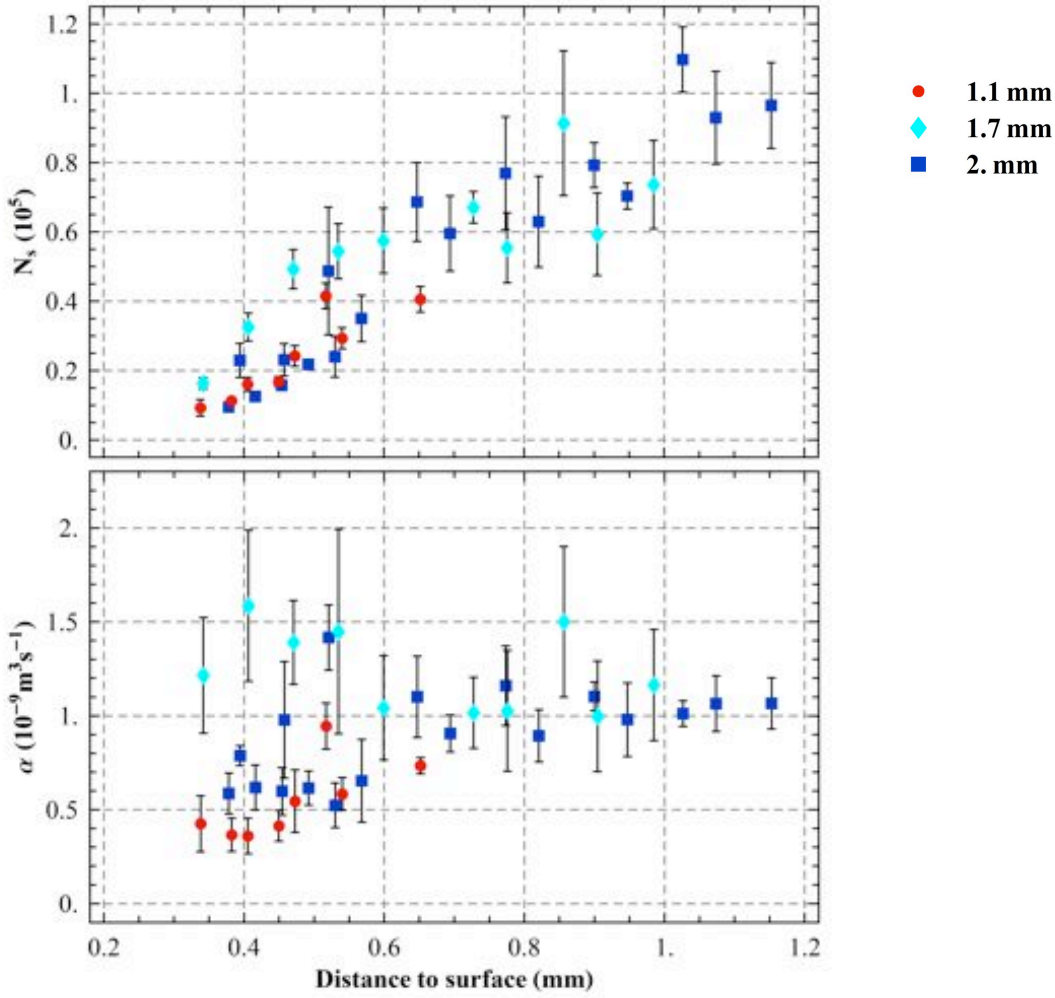

Figure 4.20: The steady state number of atoms N_S (top graph) and the capture parameter α (bottom graph) versus the distance to the pyramid surface. The steady state number of atoms drops as a result of the rapid increase in the loss rate when the distance to the pyramid surface is $\lesssim$ 600 µm. The capture parameter α, on the other hand, does not show a clear dependence on the distance to the surface. We believe that the variations of α are due to deviations of the rubidium density from the values utilised when analysing the data.

ate a certain amount of magnetic field along the x direction, small displacements of the cloud in the x direction do not have a decisive role in the determination of the distance to the pyramid mirror surface. This reduces the problem of finding the position of the trap to the determination of the y component of the position, which can be established by locating the place where the y component of the total magnetic field is equal to zero. Then, the MOT position was associated to each pair of z and y coil currents. Next, the distance of separation between the atom cloud and the pyramid walls was estimated by finding the minimal perpendicular distance between the estimated cloud position and the four pyramid faces.

The results of this last set of experiments are shown in figures 4.19 and 4.20. The procedure for recording the filling curves was the same as the one explained in section 4.2.2. The first thing to note in figure 4.19 is that the contribution to the MOT loss rate that results from the interaction between trapped atoms and a neighbouring surface becomes important when the distance of separation between the centre of the cloud and the surface becomes $\lesssim 600\,\mu$m. This threshold was already anticipated when discussing the results obtained by displacing the MOT towards the pyramid apex and the new results are in good agreement with our previous observations.

The loss rate value at which the experimental data approaches when the MOT was located away from the mirror surface is also consistent with the results obtained before. The average of the results shown in figure 4.15 resulted in a value of β of $(7.9 \pm 1.4) \times 10^{-15}\,\mathrm{m^3 s^{-1}}$. The current supplied to the Rb dispenser during the realisation of these experiments was kept constant at 5.5 A, which corresponds to a sustained Rb pressure of 5.4×10^{-9} mbar and to a Rb density of $1.3 \times 10^5\,\mathrm{cm^{-3}}$. This implies that the loss of atoms from the trap caused by collisions with background Rb atoms is characterised by a rate of $\beta n_{Rb} \approx 1.04\,\mathrm{s^{-1}}$. Similarly, in figure 4.16 the loss rate component that is independent of the Rb vapour density γ when the cloud is far from the pyramid faces is also of the order of $1\,\mathrm{s^{-1}}$. These two rates add to a value of $(\beta n_{Rb} + \gamma_B) \sim 2\,\mathrm{s^{-1}}$, which can also be seen in figure 4.19 as the value at which the total loss rate levels off for the highest values of the distance from the surface.

The two solid curves included in figure 4.16 are the result of a theoretical estimation of the loss rate caused by the interaction of the trapped atoms and the surface of the pyramid. The details of the theoretical treatment of this problem are given in appendix B. Two different regimes of MOT operation have been studied, the temperature limited regime (TL) and the multiple scattering regime (MS). While in the temperature limited regime, as more atoms are added to the trap, the cloud radius remains constant and the density is determined by the total number of trapped atoms; in the multiple scattering regime, the density remains constant as the cloud grows and the cloud radius is determined by the total number of trapped atoms [103]. The red solid line included in figure 4.19 corresponds to the tendency predicted for the temperature limited regime (equation B.4).

$$\gamma_{TL} = \frac{\bar{v} e^{-\frac{1}{2}\left(\frac{d}{\sigma}\right)^2}}{\sqrt{8\pi}\sigma\left[1 + \mathrm{Erf}(\frac{d}{\sqrt{2}\sigma})\right]} \tag{4.9}$$

where $\mathrm{Erf}(x)$ denotes the Gauss error function

$$\mathrm{Erf}(x) = \frac{2}{\sqrt{\pi}} \int_0^x e^{-t^2} dt$$

In the range of positions investigated, our measurements (bottom graph in figure 4.20) indicate that the capture parameter α takes a typical value of $10^{-9}\,\mathrm{m^3 s^{-1}}$. This, together with the Rb density at which these experiments were performed, results in a capture rate of $1.3 \times 10^5\,\mathrm{s^{-1}}$. In addition, we measured the $1/e$ radius of atom clouds with small numbers of atoms both along its shortest and its longest directions, resulting in 80 µm and 120 µm respectively. Finally, $(\beta n_{Rb} + \gamma_B)$ was taken to be $2\,\mathrm{s^{-1}}$. The blue solid line is the result of considering a MOT in the multiple scattering regime (see equation B.7). The capture rate used to generate this curve was the same as the one in the temperature limited case. The trap density in this case should be independent of the total number of atoms contained in the cloud; its value was estimated by considering an

elliptical cloud containing 3×10^4 atoms and extending over the same space considered in the temperature limited case.

The differences on the trends followed by each set of loss rates is a result of a dependence of the loss to the wall on the capture rate R. We have already shown that the capture rate is a function of the trap position along the pyramid axis. Each of the data sets shown in figure 4.19 was taken with a different value of current running through the z bias coil. Therefore the component of the trap to apex distance that points along the pyramid axis direction was different in each case. This distance has been given for each data set at the top right corner of the figure. Similarly, although care was taken in ensuring that the Rb partial pressure in the chamber, and therefore the capture rate R, was maintained constant during the recording of the filling curves, there was a small variation between the recording of the different data sets.

The values of the capture parameter α which correspond to each data set in figure 4.19 are shown in the bottom graph in figure 4.20. It is possible to appreciate that for each set of points, α remains relatively constant as the trap position approached the mirror surface. We attribute the variations of this parameter to deviations of the Rb density from the value of $n_{Rb} = 1.3 \times 10^8\,\mathrm{cm}^{-3}$ used for analysing the data. Even for each z bias coil current, a build up of the Rb pressure in the chamber during the recording of the filling curves could have been responsible for a variation of the capture rate and consequently of the resulting trend followed by each set of loss rates.

The steady state number of atoms N_S as a function of the distance to the mirror surface is shown in the top graph in figure 4.20. This graph reflects the variation of the loss rate. In the range between 600 μm and 1 mm, where the loss rate is nearly constant, the number of atoms also appears to be insensitive to the distance to the mirror. On the other hand, at distances below 600 μm the number of atoms collected in these traps drops as the position of the MOT approaches to the mirror surface. This is clearly a consequence of the steep increase in the loss rate value as the capture rate does not show any appreciable change in this same range of distances.

4.3 Summary

We have demonstrated that the geometry of the pyramidal mirrors fabricated in silicon wafers is suitable for cooling and trapping atoms. For this purpose, we fabricated a glass replica of the silicon pyramid. A detailed numerical and experimental investigation of the optical properties of these pyramids led us to conclude that light firstly reflected in the vicinity of these pyramid edges induces an imbalance in the MOT forces. Both the orientation and the polarisation state of this light when it crosses through the trapping region are responsible for this imbalance. We also found that this undesired effect can be either significantly reduced by depositing a limited reflectivity coating on the 70.5° pyramids, or completely eliminated by patterning the reflective coating with the aim of suppressing these reflections. We tested a series of different reflectivity coatings and concluded that a $\sim 78\%$ reflectivity gives the best results, generating a trap with 10^7 atoms, while a highly reflective (95%) gold coating prevented the MOT from functioning. To make a MOT in a 70.5° pyramid with such high reflectivity, we avoided depositing the reflective layer in the area sections which produce these imbalancing reflections. This procedure was also succesful and resulted in MOTs that collected up to 10^7 atoms.

To estimate the number of atoms that can be trapped in micro-pyramids fabricated on the surface of an atom chip, we used the glass replica to measure the scaling law for

the number of atoms trapped at various distances from the pyramid apex. We found that the number of atoms can be described by a power law $N \propto h^{4.0(1)}$, where h is the distance from the MOT to the pyramid apex. We next studied the capture and loss rates of the pyramid MOT at various distances from the apex. In the range of distances investigated $h \in [1.25, 3]$ mm, the loss rate term that is independent of the rubidium density γ was found to be insensitive to h, and the term proportional to this density β increased at the bottom end of the measured range. The capture rate, on the other hand, showed a dependence comparable to the one obtained for the number of atoms, $R \propto h^{3.5(3)}$. These results were corroborated in two different measurements. In addition, we studied the loss rate dependence on the distance to a single pyramid surface. The results of this indicate that the interaction between the trapped atoms and the surface becomes important at distances below 600 µm.

In the introductory chapter of this thesis, it is explained that the MOT capture rate is estimated by summing up the atoms crossing through the surface that delimits the trap volume. When the cloud is far from the apex, atoms are pushed towards the trap centre from all directions and the assumptions that lead to this estimation remain valid. However, when the trap is located at a short distance from the pyramid apex, the flux of atoms seems to be limited to those atoms that come from outside the pyramid.

Another factor influencing the drop in the number of trapped atoms observed in our experiments can be a reduction in the space available for cooling down atoms. The deceleration resulting from the scattering of photons saturates at a maximum value of $\vec{a}_{max} = \hbar\vec{k}\gamma/2M$ [77]. For instance, this deceleration would require approximately 3 mm for bringing down to rest a ^{85}Rb atom initially moving at a velocity of 10 m/s. As long as the distance of separation between the atom cloud and the pyramid walls is such that there is still enough space around the trap for cooling down atoms moving at the capture velocity, the trap will continue capturing atoms from all directions. However, if this separation is shorter than the minimum distance required for capturing these atoms, the rate at which the trap collects atoms will decrease. With the atom cloud located 3 mm away from the pyramid apex, the distance to the mirrors is already 1.7 mm. Therefore, the reduction in the space available for cooling down atoms can definitely be considered as a cause for the drop in the number of atoms represented as red squares in figure 4.10.

A cold atom in a MOT which collides with a room temperature surface would either receive enough thermal energy to escape the trap or be absorbed by the surface. In any case, the atom would be definitely lost from the trap. Hence, if the trap position is located in the vicinity of the pyramid apex, the possibility of losing atoms as a result of collisions with the surrounding walls increases. Consequently, the rate at which cold atoms are lost from a MOT located in the vicinity of the pyramid apex is enhanced as a result of the proximity of the four pyramid faces only when the distance to these surfaces is comparable to the size of the cold atom cloud.

The results of the scaling law measurements allowed us to estimate that as many as a few 10^4 atoms can be trapped in a pyramid characterised by a 1.2 mm side length, and as few as some tens of atoms can be trapped in a pyramid with a 200 µm side length. Consequently, this is the range of pyramid side lengths that we decided to include in the pyramid atom chip that is described in the next chapter of this thesis.

Chapter 5

The pyramid atom chip

In this chapter, I present a method for integrating arrays of micromirrors into the surface of an atom chip. We have designed this device with the aim of creating magneto-optic microtraps on the surface of the chip. We have proposed that this atom chip can be used to load atoms in an array of traps directly on the chip surface. The main elements of this design are micro-fabricated pyramidal hollow mirrors. The fabrication procedure of the first prototype of an atom chip with hollow pyramids integrated on its surface is presented in the first part of the chapter. The steps followed in the fabrication process, as well as the specific features of the device design are included in this description.

These pyramidal mirrors are created by chemically etching silicon wafers and depositing a reflective coating on their surface. In addition, we have explored two different methods for integrating sources of magnetic field on the surface of these silicon devices. In the first place, micro-fabricated current carrying wires have been integrated on the surface of silicon wafers in which pyramidal pits have been previously etched. Secondly, a method for creating square openings on the active layers of a magneto-optic thin film has been developed. This procedure exposes the silicon surface on top of which the MO film was grown, and creates the possibility of etching pyramidal pits through these openings.

5.1 Pyramidal hollow mirrors etched in silicon wafers

The silicon micro-fabrication techniques developed by the microelectronics industry over the past twenty years provide wide control on the characteristics and properties of micro and mesoscopic structures. In particular, the surface roughness of a device micro-fabricated in silicon approaches the scale of the constituent atoms, which results in extremely smooth surfaces ideal for creating high quality reflective devices. Although alternative materials could provide geometrical features more suitable for atom optics applications, these materials building blocks would most probably be more complicated molecular structures which would result in surfaces not as smooth as that obtained with silicon wafers.

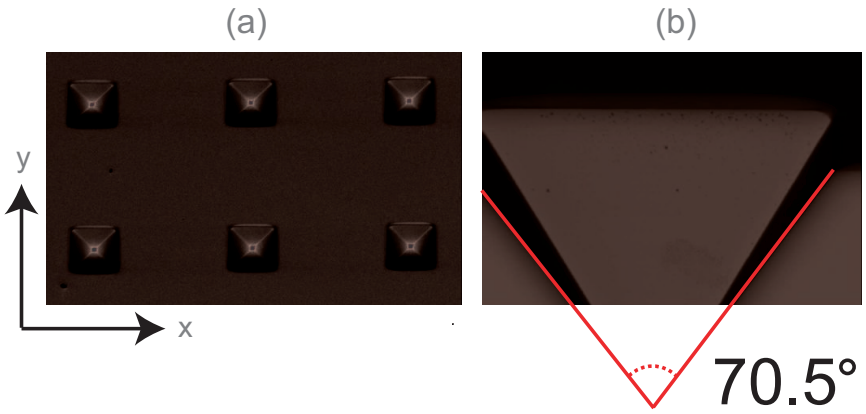

Figure 5.1: SEM images of the micro-fabricated pyramids. (a) Top view showing pyramids in a rectangular array with a pitch of 100 µm. These pyramids base has a side of length 30 µm, corresponding to a perpendicular depth of 21.3 µm. (b) Cross-sectional view of a single pyramid. The crystal structure of silicon is face-centred cubic (FCC), hence the pyramids that result from the etching process are characterized by an angle of 70.5° between opposing faces.

5.1.1 Fabrication details

It is a long known fact that anisotropic etching of silicon results in pyramidal pits [104]. This is a standard technique widely used in the fabrication of Micro-optoelectromechanical systems (MOEMS). For instance, de Lima Monteiro *et al.* [70] state that anisotropic etching of (100) silicon through a mask produces a pyramidal pit formed by four (111) planes.

The array of microscopic hollow pyramids shown in figure 5.1 was fabricated by selectively etching the surface of a silicon substrate. The fabrication of an array of pyramids begins with a 4 in, 1 mm thick silicon wafer cut on the $(1, 0, 0)$ plane. After cleaning the wafer using standard RCA and fuming nitric acid,[1] a 170 nm thick silicon dioxide insulation layer is deposited by wet oxidation in a furnace at 1000 °C. Next, 50 nm of low-stress silicon nitride are deposited on top of the silicon dioxide layer by Low-Pressure Chemical Vapor Deposition (LPCVD). Then, alignment marks are etched into the back side of the wafer using reactive ion plasma etch.

Square openings are made in the silicon nitride using optical lithography. First, a 1 µm layer of photoresist AZ6612 is spun onto the wafer. Next, the photoresist is patterned using a photomask which has to be precisely aligned to the wafer crystal structure. Then, the silicon nitride and dioxide layers are etched through the square openings down to the silicon wafer using dry plasma etch. Finally, the resist is stripped in a plasma asher. In order to create the hollow pyramids, the wafers are etched through the square openings in the anisotropic etchant potassium hydroxide (KOH) at a concentration of 33% by volume and at a temperature of 80 °C for 19 hours. In this process, the Si(100) plane is attacked more rapidly than the Si(111) plane. This results in pyramidal pits bounded by planes whose normal directions are given by $(1, 1, 1)$, $(\bar{1}, 1, 1)$, $(1, \bar{1}, 1)$, and $(\bar{1}, \bar{1}, 1)$.

[1] Standard RCA is a procedure for removing organic residue and films from silicon wafers. In the process, the silicon is oxidised and a thin oxide layer is left on the wafer surface. (RCA-1 Silicon Wafer Cleaning. INRF application note. Mark Bachman, Fall 1999.)

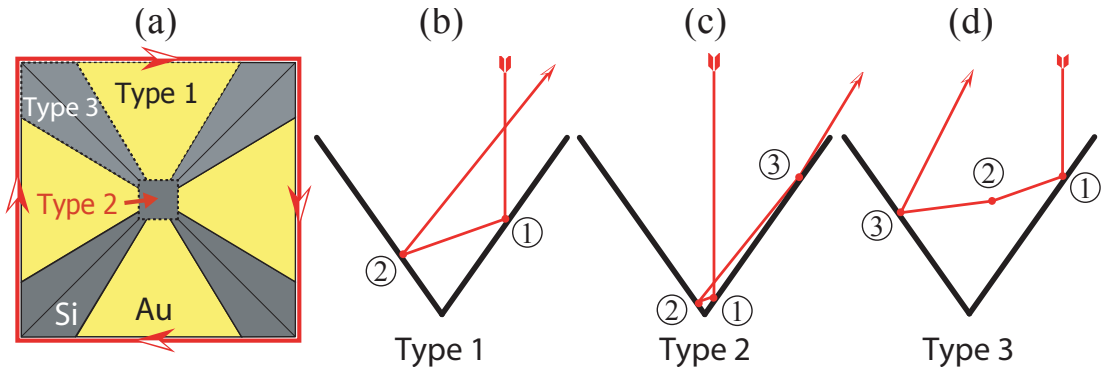

Figure 5.2: In (a), The reflection areas were each one of the three ray types are produced are shown in a top view of the pyramid. (b), (c), and (d) represent examples of the paths followed by these rays, which are sketched in a cross section of the pyramid.

The oxide layer is then stripped away and finally a metallic reflective layer is sputtered on the sample. As gold is a good reflector for infrared (IR) light (see table 3.1), a 5 nm adhesion chromium layer and a 100 nm gold layer were sputtered on top of a pyramids array sample. In conclusion, an array of hollow pyramidal highly reflective mirrors has been fabricated on the surface of a silicon wafer. The next step of this project was therefore to determine the optical properties of these mirrors.

5.1.2 Geometrical characteristics

The angle between the opposing faces of the pyramids etched in silicon can be easily calculated. Take for example the $\{1,1,1\}$ and the $\{\bar{1},\bar{1},1\}$ planes of the silicon crystal. The angle θ between the two vectors $(1,1,1)$ and $(-1,-1,1)$ is given by:

$$(1,1,1)\cdot(-1,-1,1) = (\sqrt{3})^2\cos\theta.$$

Therefore

$$\theta = \cos^{-1}\left(\tfrac{1}{3}\right) \approx 70.53^\circ, \tag{5.1}$$

which is the value quoted in figure 5.1. This is also the apex angle of the pyramid studied in chapter 4.

5.1.3 Optical properties

With respect to the optical reflections that these pyramids generate, their surface can be separated into three regions, schematically represented in figure 5.2**(a)**. A ray parallel to the axis of the pyramid is first reflected at the point marked ① in diagrams **(b)**,**(c)** and **(d)**. It then travels along a diagonal line which points down to the pyramid apex and towards the opposite pyramid face. The propagation direction after the first reflection makes an angle of $\pi-\theta$ with the pyramid axis. Light that is first reflected in the middle of a pyramid face travels through the pyramid internal volume and reaches the opposite face. These rays are reflected a second time, as represented by points ② in diagrams **(b)** and **(c)**. The direction of propagation after this second reflection is also diagonally oriented, but this time it points away from the pyramid apex. This new direction makes an angle of $\pi-2\theta$ with the pyramid axis. This angle is bigger than the 35.25°

angle between the pyramid faces and axis. Consequently, the ray has to intersect the plane defined by the pyramid face at some point. Beams that follow this two reflection pattern and leave the pyramid without suffering a third reflection have been denoted as type 1 reflections (diagram **(b)**). When there is a third reflection inside the pyramid, as shown in diagram **(c)**, the ray is denoted as type 2. Only the central region of the incoming beam, the one that is firstly reflected near the pyramid apex, gives rise to type 2 reflections. Rays initially reflected close to the pyramid edges intersect the adjacent pyramid face before reaching the opposite one. The path followed by such ray, called type 3, is represented in diagram **(d)**. The second reflection, point ② in this diagram, is on the adjacent mirror. After the third reflection, which is shown as point ③, these rays finally leave the pyramid volume, crossing through the pyramid axis at an angle of 31.59°.

Type 1 and 2 reflections

A ray contained in the section of light that makes up a type 1 or a type 2 reflection remains in its initial plane of incidence. The incident light propagates parallel to the pyramid axis. Consequently, an incident ray makes an angle of $\theta/2 = \frac{1}{2}\cos^{-1}(1/3)$ with the pyramid face and the angle of incidence is $\pi/2 - \theta/2 = \frac{1}{2}(\pi - \theta)$. This firstly reflected section of light crosses through the pyramid internal volume making an angle of $\pi - \theta$ with a vector pointing out of the pyramid and along its axis. A ray that crosses through the pyramid axis forms a triangle with the lines generated by the intersections of the pyramid faces and the plane of incidence. In consequence, the angle this ray makes with the pyramid face in which the second reflection is produced is $\pi - \frac{3}{2}\theta$. Correspondingly, the second reflection angle of incidence turns out to be $\frac{1}{2}(3\theta - \pi)$. A new triangle can now be used to deduce the angle that this secondly reflected ray makes with the pyramid axis. This time, the sides of this triangle are formed by the pyramid axis, the pyramid face in which the second reflection was produced, and the secondly reflected ray itself. From these considerations we conclude that the secondly reflected ray makes an angle of $\pi - 2\theta$ with the pyramid axis.

Type 3 reflections

In contrast to what happens in a 90° pyramid, after the first reflection into the pyramid, light travels diagonally towards the pyramid apex. Because of this, some light intersects the pyramid face that is adjacent to that of the first reflection. The normal to this new reflection plane is not longer parallel to the plane defined by the first reflection. This complicates the derivation from simple geometrical arguments of the second reflection angle of incidence. However, a ray tracing analysis of the pyramid allows us to calculate both the incidence angles and the angles at which type 3 reflections cross the pyramid axis. The angle of incidence at the second reflection has been calculated to be 78.9°, while for the third reflection the angle of incidence is 33.49°. After suffering this third reflection, a type 3 ray escapes the pyramid crossing through its axis at an angle of 31.59°.

The reflected light intensity distribution

The first test we made on an array of pyramidal micromirrors, (see figure 5.1) consisted of shining a collimated 1 mm-diameter laser beam on the surface of an array pyramidal

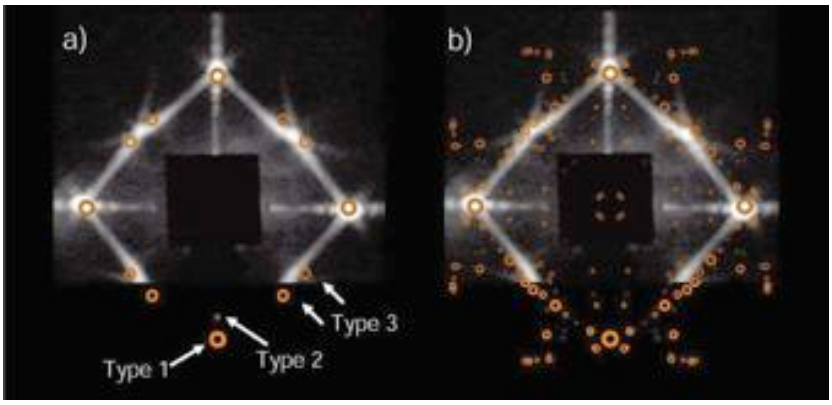

Figure 5.3: The intensity distribution of light reflected from the array of pyramids, when it is illuminated at normal incidence. The orange circles in (a) show the reflection pattern expected for a perfect pyramid, while the orange circles in (b) indicate the calculated reflection pattern for a pyramid with rounded corners. Size indicates expected relative intensity.

micro-mirrors. The wavelength of this light was 633 nm and it was incident perpendicularly to the silicon wafer surface. We then imaged the reflected intensity pattern generated on a screen located 7 cm away from the wafer surface. The result of this experiment is given in figure 5.3. Along with the reflected intensity image, the results of a ray tracing analysis of the 70.5° pyramidal geometry are also included in these images.

The reflection pattern features corresponding to each of the three ray types can be identified with the help of the ray tracing model. First, in figure 5.3(a) perfect 70.5° pyramids with sharp edges are considered in the ray tracing model. The orange circles superimposed on this image represent the reflection positions predicted by this simplified model. The size of these circles indicates the relative intensity predicted by the model for each one of the different reflections. For instance, the predicted intensity of a type 2 reflection is approximately 100 times smaller than that of a type 1 ray. The reason for this is that the surface area of the region which gives rise to type 2 rays is limited to a small section around the pyramid apex. Consequently, the small contribution of type 2 rays in this intensity distribution is hidden on the diffracted wings of the type 1 reflections.

In spite of the insight gained with this simple ray tracing calculation, this model is not enough for describing with detail the features observed in the reflected intensity pattern. The background of light between the features caused by the three ray types is caused by the round corners of the micro-pyramid. This roundness, which can be clearly seen in figure 5.1, is a consequence of the particular etching mechanisms that gave rise to the pyramidal pits. This additional feature needs to be taken into account when analysing the reflected intensity pattern. Figure 5.3(b) shows the result of considering a pyramid with rounded edges in the ray tracing model. The roundness is approximated by means of cone sections whose radii is 2.5 μm at the pyramid entrance and 0.825 μm at the apex. The features predicted by the new ray tracing analysis recreate more closely the photographed intensity distribution. The features corresponding to the type 2 rays are hidden behind the diffracted wings of the type 1 reflections.

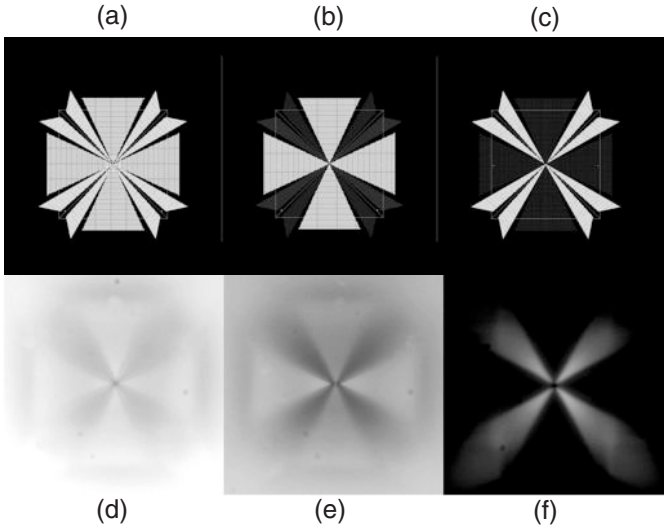

Figure 5.4: The polarisation orientation of a linearly polarised light beam suffers rotations when reflected in a 70.5° pyramid. The top row of images shows the result of a ray tracing analysis of the reflection pattern. The bottom row is an optical microscope measurement of a micro-pyramid. The microscope images show first **(d)** the reflected light irrespective of its polarisation state, then **(e)** the light for which the initial direction of polarisation is preserved, and finally **(f)** the light that suffers a rotation of the polarisation direction. The results of the ray tracing analysis are in very good agreement with the microscope observations: **(a)** shows all the reflected rays; **(b)** shows only the rays that come out polarised in the same direction as the input light; and **(c)** shows the rays for which the polarisation is rotated.

Linearly polarised light

The rotation induced in the polarisation of linearly polarised white light as a result of the multiple reflections that occur in the 70.5° pyramid faces is shown in figure 5.4. The light once more propagates perpendicularly to the wafer surface and we looked at one of the silicon hollow pyramids under a microscope. The focal plane in these microscope images is located at the apex of the pyramid. A pair of linear polarisers is used to investigate the polarisation rotation induced on the different types of rays. The first polariser defines the polarisation of the incident light, which was set to be parallel to one of the pyramid entrance sides, while the second polariser analyses the polarisation of the light that comes out from the pyramid. The results of these tests were also compared to the predictions of a ray tracing analysis. In this analysis, the incident light is set to be linearly polarised parallel to one side of the pyramid square aperture and the reflection pattern is generated by selecting the point where each ray crosses through a plane located at the entrance of the pyramid.

Images **(a)** and **(d)** in figure 5.4 show respectively the ray tracing and microscope results for the total reflected intensity distribution. The features corresponding to type 1 and type 3 reflections can be easily discerned in the ray tracing results shown in figure 5.4**(a)**. In contrast, the type 3 rays contributions to the reflection pattern shown in figure 5.4**(d)** can not be easily distinguished. The type 3 features are not as intense

as the type 1 light components. Therefore, the former are hidden in the total intensity distribution between the contributions of the type 1 rays.

Next, the polarisation state of the reflection pattern was analysed with the linear polariser. Firstly, the polarisation axis of the analyser was set parallel to the initial direction of light polarisation. The result of this experiment is given in figure 5.4**(e)** and can be compared to the result of the ray tracing model presented in figure 5.4**(b)**. The later image shows bright type 1 reflections, but the type 3 features have been severely dimmed. This is the result of the polarisation rotation induced by the multiple reflections undergone by type 3 rays. This effect can be fully appreciated in figure 5.4**(b)** by comparing it with figure 5.4**(d)**. The type 3 contributions to the reflection pattern are evidently blocked by the analyser, resulting in dark areas between the type 1 reflection features.

The polarisation rotation induced in the type 3 rays becomes much more evident when the analyser polarisation direction is rotated until the image shown in figure 5.4**(f)** is obtained. At this point, the analyser polarisation direction is aligned to the final polarisation direction of a type 3 ray and blocks almost entirely all the type 1 rays contributions. This is once more confirmed by the results of our ray tracing analysis, which is shown in figure 5.4**(c)**.

By means of the two methods exemplified in figure 5.4, we have been able to quantify the polarisation rotation induced in the light reflected by the 70.5° pyrmaid. First of all, we have found that type 1 and type 2 reflections do not modify the polarisation state of linearly polarised light initially directed parallel to the pyramid entrance sides. In contrast, type 3 rays generate rotations of ±53° or ±78° in the polarisation direction of this light. We used the optical microscope to determine these rotations. They correspond to the orientation of the second polariser at which the visibility of the type 3 rays is maximum, as measured with respect to the orientation of the first polariser.

Circularly polarised light

Upon reflection from a metallic surface, the state of polarisation of light is modified. According to Friedmann *et al.* [105], the phases of the electric field components which are parallel and normal to the plane of incidence suffer changes which depend on the angle of incidence. In consequence, the phase difference $\Delta = \delta_{\parallel} - \delta_{\perp}$ between parallel and perpendicular components of the light polarisation also depends on the angle of incidence. Near normal incidence, the electric field component which is perpendicular to the plane of incidence ($\delta_{\perp}$) suffers a phase change of π radians while the parallel component ($\delta_{\parallel}$) suffers no phase change. This therefore implies that at normal incidence there is a phase change of $\Delta = -\pi$. At grazing incidence both components suffer a phase change of π and consequently there is no phase difference induced by the reflection. As the angle of incidence increases from 0° to 90°, the reflection induces a phase difference which varies continuously between $-\pi$ and 0. At a certain value of the incident angle which is called the principal angle of incidence, the phase difference is equal to $-\pi/2$.

The phase shifts induced upon specular reflection on the mutually orthogonal light polarisation components, $\delta_{\parallel}$ and $\delta_{\perp}$, can be expressed in terms of the real n and imaginary k parts of the complex refractive index of the reflecting medium [106, 107, 108]:

$$\tan \delta_{\parallel} = \frac{2 \cos \psi \left[\left(n^2 - k^2 \right) t - (2nk)\, s \right]}{\left(n^2 + k^2 \right)^2 \cos^2 \psi - \left(s^2 + t^2 \right)} \tag{5.2a}$$

$$\tan\delta_{\perp} = \frac{2t\cos\psi}{\cos^2\psi - (s^2+t^2)} \tag{5.2b}$$

where

$$2s^2 = \sqrt{\left(n^2-k^2-\sin^2\psi\right)^2 + 4n^2k^2} + \left(n^2-k^2-\sin^2\psi\right) \tag{5.3a}$$

$$2t^2 = \sqrt{\left(n^2-k^2-\sin^2\psi\right)^2 + 4n^2k^2} - \left(n^2-k^2-\sin^2\psi\right) \tag{5.3b}$$

With the aim of confirming this information and characterising the metallic mirrors fabricated in the Centre for Cold Matter, we made a measurement of the retardation induced between the two mutually orthogonal components of a circularly polarised laser beam upon reflection from a gold mirror. The mirror utilised in this experiment was fabricated by sputter deposition of the metallic material on the surface of a glass slide. To begin with, a thin chromium adhesion layer (5 nm) was laid on the surface of the glass slide. Then, an optically thick 100 nm layer of gold was sputtered on top of the chromium layer. This is the standard method used in our laboratory for fabricating gold mirrors and results in highly reflective ($\sim 95\%$) surfaces for infrared light.

In this experiment, a circularly polarised beam was reflected by the gold mirror and the reflected beam was analysed by means of a quarter wave plate and a linear polariser. The procedure was repeated for various angles of incidence. A laser beam in a linear horizontal polarisation state was firstly obtained by taking the light transmitted through a polarising beam cube. The circular polarisation was next prepared by sending the horizontally polarised light beam through a quarter wave plate whose fast axis was oriented at an angle of 45° with respect to the initial light polarisation state. This circularly polarised light beam was then reflected by the gold mirror, which was held on a mount that allowed us to vary the angle of incidence ψ. Finally, the reflected beam was sent through a second quarter wave plate and a horizontal linear polariser before reaching a detector in which the transmitted power was measured. For a given angle of incidence, the polarisation state of the reflected light can be determined by measuring the dependence between the power transmitted through the linear polariser and the orientation of the second quarter wave plate.

Using the Jones Matrix formalism, the polarisation state of the beam before the reflection is given by [100]:

$$\mathbf{J}_I = \frac{1}{\sqrt{2}}\begin{pmatrix} 1 \\ j \end{pmatrix}$$

The effect that the mirror has on the polarisation state of the light can be expressed as a wave retarder having a fast axis parallel to the plane of incidence. This way, the polarisation state of the light after the reflection can be expressed in the following way:

$$\mathbf{J}_R(\phi) = \mathbf{T}_M(\phi)\cdot\mathbf{J}_I = e^{-j\phi/2}\begin{pmatrix} 1 & 0 \\ 0 & e^{j\phi} \end{pmatrix}\cdot\frac{1}{\sqrt{2}}\begin{pmatrix} 1 \\ j \end{pmatrix} = \frac{e^{-j\phi/2}}{\sqrt{2}}\begin{pmatrix} 1 \\ je^{j\phi} \end{pmatrix}$$

Next, the polarisation state of the reflected beam is interrogated by means of a quarter wave plate $\mathbf{T}_{\lambda/4}$ and a horizontal linear polariser $\mathbf{T}_{lh}$

$$\mathbf{J}_E(\phi,\theta) = \mathbf{T}_{lh}\cdot\mathbf{T}_{\lambda/4}(\theta)\cdot\mathbf{J}_R$$

where

$$\mathbf{T}_{lh} = \begin{pmatrix} 1 \\ 0 \end{pmatrix}$$

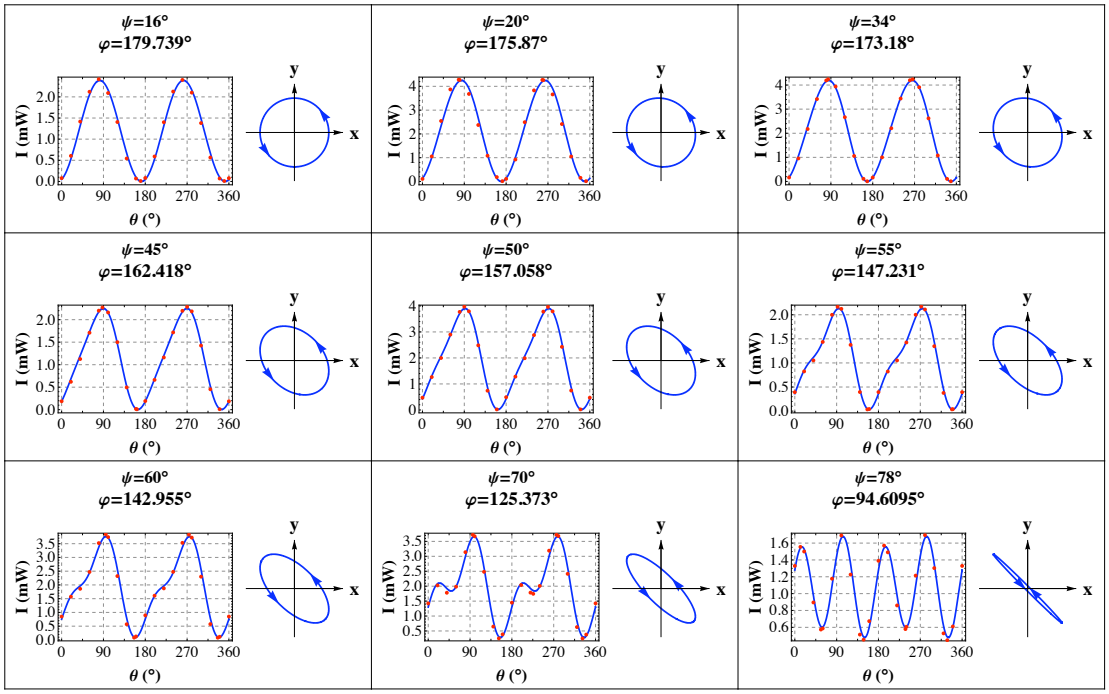

Figure 5.5: Measurement of the phase retardation induced on circularly polarised light upon reflection from a gold coated mirror. The red points on each graph represent the experimental data points for the light intensity as a function of the reflection angle of incidence ψ and the angle θ between the quarter wave plate fast axis and the polariser transmission axis. The blue curves on each graph are the result of fitting this data to equation 5.4 with the phase ϕ as the fitting parameter. The value of ϕ quoted on top of each graph is the absolute value of the induced phase. The polarisation state of the reflected light is depicted next to each graph.

and

$$\mathbf{T}_{\lambda/4}(\theta) = \frac{1}{\sqrt{2}} \begin{pmatrix} 1 + j\cos(2\theta) & 2j\cos(\theta)\sin(\theta) \\ 2j\cos(\theta)\sin(\theta) & 1 - j\cos(2\theta) \end{pmatrix}$$

Then, the polarisation state of the light before it reaches this quarter wave plate and the angle θ that the quarter wave plate fast axis makes with the polariser transmission axis determine the amount of light that goes through the linear polariser. Consequently, the light intensity measured by the detector depends on both the orientation θ of the quarter wave plate fast axis and the phase ϕ induced by the reflection

$$I(\phi, \theta) = \frac{I_0}{8\eta} |1 - j\cos(2\theta) + e^{j\phi}\sin(2\theta)|^2 \tag{5.4}$$

where η is the impedance of the medium, which in this case is taken to be free space.

The results obtained by means of the experiment detailed before are shown in figure 5.5. Each graph refers to a particular incidence angle ψ where the red points correspond to the measurement of the light intensity transmitted through the linear polariser as a function of the quarter wave plate orientation angle θ. The blue curve in each graph is the line shape described by equation 5.4 with the phase retardation ϕ given by a least-square fitting of the data. These graphs show that the fitted curves closely reproduce

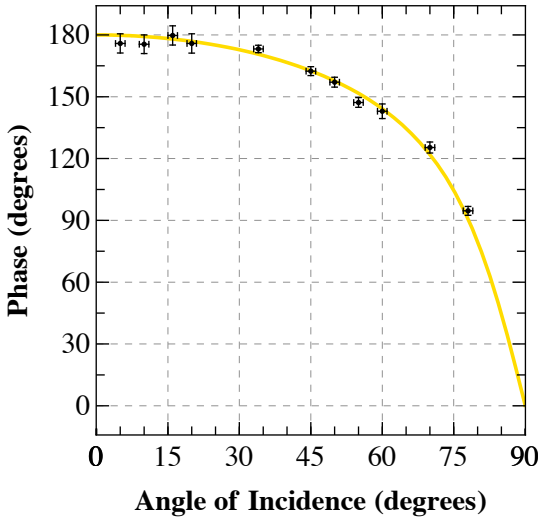

Figure 5.6: The absolute value of the phase retardation ϕ induced upon reflection from a gold coated mirror as given by equations 5.2 and 5.3 is compared with the measurement performed in our experiments.

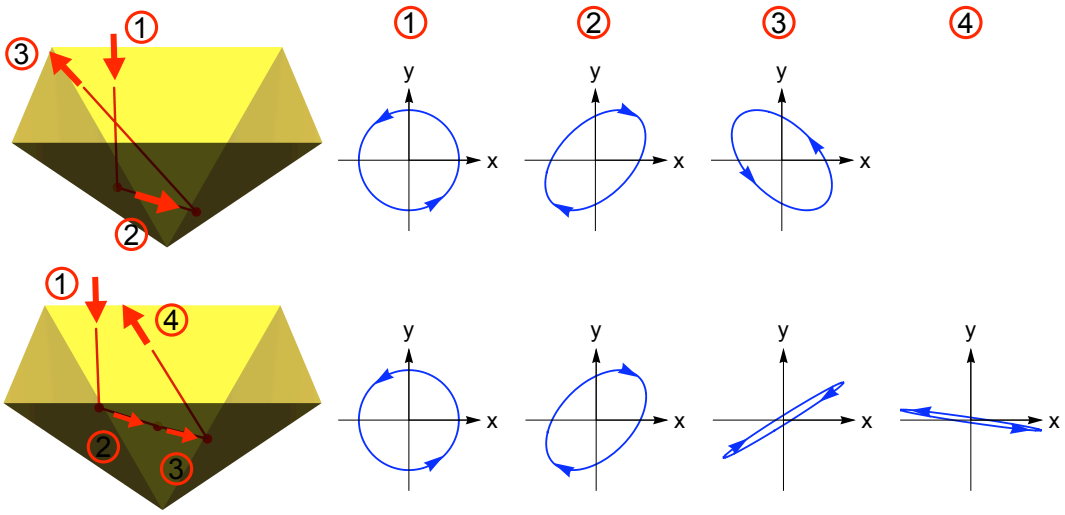

Figure 5.7: This figure compares the changes induced in the polarisation state of type 1 and type 3 rays. In the first place, the phase retardations induced on the polarisation of type 1 rays are small. Consequently, the polarisation state of type 1 rays does not deviate substantially from the initial circular polarisation. On the other hand, the second reflection suffered by type 3 rays induces a large phase retardation in the light polarisation. This leaves the light nearly linearly polarised, state which is maintained after the third reflection.

the experimental data in all instances. The ellipticity of the reflected light on a plane $\{x, y\}$ perpendicular to the light propagation direction is shown to the right of each graph. This shows that the polarisation of the reflected light goes from circular, at normal incidence where the retardation is $\phi = \pi$, to almost linear, at $\psi \sim 78°$ with a phase retardation $\phi \sim \pi/2$.

To compare these experimental results with the theoretical phase shifts predicted by equations 5.2 and 5.3, in figure 5.6 I have plotted the phase retardation values obtained in the experiment, together with the curve generated when the real and imaginary parts of the refractive index of gold,[2] $n = 0.08$ and $k = 4.56$, are substituted in these equations. The agreement between experiment and theory is surprisingly good.

At the beginning of this section, when describing the three types of rays, I mentioned the various incidence angles involved in the reflections that take place in the 70.5° pyramid. To see how these reflections affect the polarisation of the light, some of the measurements shown in figure 5.5 correspond to these incidence angles. These angles are $\frac{1}{2}(\pi - \theta) \sim 55°$, $\frac{1}{2}(3\theta - \pi) \sim 16°$, 78°, and 34°; they correspond respectively to the first reflection incurred by all rays, the second reflection suffered by type 1 and type 2 rays, and the second and third reflections of type three rays. These measurements demonstrate that the polarisation of type 1 and type 2 rays after the first and second reflections is still characterised by a strong circular component, as it is also shown in figure 5.7. In contrast, figure 5.7 also shows that as a result of the large incident angle of the second reflection incurred by type 3 rays, the light becomes nearly linearly polarised. This is the cause of the imbalance effect that type 3 rays have on MOTs generated in these pyramids.

5.1.4 The creation of MOTs in 70.5° pyramidal hollow mirrors

A comparison of the two very different light configurations generated by the 70.5° pyramid type 1 rays and the 90° pyramid can be seen in figure 5.8. These ray sketches are the result of cutting in half a pyramid with a plane parallel to the pyramid axis. In the 90° pyramid geometry, the scattering force balance necessary for creating a MOT is automatically produced over the entire volume of the pyramid, as seen in figure 5.8 (b). By contrast, figure 5.8(a) is the ray geometry obtained in the silicon pyramids. This light configuration creates the required scattering force balance only where the three arms of the type 1 reflections are present. For this reason, while in the 90° configuration the magnetic field zero position can be located anywhere in the volume of the pyramid, in the 70.5° pyramid care most be taken to ensure that the point of zero magnetic field is located within the region in which the three light components are present.

To complement this information, the diagram given in figure 5.9 shows some useful scale considerations. In this sketch, the horizontal and vertical dimensions of the most important features of the type 1 rays configuration are respectively expressed in units of the pyramid side length s and the pyramid depth d. Considering exclusively generating the trap on the pyramid axis, the middle point of the line section in which the scattering force is balanced is located at a distance equal to $0.42d$ from the pyramid apex. This geometric estimate of the MOT optimal position is consistent with the measurements described in the previous chapter. In section 4.2.1 we showed that the MOT optimal position h is such that $h \simeq 0.62A$, where the radius of the circular aperture A in this experiment can be related to the corresponding pyramid depth by $A = d/\sqrt{2}$. Hence,

[2] These values were taken from table 3.1

this measurements indicate that the MOT is optimal when $h \simeq 0.62d/\sqrt{2} = 0.44d$, which is in very good agreement with the value given in figure 5.9. For simplicity, in the following we will consider that the optimal trap position is $^{d}/_{2}$ away from the pyramid entrance.

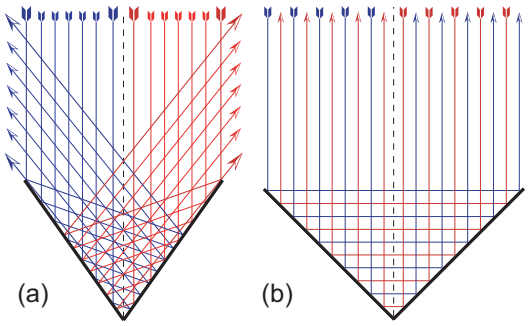

Figure 5.8: Comparison of type 1 rays in the (a) 70.5° and in the (b) 90° pyramids. In the 70.5° pyramid, there might be an imbalance of the force in the trap due to the misalignment of the rays that arise from first and second reflections. In contrast to what happens in the 90° pyramid, atoms can only be trapped in a limited region of the pyramid internal volume.

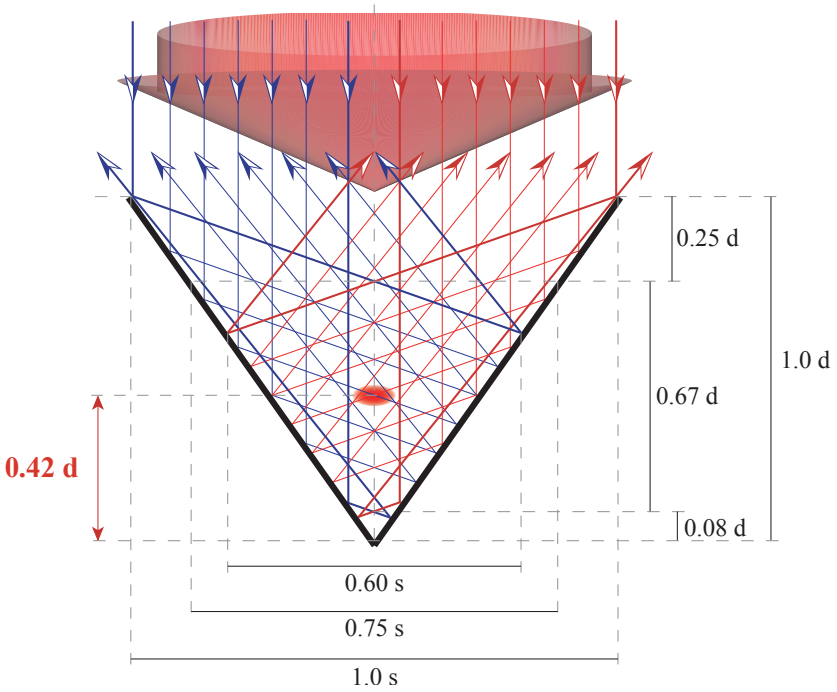

Figure 5.9: The ray geometry generated in a 70.5° pyramid when illuminated with collimated light propagating along the pyramid axis direction produces a diamond shaped region in which the scattering force is balanced. This trapping region is generated by the type 1 rays.

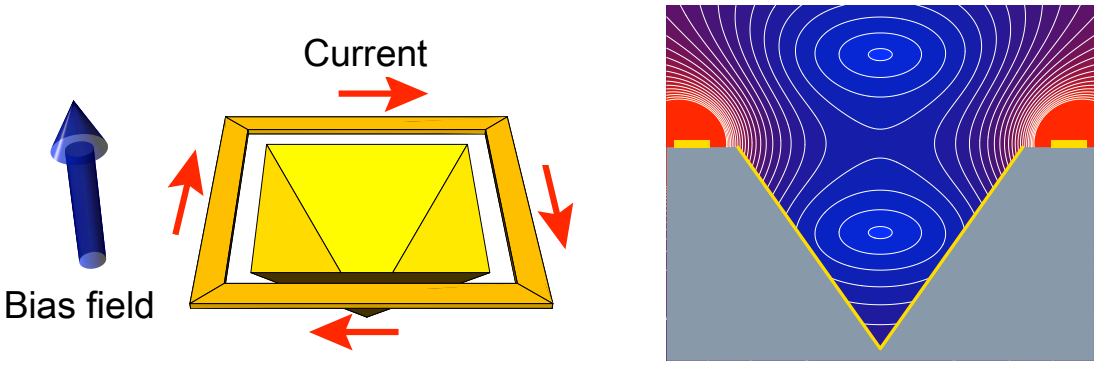

Figure 5.10: A current carrying square loop encircling the pyramid aperture can be used in combination with a bias field perpendicular to the loop plane to generate an spherical quadrupole inside of the pyramid.

5.2 Micro-pyramids atom chips

Together with the arrays of pyramidal mirrors described in section 5.1, we have integrated magnetic field sources on the surface of our atom chips. As explained in the beginning of this chapter, two different method have been contemplated. The first method consists of including a current carrying wire loop around the entrance of each pyramid. The second method aims at exploiting the magnetic properties of magneto-optic thin films.

5.2.1 The square loop magnetic field

The two methods proposed for integrating magnetic field sources on the surface of the pyramid atom chips are equivalent. The magnetic field generated by either of these two methods can be recreated by considering a current-carrying closed loop running around each pyramid square opening. Then, a quadrupole field can be generated by adding up a uniform bias magnetic field parallel to the pyramid axis, as schematically shown in figure 5.10. With the appropriate choice of loop current and bias field, a point of zero magnetic field is produced on the pyramid axis. From this point, the field magnitude increases linearly with position. Additionally, a complementary mirror image of the quadrupole field generated inside the pyramid is also created on the opposite side of the loop plane. We have anticipated that the pair of zero magnetic field points can be a useful feature of our devices. A cold atom cloud initially magneto-optically collected inside the pyramid can then be held in a purely magnetic trap and transferred to the field minimum located outside of the pyramid.

Consider a current-carrying square loop of side length s encircling the aperture of a pyramid. When a current I is running through this loop, the magnetic field generated at the intersection point of the pyramid axis and the loop plane is

$$B_0 = \frac{2\sqrt{2}}{\pi}\frac{\mu_0 I}{s}. \tag{5.5a}$$

The axes of the pyramid and the loop coincide. From now on, we will identify this axial direction with the coordinate z. The red curve shown in figure 5.11**A** corresponds to the magnitude of the magnetic field that the square loop generates on the pyramid axis as a function of distance from the loop plane. In this graph, the field magnitude is

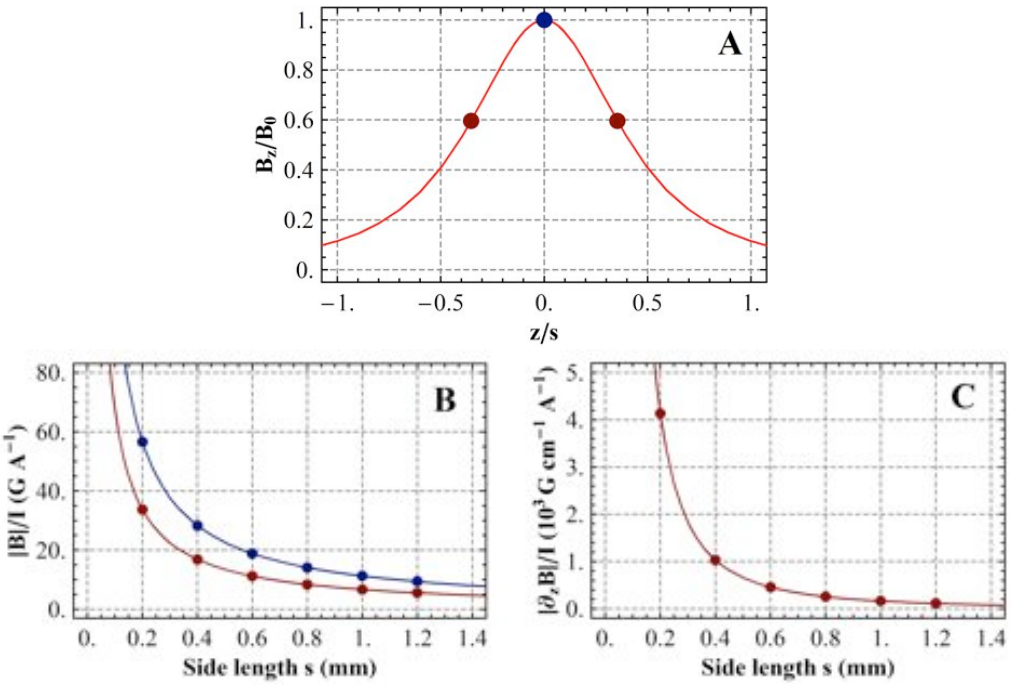

Figure 5.11: The magnetic field generated by a current carrying square loop in a hollow pyramid. The curve in graph **A** shows the axial component of the square loop field as a function of the distance from the loop plane. In this graph, the position along the pyramid axis is presented in units of the loop side length and the field axial component is given in units of its value at the loop plane. The loop plane position and the pyramid axis middle point are marked with ● and ● respectively. Graph **B** shows the magnitude of the magnetic field generated per Ampere at the pyramid axis middle point (●) and on the loop plane (●), both as a function of the pyramid side length. Graph **C** gives the axial gradient of the magnetic field at the mid-point on the pyramid axis per unit current, also as a function of the pyramid side length.

normalised to the value that it takes on the loop plane, B_0, and the distance from the loop plane is normalised to the pyramid side length s.

Let us consider generating a MOT on the pyramid axis, approximately at the middle point of the pyramid depth, as illustrated by the contour plot in figure 5.10. The loop field magnitude at this position is given by:

$$B_T = \frac{8\sqrt{2/5}}{3\pi}\frac{\mu_0 I}{s} = \frac{4}{3\sqrt{5}}B_0 \tag{5.5b}$$

In order to position the zero of magnetic field here, we need to apply a uniform bias field equal to $-B_T$ and directed along the pyramid axial direction. The dependences expressed by equations 5.5a and 5.5b are both shown graphically in figure 5.11**B**. The blue curve corresponds to B_0; B_T is represented by the dark red curve; and both curves are the field magnitudes generated per ampere applied to the square loop. Similarly, the blue (●) and the red (●) dots included on top of the curve 5.11**A** indicate, respectively, the positions to which B_0 and B_T correspond to.

Finally, the axial field gradient generated by the square loop at the trap position is

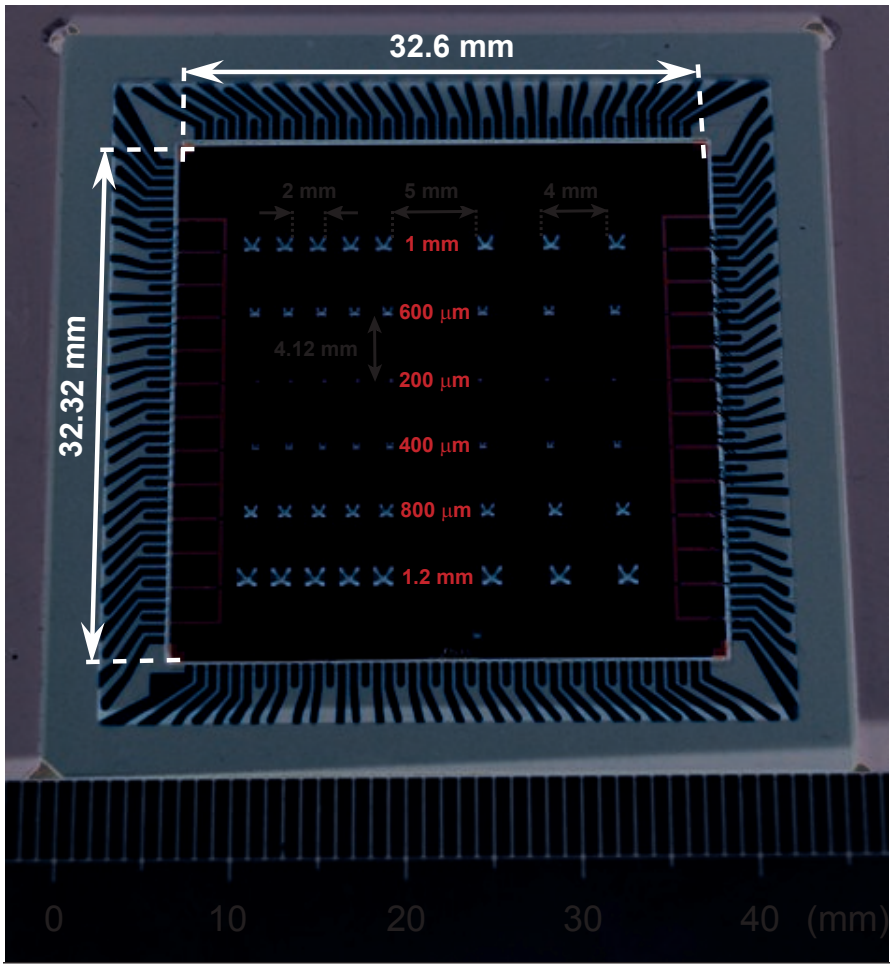

Figure 5.12: The pyramid atom chip is shown mounted on the CPGA.

given by

$$\delta_z B|_{z=z_T} = \frac{416}{45\sqrt{5}\pi}\frac{\mu_0 I}{s^2} = \frac{208}{45\sqrt{10}}\frac{B_0}{s} \tag{5.5c}$$

The dependence of this gradient on the square loop side length is represented graphically in figure 5.11**C**. As we did with the field magnitudes plotted in 5.11**B**, plot **C** presents the field gradient generated per current unit.

5.3 The pyramid and wire atom chip

The first prototype of a pyramid atom chip was fabricated in the Nanoscale Systems Integration (NSI) group in the School of Electronics and Computer Science at the University of Southampton. A photograph of this prototype can be seen in figure 5.12. Pyramid sets of six different sizes have been fabricated on the surface of this atom chip. The side length of these pyramids range from 200 µm to 1.2 mm in steps of 200 µm. The pyramids of a single size are grouped in two sets, one containing five pyramids and the second containing three pyramids.

This atom chip includes square loops of current-carrying micro-fabricated wire circling around the pyramid apertures. The wires are made of gold and constitute the

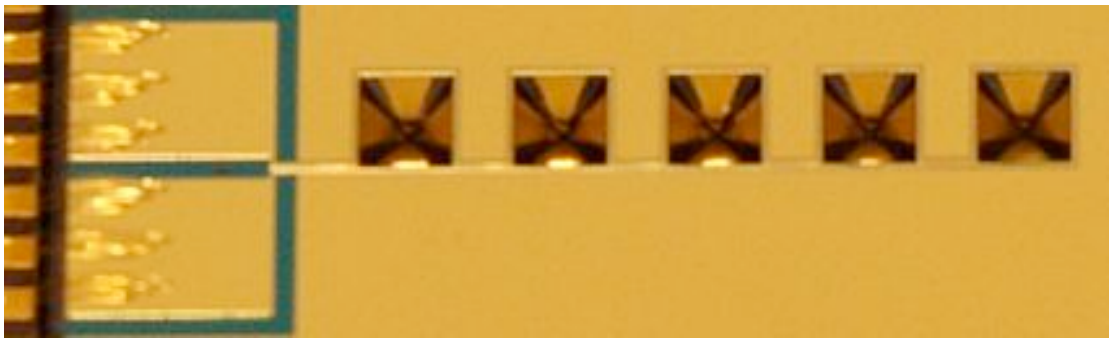

Figure 5.13: A magnified view of the 1.2 mm pyramids set of the atom chip shown in figure 5.12. This image shows in detail the internal features of the chip pyramids, the current carrying wires that run around the square pyramid apertures, the 2 mm wide contact paths, and the sets of nine bond wires that connect these paths to the chip carrier paths.

main magnetic field source. As I have previously shown, these wires in combination with a bias field perpendicular to the chip surface can generate the magnetic field required for creating the pyramid MOTs on the chip pyramids. Twelve wire loops have been included in this atom chip. These loops run along the pyramid square entrances, closely recreating the loop presented in section 5.2.1. The five pyramid sets and the three pyramid sets of each side length count with separate wire loops. In figure 5.13 we show exclusively the 1.2 mm five-pyramid set with the micro-fabricated wire running around the pyramids. Wide contact paths are included at the terminals of this wire, around which the blue naked silicon surface can be seen. In addition, also evident in this image is the masking in the pyramid internal surface.

In chapter 4 we showed that in order to create a MOT in a 70.5° highly reflective pyramidal mirror it is necessary to remove or at least greatly reduce type 3 rays. We found that masking the sections of the input beam which would give rise to type 3 reflections gives very good results. However, masking the input beam to such an array is obviously highly impractical. An alternative is to pattern the reflective coating that is laid on the micro pyramids. The pattern imprinted in the silicon pyramids has to recreate the sketch shown in figure 5.2(a). This Maltese cross shape can be seen in each of the pyramids in figure 5.13. A detailed description of the fabrication procedure of this atom chip is beyond the scope of this thesis. We have published this description in [109] and this paper has been included in Appendix D.

5.3.1 Atom chip packaging

The first prototype of the pyramid atom chip contains a total of 12 connection path pairs. These paths are only 2 mm wide and there are no more than 300 µm of separation between them. Usually in atomic physics experiments, in-vacuum electrical connections are created by mechanically attaching bulky connectors to the device. However, with many connections, the processes of mounting and replacing the atom chip would be a tedious and time consuming task. Therefore, we found ourselves needing to explore new methods for incorporating our atom chips into the experimental apparatus.

We packaged the chip into a ceramic pin-grid array (CPGA) chip carrier (CPG18023, Spectrum Semiconductor Materials, Inc.). The body of this carrier is made of Alumina

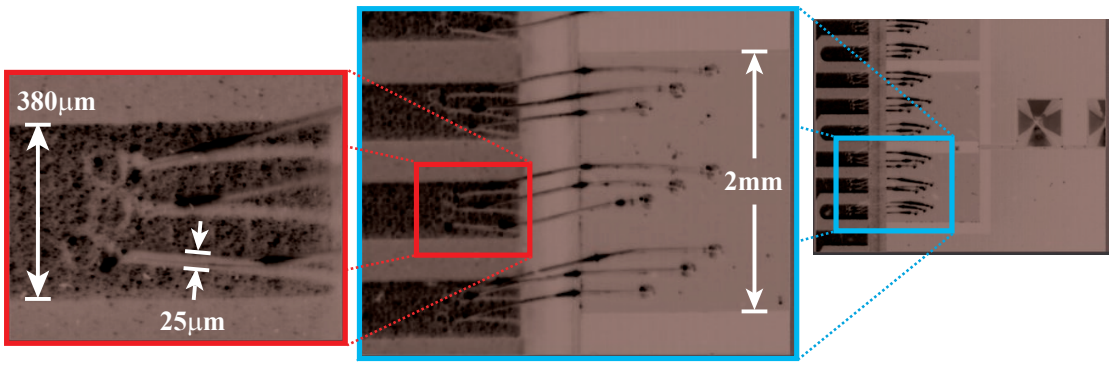

Figure 5.14: Bond wires.

(Aluminium oxide, Al_2O_3), which is a ceramic electrical insulator that has a relatively high thermal conductivity. Alumina is widely used in vacuum technology owing to its low outgassing rate $10^{-9} - 10^{-6}\,\mathrm{Wm}^{-2}$ after bakeout [110]. Both the atom chip mounting area, known as the die attach area, and the carrier connection pads are covered with a $60 - 200$ μin ($1.5 - 5.$ μm) gold plate (99.9% minimum pure Gold, Type II, Grade A) over a $50 - 350$ μin ($1.3 - 8.9$ μm) layer of nickel. Owing to the magnetisablity of this nickel layer (see section 5.3.3), the metallic coating which covered the die attach area was completely removed from the carrier that we utilised for mounting our atom chip. A two part epoxy glue, which has demonstrated being suitable for UHV applications, was utilised for bonding the atom chip to the chip carrier. Finally, the chip carrier pins are made of Kovar, a Fe-Ni-Co alloy.

Bond wires provide the electrical contact between the atom chip and the CPGA connection paths. In contrast to the electrical current requirements in micro-electronics applications, where some few mA are sufficient for operating a device, several hundreds of mA need to be supplied to the on-chip wires. For instance, to generate a $30\,\mathrm{G}\cdot\mathrm{cm}^{-1}$ axial gradient in the 1.2 mm pyramids, it is necessary to run 250 mA through the wire that surrounds the pyramid aperture. We performed a preliminary test of the in-vacuum current-carrying capabilities of 50 μm in diameter and $2 - 3$ mm long bond wires. We found that these wires can sustain a current of 1.5 A indefinitely, but a current of more than 1.75 A destroys the wire in a few seconds. Unfortunately, as a result of the limitations of the machine utilised for wire bonding our first prototype, the bond wires in this chip are only 25 μm in diameter.

To enhance the current carrying capabilities of each circuit we decided to connect a total of nine bond wires to each atom chip pad. These nine wires are distributed over three carrier pads, as shown in figure 5.14. The three microscope photographs in this figure show how the atom chip connections were made. The image on the right shows the two connection paths corresponding to the 1.2 mm pyramid set (shown before in figure 5.13), the CPGA contact paths, and several bond wires connecting the atom chip and the carrier contact pads. Next, the central image in this figure shows a single 2 mm-wide chip contact pad and the nine bond wires attached to it. The opposite ends of these wires go to three different CPGA contact paths. These CPGA pads are only 380 μm wide and it was not possible to fit more than three of the 25 μm in diameter bond wires to each carrier pad, as shown in the leftmost image provided in figure 5.14.

The industry standard method for incorporating a CPGA mounted chip into a larger system is to use a pin grid array (PGA) socket bed. We have also adopted this solution

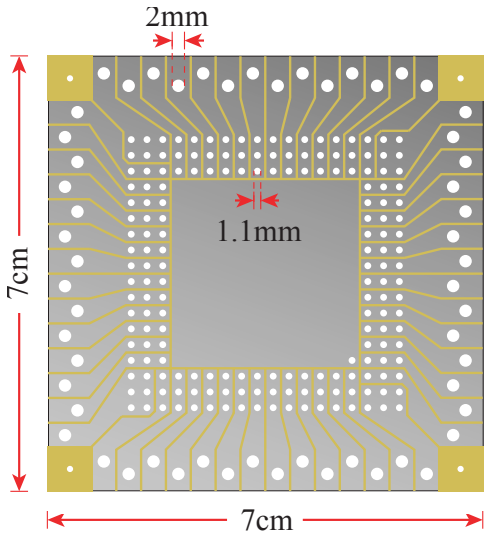

Figure 5.15: We have used standard electronics industry techniques for fabricating a vacuum compatible printed circuit board. The PCB design imprinted in the copper layer of the FR4 board gathers sets of three pin sockets and connects them together in a single copper strip. Each strip can then be accessed individually via copper barrel connectors in order to supply electric current to the atom chip wires.

because it simplifies not only the electrical connections but also the chip replacement procedure. Different CPGA mounted atom chips can be easily plugged and unplugged into the PGA sockets without the need of taking apart or replacing any other elements of the design. The terminals of the PGA sockets are made of a brass-copper alloy (C36000 ASTM-B-16; Cu 62.0%, Zn 35.5% and Pb 3.0%) and the contacts are made of beryllium-copper. The sockets are gold plated and include a lead-free (95.5Sn/4.0Ag/0.5Cu) solder preform.

In combination with the PGA socket bed, we have used an FR4 (Type 4 flame retardant) board for fabricating a printed circuit in which the sockets can be soldered. FR4 is made of an epoxy resin reinforced with woven fiberglass. Rouki *et al.* [111, 112] have demonstrated that with the proper treatment, this material is suitable for UHV applications. Some relevant physical properties of this composite material are reported in [113], including a thermal conductivity of $[0.25 - 0.29]\,\mathrm{Wm^{-1}K^{-1}}$. In addition, this data sheet states that the epoxy resin undergoes a glass transition at a temperature of 135 °C. This establishes the maximum temperature at which these boards can be baked without damaging them.

Standard electronics PCB fabrication techniques have been used for etching copper tracks on these boards, as shown in figure 5.15. We have used PCBs with a 70 µm thick copper layer. Each copper track connects together sets of three CPGA pins, with the exception of the CPGA corners where six pins are connected together. As described above, each on-chip wire connection path has been wire-bonded to three different CPGA pads. The PCB tracks gather together these three CPGA pins in a single connection that can then be easily accessed from the edge of the board. To avoid oxidation of the copper surface, a tin plating stage was added to the PCB fabrication procedure. The tin plate ensures good electrical connection between the copper tracks and each socket solder preform. The opposite end of each PCB copper track includes a 2 mm hole, in which a stainless steel M2 socket head cap screw can be attached. These screws, whose heads make good electrical contact with the copper tracks, are screwed into threaded beryllium/copper barrels. For this purpose, the internal surface of Be/Cu in-line barrel connectors (Kurt J. Lesker Company, part number FTAIBC041) was threaded and the two cross-screws were replaced by a single stainless steel grub screw. Then, Kapton insulated copper wires, 1 mm in diameter, are plugged into the opposite end of the

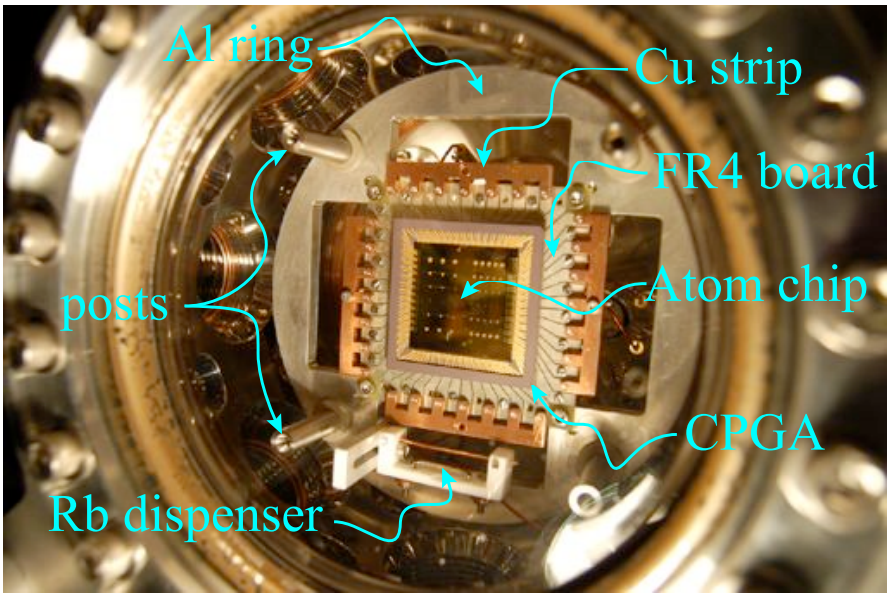

Figure 5.16: The pyramid atom chip mounted in the vacuum chamber. The atom chip is attached to the purple-coloured CPGA, that is in turn plugged into a sockets bed (not visible in the image). The sockets are soldered into the FR4 board, which is held from its corners by an aluminium ring. In addition, four copper strips are connected at each side of the FR4 board.

copper barrels. In order to limit the number of wires loaded into our vacuum system, we decided to create a common connection among the six different micro-fabricated wire sets on each side of the pyramid atom chip. This common connection was established by connecting together the corresponding PCB tracks. A set of four thick oxygen-free high conductivity (OFHC) copper strips (shown in figure 3.4, in page 45) were fabricated for this purpose.

The photograph in figure 5.16 shows the first prototype of the pyramid atom chip as seen from the bottom 8" viewport of the vacuum chamber. The pyramid atom chip, mounted on the purple-coloured CPGA, can be seen in the centre of the image. This is plugged into a PGA socket bed on the FR4 board which has four copper strips attached to its edges. All these elements are held by an aluminium ring, which in turn is attached to four steel posts. In the bottom of the image, it can also be seen that the dispenser holder position was set slightly over the atom chip surface.

This packaging has been extensively tested for compatibility with the requirements of our experiments. Both the vacuum compatibility and the magnetic properties have been evaluated. Although pressures below 10^{-11} mbar are normally required in the most demanding cold atoms experiments, a pressure of 10^{-9} mbar is sufficient for less stringent experiments such as creating a MOT. With a modest $20\,\mathrm{Ls}^{-1}$ vacuum pump, this vacuum level requires the total gas load in the system to be maintained below $2 \times 10^{-9}\,\mathrm{Pa \cdot m^3 s^{-1}}$. Secondly, the small scale of the micro fabricated pyramids makes their operation somewhat sensitive to stray fields. For instance, consider the operation of the 200 µm pyramid row. If these MOTs are generated by quadrupole magnetic fields with $30\,\mathrm{Gcm}^{-1}$ of axial gradient, a stray field of 150 mG would push the magnetic field zero positions out of these pyramids volume. Similarly, to create MOTs simultaneously in all the pyramids in this row, a field variation of less than $75\,\mathrm{mGcm}^{-1}$ must be

guaranteed across the atom chip surface.

5.3.2 Vacuum tests of chip packaging resources

The bottom end of a CF full nipple (Kurt J. Lesker Company, FN-0600) was connected to a turbomolecular pump (TurboVac 150). The nipple top end was sealed with a 6" to 2 3/4" CF reducer flange (Kurt J. Lesker Company, RF600X275). A 2 3/4" CF tee (Kurt J. Lesker Company, T-0275) connected to the reducer was used for connecting a pressure gauge (Pfeiffer Vacuum, Compact Full Range BA Gauge, PBR 260) to the chamber. The measurement range of this gauge spans from 5×10^{-10} to 10^{3} mbar.

In order to prepare this chamber for testing the atom chip packaging resources, it was pumped down while still empty. Before baking and after 12 hours of pumping time, a pressure of 10^{-7} mbar was reached. Next, a single heater tape wound around the top 6" blank flange was used for maintaining this section of the chamber at 100 °C. After 24 hours of baking at this temperature and allowing the flange to cool back down, a final pressure of 2×10^{-8} mbar was obtained. If the nominal pumping speed of the turbo $\sim 100\,\mathrm{Ls}^{-1}$ is put together with this pressure, a $\sim 10^{-6}\,\mathrm{Ws}^{-1}$ outgassing rate is deduced for the stainless steel chamber after baking. This value is still high compared with the range reported by Delchar after bake-out ($[10^{-11} - 10^{-8}]\,\mathrm{Wm}^{-2}$) [110]. However, it has to be taken into account that only a small portion of the chamber was kept at 100 °C during the bake-out period. In fact, to avoid any damage to the gauge, the 2 3/4" tee port connecting to the gauge had to be kept at no more than 50 °C.

To continue, we loaded into the test chamber a $7 \times 7\,\mathrm{cm}^2$ FR4 board patterned as shown in figure 5.15. Two aluminium posts attached to the reducer flange were used for holding this PCB into the vacuum test chamber. After 2.5 hours of pumping down, a pressure of 2×10^{-6} mbar was reached. Next, two heater tapes were wound around both the reducer flange and the top section of the nipple. The nipple top section and reducer flange were then covered with aluminium foil and the test chamber was heated until the temperature of the reducer flange reached 130 °C. After baking at this temperature for three and a half days, the minimum pressure attained while baking was 2×10^{-7} mbar. Next, the system was allowed to cool down to room temperature and a final pressure of 10^{-8} mbar was recorded. We were also interested in evaluating the amount of humidity absorbed by the FR4 board when exposed to air after being baked out in vacuum. Therefore, we continued our tests by venting the system to nitrogen and then to air. The chamber was left open to air for one hour and afterwards the system was pumped down again. The 10^{-8} mbar pressure found before was recovered after just one day of pumping without needing to bake the test chamber again.

Finally, the PCB was replaced by a new FR4 board which included PGA sockets and a CPGA. A pressure of 1.5×10^{-6} mbar was reached after pumping for two days without baking the system. Next, the chamber was baked at 130 °C for two days and a minimum pressure of 8.6×10^{-7} mbar was obtained while baking. When the system was allowed to go back down to room temperature, we measured a pressure of 3×10^{-8} mbar. The chamber was then vented to air for a couple of hours and pumped back down again. A pressure of 2×10^{-8} mbar was recovered in 4 hours. Baking the system by heating the 6" nipple at 150 °C for up to 5 days resulted in a final pressure, after cooling down, of 3×10^{-9} mbar. The chamber was opened, closed and pumped down once more. A pressure of 10^{-8} mbar was recovered in one day, but it finally came down to 3×10^{-9} mbar in a week.

Thus, the vacuum compatibility of each element of the chip packaging arrangement

has been thoroughly assessed. The vacuum compatibility of both FR4 and Alumina has been studied elsewhere [111, 110]. The authors of [111] established that, with the appropriate treatment, the FR4 outgassing rates can be reduced to a few $10^{-9}\,\mathrm{Wm}^{-2}$. The PCBs fabricated for our atom chips are squares with a 7 cm side length. A board like this, according to [111], would result in a gas load on the order of $10^{-11}\,\mathrm{Pa}\cdot\mathrm{m}^3\mathrm{s}^{-1}$. Similarly, the chip carriers have roughly a total area of $50\,\mathrm{cm}^2$. This surface area, combined with the $3.7\times10^{-7}\,\mathrm{Wm}^{-2}$ outgassing rate suggested in [111] for Alumina, results in a gas load of $1.5\times10^{-9}\,\mathrm{Pa}\cdot\mathrm{m}^3\mathrm{s}^{-1}$. The results of our independent assessment of the chip packaging arrangement vacuum compatibility were consistent with this estimate. Moreover, when the PCB board, PGA sockets and CPGA composite system was loaded into the test vacuum chamber, a pressure as low as 10^{-9} mbar was obtained after baking out at a temperature of 100 °C for 5 days. In addition, the entire chip packaging solution described in this section has been loaded into the definitive experiment vacuum chamber, and a pressure below 10^{-9} mbar is routinely maintained by a single $20\,\mathrm{Ls}^{-1}$ ion pump.

5.3.3 The chip package magnetic properties

Unfortunately, there are some ferromagnetic materials in the PGA sockets and CPGA. The CPGA pins contain Kovar, the CPGA chip attachment area has a thin nickel layer, and the PGA sockets contain a brass-copper alloy, all of them known to be magnetic. We have therefore performed detailed measurements of the magnetic field present above an FR4, CPGA and PGA socket arrangement. Particular attention was paid to the region where the atom chip would be located.

An FR4 board was mounted approximately 10 cm away from, and oriented parallel to the surface of an optical table. A Hall probe was then mounted on a 2D translation stage and placed approximately 5 mm above the FR4 surface, allowing this way enough space for later including the PGA sockets and the CPGA. The Hall probe tip position was scanned horizontally over the central area of the FR4 board. The investigated region comprised one quadrant of the board section covered by the CPGA, including a portion of the area occupied by the CPGA pins. Although particular care was taken in determining the field component perpendicular to the board surface, B_z, the complementary B_x and B_y components were also monitored.

We first created a map of the magnetic field above the FR4 surface exclusively. The field variation registered in this measurement recreated closely a previous measurement of the ambient field. To continue, we included the PGA sockets and measured the magnetic field present above the composite system. Although a difference of approximately 20 mG was registered between the values obtained with and without including the sockets bed on top of the FR4 board, these discrepancies were observed exclusively on top of the areas occupied by the sockets. In the middle of the FR4, which is the area where the atom chip would be located, the two measurements resulted in values whose differences are well within the uncertainty of the measurement of a few mG. Next, the CPGA was put on top of the FR4 and sockets arrangement and a new field measurement was performed. This showed that on top of the carrier pins the magnetic field is strongly modified. In this region, the field contribution of the carrier pins can be as high as 170 mG. Nevertheless, in the chip attachment area this strong field contribution was not observed. Moving away from the carrier pins towards the centre of the chip attachment area, the measured field went back to the ambient field values in less than 500 µm.

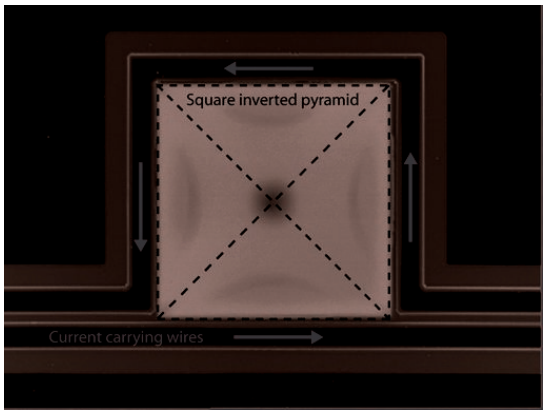

Figure 5.17: Optical microscope image of a microfabricated gold wire circling the square pit of a Si etched pyramid. This pyramid side length is of 200 μm and the wire width is 25 μm. The distance between the pyramid edge and the wire is 20 μm. A reflective gold layer can be observed on the corners of this image (light grey sections). The dark grey areas around the wires indicate that the metallic layer is completely isolated form the current carrying wires.

Finally, in order to test the magnetic susceptibility of the CPGA materials, the carrier was taken away and placed in the vicinity of a strong magnet. Then, this CPGA was put back on top of the FR4 and socket bed to repeat the field measurement. We observed that the carrier pins and, more importantly, the nickel layer present in the die attach area acquired a certain amount of magnetisation. In this case, a field variation of up to 1 G was measured in a distance of 3.5 cm, between the carrier pins and the centre of the chip attachment area. In view of this, we decided to remove the metallic layer included in the die attach area. For this purpose, the connection paths were carefully protected while the Ni+Au layer in the die attach area was sand blasted until the alumina surface was completely exposed. After removing the Ni+Au layer, the field variation over the chip attachment area remained below 5 mG.

Under typical experimental conditions, the atom chip package is exposed to magnetic fields of the order of one Gauss. Consequently, we performed a new set of measurements with the aim of determining the magnetising effect a 1 Gauss field has on both PGA sockets and CPGA. A large circular coil coplanar with the FR4 board was used to generate a 1 Gauss magnetic field at the centre of the board. Initially, a magnetic field measurement was made over the FR4 board surface both with and without including the socket bed. While the field was present, the Hall probe position was scanned across the board central region. Variations of less than 25 mG were observed over the die attach area. The biggest variations were found when the probe position was scanned on top of the pin rows, where changes of up to 100 mG were registered. After turning off the applied field and repeating the magnetic field measurement, the values obtained before applying the field were closely reproduced.

To continue, the CPGA was included in the arrangement and new scans were performed both before and after a 1 Gauss field had been applied. No traces of magnetisation were found as the differences between the two measurements were below 5 mG. We concluded that over the CPGA dip attach area, even while the 1 Gauss field was present, field variations are below 25 mG with the FR4, PGA sockets, and CPGA set.

5.3.4 The micro-fabricated current carrying wires

The wires integrated in this atom chip are 3 μm thick. This thickness was achieved by electrodepositing gold on a 100 nm base layer of sputtered gold. With the aid of equation 5.5c we can see that in order to generate the same gradient in, for example,

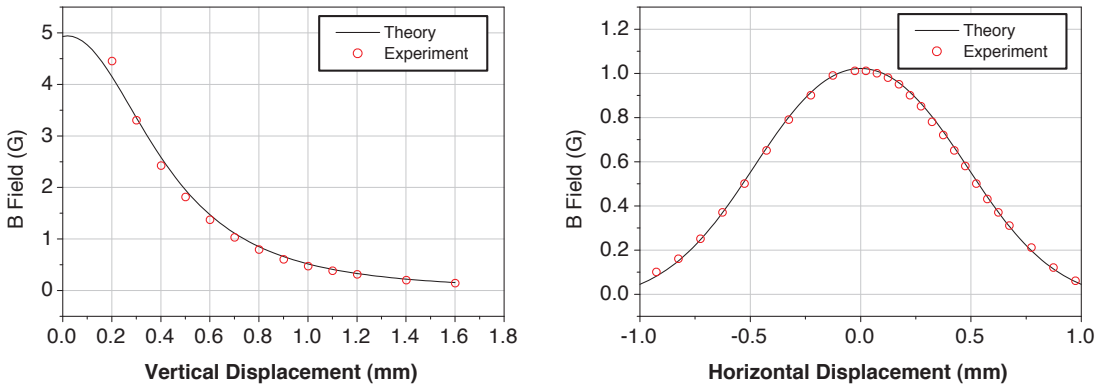

Figure 5.18: The magnetic field generated when running a 480 mA through the 800 µm on-chip square loop. For the measurement represented by the open red circles (○) the loop plane was oriented horizontally and the out of plane component of the field was measured with a Hall probe. The probe position was displaced vertically along the loop centre and horizontally at a distance of (0.7 mm) from the loop plane.

a 1.2 mm pyramid as in a 200 µm pyramid, 36 times more current needs to be run through the wire loop circling the former pyramid. Given that the thickness of all the wires is the same, a method for enhancing their current-carrying capabilities is to vary the wire width. At the same time, it is also important to keep these wires widths small compared to the corresponding pyramid side length. Taking these considerations into account, wire loops with two different wire widths were included on the pyramid atom chip. The wires encircling the 200 µm, 400 µm and 600 µm pyramids are 25 µm wide, while the remaining wires are 50 µm wide. In addition, the separation between the pyramid aperture sides and these wires is as small as 20 µm in all instances.

The optical microscope image given in figure 5.17 is an example of a pyramidal pit plus electroplated wire composite system. In this case the 200 µm square entrance of this pyramid is surrounded by a 25 µm wide gold wire. This image also shows that these wires have been separated and, consequently, completely isolated from the reflective layer that was laid over the entire chip surface.

With the aim of carefully assessing the characteristics and limitations of the wires included in the pyramid atom chip, an additional chip containing exclusively the micro-fabricated wires arrangement has been fabricated. This test chip has also been packaged into a CPGA and nine-bond wires, each of which is 25 µm in diameter, provide good electrical contact between chip and carrier contact pads.

We have verified that the field generated by the micro-fabricated wires agrees with the prediction of the Biot-Savart law for a closed square loop. The results of this comparison are shown in figure 5.18. The magnetic field generated by the 800 µm on-chip wire loops was measured with an axial Hall probe (Lake Shore Gaussmeter model 421, axial probe MNA-1904-VH) whose active area is 760 µm wide. A 480 mA current was run through the wire and the field component perpendicular to the chip plane was measured. With the test chip surface oriented horizontally, the probe position was scanned both vertically (left graph) and horizontally (right graph) on top of one of the 800 µm square loops. These measurements are represented by open red circles (○) in the graphs. The solid curves are the prediction of the Biot-Savart law for the axial magnetic

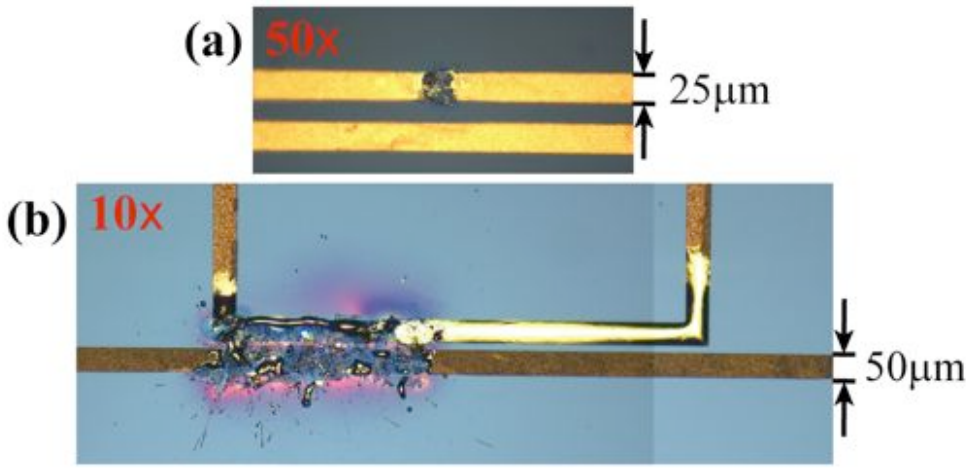

Figure 5.19: The micro-facricated wires blow up just as if they were fuses. The 50 μm-wide wire blows with a current of 1.8 A and the 25 μm-wide wire can not withstand more than 0.8 A. These optical microscope images of the failure points in each case clearly indicate that the 50 μm-wide wire melted before a short circuit destroyed it; the 25 μm-wide failure on the other hand was probably originated from a small defect in the electroplated wire.

field component generated by a closed 50 μm wide wire loop, centred on a 895 μm square and running a current of 480 mA. There is an excellent agreement between the theory and experiment.

We have also determined the maximum current that can be run through the atom chip micro-fabricated wires, and how long currents can be sustained without damaging the chip wires. For this purpose, we performed a series of tests under moderate vacuum ($\sim 10^{-5}$ mbar) conditions. The temperature variation at three different points of the chip packaging arrangement was closely monitored. Thermocouples located on top of the test chip surface, next to the CPGA pins and on the edge of the FR4 board were used for monitoring the temperature. In addition, the change in the resistance on the current carrying wires was also monitored.

The maximum current that can be applied through the chip wires was determined by increasing the current in small ~ 10 mA steps. After each increment, we waited for the temperature of the wire to stabilise before going to the next current. We repeated this procedure in a 50 μm-wide wire and in a 25 μm-wide wire. The former blows at approximately 1.8 A and the latter at 0.8 A. The images shown in figure 5.19 are optical microscope images of the points were the failure of the wires took place. The cause of the failure in the 25 μm-wide wire could have been a defect of the wire, while in the case of the 50 μm-wide wire seems clear that the heat dissipated was enough for melting the gold and producing a short circuit between the two wires. Note the differences in the wire surface roughness between the regions where the wire exploded and where it still shows the result of the electroplating process.

Figure 5.20 shows the time during which a given current can be applied through a 25 μm-wide wire (□) and through a 50 μm-wide wire (●) before its temperature reaches 120 °C, which is the safe operation limit determined by the chip packaging materials. The epoxy glue used for bonding the pyramid atom chip to the CPGA suffers a glass transition at a temperature of approximately 120 °C. Similarly, the FR4 data sheet

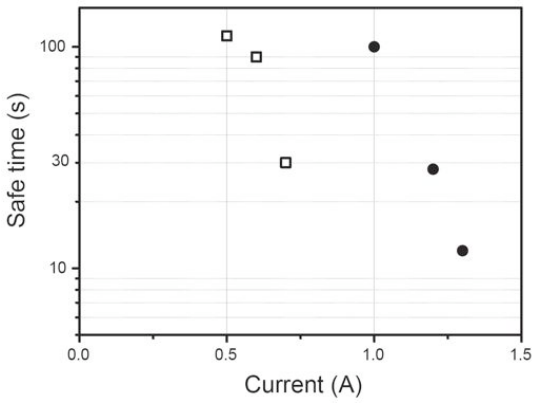

Figure 5.20: Time taken for the chip wire temperature to reach 120 °C for various currents. The filled circles (●) are the result of running current through a 50 µm-wide wire; the open squares (□) corresponds to the measurements made on the 25 µm-side wires.

states that these boards also suffer a glass transition at a temperature of 135 °C. Although the melting point of the gold wires is much higher and the wires could in principle withstand higher temperatures, these glass transition temperatures set the maximum temperature for safe operation of the atom chip. Our wire-blowing results established that a current of 1.5 A can be run indefinitely through the 50 µm-wide wire, although for avoiding damage to the chip packaging materials it is recommended that this high current should not be run for more than 10 seconds. Similarly, the 25 µm-wide wire can be safely operated at 0.5 A for an indefinite amount of time, but currents of 0.7 A need to be limited to short 10 s periods.

5.4 Summary

In this chapter, I have shown the details of the first prototype of a silicon based atom chip that incorporates micro-fabricated hollow pyramidal mirrors and current carrying wires. As a result of the crystallographic structure of the silicon wafers in which these atom chips have been developed, the pyramidal mirrors present an internal angle of 70.5° .

The optical properties of the resulting geometry has been studied thoroughly. In particular, we have gained insight into the properties of the optical field generated inside these pyramids when a circularly polarised light beam, travelling parallel to the pyramid axis, is shone into these mirrors. Three types of rays have been identified according to the reflections that they suffer inside of the pyramid. The polarisation state of the first two ray types is not severely modified by the reflections. Hence, these rays generate a scattering force balance over the axis of the pyramid that can be used to create magneto-optical traps. On the other hand, the third type of rays suffers one reflection at near grazing incidence that modifies substantially the polarisation state of the light. These rays destroy the force balance generated in the pyramid and hinder the functioning of the MOT. We have presented two strategies for eliminating these undesired reflections: utilising a limited reflectivity coating in the pyramids, and masking the reflective coating.

To generate the quadrupolar magnetic field required for creating a MOT inside the chip pyramids, current carrying wires have also been integrated into our atom chip. These wires run around the square openings of the pyramids and with the addition of an homogeneous magnetic field, points of zero magnetic field can be generated along the axis of the pyramids.

Finally, micro-electronics industry standard micro-chip packaging tools and techniques have been utilised for loading and holding the pyramids and wires atom chip into the vacuum chamber, as well as for supplying current to the on-chip wires. Extensive vacuum and magnetisability tests were performed to ensure the compatibility of these elements with the requirements of cold atom experiments. As well, the flow of the heat generated by the chip wires through the experimental apparatus was carefully studied with the aim of establishing the safe operation limits of the device.

Chapter 6

Co/Pt magneto-optic thin films

In this chapter I describe the properties of a permanently magnetised medium that is suitable for applications in atom chips. The magneto-optic thin films composed by alternating layers of cobalt and platinum (Co/Pt MO films) can be engineered to produce a medium that retains a large amount of magnetisation. Hence, the Co/Pt magneto-optic thin films are strong enough to make magnetostatic atom traps and could replace the current carrying wires in future integrated pyramid MOT chips.

To begin with, I provide a brief introduction to the physics of magnetic thin films and the required fabrication techniques. These concepts are necessary for evaluating the potential uses of these films. Then, the properties of the Co/Pt multilayer structure will be outlined to show why these films are particularly suitable for creating cold atom micro-traps. To continue, I describe the thermomagnetic recording technique that we have used for creating microscopic magnetic patterns on the surface of Co/Pt MO thin films. Finally, the results obtained by means of this technique are shown together with numerical estimates of the corresponding magnetic fields.

6.1 Magneto-optic multi-layer thin films

Magneto-optic (MO) films have been commercially used to produce high density recording media such as the minidisk. According to [114], the high anisotropy of these films allows thermally stable magnetic grains with sizes below 10 nm. Among other interesting properties, these magnetic films are characterised by a large out-of-plane magnetisation, an exceptionally strong remanent field, a high room-temperature coercivity and a large Kerr angle at short wavelengths. These properties make MO films technology specially suitable for applications in atom optics.

6.1.1 Preparation of multi-layer films

A magneto optic thin film is composed by a series of material layers. First of all, a *substrate* provides a surface that can be assumed as perfectly smooth. Then, a *seed layer* or *insulation layer* provides an initial texture and grain growth templates. This

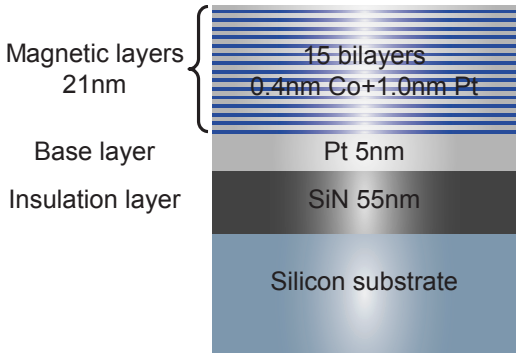

Figure 6.1: The structure of the MO film that has been used in this experiment. These MO films have been deposited on a silicon substrate. A SiN insulation layer and a platinum underlayer are first deposited on the substrate and then 15 Co/Pt bilayers are grown on top.

is still assumed as a smooth surface and it may also provide an epitaxial growth surface condition for obtaining the desired crystallographic orientation of an *underlayer*, also known as *base layer*. This orientation is transferred to the magnetic layer through the underlayer via epitaxial growth. Therefore, the grain sizes of the underlayer mainly determine the grain size and the grain size distribution of the magnetic layer.

The structure and final properties of a magneto optic thin film are strongly influenced by the manufacturing conditions. Parameters such as the growth rate, the pressure in the vacuum chamber during the evaporation process, and the temperature of the substrate must be optimized [74, 73]. The purpose of the thin film multi-layer structure is to obtain a controlled grain size, grain isolation, low intergranular exchange coupling, high coercivity, and the preferred crystallographic orientation on the magnetic layer [114].

There are several methods for the fabrication of multi-layer thin films. In the technique used to prepare the Co/Pt films for this research, the materials that constitute each of the layers are evaporated onto the film. The energy required to evaporate the material is supplied by an electron-beam. Therefore, this technique is called *Electron-Beam Evaporation*. Crucibles inside a vacuum chamber contain the materials that are to be deposited. An electron gun produces a beam whose path can be controlled by means of a uniform magnetic field, allowing the electrons to be directed towards either of the crucibles. The material contained in the crucible is heated up by the electron-beam and the evaporation is produced. The material vapour rises until it reaches the substrate, where it is finally deposited. The rate at which the material is deposited on the substrate, known as the *growth rate*, can be controlled by the power of the electron-beam. If the growth rate is kept low, the thickness of each layer can be carefully regulated. Once the desired thickness of a given layer has been attained, a shutter is interposed between the crucibles and the film holder. Then, the magnetic field magnitude is changed for directing the electron beam to a different crucible. Finally, the shutter is re-opened and the deposition of the second material begins.

6.2 The Co/Pt multilayer film

The magnetic, magneto-optical and structural properties of Co/Pt multilayers have been extensively studied by several authors over the last two decades [74, 115, 116]. In particular, Lin *et al.* presented Co/Pt multilayer thin films as a potential material for fabricating magneto-optical recording media. In their 1991 publication, these authors

explain that the largest perpendicular anisotropy occurs for Co layer thickness of 1-2 monolayers and that perfectly square hysteresis loops are obtained for multilayers of Co3 Å/Pt10 Å with thickness up to about 10 periods. Similarly, the domain structure and magnetisation reversal processes in these films have been extensively studied [117, 118, 119, 120].

The fabrication of the Co/Pt multilayer thin films in this thesis was optimised for creating microscopic atom traps and guides. We wanted a large perpendicular anisotropy to allow the creation of well defined patterns with extremely thin boundaries between regions magnetised in opposite directions. We also wanted strong saturation magnetisation and coercivity. These allow tight atom traps to be generated at very short distances from these films.

As shown in Fig. 6.1, the magneto-optical films were deposited on silicon substrates with a 550 Å silicon-nitride (SiN) insulation layer. The insulation layer was held at 200 °C while a thick platinum base layer of 50 Å established a good 111 texture. Later, 15 bi-layers of alternating Co (4 Å) and Pt (10 Å) were prepared by electron-beam evaporation onto the 111 base layer. In order to ensure good control of the layer thickness, the evaporation rate was kept as low as 0.1 Ås^{-1}.

6.2.1 Crystal structure

The magnetic properties of the Co/Pt thin films and particularly its magnetic anisotropy depend strongly on the crystallographic orientation of the layers. In a ferromagnetic crystal, the magnetisation is directed along certain definite crystallographic axes, called directions of easy magnetisation or just *easy directions*. For example, while bulk platinum establishes a cubic close-packed (ccp) crystal structure, the crystal structure adopted by bulk cobalt is hexagonal closed-packed (hcp). The hcp structure of bulk cobalt has an easy direction along its hexagonal axis.

In our case, the platinum underlayer is used to provide epitaxial growth conditions for face-centered tetragonal (fct) CoPt grains. These grains grow with their magnetic easy axis perpendicular to the film plane. The cobalt layers in our multi-layer films are extremely thin and are sandwiched between layers of platinum with well established 111 texture. The growth conditions should assure that the good 111 texture established on the platinum base layer is transferred by epitaxial growth to the CoPt layers. In CoPt alloys, the ordered face-centered tetragonal structure ($L1_0$ phase) is adopted in the composition range that goes from 40 to 60 at. %Co [114]. The crystal structure of this fct phase is shown in figure 6.2. It has a superlattice structure consisting of Co and Pt monoatomic layers stacked alternately along the c-axis, which is the magnetic easy axis. This ordered phase can be obtained by deposition of the films on a heated substrate [114].

6.2.2 Magnetic and optical properties

The ferromagnetic component of Co/Pt MO films exhibits a spontaneous magnetisation. This suggests that electron spins and magnetic moments are arranged in a regular manner within the multi-layer structure of the film. Microscopically, even in the unmagnetised state, the magnetisation of a film is not uniform. The entire magnetic layer is divided into *magnetic domains*, each with its own magnetisation state. These domains are tiny volumes uniformly magnetised with a spontaneous magnetisation M_s in an easy direction, which in our case is perpendicular to the film surface. The transition volumes

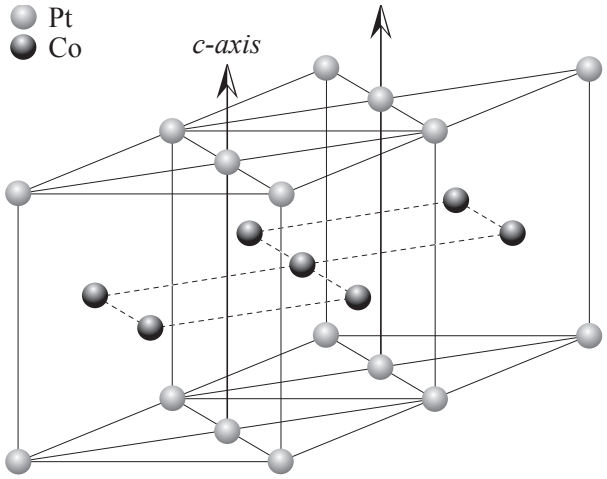

Figure 6.2: The face-Centred tetragonal (fct) structure $L1_0$ phase ensures that the CoPt grains grow with their magnetisation axis perpendicular to the film surface [114].

between domains of different magnetisation are called *domain walls*, also known as *Bloch Walls*. The typical width of a magnetic domain is between 10 and 100 µm, while the typical domain wall thickness lies between 10 and 100 nm [114].

Domain structure has its origin in the possibility of lowering the energy of a system by going from a saturated configuration with certain magnetic energy to a domain configuration with a lower energy. Domain structure is therefore a consequence of the various contributions to the energy of a ferromagnetic body. Walls need energy to be established and the energy of a reversed magnetised domain has four major contributions: the *external field energy*, the *anisotropy energy*, the *exchange energy* and the *self (demagnetising) energy*. The contribution of each of these sources to the total energy of the system depends on the size of both domains and walls, as well as on the thickness of the film and of its multiple layers.

The external field energy is the difference between the energy in the absence of magnetic domains and the energy in the presence of a domain. The anisotropy energy is a consequence of the deviation of the magnetisation vector from the easy axis, which in the case of the Co/Pt MO film is perpendicular to the film surface [114]. This is also called *magnetocrystalline energy* because in a ferromagnetic crystal, this energy directs the magnetisation along certain definite crystallographic axes. For example, bulk cobalt forms an hexagonal crystal and, at room temperature, the hexagonal axis corresponds to its direction of easy magnetisation [121]. The exchange energy consists of an increase in the free energy when a domain appears in a magnetic medium; it can be described in terms of the variation in the direction of magnetisation across the plane of the film [114]. The exchange field is an internal interaction tending to line up the magnetic moments parallel to each other. The orienting effect of the exchange field is opposed by thermal agitation, and at elevated temperatures the spin order is destroyed [121]. Finally, the self (demagnetising) energy is a long range interaction that tends to take the system to a demagnetised state. The change in the direction of the magnetic moments within a domain wall is gradual over many atomic planes. The distribution of the change of the direction of magnetisation over many magnetic moments results in a decrease of the exchange energy.

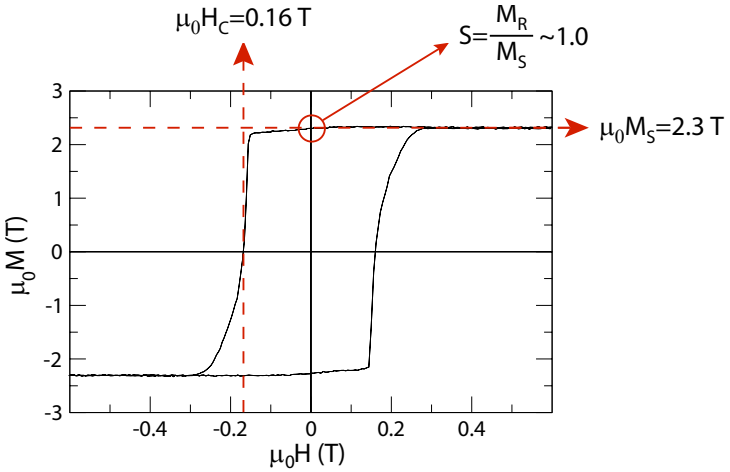

Figure 6.3: Hysteresis loop of one of our Co/Pt MO films.

Two processes contribute to the magnetisation reversal of the magnetic layer of MO films: *nucleation* and *wall motion*. Nucleation is the process in which the magnetisation within the volume of a domain is reversed. Wall motion is responsible for the growth of domains already formed at the expense of the volume of neighbouring domains. The processes of nucleation and wall motion are very complex. Several factors may influence them: an external magnetic field; defects, impurities or any kind of anisotropy in the crystal structure; temperature changes, among others. Magneto crystalline anisotropy and exchange energy are important in wall energy. In a magnetisation reversal process, domain walls move to increase domains volume. This motion is caused by the torque acting on the magnetic moments within the tiny volume of the wall, where the exchange and the anisotropy energies are in balance.

The surface magneto-optic Kerr effect (SMOKE)

The polar and longitudinal Kerr effects consist of a complex rotation of the plane of polarisation of linearly polarized light upon reflection from the surface of a ferromagnetic material. This rotation is directly related to the magnetisation of the material within the probing region of the light. If the magnetisation increases, so does the Kerr rotation angle, thought not linearly. When this magneto-optic Kerr effect is produced by a magnetic surface, then the phenomenon is known as *Surface Magneto-Optic Kerr Effect* (SMOKE) [122, 123].

Magneto-optic effects can be described by either macroscopic dielectric theory or microscopic quantum theory. Macroscopically, these effects arise from the antisymmetric, off-diagonal elements in the dielectric tensor. On the other hand, microscopically these effects are related to the coupling between the electric field of the light and the electron spin within the magnetic medium [122, 123].

In a magnetic high density recording medium such as the Co/Pt film, the readout is done by detecting changes in the rotation of the plane of polarisation of light upon reflection from the film surface. In our experiment the SMOKE can be used as a tool for analysing the patterns written in an MO film.

6.2.3 Characterization of MO films

The magnetic properties of the films used in this experiment were determined using an *alternating gradient force magnetometer* (AGFM) [118]. The sensitivity of this device is on the order of 10^{-8} emu $= 10^{-13}\,\mathrm{A}\cdot\mathrm{m}^2$. In the AGFM, the sample to be analysed is initially magnetised by a field produced by an electromagnet. At the same time, the sample is subject to a small alternating field gradient on the order of a few Oe/mm to a few tens of Oe/mm. This alternating gradient field exerts a force $F_x = \mu\frac{dB}{dx}$ on the sample, which rests on one end of an extension cantilever. The opposite end of this cantilever is held by a piezo-electric biomorph unit, which senses the force exerted on the sample and converts it into an electric signal. The proportionality between the force and the field gradient, which is given by the magnetic moment μ of the sample, is determined by this measurement. The magnetisation is in turn defined as the quantity of magnetic moment per unit volume. Consequently, the AGFM allows us to determine a direct relation between the electric signal produced by the piezo unit and the magnetisation of the sample [114].

A set of key properties of a magnetic sample can be determined by analysing the curve obtained for the magnetisation of the sample versus the applied field, namely hysteresis loop. Figure 6.3 shows an example of the hysteresis loop for one of our MO films. If the sample is initially demagnetised and a low magnetic field is applied, a magnetisation is induced on the sample by means of a reversible domain wall motion. This means that, if this field is turned off at this point, the sample will recover its unmagnetised state. By increasing the applied field above this reversible stage, the walls will move further away and a state of irreversible magnetisation is reached. This happens because the magnetisation rotation has to be done against the anisotropy energy. Then, once the magnetisation has been reversed, the anisotropy energy prevents the magnetic moments from relaxing to its initial direction. A further rise of the magnetic field will eventually make the sample reach its saturation magnetisation M_S. At this point, the sample has been fully magnetised in the direction of the field and its magnetisation does not grow further on increasing the magnetic field. Moreover, after the saturation has been reached and the magnetic field has been turned off, the magnetisation of the sample will relax to its remanent magnetisation M_R.

The ratio $S = \frac{M_R}{M_S}$ is known as the squareness of the hysteresis loop and is a measure of the relaxation of the magnetisation that the sample suffers when the magnetising field disappears. If the field is now applied in the opposite direction and gradually increased as before, the magnetisation of the sample will eventually be reduced to zero again. The value of the applied magnetic field at which the magnetisation is reduced to zero is called the *coercivity* of the film. From the hysteresis loop shown in figure 6.3, the film coercivity is found to be $\mu_0 H_c = 0.16\,\mathrm{T}$, while the saturation magnetisation $\mu_0 M_S = 2.3\,\mathrm{T}$. This represents a magnetisation $\sim 30\%$ higher in the Co layers than that of bulk Co. This occurs because the cobalt layers polarise the nighboring platinum atoms, which in turn contribute to the magnetisation of the sample. In addition, the squareness of this hysteresis loop ($S \simeq 1$) guarantees that the sample remains in a highly magnetised state ($\mu_0 M_R \simeq 2.3\,\mathrm{T}$) even after the magnetising external field has been removed.

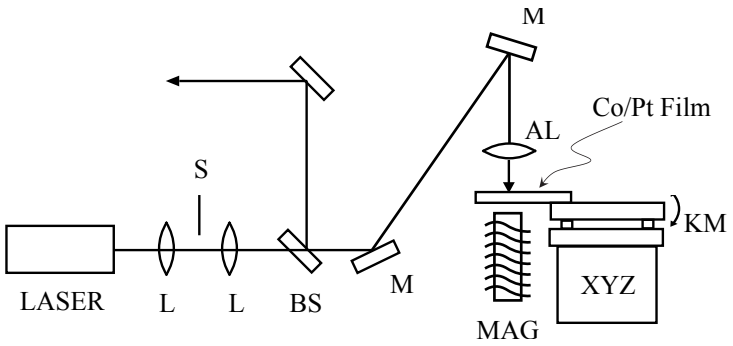

Figure 6.4: Diagram of the apparatus used for writing magnetisation patterns on the Co/Pt MO film surface. The Co/Pt film is suspended on top an electromagnet (MAG). An aspheric lens (AL) focused down a laser beam creating an intense light spot on the film surface. Then, a translation stage (XYZ) is used to translate film.

6.3 Thermo-magnetic recording technique

The next step of this project was to write well defined magnetic patterns on these films. With features on a scale of a few microns, the full size of these periodic patterns should extent up to a few millimeters. The thermo-magnetic recording technique used for this purpose relies on the thermal modification of the magnetic properties of the recording medium [73]. Particularly, the coercivity of the MO film decreases when the temperature rises. According to this, a laser beam can be used to transfer energy to a very small area of the magneto-optic film. This small surface section is heated up by the beam hot spot and the coercivity is locally decreased. If a magnetic field lower than the room temperature coercivity of the sample is simultaneously applied in a direction opposite to that of the initial magnetisation of the sample, the magnetic domains can be controllably reversed. Finally, an appropriate displacement of the position where the laser heats the surface creates the desired magnetisation patterns. The physics involved in the thermo-magnetic recording process are beyond the scope of this thesis. However, this is the subject of a long list of publications [124, 125, 126, 127, 128, 73].

Due to the nature of this procedure, the main parameters involved in thermo-magnetic recording are, firstly, the magnitude of the magnetic field to which the magnetic medium is exposed during the recording process and, secondly, the amount of energy transferred to the magnetic medium by the laser beam. As the position where the laser hits the surface is not fixed, not only the power of the laser is important, but also the velocity at which the laser hot spot travels across the film surface has to be taken into account.

6.3.1 The writing apparatus

The experimental apparatus used to write magnetic patterns in the MO films is shown in figure 6.4. First, a frequency doubled Nd:YVO laser operating at 532 nm on a single transverse mode (TEM_{00}) delivers the energy needed to decrease the coercivity of the film. The beam is focused to a small spot, filtered through a small aperture, and then

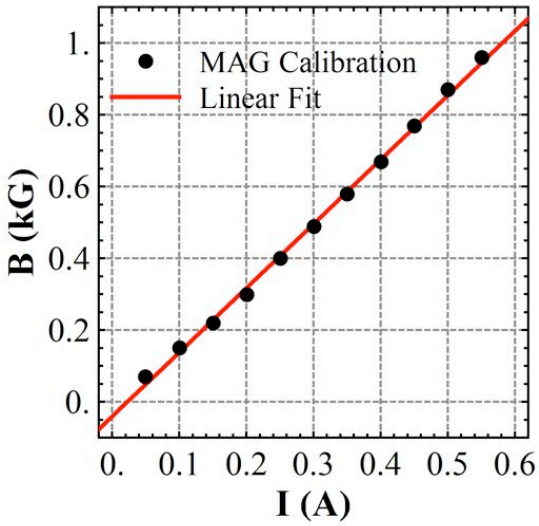

Figure 6.5: The measurement of the magnetic field produced near the core of the electromagnet included in the writing apparatus against the current that flows through it. This graph is used for calibrating the electromagnet.

brought to its original diameter by a pair of lenses (L), both with the same focal length ($f \sim 4.5\,\text{cm}$). In the focus of this spatial filter, a mechanical shutter (S) is responsible for the interruption of the beam. This allows the writing to be interrupted while the film is translated to a position where the writing has to be re-established. When the shutter is opened, the beam travels through a non-polarising beam-splitter. Then, a pair of mirrors direct the beam to the film surface and a final aspherical lens (AL), $f = 4.51\,\text{mm}$, is used to create a tight focus on the surface of the film. The MO film rests on translation stages denoted by XYZ in figure 6.4. These are used not only to perform the displacements which give rise to the magnetic patterns, but also to ensure that the beam focus is uniform all over the surface of the film. Finally, an electromagnet (MAG) placed directly below the film produces a homogeneous magnetic field of up to 0.4 T over the area heated by the laser. The data resulting from the calibration of the electromagnet can be seen in figure 6.5. A linear fit was performed to this data. As a result of this, the empiric relation between the current applied to the electromagnet in Amperes and the corresponding magnetic field in kGauss is:

$$B = -0.04(1) + 1.79(3)\, I \tag{6.1}$$

This accurate calibration of the electromagnet is essential for the operation and characterisation of the thermomagnetic recording technique. The magnetic field present at the surface of the MO film is one of the main energy sources that act against the initial magnetisation the film.

The focal spot

To evaluate the capabilities of the writing apparatus described in the previous section and to define a base scale for analysing the magnetic patterns presented in section 6.4, it is necessary to estimate the size of the laser beam spot formed at the film surface. According to [94], the radius w of a Gaussian beam, also known as the spot size of the beam, is defined as the radial distance $r = \sqrt{x^2 + y^2}$ from the axis of the beam where the amplitude has decreased to a fraction $1/e$ of its value on the axis. In accordance

with this definition, the intensity of the beam at w has decreased to a ratio $1/e^2$ from its value on the axis. For a Gaussian beam propagating along the z direction, the spot size is such that

$$w^2(z) = w_0^2 \left(1 + \left(\frac{\lambda z}{\pi w_0^2}\right)^2\right) \tag{6.2}$$

In the focal plane of the beam, this radius is minimum and its value is called the *waist* of the beam, $w_0 \equiv w(z = 0)$. In order to analyse the profile of this beam when is focused by a lens of focal length f, we define the spot size at the lens w_s as the value of the $1/e$ radius w at the position of the lens,

$$w_s^2 \equiv w^2(-f) = w_0^2 \left(1 + \left(\frac{\lambda f}{\pi w_0^2}\right)^2\right)$$

This results in a fourth order equation in w_0

$$w_0^2(w_0^2 - w_s^2) = -\left(\frac{\lambda f}{\pi}\right)^2,$$

which has the following four solutions:

$$w_0^2 = \left(\frac{w_s^2}{2} \pm \frac{1}{2}\sqrt{w_s^4 - 4\left(\frac{\lambda f}{\pi}\right)^2}\right) \tag{6.3}$$

The 532 nm green light laser used in our experiment produces a spot with a $1/e^2$ radius of $w_s \sim 1.3$ mm at the lens. Then, for a focal length $f = 4.51$ mm, one of the solutions of equation (6.3) can be used to estimate that in the writing apparatus $w_0 \sim 0.584$ µm. Therefore, the $1/e^2$ beam diameter in the focal plane is 1.168 µm.

The *waist length* or *Rayleigh length* z_R of the beam is defined as the distance from the waist where the spot size has increased to $\sqrt{2}w_0$. This means that

$$w(z_R) \equiv \sqrt{2}\, w_0,$$

which yields

$$z_R = \frac{\pi\, w_0^2}{\lambda} \tag{6.4}$$

For the waist estimated before, the resultant Rayleigh length is $z_R = 2.016$ µm. Finally, the MO-film surface reflectiveness was measured to be around 54% at the working wavelength of 532 nm.

6.3.2 Writing magnetic patterns

In the thermo-magnetic writing device described above, the magnetisation reversal process depends on several factors. The external magnetic field applied in the direction opposite to that of the initial magnetisation of the sample is the primary energy source that works against the domain internal energies. Remember that these internal energies are responsible for the orientation of the magnetic moments and, consequently, for the creation of the magnetic domains. Consequently, the energy supplied by the external magnetic field has to balance these internal energies in order to reverse the direction of the magnetic moments and modify the domains.

The laser beam is used to locally decrease the coercivity of the film. Thermal agitation acts against the orienting effect of the exchange field energy. Hence, the laser beam intensity is also an important parameter that has to be taken into account during the process of thermo-magnetic writing. As a matter of fact, the laser intensity is so important that small displacements of the film surface from the focal plane of the beam are enough to prevent any writing on it.

Additionally, the temperature increase of a region of a film is a function of the time that the beam spends on it or near it. Due to the displacement of the film during the writing process, the time that a section of area of the film is illuminated by the laser depends on the velocity of the translation stage. Once that the beam has transmitted energy to the surface of the film and produced certain amount of heating, the energy diffuses through the crystal structure of the film.

6.4 Magnetic patterns

We have successfully written two different patterns on the surface of our Co/Pt films. Figure 6.6 shows a section of the first pattern, an array of parallel lines. The second pattern, shown in figure 6.8, is analogous to a wire Z-trap. A step-like pattern based on a $40 \times 40\ \mu m^2$ square is the elementary brick that builds up this periodic structure.

The images given in figures 6.6**(a)** and 6.8 **(b)** correspond to Magnetic Force Microscope (MFM) measurements of the magnetic patterns. The MFM is a powerful tool for analysing the small-scale features of a magnetised surface; it measures changes in the vibration of a magnetic tip induced by the gradient of the force that the magnetised surface exerts on it. This tip is magnetised and held by a cantilever that sustains the tip vibration near its resonance frequency. Simultaneously, the vibrating tip closely scans the surface of the film. Then, the tiny vibration of the tip is registered by a laser beam that is reflected on its upper surface. After this reflection, the beam reaches a photo-detector that measures the changes of the vibration of the tip. The resolution of this microscope allows us to detect sub-micron features. Consequently, this device is the main tool used in the analysis of the written patterns.

A set of 100 lines is particularly representative of my work. A reverse field of 500 G, a laser power of 74.7 mW and a translation speed of $0.25\ m \cdot s^{-1}$ were used to write these lines. This is equivalent to the magnetic mirror described in [29]. The MFM measurement of this pattern (figure 6.6**(a)**) shows that these lines are $\sim 1\ \mu m$ wide and are 2 μm away from each other. In addition, in this case each line was 200 μm long. To analyse the periodicity of this array, I have taken a single line of pixels perpendicular to the written lines, as indicated by the vertical red line included in the middle of the MFM image. The result of this is given in the graph **(b)** in figure 6.6. The nearly square steps demonstrate that each line is fully magnetised in a single direction and that, at the border of these lines, the magnetisation is reversed in a thin section of surface that is not wider than 200 nm. The Fourier transform of the plot given in figure 6.6**(b)** can be used to determine the period of the array of lines. This is shown in graph **(c)**, figure 6.6. The narrow peak clearly indicates that the period λ of this array is $\sim 2\ \mu m$

An additional feature of these lines can be seen in figure 6.6**(a)** and in more detail in figure 6.7**(a)**. The edges of the lines, which are the boundaries between regions of opposite magnetisation, are not straight. On the contrary, they oscillate along the line direction creating a jagged boundary between regions of opposite magnetisation. The inset shown in figure 6.6**(a)** is an MFM measurement of the unmagnetised MO film

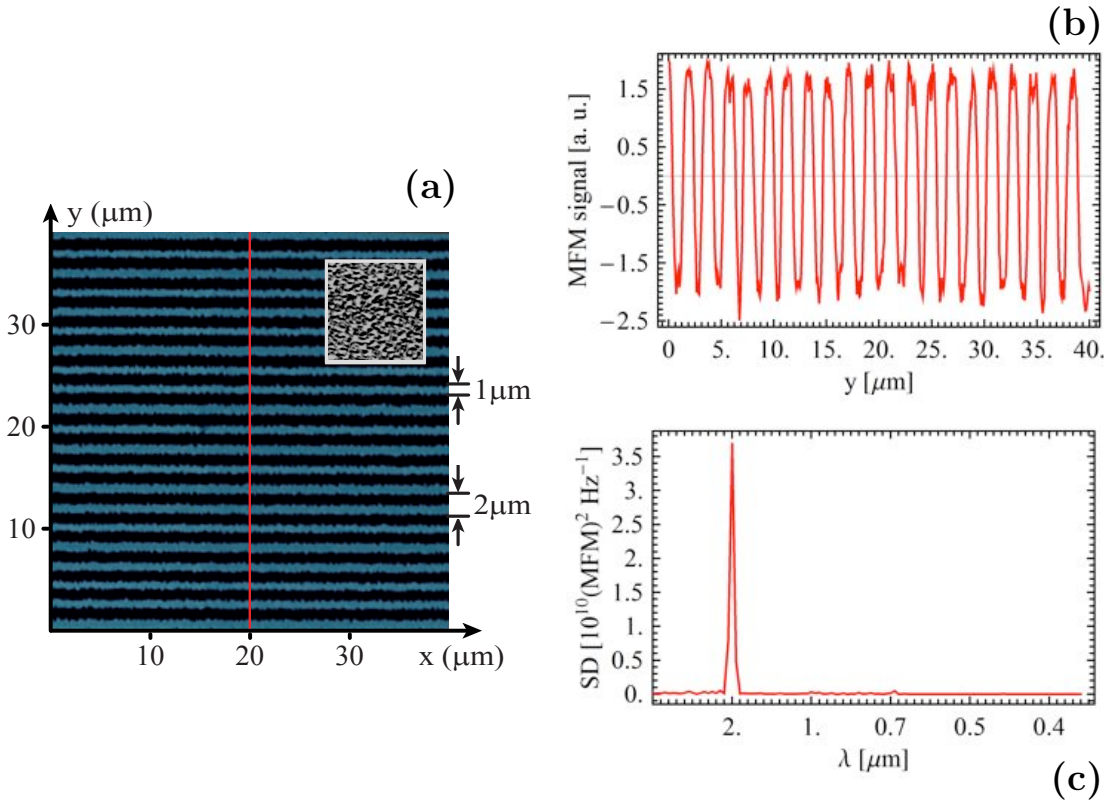

Figure 6.6: **(a)** Magnetic force microscope (MFM) measurement of an array of lines written at the Centre for Cold Matter. This array presents a spatial period of 2 μm and each line is ~ 1 μm wide. The oscillation along the edges of these lines is a consequence of the magnetic domains on the multilayer structure. The typical size of these magnetic domains can be appreciated in the inset, which corresponds to an MFM scan of an unmagnetised sample. **(b)** The plot of a single line of MFM signal values taken perpendicularly to the array of lines and indicated by the red solid line in the MFM image. The plot demonstrates that each line is fully magnetised and that at the edge of the line the magnetisation is fully reversed. **(c)** The spectral density (SD) of the list of MFM signal values given in **(b)** confirms that the period of the array is of 2 μm.

and demonstrates that the scale of the features observed along the edges of the lines is equivalent to the scale of the film domain structure. The features of the jaggedness along these edges can be seen more clearly in figure 6.7**(a)**, which is also an MFM scan of the magnetisation pattern. This measurement allows us to determine two important characteristics of these oscillations: their periodicity and their amplitude. For this purpose, the Fourier transforms of pixel lines running along the lines in the MFM image are calculated. This is shown in the five plots included in figure 6.7**(b)**, which correspond to the range of positions between the red dashed lines drawn on the MFM image. Similarly, the third plot corresponds to the Fourier transform of the pixel values along the red solid line. These series of plots show a strong short scale periodic component $\lambda_j \sim 400\,\text{nm}$ appearing in the Fourier transform when scanning through the lines edge. In addition, the amplitude of these oscillations results to be of the order of 200 nm, as indicated by the red dashed lines in figure 6.7**(a)**.

Figure 6.8**(a)** is an optical microscope image of the second pattern that we have written. We used the optical microscope to verify that the writing attempt was successful and to locate the position of the magnetisation patterns on the surface of the film. A rotation of the plane of polarisation is induced on linearly polarized light by reflection upon the surface of the magnetic film (SMOKE). This is a result of the magnetisation of the film layers [122, 123] and areas of opposite magnetisation produce opposite rotations of the plane of polarisation. Therefore, the optical microscope must include a pair of crossed polarisers. The first polariser defines the linear polarisation of the light that illuminates the sample. Then, changes in the magnetisation of the surface are detected by adjusting the polarisation direction of the second polariser to maximise their visibility. Although the shape of the written patterns can be distinguished by means of the optical microscope, its spatial resolution is not high enough to resolve the sub-micron features of the microtrap patterns. Nevertheless, we have used this tool to locate the position of the patterns on the surface of the film and remains a useful tool for seeing the long scale characteristics of these patterns.

The image given in figure 6.8**(a)** shows a set of Z-trap patterns written at our laboratory and figure 6.8**(b)** is an MFM measurement of the top left pattern. The brown areas are magnetised in one direction, while the lighter area is oppositely magnetised. A 10 μm long Z-trap segment has been written at the middle of the left side of a 40 μm by 40 μm square pattern. The trapping segment is 20 μm away from the top and bottom sides of the square, and 30 μm away from the right hand side of the square. The laser power applied for writing this pattern was 79 mW and the reverse field was 1 kG. Note that these values are higher than those used for writing the set of lines shown in figure 6.6. To create these patterns, areas of homogeneous reversed magnetisation have to be written. This represents the main challenge of writing this new pattern, and it was overcome by writing sets of lines so close of each other that their magnetisations are superimposed until they are indistinguishable.

6.5 Magnetostatic traps on MO films

In this section I show that the inhomogeneous magnetic field required for trapping neutral atoms can be mainly supplied by the magnetisation of a Co/Pt MO film. Auxiliary magnetic fields are used to mould the shape of the field present above the film surface. The magnetic field produced by the film, together with the auxiliary magnetic fields, should create local field minima where cold atom clouds prepared in a weak field seeking

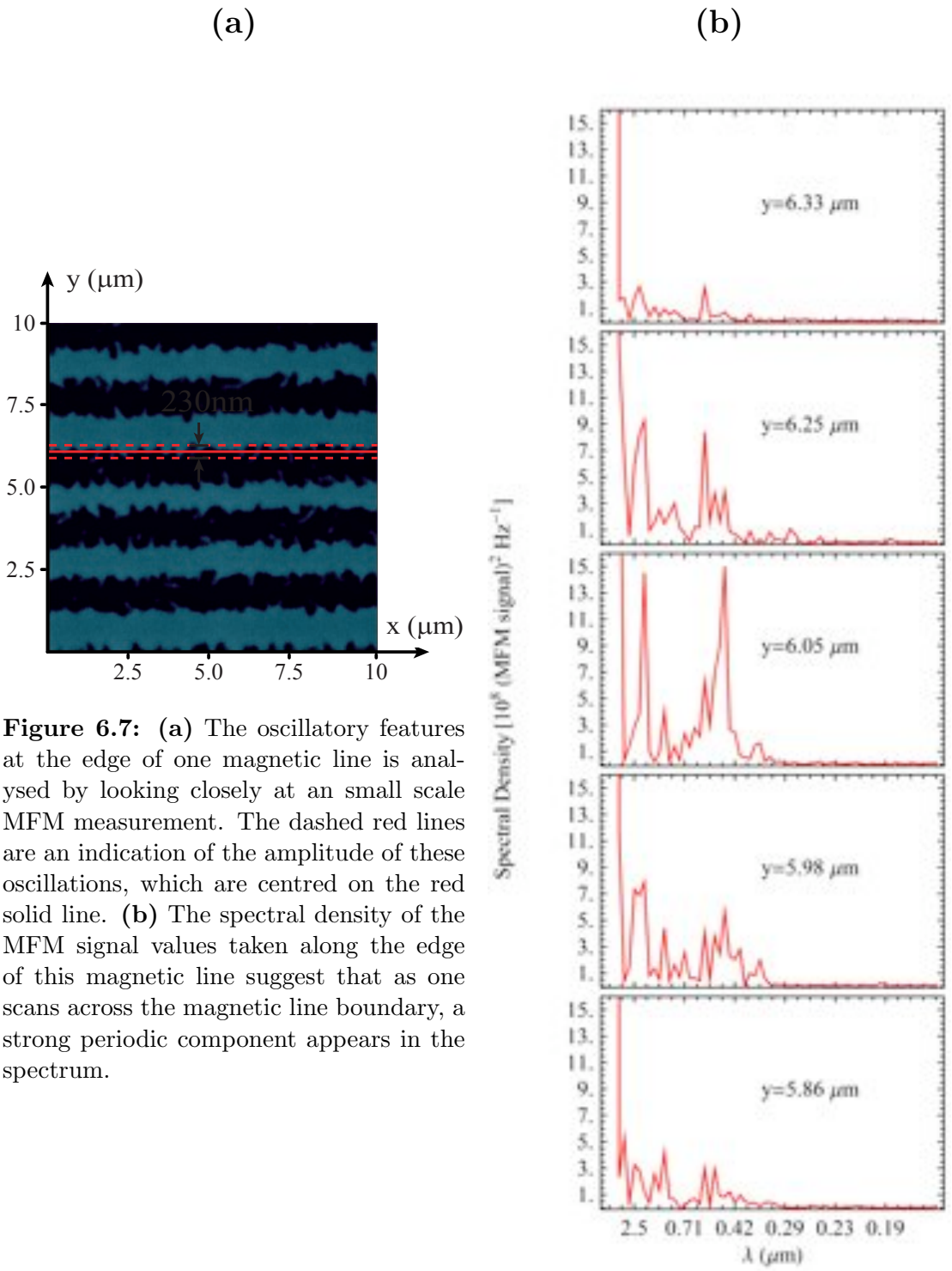

Figure 6.7: **(a)** The oscillatory features at the edge of one magnetic line is analysed by looking closely at an small scale MFM measurement. The dashed red lines are an indication of the amplitude of these oscillations, which are centred on the red solid line. **(b)** The spectral density of the MFM signal values taken along the edge of this magnetic line suggest that as one scans across the magnetic line boundary, a strong periodic component appears in the spectrum.

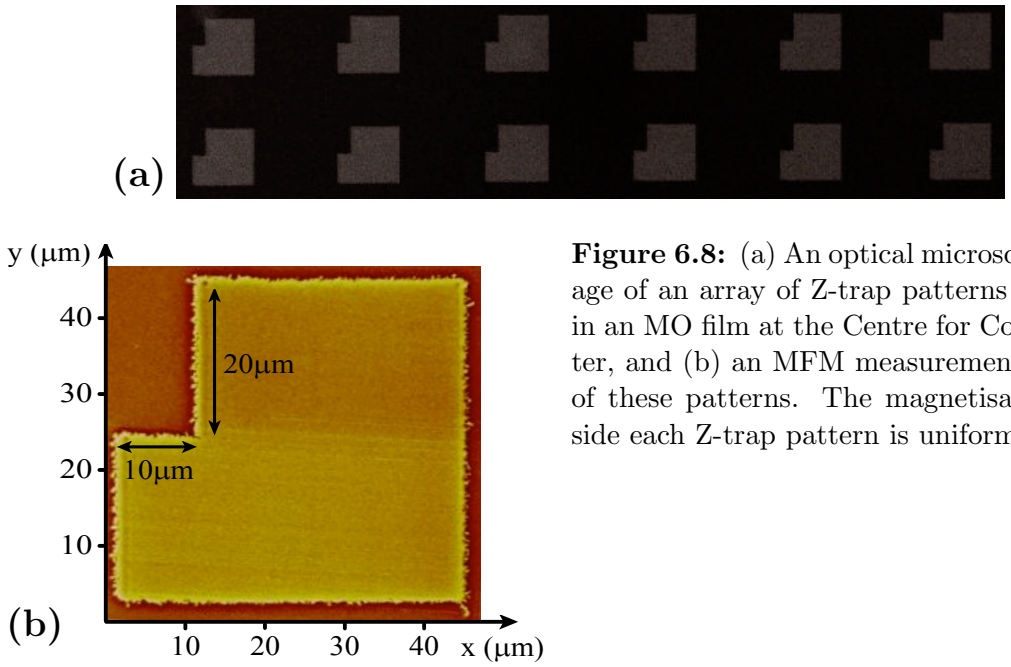

Figure 6.8: (a) An optical microscope image of an array of Z-trap patterns written in an MO film at the Centre for Cold Matter, and (b) an MFM measurement of one of these patterns. The magnetisation inside each Z-trap pattern is uniform.

state can be confined. The field magnitude at the centre of the trap has to be enough to lift the degeneracy between magnetic sublevels to avoid Majorana transitions. We will consider the potential depth, the trap frequency and the field magnitude at the bottom of the trap. We will also show that the roughness of the trap potential becomes significant when these traps are created close to the film surface.

Due to the squareness of the hysteresis loop that characterize the Pt/Co MO-films fabricated for our experiment, the saturation and remanent magnetisations are practically equal, $\mu_0 M_s = 2.3\,\mathrm{T}$. In addition, the thickness of the active layers of our Pt/Co MO-films is 6 nm. Hence, equation 2.46 can be used to establish a fictitious current of $I = 22\,\mathrm{mA}$ across boundary wires.

The array of lines

The anisotropy of the video tape, instead of being perpendicular as that of the Co/Pt MO films, defines an easy direction of magnetisation along the surface of the film. Nevertheless, a resource equivalent to the magnetic mirror presented in [29] can be created with an array of parallel lines written in an MO film.

In order to create trapping potentials with a set of parallel lines such as the one shown in figure 6.6, it is necessary to write longer lines without modifying the wavelength of the pattern. To model the characteristics of these traps, we have performed a numerical calculation of the magnetic field produced above the surface of an MO film patterned with a set of 2 mm long lines. These lines extend along the x-axis and, as in the set of lines shown in figure 6.6, the wavelength of the model pattern is 2 μm.

The results of our magnetic field estimations are summarised in the plots given in figure 6.9. The contour plots in this figure show three elongated traps located at the middle of the magnetic pattern. The first plot is a transversal cut of these traps and the second one is a longitudinal cut taken at the height at which these traps form. This

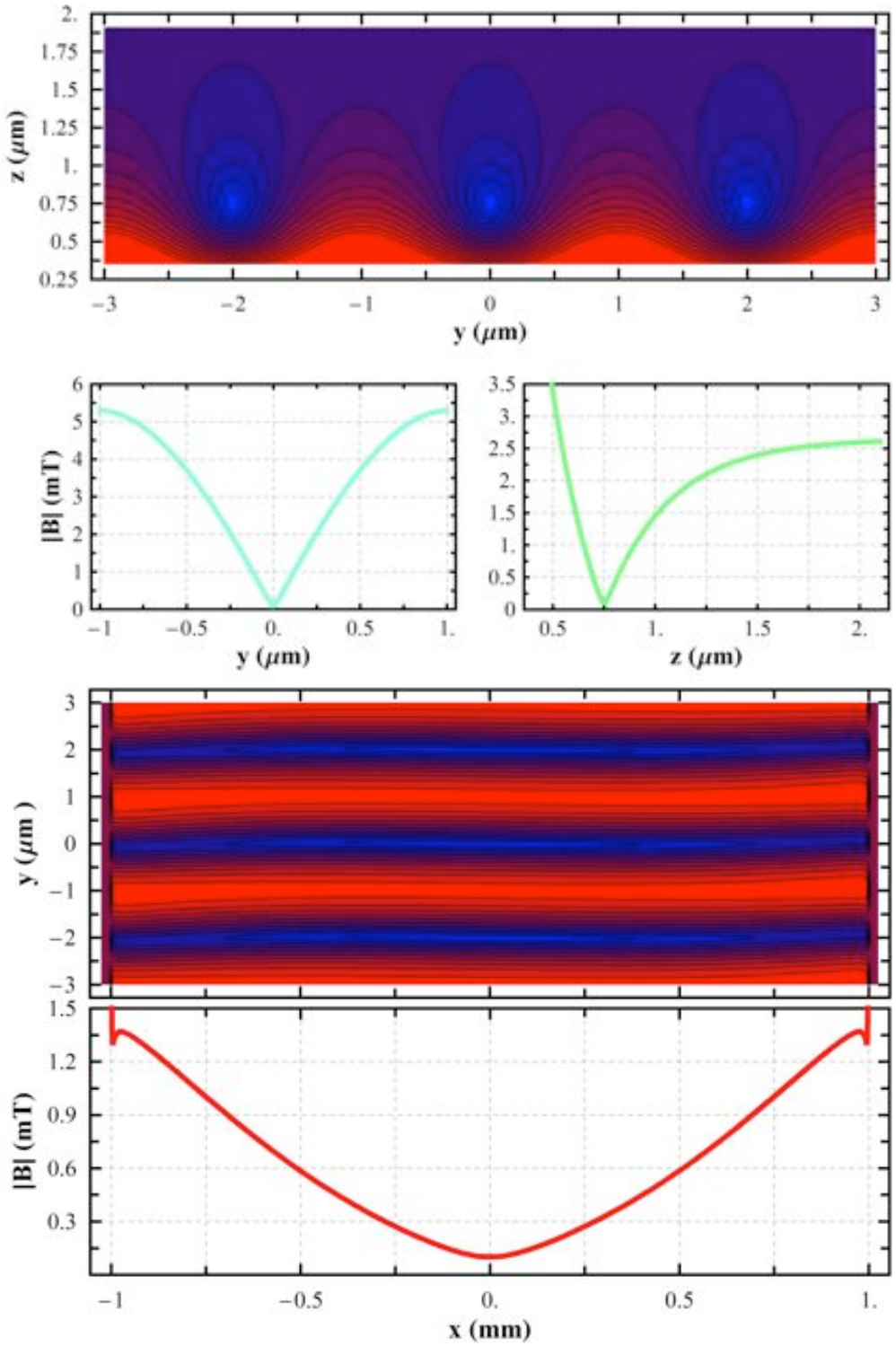

Figure 6.9: The trapping magnetic potential created above the surface of the MO film patterned with an array of lines. The high curvatures generated along the y and z directions, combined with the low residual field at the bottom these traps, results in high harmonic frequencies at the bottom of the elongated confining potentials.

calculation suggests that atom guides form at a height of $z = 0.75\,\text{mm}$ above an array of lines written in an MO film if a bias field $B_{bias} = -2.644\,\text{mT}$ perpendicular to the lines is applied. Two parallel wires have been included in the calculation to provide confinement along the x-axis. Each wire carries a current of 10 A along a direction perpendicular to the written lines. These wires are 2 mm away from each other and are located at a distance of $z = 750\,\mu\text{m}$ below the film surface. In addition, a small field 0.1 mT is included along the x direction to maintain the quantisation at the centre of the trap. The series of tube-like trapping potentials that run along the x direction present high curvatures along the y and z directions, as indicated by the blue and green curves shown in the figure. This together with the residual field at the centre of these traps, which is $B_0 = 0.1\,\text{mT}$, produce strong confining potentials. The harmonic frequencies around the minimum of these traps are higher than 1.1 MHz in the direction that is perpendicular to the surface (z) and in the direction perpendicular to the written lines (y). In the longitudinal direction of these elongated traps, which corresponds to the red curve given at the bottom of the figure, the harmonic frequency is found to be 122 Hz. The depth of these trapping potentials is given by the difference between the bias field and the residual field at the centre of these traps, which results to be $\sim 2.5\,\text{mT}$. Finally, these traps have a depth of 1.7 mK.

The Z-Trap

Figure 6.10 shows that, according to a calculation, a Ioffe-Pritchard trap is formed at a distance of $z = 0.75\,\mu\text{m}$ from the surface when a bias field $B_{bias} = 5.79\,\text{mT}\hat{y}$ is applied. The three contour plots given in this figure are cuts of the magnetic field that cross through the centre of the trap. The field magnitude at the centre of the trap is 0.12 mT. At long distances from the film surface, the field magnitude converges to the magnitude of the bias field, which in this case is 5.79 mT. Therefore, the depth of this trap is approximately 3.8 mK. The harmonic frequencies of this trap are calculated according to equations 2.43 and 2.45. In the radial direction, the trap frequency is found to be as high as $\omega_r = 0.9\,\text{MHz}$. This tightly confining potential can be appreciated in the red and green curves presented in the figure. In the axial direction, a much broader field profile, represented by the blue curve included in the figure, results in a much lower frequency $\omega_a = 19.3\,\text{kHz}$. In the Z-trap patterns, the jaggedness of the edges appears to be bigger than in the case of the array of lines. This is related to the longer periods of time that the laser spends heating the surface and the differences in the applied magnetic field and laser power during the writing period.

Roughness of trapping potentials

The MFM measurements provided in figures 6.6 and 6.8 show that the boundaries between regions magnetised in opposite directions are not straight lines as assumed in our field calculations. The structure on the boundaries between areas of opposite magnetisation is a consequence of the mechanisms by which the heat diffuses through the multilayer structure and of the strong internal energies that sustain the magnetic domains inside the film [129]. The inset included in the top right corner of figure 6.6 is an MFM measurement of a demagnetised sample. This demonstrates that even in its demagnetised state, the MO film is naturally divided in domains with magnetisations pointing in opposite directions. This inset has the same scale as the main picture. The jaggedness along the edges of the lines written in the MO film can therefore be compared

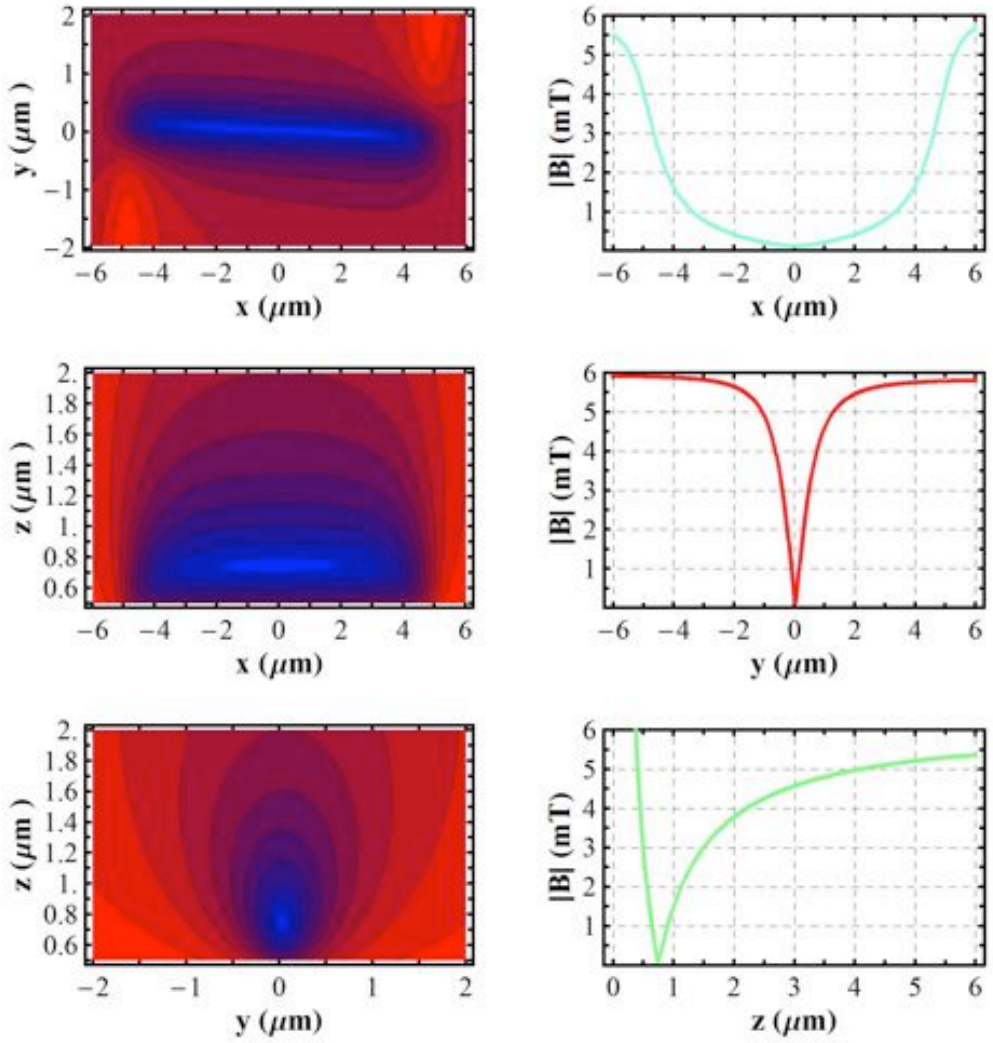

Figure 6.10: Plots and contour plots of the trapping field created above the surface of the MO film patterned with the equivalent of a Z-current.

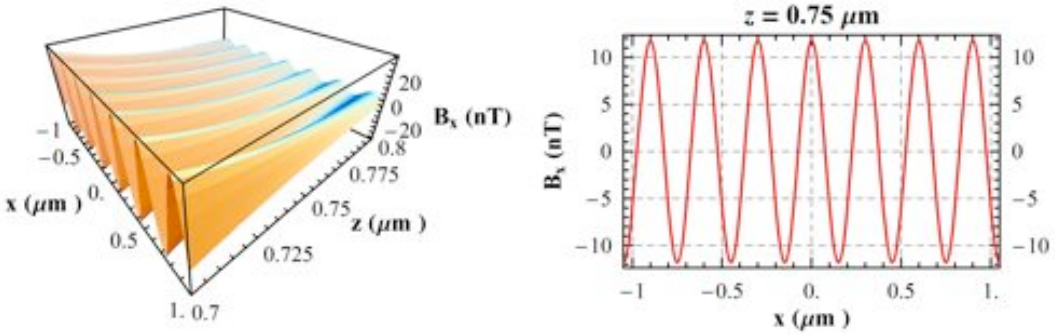

Figure 6.11: The anomalous magnetic field caused by the jaggedness at the border of regions of opposite magnetisation.

with the characteristic length scale of the domains in the unmagnetised sample. This comparison suggests that the quality of the magnetisation patterns created in the Co/Pt MO films is limited by the size of the magnetic domains formed in the material.

As a result of the boundary jaggedness, the fictitious currents oscillate in the plane of the film. As we reported in [76] (see Appendix E), the analysis of our MFM measurements has allowed us to estimate that the typical amplitude of these oscillations is $a_j = 125\,\text{nm}$ and the typical wavelength is $\lambda_j = 300\,\text{nm}$. Previous work in our group has demonstrated that the anomalous field generated in the vicinity of a current carrying wire can be represented with a periodic function multiplied by the modified Bessel function [58]. An example of such anomalous field is shown in figure 6.11. The oscillation of the fictitious currents in the MO films is analogous to the anomalous current generated by a wire. In consequence, we have proposed that at a height $z \gg a_j$ above the boundary of two regions with opposite magnetisations the main field component is given by

$$B_y \simeq \mu_0 I / 2\pi z$$

Meanwhile, the transverse oscillations along the edges of the magnetic patterns produce a field which here we approximated by an oscillating field along the wire

$$B_x \simeq \frac{\mu_0 I}{2\pi} k^2 a K_1(kz)\cos(kx)$$

where $k = 2\pi/\lambda_j$ and K_1 is the modified Bessel function.

As demonstrated in figure 6.11, the magnetic field generated by this idealised anomalous oscillation of the pattern boundaries has an amplitude at the trapping height $z = 0.75\,\mu\text{m}$ of 24 nT. This corresponds to corrugations in the trapping potential with a characteristic depth of 16 nK. To get an idea of what this means in terms of the latest advances on cold atoms research, let us compare this depth with the chemical potential μ of a BEC. According to Ketterle *et al.* [24],

$$\mu = \frac{4\pi n a \hbar^2}{m} \tag{6.5}$$

where n is the condensate density; a is the s-wave scattering length; and m is the mass of the atom. For a ^{87}Rb condensate, n is typically 10^{14} atoms/cm^3, and $a \simeq 100 a_0$, with $a_0 = 0.529\,\text{Å}$. This leads us to a chemical potential of $\mu/k_B \simeq 37\,\text{nK}$. Although this value is higher than the potential depth estimated for the corrugations in the trapping potential, these values are of the same order of magnitude and is reasonable to believe that a Bose-Einstein condensate confined in these traps would exhibit fragmentation at such short distances from the film surface.

6.6 Pyramids and MO films

The Co-Pt multilayer thin films can also be combined with the micro-pyramids presented in the previous chapter; the multilayer film in this case would be used as the primary source of magnetic field for generating the magneto-optic traps. A new procedure for selectively etching small areas of a Co-Pt multilayer thin film, without substantially modifying its magnetic properties, has been demonstrated. The Co-Pt multilayer structure of these Magneto-Optic (MO) films was deposited on a silicon under layer. The etching process used to make apertures in the MO film leaves this under layer unaffected. Hence, a further process of chemical etching can be applied to these substrates

in order to create micrometric pyramids on the silicon under layer. Finally, a thin reflective coating can be deposited on top of the array of pyramids and the remaining MO film.

Due to the perpendicular magnetisation of the Co-Pt multilayer structure, the magnetic field created at an aperture made on them can be thought as that produced by a single closed loop. The corresponding magnetic field circulates around the fictitious current loop and right at the surface it is always perpendicular to the film. Consequently, an external magnetic field can be applied in order to create and move a point of zero magnetic field strength along the axis of each aperture. In addition, due to the small scale of these features and the strong remanent magnetization of the MO film, high gradients can be produced in the region of the hollow pyramid. Therefore, it is justified to believe that magneto-optic traps can be created with these resources.

Let us consider a saturation magnetisation $\mu_0 M_S = 2.3\,\mathrm{T/m}$ and a cobalt total thickness $t = 6\,\mathrm{nm}$ (see figures 6.3 and 6.1 in pages 128 and 125 respectively). Then, with the aid of equation 2.46 (page 40) we estimate that the fictitious current running through the edge of a square aperture made on the MO film is 11 mA. If we now substitute this value in equation 2.46, we find that to obtain a gradient of 20 G/cm we need to create a square opening and a silicon pyramid with a side length of approximately 300 μm. This length scale is well within the fabrication capabilities of the techniques described at the beginning of chapter 5.

6.7 Summary

Here I have shown that the remanent field generated by the Co/Pt MO films is as high as 2.3 T. This is ten times higher than the one that is present above the video tape atom chip used in the work reported by Sinclair *et al.* [68, 67]. In addition, I have shown that the periodic patterns written on the surface of the MO films have features of just a couple of micrometres. Compared to the patterns that have been utilised in the video tape experiments, which have a period of approximately 100 μm, the Co/Pt films represent an important improvement in the development of atom chips based on permanently magnetised media. This is reflected in the numerical calculations of the micro traps that have been presented in this chapter and reported in [76] (see appendix E), where the resulting trapping frequencies have been estimated to be as high as one megahertz in the radial direction and several hundred kilohertz in the longitudinal direction.

As a result of the domain structure of the Co/Pt films, on the edges of the written patterns we have observed features with a length scale on the order of hundreds of nanometres. We have estimated that these features would produce corrugations in the trapping field. For an atom cloud located at distance of 750 nm from the surface of the film, we calculated that these corrugations would have a characteristic depth of 16 nK. These kind of corrugations have also been observed in the video tape micro traps, but in this case these appeared as far as 50 μm away from the chip surface and had potential depths of up to 1 μK.

This work has demonstrated the potential that MO films have for creating cold atom micro traps. In spite of this, an atom chip based on this technology has not yet been fabricated and loaded into a cold atom experiment. Our numerical estimations allowed us to predict the details of the interaction between a cold atom cloud and the field generated above the Co/Pt MO films. These results are sufficient for establishing the adequacy of this technology. In conclusion, Co/Pt magneto-optical thin films

are presented in this chapter as a powerful tool that can be incorporated into future generations of atom chips. For instance, we have proposed that an atom chip combining micro-fabricated optical components, such as hollow pyramidal mirrors, and a permanently magnetised medium like the Co-Pt magneto-optic film can be fabricated.

Chapter 7

Conclusions

We have built an experimental apparatus for testing new generations of atom chips. This apparatus consists of a vacuum system, three laser light sources, magnetic field sources, and an imaging system. The vacuum chamber is characterised by a large internal volume and wide optical axis. Sets of coils for the generation of the magnetic fields required for creating magneto-optic traps in macroscopic hollow pyramidal mirrors have been designed, built, and incorporated to the experimental apparatus. In addition, coils for balancing stray fields and for manipulating the position of the MOT were also included in the experimental apparatus.

Three external cavity diode lasers were incorporated to the experimental apparatus. The optics and electronic devices required for locking these lasers, as well as for preparing and delivering the laser beams to the main experimental chamber were also built. Locking signals for the three lasers are derived from Doppler free polarization spectrums and a dichroic-atomic-vapor laser lock (DAVLL). The first scheme provides an stable frequency reference for determining the detuning of the trapping light. The two DAVLL locks provide in addition the means for tuning the trapping and repump light.

We have demonstrated that in spite of the angle difference between a 90° pyramid and the 70.5° of chemically etched pyramids on silicon wafers, the latter are still capable of generating magneto-optical traps. For this we fabricated on glass two pyramidal hollow mirrors, the first with an angle of 70.5° between its opposing faces and the second one with an angle of 90°. The side length of these two pyramids is approximately 16 mm. To identify possible causes of imbalance in the MOT forces as a result of the pyramidal geometry generated in silicon, the optical properties of the these pyramids were carefully studied, both numerically and experimentally. We found that the pyramid surface sections located next to the edges of the pyramid faces are responsible for the generation of light rays with the wrong polarisation. After going through three reflections, these light component cross through the pyramid axis creating a force imbalance that is sufficient for destroying the trap.

In view of these results, we have identified methods for reducing and eliminating the undesired effect of these light sections. First, as this light suffers one more reflection

from the pyramid faces than the rest of the light components contributing to the trap, we proposed to use a limited reflectivity coating in the pyramid faces. This way, we found that an aluminium based coating characterised by a reflectivity of 78% takes care efficiently of the imbalance generated by these parasitic light components. We demostrated that as many as 10^7 rubidium atoms can be trapped in our 70.5° glass pyramid coated in aluminium. We compared the MOTs generated in this pyramid with the one formed in the 90° pyramid, both of comparable sizes and both coated with aluminium, and found no appreciable differences in the MOTs generated in these two pyramids. A summary of these results and a complete optical characterisation of the 70.5° pyramidal geometry has been published in [72] and this paper is included in appendix C.

We have also shown that the undesired reflections generated in a 70.5° pyramid can be eliminated if the surface of the pyramid is appropriately masked during the deposition of the reflective coating. The regions where the undesired reflections originate, which were identified by means of a ray tracing analysis, can be covered with these masks. This method gives satisfactory results when a high reflectivity gold coating ($\rho \sim 95\,\%$) is deposited in the regions not covered by the masks.

We measured scaling laws for the parameters that determine the MOT dynamics in 70.5° pyramids. We found that the number of atoms that can be trapped on pyramids of different sizes is mainly determined by the MOT capture rate. As anticipated in section 2.4.1, the change of the capture parameter with the pyramid dimensions can be described by means of a power law. To begin with, a measurement of the capture rate far from the pyramid apex allowed us to corroborate the validity of this power law. Based on this measurement, we suggested that the perpendicular distance from the MOT centre to the pyramid surface is the defining distance on the operation of these MOTs. Next, the experiments performed in the vicinity of the pyramid apex also resulted in a power law dependence of the capture rate on the distance to the pyramid apex. In this case we found that the capture rate divided by the rubidium vapour density, which we denoted as α, is proportional to $h^{3.5(3)}$, h being the distance between the cold atom cloud and the apex of the pyramid. Also, our experiments have shown that the loss rate parameter is practically insensitive to the size of the pyramid as long as the trap to surface distance is $> 600\,\mu$m. Below this limit, we found that the increase in the loss rate can be appropriately described by considering that the cloud remains in the temperature limited regime and that atoms colliding with the room temperature pyramid surface are irremediably lost from the trap. Based on these scaling law measurements, we concluded that on the order of 10^4 atoms can be trapped in pyramids with a 1.2 mm side length, and some tens of atoms can be trapped in 200 μm side length pyramids.

In this thesis I have presented an atom chip that integrates pyramidal micro-mirrors and sources of magnetic field. Standard silicon micro-fabrication techniques have been used to create an array of pyramidal pits, which coated with the appropriate metallic material, can create high quality optical components on the chip surface. I have given a complete characterisation of the resulting micro-mirrors, including their most relevant physical and optical properties. These micro-fabricated optical components have been combined with surface mounted wires to create a hybrid new device. In this chip, square current currying wire loops run around the pyramid apertures. Then, the magnetic field generated by these loops can be complemented with an homogeneous magnetic bias field perpendicular to the chip surface. With the right choice of current and bias field

magnitude, spherical quadrupole potentials are created inside the atom chip pyramids. Both the reflective coating and the wires are made of gold. Hence, the masked coating of the pyramid faces that was tested in the glass 70.5° was recreated in the atom chip fabrication.

I have described how the pyramid atom chip was mounted and bond wired in a CPGA chip mount. Extensive thermal, electric, magnetic and vacuum compatibility characterisations of the full chip arrangement have been carried out. Vacuum tests and magnetic field estimations and measurements have been performed with the aim of establishing the conditions under which the chip mount elements can be used. We have demonstrated that pressures below 10^{-9} mbar can be achieved in a vacuum system in which a set composed by a ceramic pin grid array (CPGA), a sockets array and a printed circuit board has been loaded. Also, it has been verified under which circumstances the stray magnetic field generated above the chip carrier is low enough to allow the creation of the micro-MOTs. In particular, we found that in order to keep the stray magnetic field generated in the chip attachment area of the CPGA at an acceptable level, it is necessary to remove the nickel layer present in this area. A paper that describes the pyramid atom chip fabrication procedure and the characterisation of the full packaging solution has been recently accepted for publication in the Journal of Microelectromechanical Systems. This paper (see reference [109]) has been included in appendix D.

Co/Pt magneto optic thin films have been fabricated with the aim of determining how suitable is this media for creating a permanently magnetised atom chip. I have shown that these films are characterised by a large perpendicular anisotropy, a high remanent magnetisation, a large room temperature coercivity, and the squareness ratio of its hysteresis loop is close to one. Then, a thermo-magnetic writing apparatus was built and magnetic patterns for creating local field minima were successfully created on the surface of these films. We have demonstrated that atomic micro-traps based on these magnetic patterns can be produced. The large remanent magnetisation of these films, given by $\mu_0 M_s = 2.3\,\mathrm{T}$, combined with micron-sized features, permit trap frequencies of up to 1.1 MHz. In addition, the high room-temperature coercivity of these films not only allows the creation of well defined micron sized magnetic patterns, but also assures that the patterns will remain intact even under the influence of an external magnetic field. This represents an important improvement with respect to the performance of the video tape atom chip.

Two magnetic patterns have been written in the Co/Pt MO films. An array of lines can be used to create a series of elongated atom traps above the chip surface. The second pattern consists of an array of Z-traps, which can be used to create cigar shaped traps above the film surface. These patterns were carefully analysed via optical and magnetic force microscopy. These patterns consist of well defined and uniformly magnetised areas in which the direction of the magnetisation vector was reversed. The borders between regions magnetised in opposite directions present jaggedness, which we have shown to be a result of the film domain structure. As a consequence of this, the trapping potentials generated above these films would have a corrugated structure. We have estimated that this corrugation would produce 16 nK deep wells at the bottom of a trapping potential located 0.75 μm above the film surface. Although lower than the self interaction energy of atoms in a BEC ($\sim 40\,\mathrm{nK}$), this potential wells could generate fragmentation of the atom cloud. The results presented in this thesis allowed us to estimate the performance of the Co/Pt in atom optics applications so accurately that we decided not to attempt

loading an atom chip made exclusively of this magnetic material into a cold atoms experiment. However, these MO films remain as a an extremely versatile and powerful tool for more complicated atom optics devices. Further optimisation of these MO films would require a reduction of the length scale of their domain structure with maintaining both the strong remanent magnetisation, and the large coercivity that characterise these magnetic films. The most important results of this investigation were published in [76]. This paper is included in appendix E.

This thesis concludes with the fabrication of the first pyramid atom chip and its incorporation into the experimental apparatus. Naturally, the steps that follow in this research project include testing the functioning of this atom chip and determining its optimal operation parameters. Therefore, the creation of magneto optical traps on the surface of this atom chip is being currently investigated at the Centre for Cold Matter. At the time of writing this thesis, no atoms have been observed in the atom chip pyramids. The causes for this are been investigated in order to optimise loading and imaging systems, and even the micro fabrication process. Once that MOTs have been produced in the atom chip pyramids, it will be necessary to determine the currents required for optimal operation of each one of the various pyramid side lengths included in this atom chip. This information results particularly interesting because it will determine the possibility of integrating both micro-fabricated pyramids and magneto-optic thin films in a future atom chip. An additional feature of these micro-MOTs that would need to be properly characterised is their sensitivity to magnetic fields. It has been proposed that a highly sensitive magnetometer can be fabricated utilising these micro-fabricated pyramid MOTs. We have shown that the cold atom clouds magneto-optically collected in these pyramids could then be held by a purely magnetic trap. Consequently, a further goal of this research would be to magnetically trap these atom clouds and extract them from the pyramids internal volume. These clouds would then be held by a mirror image of the magnetic quadrupole potential generated inside the pyramids.

Bibliography

[1] William D. Phillips. Nobel lecture: Laser cooling and trapping of neutral atoms. *Reviews of Modern Physics*, 70(3):721–741, 1998.

[2] Steven Chu. Nobel lecture: The manipulation of neutral particles. *Reviews of Modern Physics*, 70(3):685, 1998.

[3] Claude N. Cohen-Tannoudji. Nobel lecture: Manipulating atoms with photons. *Rev. Mod. Phys.*, 70(3):707–719, Jul 1998.

[4] S. Chu, L. Hollberg, J. E. Bjorkholm, A. Cable, and A. Ashkin. 3-dimensional viscous confinement and cooling of atoms by resonance radiation pressure. *Physical Review Letters*, 55(1):48–51, 1985.

[5] P. D. Lett, W. D. Phillips, S. L. Rolston, C. E. Tanner, R. N. Watts, and C. I. Westbrook. Optical molasses. *Journal of the Optical Society of America B-Optical Physics*, 6(11):2084–2107, 1989.

[6] D. J. Wineland and W. M. Itano. Laser cooling of atoms. *Physical Review A*, 20(4):1521–1540, 1979.

[7] J. Dalibard and C. Cohen-Tannoudji. Laser cooling below the Doppler limit by polarization gradients - simple theoretical-models. *Journal of the Optical Society of America B-Optical Physics*, 6(11):2023–2045, 1989.

[8] Paul D. Lett, Richard N. Watts, Christoph I. Westbrook, William D. Phillips, Phillip L. Gould, and Harold J. Metcalf. Observation of atoms laser cooled below the Doppler limit. *Phys. Rev. Lett.*, 61(2):169–172, 1988.

[9] D. S. Weiss, E. Riis, Y. Shevy, P. J. Ungar, and S. Chu. Optical molasses and multilevel atoms - experiment. *Journal of the Optical Society of America B-Optical Physics*, 6(11):2072–2083, 1989.

[10] E. L. Raab, M. Prentiss, A. Cable, S. Chu, and D. E. Pritchard. Trapping of neutral sodium atoms with radiation pressure. *Physical Review Letters*, 59(23):2631–2634, 1987.

[11] C. Monroe, W. Swann, H. Robinson, and C. Wieman. Very cold trapped atoms in a vapor cell. *Physical Review Letters*, 65(13):1571–1574, 1990.

[12] A. E. Cable, M. Prentiss, and N. P. Bigelow. Observations of sodium atoms in a magnetic molasses trap loaded by a continuous uncooled source. *Opt. Lett.*, 15(9):507, 1990.

[13] K. E. Gibble, S. Kasapi, and S. Chu. Improved magnetooptic trapping in a vapor cell. *Optics Letters*, 17(7):526–528, 1992.

[14] Alan L. Migdall, John V. Prodan, William D. Phillips, Thomas H. Bergeman, and Harold J. Metcalf. First observation of magnetically trapped neutral atoms. *Phys. Rev. Lett.*, 54(24):2596–2599, 1985.

[15] Wolfgang Paul. Electromagnetic traps for charged and neutral particles. *Reviews of Modern Physics*, 62(3):531–540, 1990.

[16] T. Bergeman, G. Erez, and H. J. Metcalf. Magnetostatic trapping fields for neutral atoms. *Physical Review A*, 35(4):1535–1546, 1987.

[17] H. Metcalf. Magneto-optical trapping and its application to helium metastables. *Journal of the Optical Society of America B-Optical Physics*, 6(11):2206–2210, 1989.

[18] M. H. Anderson, J. R. Ensher, M. R. Matthews, C. E. Wieman, and E. A. Cornell. Observation of Bose-Einstein condensation in a dilute atomic vapor. *Science*, 269(5221):198–201, 1995.

[19] C. C. Bradley, C. A. Sackett, J. J. Tollett, and R. G. Hulet. Evidence of Bose-Einstein condensation in an atomic gas with attractive interactions. *Phys. Rev. Lett.*, 75(9):1687–1690, 1995.

[20] K. B. Davis, M. O. Mewes, M. R. Andrews, N. J. van Druten, D. S. Durfee, D. M. Kurn, and W. Ketterle. Bose-Einstein condensation in a gas of sodium atoms. *Phys. Rev. Lett.*, 75(22):3969–3973, 1995.

[21] E. A. Cornell and C. E. Wieman. Nobel Lecture: Bose-Einstein condensation in a dilute gas, the first 70 years and some recent experiments. *Rev. Mod. Phys.*, 74(3):875–893, 2002.

[22] Wolfgang Ketterle. Nobel lecture: When atoms behave as waves: Bose-einstein condensation and the atom laser. *Rev. Mod. Phys.*, 74(4):1131–1151, 2002.

[23] Eric A. Cornell, Jason R. Ensher, and Carl E. Wieman. Experiments in Dilute Atomic Bose-Einstein Condensation. *arXiv:cond-mat/9903109v1*, 1999.

[24] W. Ketterle, D.S. Durfee, , and D.M. Stamper-Kurn. Making, probing and understanding Bose-Einstein condensates. *arXiv:cond-mat/9904034v2*, 1999.

[25] D. W. Sesko and C. E. Wieman. Observation of the cesium clock transition in laser-cooled atoms. *Optics Letters*, 14(5):269–271, 1989.

[26] C. Monroe, H. Robinson, and C. Wieman. Observation of the cesium clock transition using laser-cooled atoms in a vapor cell. *Optics Letters*, 16(1):50–52, 1991.

[27] C. Monroe. Quantum information processing with atoms and photons. *Nature*, 416:238–246, 2002.

[28] D. Muller, D. Z. Anderson, R. J. Grow, P. D. D. Schwindt, and E. A. Cornell. Guiding neutral atoms around curves with lithographically patterned current-carrying wires. *Physical Review Letters*, 83(25):5194–5197, 1999.

[29] E. A. Hinds and I. G. Hughes. Magnetic atom optics: mirrors, guides, traps, and chips for atoms. *Journal of Physics D-Applied Physics*, 32(18):R119–R146, 1999.

[30] R. Folman, P. Kruger, D. Cassettari, B. Hessmo, T. Maier, and J. Schmiedmayer. Controlling cold atoms using nanofabricated surfaces: Atom chips. *Physical Review Letters*, 84(20):4749–4752, 2000.

[31] D. Cassettari, A. Chenet, R. Folman, A. Haase, B. Hessmo, P. Kruger, T. Maier, S. Schneider, T. Calarco, and J. Schmiedmayer. Micromanipulation of neutral atoms with nanofabricated structures. *Applied Physics B-Lasers and Optics*, 70(5):721–730, 2000.

[32] J. Fortagh, H. Ott, A. Grossmann, and C. Zimmermann. Miniaturized magnetic guide for neutral atoms. *Applied Physics B-Lasers and Optics*, 70(5):701–708, 2000.

[33] J. Reichel, W. Hansel, P. Hommelhoff, and T. W. Hänsch. Applications of integrated magnetic microtraps. *Applied Physics B-Lasers and Optics*, 72(1):81–89, 2001.

[34] J. D. Weinstein and K. G. Libbrecht. Microscopic magnetic traps for neutral atoms. *Phys. Rev. A*, 52(5):4004–4009, 1995.

[35] S. Eriksson, M. Trupke, H. F. Powell, D. Sahagun, C. D. J. Sinclair, E. A. Curtis, B. E. Sauer, E. A. Hinds, Z. Moktadir, C. O. Gollasch, and M. Kraft. Integrated optical components on atom chips. *European Physical Journal D*, 35(1):135–139, 2005.

[36] G. Birkl, F. B. J. Buchkremer, R. Dumke, and W. Ertmer. Atom optics with microfabricated optical elements. *Optics Communications*, 191(1-2):67–81, 2001.

[37] N. H. Dekker, C. S. Lee, V. Lorent, J. H. Thywissen, S. P. Smith, M. Drndic, R. M. Westervelt, and M. Prentiss. Guiding neutral atoms on a chip. *Physical Review Letters*, 84(6):1124–1127, 2000.

[38] D. Cassettari, B. Hessmo, R. Folman, T. Maier, and J. Schmiedmayer. Beam splitter for guided atoms. *Physical Review Letters*, 85(26):5483–5487, 2000.

[39] A. E. Leanhardt, A. P. Chikkatur, D. Kielpinski, Y. Shin, T. L. Gustavson, W. Ketterle, and D. E. Pritchard. Propagation of Bose-Einstein condensates in a magnetic waveguide. *Physical Review Letters*, 89(4):040401, 2002.

[40] E. A. Hinds, C. J. Vale, and M. G. Boshier. Two-wire waveguide and interferometer for cold atoms. *Physical Review Letters*, 86(8):1462–1465, 2001.

[41] H. Ott, J. Fortagh, G. Schlotterbeck, A. Grossmann, and C. Zimmermann. Bose-Einstein condensation in a surface microtrap. *Physical Review Letters*, 87(23):230401, 2001.

[42] J. Reichel. Microchip traps and BoseEinstein condensation. *Applied Physics B: Lasers and Optics*, 75:469–487, 2002.

[43] W. Hansel, P. Hommelhoff, T. W. Hänsch, and J. Reichel. Bose-Einstein condensation on a microelectronic chip. *Nature*, 413(6855):498–501, 2001.

[44] S. Schneider, A. Kasper, Ch. vom Hagen, M. Bartenstein, B. Engeser, T. Schumm, I. Bar-Joseph, R. Folman, L. Feenstra, and J. Schmiedmayer. Bose-Einstein condensation in a simple microtrap. *Phys. Rev. A*, 67(2):023612, 2003.

[45] A. Kasper, S. Schneider, C. vom Hagen, M. Bartenstein, B. Engeser, T. Schumm, I. Bar-Joseph, R. Folman, L. Feenstra, and J. Schmiedmayer. A Bose-Einstein condensate in a microtrap. *Journal of Optics B-Quantum and Semiclassical Optics*, 5(2):S143–S149, 2003.

[46] H. Ott, J. Fortagh, S. Kraft, A. Gunther, D. Komma, and C. Zimmermann. Nonlinear dynamics of a Bose-Einstein condensate in a magnetic waveguide. *Physical Review Letters*, 91(4):040402, 2003.

[47] H. Ott, J. Fortagh, and C. Zimmermann. Dynamics of a Bose-Einstein condensate in an anharmonic trap. *Journal of Physics B-Atomic Molecular and Optical Physics*, 36(13):2817–2822, 2003.

[48] J. Fortagh, H. Ott, S. Kraft, A. Gunther, and C. Zimmermann. Bose-Einstein condensates in magnetic waveguides. *Applied Physics B-Lasers and Optics*, 76(2):157–163, 2003.

[49] R. Long, T. Steinmetz, P. Hommelhoff, W. Hansel, T. W. Hänsch, and J. Reichel. Magnetic microchip traps and single-atom detection. *Philosophical Transactions of the Royal Society of London Series a-Mathematical Physical and Engineering Sciences*, 361(1808):1375–1389, 2003.

[50] R. Long, T. Rom, W. Hansel, T. W. Hänsch, and J. Reichel. Long distance magnetic conveyor for precise positioning of ultracold atoms. *European Physical Journal D*, 35(1):125–133, 2005.

[51] Philipp Treutlein, Peter Hommelhoff, Tilo Steinmetz, Theodor W. Hänsch, and Jakob Reichel. Coherence in microchip traps. *Physical Review Letters*, 92(20):203005, 2004.

[52] C. Henkel, S. Potting, and M. Wilkens. Loss and heating of particles in small and noisy traps. *Applied Physics B-Lasers and Optics*, 69(5-6):379–387, 1999.

[53] C. Henkel and S. Potting. Coherent transport of matter waves. *Applied Physics B-Lasers and Optics*, 72(1):73–80, 2001.

[54] M. P. A. Jones, C. J. Vale, D. Sahagun, B. V. Hall, and E. A. Hinds. Spin coupling between cold atoms and the thermal fluctuations of a metal surface. *Physical Review Letters*, 91(8):080401, 2003.

[55] C. Henkel, P. Kruger, R. Folman, and J. Schmiedmayer. Fundamental limits for coherent manipulation on atom chips. *Applied Physics B-Lasers and Optics*, 76(2):173–182, 2003.

[56] J. Fortagh, H. Ott, S. Kraft, A. Gunther, and C. Zimmermann. Surface effects in magnetic microtraps. *Physical Review A*, 66(4):041604, 2002.

[57] S. Kraft, A. Gunther, H. Ott, D. Wharam, C. Zimmermann, and J. Fortagh. Anomalous longitudinal magnetic field near the surface of copper conductors.

Journal of Physics B-Atomic Molecular and Optical Physics, 35(21):L469–L474, 2002.

[58] M. P. A. Jones, C. J. Vale, D. Sahagun, B. V. Hall, C. C. Eberlein, B. E. Sauer, K. Furusawa, D. Richardson, and E. A. Hinds. Cold atoms probe the magnetic field near a wire. *Journal of Physics B-Atomic Molecular and Optical Physics*, 37(2):L15–L20, 2004.

[59] R. Folman, P. Kruger, J. Schmiedmayer, J. Denschlag, and C. Henkel. Microscopic atom optics: From wires to an atom chip. *Advances in Atomic, Molecular, and Optical Physics*, 48:263–356, 2002.

[60] S. Groth, P. Kruger, S. Wildermuth, R. Folman, T. Fernholz, J. Schmiedmayer, D. Mahalu, and I. Bar-Joseph. Atom chips: Fabrication and thermal properties. *Applied Physics Letters*, 85(14):2980–2982, 2004.

[61] V. Dikovsky, Y. Japha, C. Henkel, and R. Folman. Reduction of magnetic noise in atom chips by material optimization. *European Physical Journal D*, 35(1):87–95, 2005.

[62] S. Scheel, P. K. Rekdal, P. L. Knight, and E. A. Hinds. Atomic spin decoherence near conducting and superconducting films. *Physical Review A*, 72(4):042901, 2005.

[63] U. Hohenester, A. Eiguren, S. Scheel, and E. A. Hinds. Spin-flip lifetimes in superconducting atom chips: Bardeen-Cooper-Schrieffer versus Eliashberg theory. *Physical Review A*, 76(3):033618, 2007.

[64] I. G. Hughes, P. A. Barton, T. M. Roach, M. G. Boshier, and E. A. Hinds. Atom optics with magnetic surfaces .1. storage of cold atoms in a curved 'floppy disk'. *Journal of Physics B-Atomic Molecular and Optical Physics*, 30(3):647–658, 1997.

[65] I. G. Hughes, P. A. Barton, T. M. Roach, and E. A. Hinds. Atom optics with magnetic surfaces .2. microscopic analysis of the 'floppy disk' mirror. *Journal of Physics B-Atomic Molecular and Optical Physics*, 30(9):2119–2132, 1997.

[66] E. A. Hinds, M. G. Boshier, and I. G. Hughes. Magnetic waveguide for trapping cold atom gases in two dimensions. *Physical Review Letters*, 80(4):645–649, 1998.

[67] C. D. J. Sinclair, J. A. Retter, E. A. Curtis, B. V. Hall, I. L. Garcia, S. Eriksson, B. E. Sauer, and E. A. Hinds. Cold atoms in videotape micro-traps. *European Physical Journal D*, 35(1):105–110, 2005.

[68] C. D. J. Sinclair, E. A. Curtis, I. L. Garcia, J. A. Retter, B. V. Hall, S. Eriksson, B. E. Sauer, and E. A. Hinds. Bose-Einstein condensation on a permanent-magnet atom chip. *Physical Review A*, 72(3):031603(R), 2005.

[69] W. Petrich, M. H. Anderson, J. R. Ensher, and E. A. Cornell. Behavior of atoms in a compressed magneto-optical trap. *Journal of the Optical Society of America B-Optical Physics*, 11(8):1332–1335, 1994.

[70] D.W. de Lima Monteiro, O. Akhzar-Mehr, P.M. Sarro, and G. Vdovin. Single-mask microfabrication of aspherical optics using KOH anisotropic etching of Si. *Optics express*, 11(18):2244–2252, 2003.

[71] K. I. Lee, J. A. Kim, H. R. Noh, and W. Jhe. Single-beam atom trap in a pyramidal and conical hollow mirror. *Optics Letters*, 21(15):1177–1179, 1996.

[72] M. Trupke, F. Ramirez-Martinez, E. A. Curtis, J. P. Ashmore, S. Eriksson, E. A. Hinds, Z. Moktadir, C. Gollasch, M. Kraft, G. V. Prakash, and J. J. Baumberg. Pyramidal micromirrors for microsystems and atom chips. *Applied Physics Letters*, 88(7):071116, 2006.

[73] M. Mansuripur. *The physical principles of magneto-optical recording*. Cambridge University Press, Cambridge, 1995.

[74] C. J. Lin, G. L. Gorman, C. H. Lee, R. F. C. Farrow, E. E. Marinero, H. V. Do, H. Notarys, and C. J. Chien. Magnetic and structural properties of Co/Pt multilayers. *Journal of Magnetism and Magnetic Materials*, 93:194–206, 1991.

[75] Jocelyn Anna Retter. *Cold Atom Microtraps above a Video Tape Surface*. PhD thesis, University of Sussex, 2002.

[76] S. Eriksson, F. Ramirez-Martinez, E. Curtis, B. Sauer, P. Nutter, E. Hill, and E. Hinds. Micron-sized atom traps made from magneto-optical thin films. *Appl. Phys. B*, 79:811, 2004.

[77] H. J. Metcalf and P. Van der Straten. *Laser Cooling and Trapping*. Springer-Verlag, New York, 1999.

[78] K. Lindquist, M. Stephens, and C. Wieman. Experimental and theoretical study of the vapor-cell Zeeman optical trap. *Physical Review A*, 46(7):4082–4090, 1992.

[79] A. M. Steane, M. Chowdhury, and C. J. Foot. Radiation force in the magneto-optical trap. *Journal of the Optical Society of America B-Optical Physics*, 9(12):2142–2158, 1992.

[80] J. A. Kim, K. I. Lee, H. R. Noh, W. Jhe, and M. Ohtsu. Atom trap in an axicon mirror. *Optics Letters*, 22(2):117–119, 1997.

[81] Young-Tak Chough and Wonho Jhe. A computational analysis of an axicon magneto-optical trap. *Journal of the Physical Society of Japan*, 69(5):1366–1373, May 2000.

[82] E. Arimondo, M. Inguscio, and P. Violino. Experimental determinations of hyperfine-structure in alkali atoms. *Reviews of Modern Physics*, 49(1):31–75, 1977.

[83] D. Sesko, T. Walker, C. Monroe, A. Gallagher, and C. Wieman. Collisional losses from a light-force atom trap. *Physical Review Letters*, 63(9):961–964, 1989.

[84] Frederick Reif. *Fundamentals of statistical and thermal physics*. McGraw-Hill series in fundamentals of physics. McGraw-Hill, New York, 1965.

[85] U. D. Rapol, A. Wasan, and V. Natarajan. Loading of a Rb magneto-optic trap from a getter source. *Physical Review A*, 64(2):023402, 2001.

[86] J. A. Kim, K. I. Lee, H. Nha, H. R. Noh, and W. Jhe. Simple atom trap in a conical hollow mirror: Numerical analysis. *Journal of the Korean Physical Society*, 30(2):387–390, 1997.

[87] K. H. Kim, K. I. Lee, H. R. Noh, W. Jhe, N. Kwon, and M. Ohtsu. Cold atomic beam produced by a conical mirror funnel. *Physical Review A*, 64(1):013402, 2001.

[88] H. R. Noh and W. Jhe. Atom optics with hollow optical systems. *Physics Reports-Review Section of Physics Letters*, 372(3):269–317, 2002.

[89] J. M. Kohel, J. Ramirez-Serrano, R. J. Thompson, and L. Maleki. Generation of an intense cold-atom beam from a pyramidal magneto-optical trap: experiment and simulation. *Journal of the Optical Society of America B-Optical Physics*, 20(6):1161–1168, 2003.

[90] A. S. Mellish and A. C. Wilson. A simple laser cooling and trapping apparatus for undergraduate laboratories. *American Journal of Physics*, 70(9):965–971, 2002.

[91] W. A. Nierenberg. The measurement of the nuclear spins and static moments of radioactive isotopes. *Annu. Rev. Nucl. Sci.*, 7:349–406, 1957.

[92] G. Breit and I. I. Rabi. Measurement of nuclear spin. *Physical Review*, 38(11):2082, 1931.

[93] D. M. Brink and C. V. Sukumar. Majorana spin-flip transitions in a magnetic trap. *Physical Review A*, 74(3):035401, 2006.

[94] W. Demtröder. *Laser spectroscopy : basic concepts and instrumentation*. Advanced texts in physics. Springer, New York, 3rd edition, 2003.

[95] Daniel A. Steck. Rubidium 87 D Line Data. The current version of this document is available at http://steck.us/alkalidata, October 2003.

[96] A. S. Arnold, J. S. Wilson, and M. G. Boshier. A simple extended-cavity diode laser. *Review of Scientific Instruments*, 69(3):1236–1239, 1998.

[97] C. P. Pearman, C. S. Adams, S. G. Cox, P. F. Griffin, D. A. Smith, and I. G. Hughes. Polarization spectroscopy of a closed atomic transition: applications to laser frequency locking. *Journal of Physics B-Atomic Molecular and Optical Physics*, 35(24):5141–5151, 2002.

[98] Sacher Lasertechnik Group. Technical documentation: Spectroscopy with diode lasers. http://data.sacher-laser.com/techdocs/dlspec.pdf.

[99] K. L. Corwin, Z. T. Lu, C. F. Hand, R. J. Epstein, and C. E. Wieman. Frequency-stabilized diode laser with the Zeeman shift in an atomic vapor. *Applied Optics*, 37(15):3295–3298, 1998.

[100] Bahaa E. A. Saleh and Malvin Carl Teich. *Fundamentals of photonics*. Wiley, 1991.

[101] David W. Allan. Time and frequency (time-domain) characterization, estimation, and prediction of precision clocks and oscillators. *IEEE Transactions on Ultrasonics, Ferroelectrics, and Frequency Control.*, URC-34(6):647–654, 1967.

[102] Marvin J. Weber. *Handbook of Optical Materials*. CRC Press, 2003.

[103] C. G. Townsend, N. H. Edwards, C. J. Cooper, K. P. Zetie, C. J. Foot, A. M. Steane, P. Szriftgiser, H. Perrin, and J. Dalibard. Phase-space density in the magnetooptical trap. *Physical Review A*, 52(2):1423–1440, 1995.

[104] E. Bassous. Fabrication of novel 3-dimensional microstructures by anisotropic etching of (100) and (110) silicon. *IEEE Transactions on Electron Devices*, 25(10):1178–1185, 1978.

[105] G. B. Friedmann and H. S. Sandhu. Phase changes on reflection from a metallic surface. *American Journal of Physics*, 56:270–273, 1988.

[106] L. B. Wolff. Polarization-based material classification from specular reflection. *IEEE Transactions on Pattern Analysis and Machine Intelligence*, 12(11):1059–1071, 1990.

[107] H. Chen and L. B. Wolff. Polarization phase-based method for material classification in computer vision. *International Journal of Computer Vision*, 28(1):73–83, 1998.

[108] Robert Siegel and John R. Howell. *Thermal radiation heat transfer.* Taylor & Francis, New York, 4th edition, 2001.

[109] G. Lewis, Z. Moktadir, C. Gollasch, M. Kraft, S. Pollock, F. Ramirez-Martinez, J. P. Ashmore, A. Laliotis, M. Trupke, and E. A. Hinds. Fabrication of magneto-optical atom traps on a chip. *arXiv:0804.4593v1 [physics.atom-ph]*, 2008.

[110] T. A. Delchar. *Vacuum physics and techniques.* Number 6 in Physics and its applications. Chapman & Hall, London, 1993.

[111] C. Rouki, L. Westerberg, and Chicsi Dev Grp. Ultra-high vacuum compatibility measurements of materials for the CHICSi detector system. *Physica Scripta*, T104:107–108, 2003.

[112] L. Westerberg, V. Avdeichikov, L. Carlen, P. Golubev, B. Jakobsson, C. Rouki, A. Siwek, E. J. van Veldhuizen, and H. J. Whitlow. CHICSi - a compact ultra-high vacuum compatible detector system for nuclear reaction experiments at storage rings. I. General structure, mechanics and UHV compatibility. *Nuclear Instruments & Methods in Physics Research Section a-Accelerators Spectrometers Detectors and Associated Equipment*, 500(1-3):84–95, 2003.

[113] FR4 Data Sheet. http://www.p-m-services.co.uk/fr4_data_sheet.htm.

[114] H. S. Nalwa. *Handbook of thin film materials: Nanomaterials and Magnetic Thin Films.*, volume 5. Academic Press, New York, 2002.

[115] S. Uba, L. Uba, A. N. Yaresko, A. Y. Perlov, V. N. Antonov, and R. Gontarz. Optical and magneto-optical properties of Co/Pt multilayers. *Physical Review B*, 53(10):6526–6535, 1996.

[116] R. A. Fry, L. H. Bennett, E. Della Torre, and R. F. C. Farrow. Magneto-optical behavior in Co/Pt ultrathin film multilayers. *Journal of Applied Physics*, 87(9):5765–5767, 2000.

[117] G. N. Phillips, K. O'Grady, Q. Meng, and J. C. Lodder. Domain structure and magnetisation processes in magneto-optic Co/Pt thin films. *IEEE Transactions on Magnetics*, 32(5):4070–4072, 1996.

[118] G. N. Phillips, K. OGrady, and J. C. Lodder. Magnetization reversal at elevated temperatures in Co/Pt multilayer thin films. *Journal of Physics D: Applied Physics*, 34:29602971, 2001.

[119] Y. C. Cho, S. B. Choe, and S. C. Shin. Magnetic field dependence of magnetization reversal behavior in Co/Pt multilayers. *Journal of Applied Physics*, 90(3):1419–1421, 2001.

[120] M. Kisielewski, A. Maziewski, M. Tekielak, J. Ferre, S. Lemerle, V. Mathet, and C. Chappert. Magnetic anisotropy and magnetization reversal processes in Pt/Co/Pt films. *Journal of Magnetism and Magnetic Materials*, 260(1-2):231–243, 2003.

[121] Ch. Kittel. *Introduction to Solid State Physics*. John Wiley and Sons, New York, 1971.

[122] Z. Q. Qiu and S. D. Bader. Surface magneto-optic kerr effect. *Review of Scientific Instruments*, 71(3):1243–1255, 2000.

[123] Z. Q. Qiu and S. D. Bader. Surface magneto-optic kerr effect (SMOKE). *Journal of Magnetism and Magnetic Materials*, 200(1-3):664–678, 1999.

[124] M. Mansuripur, G. A. N. Connell, and J. W. Goodman. Laser-induced local heating of multilayers. *Applied Optics*, 21(6):1106–1114, 1982.

[125] M. Mansuripur and G. A. N. Connell. Laser-induced local heating of moving multilayer media. *Applied Optics*, 22(5):666–670, 1983.

[126] M. Mansuripur and G. A. N. Connell. Thermal aspects of magneto-optical recording. *Journal of Applied Physics*, 54(9):4794–4798, 1983.

[127] M. Mansuripur and G. A. N. Connell. Energetics of domain formation in thermomagnetic recording. *Journal of Applied Physics*, 55(8):3049–3055, 1984.

[128] M. Mansuripur and T. W. Mcdaniel. Magnetization reversal dynamics in magneto-optic media. *Journal of Applied Physics*, 63(8):3831–3834, 1988.

[129] B. E. Bernacki and M. Mansuripur. Characterization of magnetooptical recording media in terms of domain boundary jaggedness. *Journal of Applied Physics*, 69(8):4960–4962, 1991.

[130] D. W. Sesko, T. G. Walker, and C. E. Wieman. Behavior of neutral atoms in a spontaneous force trap. *Journal of the Optical Society of America B-Optical Physics*, 8(5):946–958, 1991.

Appendix A

Pumping down procedure

Initially, the chamber is pumped through the angle valve by a turbo molecular pump for at least one hour before attempting to turn on the ion pump. After this initial pumping stage, the ion pump is switched on and an initial reading in the middle 10^{-4} mbar region is normally obtained. At this point and provided that the pressure is in this range, the ion pump can be left pumping for a few hours.

When the pressure reading in the ion pump controller is in the low 10^{-5} mbar or high 10^{-6} mbar region, it is possible to begin outgassing the contents of the chamber. These contents are a pair of anti-Helmholtz coils which is described in section 3.4.1, the rubidium dispenser described in section 3.1.2, and the atom chip assembly that is fully described in section 5.3.1. We begin by heating up the coil pair by running current through them and monitoring the corresponding temperature variation by recording the change in the coil resistance. As the coil temperature increases, so does the outgassing rate and this is reflected in the chamber pressure. However, once the coil temperature has stabilised at a certain value, the outgassing rate gradually decreases and the pressure comes back down. The current supplied to these coils is raised in small amounts, always keeping the pressure in the chamber below 10^{-4} mbar.

Once the coil temperature has been stabilised at around 100 °C and the pressure has dropped below 10^{-6} mbar, it is possible to begin outgassing the rubidium dispenser. Although the nominal activation current of these dispensers is as high as 4.5 A, immediately after loading a dispenser into the vacuum chamber, currents as low as a few hundreds of mA are enough to expel a large amount of material. We have found that during the initial dispenser outgassing stages, the current needs to be raised in steps as small as 250 mA. Each one of these steps pushes the pressure briefly up to the 10^{-4} mbar range, before the turbo pump brings the pressure back down into the 10^{-7} mbar range in a few minutes. This procedure is repeated until a current of up to 6 A has been reached. Once the 4.5 A activation threshold has been crossed, a laser beam tuned to one of the rubidium transitions is sent into the vacuum chamber. The appearance of fluorescence in the path of this resonant beam indicates the presence of Rb in the chamber and, in consequence, the correct operation of the dispenser. At this point, the current supplies can be turned off and both vacuum pumps are left pumping for several hours. Next, the angle valve is closed and from this point onwards the ion pump alone will suffice to

take the pressure below 10^{-8} mbar in a few days and below 10^{-9} mbar in less than a week.

When the atom chip assembly, which is described in sections 3.1.3 and 5.3.1, were included in the experimental apparatus, we found it necessary to add a full chamber bake-out stage to the pumping down procedure. We do this with the aim of keeping the pumping-down period as short as possible. In this stage, three heaters are wound around the vacuum chamber, especially in the top 8" port area. This is because all the elements of our experiments are attached to the flange that seals that port. This flange is then kept at a temperature between 100 °C and 120 °C for two or three days, while both the turbo pump and the ion pump are kept working. Following this procedure, a pressure below 10^{-9} mbar can be achieved in approximately one week.

Appendix B

The rate of losses to a wall

The loss rate can be estimated by considering the number of atoms per unit time colliding with a surface located at a distance d from the trap centre. The atom flux can be simply written as $\Phi_0 = \frac{1}{4} n\bar{v}$ and, as we are interested in clouds containing $\lesssim 10^5$ atoms, it is justified to consider an atom density following a gaussian distribution around the trap centre. Hence, the total number of atoms striking the surface per unit time is estimated by summing this flux over the entire wall surface, $L = \int \Phi_0 dA$,

$$L = \frac{1}{4}\bar{v}\int_{-\infty}^{\infty}\int_{-\infty}^{\infty} n_0 e^{-\frac{1}{2}(\frac{x}{\sigma_x})^2} e^{-\frac{1}{2}(\frac{y}{\sigma_y})^2} e^{-\frac{1}{2}(\frac{z}{\sigma_z})^2} dxdz \tag{B.1}$$

This is then evaluated at $y = d$ to give:

$$L = \frac{\pi}{\sqrt{2}}\bar{v} n_0 \sigma^2 e^{-\frac{1}{2}\left(\frac{d}{\sigma}\right)^2} \tag{B.2}$$

Here we have considered that the cloud extent in each direction is determined by the magnetic field gradient and $\sigma = \sigma_x = \sigma_y = \sqrt{2}\sigma_z$.

The maximum number of atoms recorded in the loss rate measurements is of the order of 10^5 atoms. This suggest that in these extreme cases we are operating in the frontier between the temperature limited and the multiple scattering regimes, although in general the number of atoms was below this limit [103]. Consequently, our model must be developed for either of the two possible regimes. Firstly, in the temperature limited regime, as more atoms are added to the trap, the cloud radius remains constant and the density is determined by the total number of trapped atoms. However, the extent of the cloud is restricted by the proximity of the wall. Consequently, the cloud population N can be calculated by integrating the gaussian atom distribution with the restriction imposed by the wall:

$$N = \int_{-\infty}^{\infty}\int_{-\infty}^{d}\int_{-\infty}^{\infty} n_0 e^{-\frac{1}{2}(\frac{x}{\sigma_x})^2} e^{-\frac{1}{2}(\frac{y}{\sigma_y})^2} e^{-\frac{1}{2}(\frac{z}{\sigma_z})^2} dxdydz$$

This leads to

$$N = 2\pi^{3/2}\sigma^3 n_0 \left[1 + \mathrm{Erf}(\frac{d}{\sqrt{2}\sigma})\right] \tag{B.3}$$

where $\mathrm{Erf}(x)$ denotes the Gauss error function

$$\mathrm{Erf}(x) = \frac{2}{\sqrt{\pi}} \int_0^x e^{-t^2} dt$$

This result can be used to express the cloud density in terms of the number of atoms collected in the trap, which then can be substituted into equation B.2. Furthermore, the wall loss rate results to be proportional to the number of atoms in the trap and we can write $L_{TL} = \gamma_{TL} N$, where

$$\gamma_{TL} = \frac{\bar{v} e^{-\frac{1}{2}\left(\frac{d}{\sigma}\right)^2}}{\sqrt{8\pi}\sigma \left[1 + \mathrm{Erf}(\frac{d}{\sqrt{2}\sigma})\right]} \tag{B.4}$$

is the wall contribution to the loss rate in the temperature limited regime (TL). The overall loss rate can then be expressed as $\gamma = \beta n_{Rb} + \gamma_B + \gamma_{TL}$, which is the parameter that we have determined experimentally.

In the multiple scattering regime, the cloud density is limited by the reabsorption of photons within the trap. The cloud radius is then determined by the total number of trapped atoms and, as it has been pointed out in [130], in this regime the cloud begins to differ from a gaussian distribution. However, the clouds generated in our experiments are not far from the border between the two regimes and for this estimation we assume that the distribution is still very close to a gaussian, which is consistent with what we have seen in our experiments. Then, the number of atoms collected in the trap is given by

$$N = (2\pi)^{3/2} n_0 \sigma^3 \tag{B.5}$$

In order to determine the actual density at which the atom cloud saturates, we considered a cold atom cloud in a MOT generated far from the wall. In this situation,

$$n_{MS} = \frac{N}{4\pi^{3/2}\sigma^3} \tag{B.6}$$

and N and σ are taken to be typical values for a large cloud.

This density can now be utilised to express the cloud radius in terms of the number of atoms in the trap and the result can be substituted in equation B.2,

$$L_{MS} = \frac{2^{1/6}}{4} \bar{v} N^{2/3} n_{MS}^{1/3} \exp\left(-\frac{2^{1/3}\pi d^2 n_{MS}^{2/3}}{N^{2/3}}\right) \tag{B.7}$$

In contrast to what was found for the temperature limited regime, L_{MS} is a complicated function of the number of atoms collected in the trap. Therefore, to see how this estimation compares with the results of our experiments, we need to insert this expression in the MOT filling equation considering the losses to the wall separately,

$$\frac{dN}{dt} = R - (\beta n_{Rb} + \gamma_B) N - L_{MS} \tag{B.8}$$

Considering the steady state situation $\frac{dN}{dt} = 0$, we can write

$$R - (\beta n_{Rb} + \gamma_B + \gamma_{MS}) N_S = 0 \tag{B.9}$$

with $\gamma_{MS} = {N_S}^{-1} L_{MS}$. This equation can be solved numerically for N_S and the solution can be used in B.7 to express the dependency of the MOT loss rate on the distance to the surface in the multiple scattering regime.

We have shown how the interaction between the cold atom cloud and a room temperature surface is expected to influence the trap loss rate. In our analysis, a distinction was made between the temperature limited (TL) and the multiple scattering (MS) regimes. In order to demonstrate how these models recreate the real situation, in figure 4.19 we have included a pair of curves corresponding to each of these models. The values of the parameters that were utilised for generating these curves are typical of our experiments, but do not represent a fitting of the model to the experimental data.

Appendix C

Pyramidal micromirrors for microsystems and atom chips

APPLIED PHYSICS LETTERS **88**, 071116 (2006)

Pyramidal micromirrors for microsystems and atom chips

M. Trupke,[a] F. Ramirez-Martinez, E. A. Curtis, J. P. Ashmore, S. Eriksson, and E. A. Hinds
Blackett Laboratory, Imperial College, Prince Consort Road, London SW7 2BW, United Kingdom

Z. Moktadir, C. Gollasch, and M. Kraft
School of Electronics and Computer Science, University of Southampton, Southampton, SO17 1BJ, United Kingdom

G. Vijaya Prakash[b] and J. J. Baumberg
School of Physics and Astronomy, University of Southampton, Southampton, SO17 1BJ, United Kingdom

(Received 30 August 2005; accepted 22 December 2005; published online 15 February 2006)

Concave pyramids are created in the (100) surface of a silicon wafer by anisotropic etching in potassium hydroxide. High quality micromirrors are then formed by sputtering gold onto the smooth silicon (111) faces of the pyramids. These mirrors show great promise as high quality optical devices suitable for integration into micro-optoelectromechanical systems and atom chips. We have shown that structures of this shape can be used to laser-cool and hold atoms in a magneto-optical trap.
© *2006 American Institute of Physics*. [DOI: 10.1063/1.2172412]

The miniaturization of optical components leads to higher packaging density and increased speed of devices that manipulate light. This is part of the vast field of Microsystems technology, designated by micro-optoelectromechanical systems (MOEMS), in which electronic, mechanical, and optical devices are integrated on the micron scale. As mirrors are fundamental components of most optical systems, techniques for the integration of high-quality mirrors are relevant for the advancement of this field. In the context of atomic physics, there has been a recent drive to integrate optical elements with atom chips[1–3] for the purposes of detection and quantum-coherent manipulation of cold atoms.[4,5] Just as pyramidal mirrors have been used[6] to form macroscopic magneto-optical traps (MOTs), so these microscopic pyramids may be used to cool and trap an array of small atom clouds on a chip.

We have fabricated two-dimensional arrays of micromirrors in silicon using a method that is simple, economical, and compatible with MOEMS. We start with a (100)-oriented silicon wafer, coated with a thin layer of oxide. Optical lithography is then used to make square openings in the oxide, through which the silicon can be etched. We use the anisotropic etchant potassium hydroxide at a concentration of 25% by volume and a temperature of 80 °C. This attacks the Si(100) plane more rapidly than the Si(111) plane, resulting in a pyramidal pit[7] bounded by the four surfaces (1, 1, 1), $(\bar{1},1,1)$, $(1,\bar{1},1)$, and $(\bar{1},\bar{1},1)$. Typical resulting pyramids are shown in Fig. 1. The Si(111) faces of the pyramids are expected to be extremely smooth because of the layer-by-layer etching mechanism involved.[8,9] Atomic force microscope measurements confirm this, giving an rms surface roughness value of less than 0.5 nm for the uncoated pyramid faces. This makes them ideal as substrates for high-quality optical mirrors. After stripping the oxide mask away, a layer of gold of 100 nanometers thickness is applied to the silicon. Gold was chosen as it is a good reflector for infrared light, but other metals or dielectric coatings can also be applied. After sputtering gold, the surface roughness increases to 3 nm (rms). With this amount of roughness one can calculate that the scattering loss of the specularly reflected intensity should be less than 0.5% in the near-infrared range.[10]

Figure 1(a) shows a small section of the array viewed under a scanning electron microscope after completion of the gold coating. In this particular sample, the square pyramids have 30 μm sides and are arranged in a square lattice with a pitch of 100 μm. Both the etching and the sputtering are standard processes that can be accurately controlled to give reproducible results and to make large numbers of mirrors in a single batch. In the rest of this letter we analyze and measure directly how the pyramids respond to polarized and unpolarized light. We also test a macroscopic model to show that this silicon pyramid mirror geometry is suitable for making a MOT.

The sides of the pyramids define x and y axes, as shown in Fig. 1. Our first test of the mirrors is to illuminate them with a collimated 1-mm-diameter laser beam (wavelength 633 nm) propagating along the z axis, i.e., normal to the silicon surface and along the symmetry axis of the pyramids. Figure 2(a) shows the reflected pattern of light observed on a screen 7 cm away from the mirrors. On this image we have drawn circles indicating the position of spots as expected from a perfect pyramid. The three prominent spots at the corners of the square are due to doubly reflected rays, which

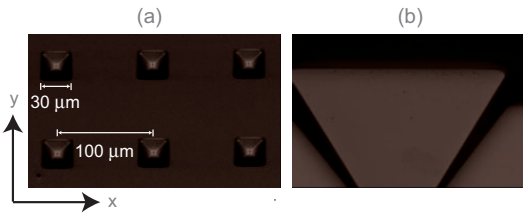

FIG. 1. Scanning electron microscopy micrographs of the etched and gold-coated pyramids. (a) Top view showing pyramids in a rectangular array with a pitch of 100 μm. (b) Cross-sectional view of a single pyramid. This was obtained by cleaving the pyramid parallel to one of its edges. The base of the pyramid has a side of length 30 μm, corresponding to a perpendicular depth of 21.3 μm.

[a]Electronic mail: michael.trupke@imperial.ac.uk
[b]Present address: Department of Physics, IIT, Delhi, India.

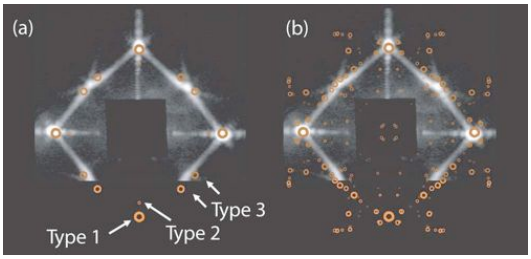

FIG. 2. (Color online) Measured intensity distribution of reflected light, at a distance of 7 cm from the array of pyramids, when it is illuminated at normal incidence. A central bright spot, which is caused by reflection from the region between pyramids, was blocked to improve the visibility of light reflected from the pyramids. The circles in (a) show the reflection pattern expected for a perfect pyramid, while the circles in (b) indicate the calculated reflection pattern for a pyramid with rounded corners. Size indicates expected relative intensity.

we classify as type (1). These reflect from opposite faces of the pyramid, as illustrated by the solid line in Fig. 3(a). There should be a fourth spot at the bottom of the photographs, but this is blocked by a mount holding the beamsplitter through which the array is illuminated.

If the angle between opposite mirrors is α, the type (1) beams make an angle of $(\pi-2\alpha)$ with the z axis. From the angles measured, we find that $\alpha=(70.6\pm0.7)°$, in agreement with the expected angle between opposing faces of $\arccos(1/3)=70.5°$.

When the incident ray is close to the apex of the pyramid (within 1.6 μm for a pyramid of 30 μm base length), it is reflected twice by the first mirror, as illustrated by the dashed line in Fig. 3(a). These rays, which we call type (2), should produce secondary spots just inside the type (1) spots. However, the power in the type (2) reflected beams is expected to be 100 times smaller because of the small area from which they originate, as shown in Fig. 3(b). Consequently, it is not possible to identify the type (2) beams clearly against the diffracted wings of the type (1) beams. Furthermore, there is a background of light along the x and y axes caused by reflection from rounded edges on the entrance aperture of the pyramid, which can be seen in Fig. 1(b).

If a ray is incident near one of the corners of the pyramid, the first reflection sends it off towards the opposite mirror, but it is intercepted and deflected by the adjacent mirror before the opposite mirror sends it out of the pyramid as a type (3) ray. These rays make an angle of 31.5° with the z

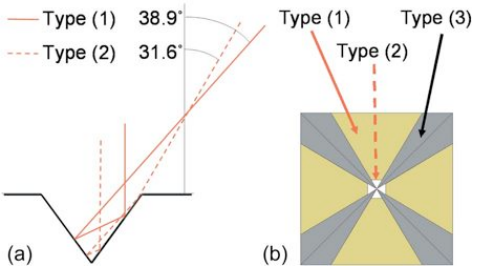

FIG. 3. (Color online) (a) Cross section in the x-z plane through a pyramid, showing type (1) and (2) trajectories. These involve reflections from mirrors on opposite sides of the pyramid. (b) View of the entrance aperture of the pyramid, showing the regions that produce type (1), (2), and (3) rays.

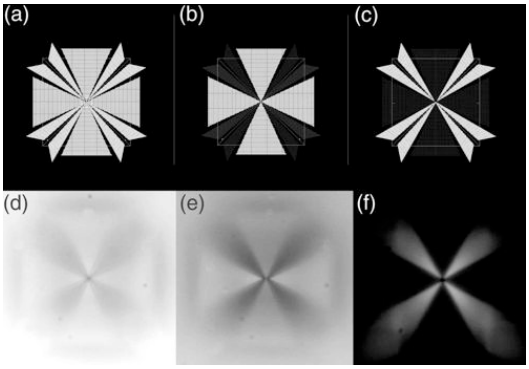

FIG. 4. Views of the vertex pyramidal mirror under an optical microscope at 100× magnification. Top row: Raytracing simulation. Bottom row: Photographs. (a) and (d) without polarizers; (b) and (e) parallel polarizer and analyzer; (c) and (f) crossed polarizer and analyzer.

axis and form double spots at azimuthal angles of 36.9°, 53.1°, etc. as shown in Fig. 2(a). These spots are less distinct than those of type (1) because the corners of the pyramid are rounded, a feature that does not affect the type (1) rays. Figure 2(b) shows the same photographed reflection pattern, but here the superimposed circles indicate the expected position and magnitude of spots reflected from a pyramid with rounded corners. The roundness is included in the ray-tracing model by four additional surfaces at each corner. These are shaped to form approximate cone sections with radii of 2.5 μm at the base and 0.825 μm at the apex of the pyramid. The reflection pattern predicted for this modified shape matches many of the features of the photographed intensity distribution more closely.

The three types of ray described earlier also present different characteristics when observed using polarized light. For our observations, we use light which is polarized parallel to the x axis. Reflections of types (1) and (2) leave the linear polarization of the light unchanged in the x-y plane. The type (3) reflections produce rotations of ±53° or ±78° about the z axis, depending on whether the pyramid face on which the first bounce occurs is parallel to the polarization of incoming beam. The rotations are caused by the obliquity of the second and third bounces of the type (3) reflections.[11] This is investigated in our second test of the mirrors, in which we examine them with white light under an optical microscope, illuminating them once again along the z axis. Figure 4(a) shows the image calculated by ray tracing for unpolarized light with the microscope focussed in the plane of the apex of a perfect pyramid. In this figure most of the area is bright. In Fig. 4(b) we show the expected image for linearly polarized light, viewed through a parallel analyser, which suppresses the type (3) contribution. This leads to a reduction in the intensity of reflections from the corner region. In Fig. 4(c), the analyzer is crossed with the polarizer and only type (3) rays contribute, making the corner region bright. The intensity patterns observed in the laboratory are shown in Figs. 4(d)–4(f). They correspond closely to the calculated distributions, indicating that the pyramid reflects light as expected.

Our immediate application for these structures is to build an array of small magneto-optical traps, integrated into an atom chip in a single additional etching step. As in a 90° pyramid MOT,[6] lateral confinement is given by the first re-

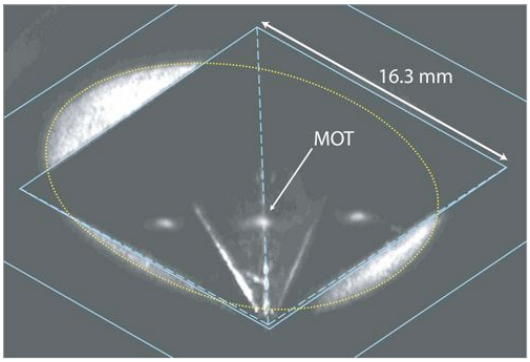

FIG. 5. (Color online). Fluorescence image of 1.6×10^8 atoms magneto-optically trapped in a 70.5° pyramid. Two reflections are also visible. The 16.3 mm aperture of the pyramid (solid line) and its sloping edges (dashed lines) have been added to guide the eye of the reader. The outline of the incident laser beam is shown dotted. Some light is scattered from the edges of the pyramid and from the plane outside.

flections of the type (1) beams, while the vertical trapping forces arise from the input beam and the second reflections of the type (1) beams. In the present pyramid the beams are not orthogonal and there are additional rays, which could also disturb the balance of forces in the trap. To test whether it is nonetheless possible to trap atoms in such a pyramid, we constructed a macroscopic glass model with a base length of 16.3 mm, coated with aluminium and a protective layer of SiO_2. Figure 5 shows the fluorescence image from a cloud of atoms trapped in this pyramid MOT, together with two reflections of the cloud. There are also reflections from the top face of the pyramid and from the edges. In order to assist the eye, we superimpose the entrance aperture of the pyramid as a solid line and we show the edges dashed. We have also built and tested a 90° pyramid MOT of similar volume and with the same coating, and find that there is no significant difference in the number of trapped atoms or in the stability of the MOT.

In the microscopic version, we anticipate using pyramids with a 200 μm base and will supply the required magnetic quadrupole field using existing microfabrication methods[1,12] to produce small current loops around each pyramid. We estimate that such a MOT can collect as many as 1000 atoms or as few as 1, according to the choice of operating parameters. Compared with other methods of creating arrays of microscopic traps on a chip,[13,14] this relies on a simple fabrication method and requires only a single input laser beam to give all the necessary trapping beams. It has been shown that Bose-Einstein condensation can be achieved on atom chips, both with current-carrying wire traps[15] and with permanent magnet traps.[16] Consequently it may be possible to create an array of condensates loaded from these MOTs. Alternatively, if there is just one atom per site, the array would have possible applications in quantum information processing.[4]

Further potential applications for the pyramids are in the areas of photonics and telecommunications. For example, by filling the pits with ferroelectric material or liquid crystals and applying an electric field, it may be possible to use the pyramids as fast optical switches.

In summary, we have designed, fabricated and characterized a new type of micromirror, produced by anisotropic etching through square apertures on a silicon single crystal. As an elementary component for optics, the micromirror has a variety of possible applications in MOEMS devices. We have demonstrated that it is possible to form a magneto-optical trap with this mirror geometry, making these pyramids very promising for creating arrays of microscopic traps on atom chips. Detailed experiments and further theoretical analysis are currently under way to develop these applications.

The authors acknowledge support from the UK EPSRC Basic Technology, QIPIRC, and Physics programmes and from the FASTNET and Atom Chips networks of the European Commission.

[1]R. Folman, P. Krueger, J. Schmiedmayer, J. Denschlag, and C. Henkel, Adv. At. Mol. Phys. **48**, 263 (2002).
[2]S. Eriksson, M. Trupke, H. F. Powell, D. Sahagun, C. D. J. Sinclair, E. A. Curtis, B. E. Sauer, E. A. Hinds, Z. Moktadir, C. O. Gollasch, and M. Kraft, Eur. Phys. J. D **35**, 135 (2005).
[3]M. Trupke, E. A. Hinds, S. Eriksson, E. A. Curtis, Z. M. E. Kukarenka, and M. Kraft, Appl. Phys. Lett. **87**, 211106 (2005).
[4]S. Scheel, J. Pachos, and P. L. Hinds, and E. A. Knight, *Quantum Coherence*, Lecture Notes in Physics Vol. 689 (Springer, Berlin, 2006), pp. 47–80.
[5]P. Horak, B. Klappauf, A. Haase, R. Folman, J. Schmiedmayer, P. Domokos, and E. A. Hinds, Phys. Rev. A **67**, 043806 (2003).
[6]K. Lee, J. Kim, H. Noh, and W. Jhe, Opt. Lett. **21**, 1177 (1996).
[7]R. Brendel, in *Proceedings of the 14th European Photovoltaic Solar Energy Conference*, edited by H. A. Ossenbrink, P. Helm, and H. Ehmann (Stephens, Bedford, 1997), p. 1354.
[8]Z. Moktadir and H. Camon, Modell. Simul. Mater. Sci. Eng. **5**, 481 (1997).
[9]K. Sato, M. Shikida, T. Yamashiro, M. Tsunekawa, and S. Ito, Sens. Actuators, A **A73**, 122 (1999).
[10]P. Beckmann and A. Spizzichino, *The Scattering of Electromagnetic Waves from Rough Surfaces* (Pergamon, New York, 1963).
[11]B. A. E. Saleh and M. C. Teich, *Fundamentals of Photonics* (Wiley, New York, 1991).
[12]S. Eriksson, F. Ramirez-Martinez, E. Curtis, B. Sauer, P. Nutter, E. Hill, and E. Hinds, Appl. Phys. B **B79**, 811 (2004).
[13]A. Grabowski and T. Pfau, Eur. Phys. J. D **22**, 347 (2003).
[14]E. Hinds, in *Atomic Physics 17*, AIP Conference Proceedings Vol. 551 edited by E. Arimondo, P. D. Natale, and M. Inguscio (AIP, New York, 2001), pp. 405–413.
[15]H. Ott, J. Fortagh, G. Schlotterbeck, A. Grossmann, and C. Zimmermann, Phys. Rev. Lett. **87**, 230401 (2001).
[16]C. D. J. Sinclair, E. A. Curtis, I. Llorente-Garcia, J. A. Retter, B. V. Hall, S. Eriksson, B. E. Sauer, and E. A. Hinds, Phys. Rev. A **72**, 031603 (2005).

Appendix D

Fabrication of magneto-optical atom traps on a chip

Fabrication of Magneto-Optical Atom Traps on a Chip

G. Lewis, Z. Moktadir, C. Gollasch, M. Kraft, S. Pollock, F. Ramirez-Martinez, J. P. Ashmore, A. Laliotis, M. Trupke, E. A. Hinds, *Fellow, OSA,*

***Abstract*— Ultra-cold atoms can be manipulated using micro-fabricated devices known as atom chips. These have significant potential for applications in sensing, metrology and quantum information processing. To date, the chips are loaded by transfer of atoms from an external, macroscopic magneto-optical trap (MOT) into microscopic traps on the chip. This transfer involves a series of steps, which complicate the experimental procedure and lead to atom losses. In this paper we present a design for integrating a MOT into a silicon wafer by combining a concave pyramidal mirror with a square wire loop. We describe how an array of such traps has been fabricated and we present magnetic, thermal and optical properties of the chip.**

***Index Terms*— Atom chips, Electrophoretic resist, Magneto-optical traps, Cavity patterning.**

I. Introduction

Atom chips are microfabricated devices that control electric, magnetic and optical fields in order to trap and manipulate cold atom clouds [1], [2], [3], [4] and to form Bose-Einstein condensates [5], [6], [7]. Potential applications include atomic clocks [8], atom interferometers [9], [10], and quantum information processors [11], [12]. Silicon is one of several materials used as a substrate for atom chips. It is attractive for this purpose because its properties are well-known and fabrication techniques are highly developed. The small scale of microfabricated current-carrying wires makes it easy to generate strong magnetic field gradients near the surface of the chip, forming tight traps for paramagnetic atoms. The loading of such magneto-static traps usually starts with a magneto-optical trap (MOT) typically some 3-4 mm from the surface. This collects atoms from a tenuous, room-temperature vapour and cools them, typically to 100 μK, using circularly polarised light beams in conjunction with a spherical quadrupole magnetic field. The atoms are sometimes further cooled to a few tens of μK using optical molasses, before being captured in a weak magnetic trap to form a large atom cloud, typically 1 mm in size. At this point, the atoms still have to be handed over to the microscopic magnetic traps on the chip, a process that involves further compression of the cloud and very accurate positioning of the atoms. This sequence of loading and transfer is complicated and could be largely eliminated if the MOT were integrated into the chip. Moreover, integration would open up the possibility of building arrays of MOTs to prepare large numbers of independent cold atom clouds.

This paper describes the fabrication and initial testing of an integrated array of MOTs on an atom chip, as proposed by Trupke *et al.* [13]. Each of these MOTs automatically prepares all the required light beams from a single circularly polarised input beam by reflecting the light in a concave square pyramid of mirrors [14]. This greatly reduces both the number of expensive optical components needed to prepare the light beams and the amount of laser power needed. Integrated wires encircling the opening at the base of the pyramid produce the required magnetic field distributions with modest electrical power consumption and accurate positioning. The fabrication of an integrated MOT array on a chip represents an important step towards a truly integrated atom chip for portable applications.

The atom chip we have fabricated has 6 rows of pyramids, ranging in size from 200 μm to 1200 μm, serviced by 12 separate wires to produce the magnetic fields. For pyramids up to 600 μm, the encircling wires have a width of 25 μm. The larger pyramids are serviced by wires of 50 μm width. In total there are 48 pyramid MOTs. The whole chip is packaged into a ceramic pin grid array (CPGA) with multiple wire bonds to bring high currents in and out of the chip. The silicon sidewalls of the pyramids are coated with gold to create micro-mirrors for reflecting the laser light. The pyramids formed by etching silicon have a 70.5^o apex angle, rather than the ideal 90^o. The optical properties of such a pyramid have already been investigated in [13]. In those experiments it was observed that light reflected near the diagonal edges can prevent the MOT from working. Here we have developed the necessary fabrication steps to eliminate these reflections by removing the gold near the corners of the pyramids.

This paper is organised as follows. Section II outlines the principles of atom trapping in these pyramidal micro-mirrors, section III describes the microfabrication, section IV presents initial tests of the device and section V discusses some prospects for using the chip in applications.

II. Principle of the MOT on a chip

Circularly polarised light, incident along the axis of a square pyramid, is reflected by the four metal mirrors that form the pyramid. At each reflection the helicity of the light is reversed. If the pyramid has a 90^o angle between opposite faces, these

This work was in supported by the EU SCALA project, the UK EPSRC and the Royal Society.

We are indebted to Mr J. Dyne for expert technical assistance.

G. Lewis, Z. Moktadir, C. Gollasch and M. Kraft are with the School of Electronics and Computer Science, University of Southampton, Southampton,SO17 1BJ, United Kingdom (email:Gnl04r@ecs.soton.ac.uk)

S. Pollock, F. Ramirez-Martinez, J. P. Ashmore, A. Laliotis, M. Trupke & E. A. Hinds are with the Centre for Cold Matter, Imperial College, Prince Consort Road, London, SW7 2AZ, United Kingdom (email:ed.hinds@imperial.ac.uk)

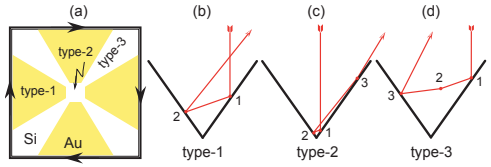

Fig. 1. (a) Plan view of pyramid showing the three regions of reflection and the encircling current. The following three figures illustrate the sequence of reflections. (b) Cross section through pyramid showing a type-1 reflection. (c) Type-2 reflection. (d) Type-3 reflection, where the ray is intercepted by the adjacent mirror at the point marked 2.

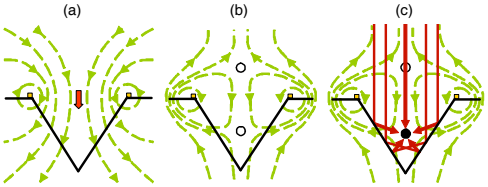

Fig. 2. (a) Dashed lines: magnetic field created solely by the wires around pyramid opening. Block arrow: maximum field strength is at the centre of the loop. (b) With the addition of a uniform bias, the net field acquires two minima, indicated by solid circles. (c) Circularly polarised light creates a magneto-optical trap at the field minimum indicated by a filled circle. The beams that contribute are shown as solid arrows.

reflections produce three counter-propagating pairs of light beams that are mutually orthogonal. Together with a magnetic quadrupole field, this configuration creates a MOT, whose radiation pressure forces cool and trap atoms from a room-temperature vapour [14], [15].

We form the pyramids by etching a silicon wafer, cut on the $\{100\}$ plane. Potassium hydroxide (KOH) etches anisotropically through square openings to reveal the $\{111\}$ planes, which form hollow pyramids with apex angle 70.5^o. This departure from a right angle causes the beams to be reflected into a variety of directions. We classify these beams as Type 1, 2, or 3, according to the region of the pyramid where the first reflection occurs, as shown in Fig. 1a. Type-1 rays are reflected on two opposite sides of the pyramid before leaving, as illustrated in Fig. 1b. Type-2 rays also reflect on opposite faces, but strike the original face again before leaving, as shown in Fig. 1c, making a total of three reflections. After the first reflection in Fig. 1d, type-3 rays head towards the opposite face, but because they are incident close to the diagonal edge of the pyramid, they are intercepted on the way by the adjacent face. Here they undergo a grazing reflection, marked (2) in the figure, where the helicity of the light is reversed. Finally, the opposite face is reached for a third reflection.

The wires electroplated on our chip form a square loop of side L around the pyramid base. A current I in this loop makes a magnetic field as shown in Fig. 2a. At the centre of the loop, in the plane of the wire, the field points downward with a magnitude of $\frac{2\sqrt{2}}{\pi}\mu_0 I/L$. We superpose a uniform vertical bias field in order to create the quadrupole field configuration required by the MOT, as shown in Fig. 2b. The strength B_T of this bias is chosen to centre the quadrupole halfway between the base and the apex, at a distance $\frac{1}{2\sqrt{2}}L$ from the surface of the chip. This requires $B_T = \frac{8\sqrt{2}}{3\pi\sqrt{5}}\mu_0 I/L = 0.54\mu_0 I/L$. The light beams needed to create the magneto-optical trap inside the pyramid are formed from the incoming circularly polarised beam by the first and second reflections of the type-1 rays, as shown in Fig. 2c. The type-2 rays produce a slight imbalance in the MOT force, but are largely unimportant. The type-3 rays tend to destabilise the MOT because they have the wrong helicity and produce a strong force that pushes the atoms out of the pyramid instead of trapping them.

We have conducted preliminary experiments using a large, glass pyramid coated with gold. Initially, this failed to produce a MOT because of the presence of the type-3 rays. Atoms were successfully trapped once the gold was removed from the areas where the type-2 and type-3 rays are produced. We were also able to make the MOT operate [13] by using a lower-reflectivity (78%) coating of aluminium, which was not cut away at the edges and centre. In such a pyramid, the intensity of the harmful type-3 light is decreased relative to the type-1 beams, because of the additional reflection by the lossy surfaces.

The current in the wire determines the vertical gradient in the MOT, which is related to the corresponding bias field according to $\frac{26\sqrt{2}}{15}B_T/L = 2.45B_T/L$. Under typical operating conditions used in most MOT experiments, the gradient is approximately 0.15 T/m. This is readily achieved on the chip because of the small scale: for example in the 1 mm loop it requires 0.1 A. The same wires can also be used to create a purely magnetic trap, with a depth of μB_T, where μ is the magnetic moment of the atom. Such a trap can hold atoms for many seconds provided its depth exceeds the temperature of the atoms by a factor of 5 or so. Ideally, we would like to be able to hold a $100\,\mu$K cloud, which requires a 0.7 mT bias field, corresponding to a current in a 1 mm loop of 1 A. The feasibility of using such currents is discussed more fully in Sec. IV-B. Further details about magnetic trapping of neutral atoms can be found in Ref. [1].

In summary, the aims of the fabrication were to create pyramidal micro-mirrors which would not reflect the damaging type-3 beams, and to surround these mirrors with wires able to create the required magnetic field strengths and gradients. In the following sections we describe how these aims have been achieved.

III. Fabrication

The fabrication processing sequence is shown in Fig. 3. We start by preparing the wafer and etching the pyramids. The whole surface is then coated with gold and patterned to remove the gold from the type-3 regions and to form the wire tracks. In these steps, the main fabrication challenge was to cover the wafer with a uniform resist layer, because the pyramid openings in the surface impeded the flow of the resist during spinning. Finally, the wires are electroplated to make them thick enough to carry the required current. These processes are described in more detail in the next three sub-sections.

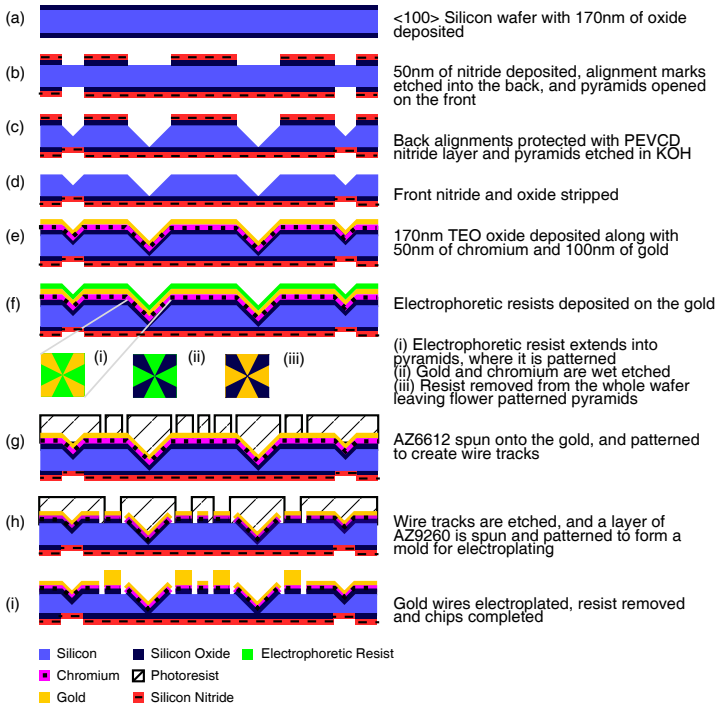

Fig. 3. Process flow for fabricating the pyramid MOT chip.

A. Wafer preparation and pyramid etch

The process begins with a 4 inch, 1mm-thick silicon wafer cut on the $\{100\}$ plane. This is given a standard RCA and fuming nitric acid clean. A 170 nm-thick layer of silicon dioxide is grown by wet oxidation in a furnace at 1000 C (Fig. 3a). Subsequently a 50 nm layer of low stress silicon nitride is deposited on both sides by LPCVD. A reactive ion plasma etch is then used to make alignment marks on the back side of the wafer for accurate positioning of all the masks used in the fabrication process.

In order to make the pyramids, a 1 μm layer of photo resist AZ6612 is spun onto the wafers. An array of square openings is patterned into the resist using a photo mask on a Karl Suss MA8 contact mask aligner. The silicon nitride and dioxide layers are removed through these openings using a dry plasma etch and the resist is then stripped in a plasma asher (Fig. 3b). Before etching the silicon, the backside alignment marks are protected by depositing a layer of PECVD silicon nitride 1μm thick and the wafer edges are protected by PTFE tape. The wafer is then etched for 19 hours in KOH at a concentration of 33% by volume and at a temperature of 80 C. This produces pyramidal pits bounded by the four most slowly etched surfaces $\{1,1,1\}$, $\{\bar{1},1,1\}$, $\{1,\bar{1},1\}$ and $\{\bar{1},\bar{1},1\}$ (Fig. 3c). The faces of the pyramids are very smooth because of the layer-by-layer etching mechanisms involved [16] and have been shown to have rms surface roughness as low as 0.5 nm [13]. The wafers are once again cleaned in a fuming nitric acid bath before the remaining silicon nitride is stripped from the front by a dry plasma etch and the remaining silicon dioxide is removed in an HF dip (Fig. 3d). Finally, the whole front surface is covered with a plasma-enhanced TEOS oxide layer, 170 nm thick. This is to provide electrical insulation between the silicon and the metallic coating that comes next.

B. Metallic coating and flower patterning

The metal coating consists of 50 nm of chromium and 100 nm of gold, evaporated onto the front of the wafer (Fig. 3e). In order to make the flower pattern on the faces of the pyramids, we require them to be covered by a uniform layer of resist. Spinning the resist at this stage does not produce a uniform layer because of the large depth of the pyramidal pits. In order to avoid this problem we use electrophoretic deposition of Eagle 2100 negative photo resist. The wafer is placed in the resist bath and heated to 33 C, where it acts as a cathode at -125 V. It remains in the bath until the current

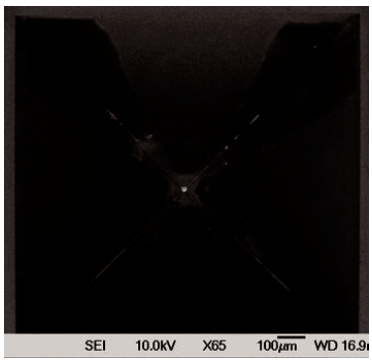

Fig. 4. SEM image showing the flower pattern created on the side walls of all the pyramids.

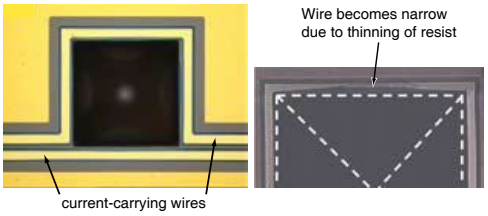

Fig. 5. Optical microscope image of the wire tracks. (a) The wires are well formed around a 200 μm pyramid. (b) On the side furthest from the axis of spinning, the wire of a 1.2 mm pyramid is malformed because the resist was too thin.

drops to zero, then it is rinsed in de-ionised water and dried in a vacuum oven at 65 C. At this point, the resist remains tacky, so the wafer is dipped into Eagle 2002 topcoat for 30 seconds and again dried in the vacuum oven. This method leaves a highly uniform layer of resist over the complex topography (Fig. 3f).

Next, the wafer is exposed to ultraviolet light for 77 s at 6.5 mW/cm^2, using a mask designed to remove the gold from the type-3 regions. This pattern is developed using Eagle 2005 developer heated to 40 C, which is sprayed onto the surface for 4 minutes. The wafer is then dipped for 1 minute in water at 80 C to remove the resist residues and to smooth the surface of the resist. It is dried in a vacuum oven and de-scummed for 3 minutes in oxygen plasma at 110 C (Fig. 3f(i)).

The exposed gold and chromium are removed by a 35 s potassium iodide etch, followed a 5 s chrome etch (Fig. 3f(ii)). The wafers are then sprayed for 15 min to strip the resist with Eagle 2007 remover at 50 C, and placed in an asher for 1 hr at 600 W and 110 C (Fig. 3f(iii)). This process leaves a flower pattern on the gold inside each pyramid, as shown in Fig. 4. This scanning electron microscope image shows that the gold has been removed in the diagonal and central regions corresponding to the type-2 and type-3 areas illustrated in Fig. 1a. We found that it was difficult to achieve a uniform exposure of the resist inside the pyramid. When the lower part of the pyramid (near the apex) is correctly exposed, the upper part tends to be over-exposed. The dark lines on the diagonals and the dark spot at the apex are due to residual resist. The colour of the silicon surface appears darker at increasing depth in the pyramid. We attribute this to charging of the silicon dioxide surface by electron bombardment from the SEM.

C. Wire fabrication

The final stage of fabrication is to form the wires around the base of each pyramid, as described in [17]. First, the tracks are patterned by optical lithography on the gold coating, then the wires are electroplated to provide the 3 μm thickness required for carrying the electrical current.

Once again, spinning a uniform layer of resist is very challenging since the radial flow is interrupted by the pyramid openings. To solve this problem we use the viscous photoresist AZ4533 as follows. A primer is spun onto the wafer to help adhesion. Then the wafer needs to be completely flooded with the resist before the spinning begins to ensure coverage inside pyramids and in the areas of the spin shadow just outside the pyramids. Spinning is carried out at 500 rpm for 10 s, followed by 30 s at 2000 rpm. We create a 5 μm layer of resist, which varies in thickness by approximately ± 3 μm where the pyramids interfere with the flow (Fig. 3g). The uniformity of the resist improves substantially around pyramids that are smaller than 1 mm, and impeccable wires are formed around the smallest pyramids, as shown in Fig. 5a. However, the thinning of the photo-resist in the spin shadow of the larger pyramids leads to overexposure and results in a thinning of the wire tracks there, as shown in Fig. 5b.

A 6 μm-thick electroplating mould is then created by optical lithography of AZ9260 which is spun at 500 rpm for 8 s, followed by 30 s at 4000 rpm. This layer is exposed at 200 mW/cm^2 for 30 s to create the plating mould with a minimum thickness of 3 μm (Fig. 3h). The electrochemical deposition is controlled by an Autolab PGSTAT30. We use a commercial cyanide-free gold plating solution (Metalor Technologies UK, with 1 g of gold per litre of solution). A standard three-electrode setup is used with a platinum counter electrode. The deposition bath is placed in a water bath kept at 50 C and the solution is agitated throughout the deposition process using a magnetic stirrer. The current is fixed at 6 mA, corresponding to a current density of 5 mA/cm^2, and the plating is run for 15 minutes to achieve a 3 μm-thick gold deposit (Fig. 3i). Finally, the resist is stripped to leave the free-standing gold wires.

Electrophoresis could potentially provide a solution to the problem of the thinning of the wires. However, it can only be used when pattering the wire tracks and not when creating the electroplating mould, since the Eagle 2100 resist can only cover areas previously covered with gold. For this reason the fabrication of the wires was entirely designed and performed with the use of spin-on positive photoresists.

D. Packaging

Figure 6 shows on the right an array of patterned pyramidal micro-mirrors with integrated current-carrying wires. The chip is fixed to a ceramic pin grid array (CPGA) package (CPG18023, Spectrum Semiconductor Materials Inc.) using

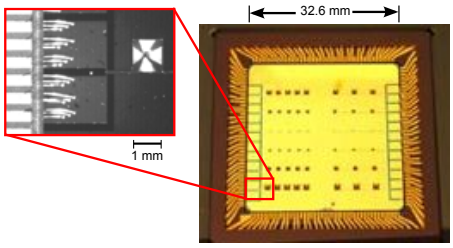

Fig. 6. Photographs of the pyramid-MOT chip mounted in its ceramic pin grid array package. Right: the the chip in its package. Left: detailed view of bond wires connecting the package to the chip wire pads, and a pyramid with the flower-patterned gold coating.

an epoxy compatible with ultra-high vacuum (Bylapox 7285). Gold bond wires connect the package pins to the microfabricated chip wires, with 9 bond wires serving each end of a chip wire. The view on the left of Fig. 6 shows the bond wires connecting the chip to the CPGA. The ceramic package is then plugged into a pin grid array (PGA) of sockets, which in turn is soldered into an FR4 printed circuit board. This design permits a large number of connections to be made in the limited space available in the high-vacuum chamber.

We place the chip assembly in a stainless steel vacuum chamber where a 20 l/s ion pump yields a pressure below the 10^{-9}mbar limit of our gauge after modest baking at 100 C for 2 days. At this low pressure, a trapped atom will remain undisturbed by the background gas for typically 10 s.

A stray magnetic field moves the zeros of magnetic field that form the centre of each MOT. To ensure that every pyramid encloses a field zero, we require the stray field to be less than 10 μT over the chip. Much stronger fields were initially found in the recess of the CPGA where the wafer is mounted, due to permanent magnetisation of the nickel/gold coating. We therefore removed the coating by sandblasting. Immediately above the Kovar pins, there remained a stray field that reached a maximum of 10 μT, but this was of short range and did not affect the 3 cm x 3 cm active area of the chip. There the field was below 500 nT, the gradients were similarly negligible, and remagnetising the assembly produced no perceptible change at that level.

IV. Device characterisation

In this section we characterise the magnetic properties of our device, demonstrating that the micro-fabricated wires can carry sufficient current for magneto-optical and purely magnetic trapping. Measurements of the heating of our chip wires allow us to infer the maximum depth and gradient achievable in our trap. Finally, it is shown that the flower patterning of the pyramid coating leads to the desired suppression of type-3 beams.

A. Magnetic field measurements

The wires around the base of each pyramid almost form a square loop, as shown in Fig. 5a. In order to calculate the magnetic field of the MOT, it is adequate to approximate this

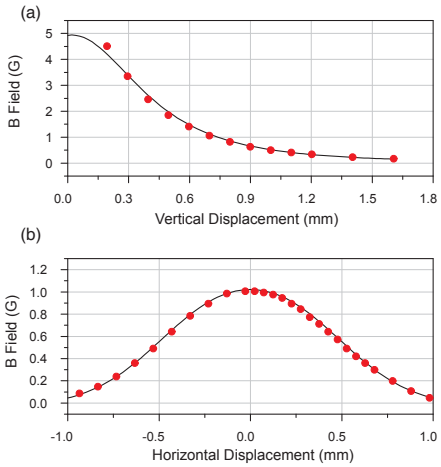

Fig. 7. Vertical component of magnetic field above an 800 μm pyramid with 480 mA in the wire. Dots: Hall probe measurement. Lines: Theory. (a) Vertical variation along the pyramid axis. (b) Transverse variation parallel to the pyramid row, through the pyramid axis at a height of 0.7 mm.

by a fully closed square loop. The solid lines in Figs. 7a and b show the vertical field component calculated for a current of 480 mA in wire 50 μm wide, centred on a 895 μm square. This corresponds to the geometry of the 800 μm pyramid. We measured the field above this pyramid using a Hall probe (Lakeshore 421 Gaussmeter), as shown by the circles in Fig. 7. On the left is a vertical scan along the axis of the pyramid, while the scan on the right is horizontal at a height of 0.7 mm. The two are entirely consistent.

B. Heating tests

Although the gold wires are very good conductors, they do of course dissipate electrical energy and, at sufficiently high currents, they blow like a fuse. Considerably below that limit, the wafer heats up to 120 C. At this temperature the epoxy used to bond the silicon to the CPGA begins to decompose, losing strength and outgassing strongly, thereby compromising both the mechanical stability of the chip and the high vacuum. This limiting temperature determines the largest current that we run through the wires, and thereby limits the field and field gradient that are available.

With the chip mounted and placed under moderate vacuum (10^{-5} mbar), we first tested how much current could be passed through individual bond wires 50 μm in diameter and 2-3 mm in length. We found that these blow at approximately 1.8 A, but can survive indefinitely at 1.5 A. Since each chip pad is normally connected by 9 wires in parallel, failure of the bond wires is not a limiting factor. In order to determine the operating currents for the chip wires, we monitored the temperature of the assembly at several points using thermocouples and we monitored the temperature of the wire itself by measuring the increase of its resistance. Passing a current through the 50 μm-wide chip wires, we measured the time it takes for the wire

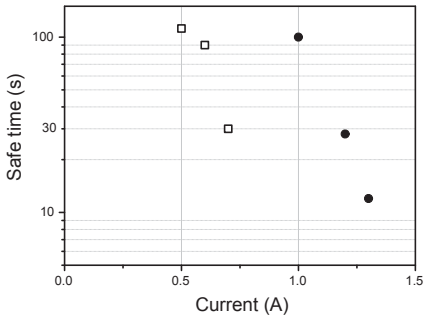

Fig. 8. Time taken for the chip wire temperature to reach 120 C for various currents. Filled circles: 50 μm-wide wires. Open squares: 25 μm-wide wires.

to reach 120 C, the results being shown by the filled circles in Fig. 8. In all cases the chip itself was much colder than the wire. Below 1 A, the temperature limit was never reached, but at 1.3 A, the wire approached 120 C in ten seconds. For the 25 μm-wide wires, the operation was continuous below 0.5 A and was limited to ten seconds at 0.75 A, as illustrated by the open squares in Fig. 8.

Since a suitable field gradient for the MOT is 0.15 T/m, the normal operating current is 5 mA for a 200 μm pyramid and 100 mA for a 1 mm pyramid. At these low currents there is negligible heating of the chip. By contrast, the 1 mm loop needs to operate at 1 A if it is to make a purely magnetic trap for a 100 μK cloud of atoms. This cannot be sustained indefinitely, as shown in Fig. 8, but substantially less than one second should suffice for most practical applications. Since the field scales as I/L, the situation is even better for purely magnetic trapping in the smaller loops.

In the course of these measurements, we found that the resistivity of the gold wire on the chip is 3.9x10$^{-8}\Omega$-m, approximately 1.6 times higher than that of bulk gold. This is typical of electro-deposited gold. The main consequence for us is a slightly higher power dissipation than we had anticipated in our design using the book value for the resistivity.

C. Optical properties

Observation of the pyramids under a microscope allowed us to check that the type-2 and type-3 reflections were indeed eliminated by removal of the gold coating to create the flower pattern. Figure 8a shows the image using unpolarized light with the microscope focussed on the apex of an unpatterned pyramid. In this figure most of the area is bright since the mirrors are reflecting light over the whole area of the pyramid. By contrast, Fig. 8b shows the same pyramid illuminated with linearly polarized light and viewed through a crossed polarizer, which suppresses all but the type-3 contribution, making the corner regions bright. Figures 8c and d show the corresponding images for a patterned pyramid. In c we see that there are no longer reflections near the apex of the pyramid, in the region of the type-2 rays. In d, we see that the removal of the gold at the edges has completely suppressed the type-3 reflections.

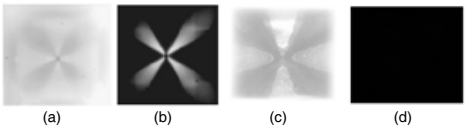

Fig. 9. Images of the pyramidal mirrors under a microscope, focussed on the apex. (a & b) unpatterned pyramids, (c & d) patterned pyramids. (a & c) No polarizers. (b & d) Crossed polarizer and analyzer.

V. Outlook

It is useful to estimate the number of cold atoms that may be captured in one of these micro-pyramids. This will depend on the usual operating variables, such as the laser detuning from the atomic transition, the positioning of the magnetic field zero, the balance of the light beams inside the pyramid and the pressure of the atomic vapour. In addition, these pyramids are at the extreme limit of small laser beam size. Normally the laser beams of a MOT are one or two centimetres in diameter, whereas these pyramids are less than a millimetre across. According to the well-established model first described by Wieman *et al.* [15], the number of atoms N captured in a MOT is expected to scale as $N \propto L^2 u_c^4$. Here the L^2 factor derives from the area of the laser beam, which in our case is set by the area of the pyramid opening. The quantity u_c is the capture velocity, i.e. the speed of the fastest atoms captured by the MOT from the thermal background vapour. Using the model of Ref. [15], we have computed u_c numerically, setting the maximum allowed stopping distance equal to the vertical height of the pyramid. The circles in Fig. 10 show the results on a log-log plot for a variety of pyramid sizes, with the laser detuning optimised separately to maximise u_c for each size. For pyramids larger than 1 mm, we find the empirical scaling law $u_c \propto L^{0.37}$ (the solid line in Fig. 10), leading to the result $N \propto L^{3.48}$. When the pyramids are smaller than that, the atom number drops a little more rapidly. We have established in a previous experiment [13] that a 16 mm pyramid made from glass blocks can capture 10^8 atoms. With the help of this model, we extrapolate our 16 mm result to predict that a 1 mm pyramid will capture some 6×10^3 atoms. The smallest pyramids on this chip, having $L = 0.2$ mm, are expected by the same argument to collect approximately 25 atoms.

Although this model is a reasonable estimate, it does neglect some aspects of the full 3-dimensional geometry. For example, it assumes that the atoms of the vapour have the normal thermal distribution close to the walls of the pyramid and it neglects the polarisation gradients in the laser field, which lead to additional Sisyphus cooling [18]. Experiment will have to determine how many atoms are actually captured. The number of atoms needed depends of course on the application. At one extreme, with an array of small clouds, each containing perhaps 10^4 atoms, the relative displacement of the clouds could provide a map of local magnetic field variations or be used to sense inertial forces. At the other extreme, the pyramids could serve as single-atom sources for loading integrated optical cavities, which have recently been demonstrated [19]. This would permit the production of single photons on demand

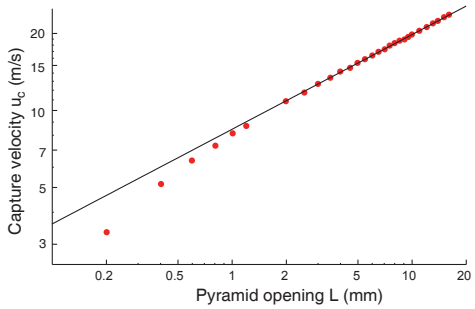

Fig. 10. Capture velocity versus the size of the pyramid opening. Circles: calculation by numerical integration using the model of [15]. Line: empirical scaling law $u_c \propto L^{0.37}$.

for applications in quantum information processing.

VI. Summary

We have fabricated a silicon chip designed to trap cold atoms in an array of integrated magneto-optical traps. The device contains 48 micro-fabricated hollow micro-pyramids surrounded by electroplated gold wires. This was packaged into a ceramic pin-grid array, and the chip's optical and magnetic properties were tested. We found that the chip wires can easily sustain the currents needed to operate the MOTs and can even operate for many seconds at the much higher currents needed to trap atoms magnetically. The use of electrochemical deposition of photoresist allowed us to pattern a flower design on the reflective coating, a feature necessary for achieving the proper optical conditions in the magneto-optical traps. Numerical estimates show that we should be able to collect small but useful numbers of atoms in these traps, providing a simple way to feed arrays of devices on future chips. This represents an important integration step because atom chips currently have to be loaded from a single large cloud by a series of somewhat involved manoeuvres.

References

[1] E. A. Hinds and I. G. Hughes, "Magnetic atom optics: mirrors, guides, traps, and chips for atoms", *J. Phys. D* **32**, 18, pp. R119-R146 (1999).
[2] R. Folman, P. Krüger, J. Schmiedmayer, J. Denschlag and C. Henkel, "Microscopic atom optics: from wires to an atom chip", *Adv. At., Mol. Opt. Phys.* **48**, pp. 263–356 (2002).
[3] J. Fortágh and C. Zimmermann, "Magnetic microtraps for ultracold atoms", *Rev. Mod. Phys.* **79**, pp. 235-289 (2007).
[4] S. Eriksson, M. Trupke, H. F. Powell, D. Sahagun, C. D. J. Sinclair, E. A. Curtis, B. E. Sauer, E. A. Hinds, Z. Moktadir, C. O. Gollasch, and M. Kraft, "Integrated optical components on atom chips", *Eur. Phys J. D* **35**, pp. 135-139 (2005).
[5] W. Hansel, P. Hommelhoff, T. W. Hansch, and J. Reichel, "Bose-Einstein condensation on a microelectronic chip", *Nature* **413**, pp. 498-501, (2001).
[6] H. Ott, J. Fortagh, G. Schlotterbeck, A. Grossmann, and C. Zimmermann, "Bose-Einstein condensation in a surface microtrap",*Phys. Rev. Lett.* **87**, 230401 (2001).
[7] C. D. J. Sinclair, E. A. Curtis, I. Llorente-Garcia, J. A. Retter, B. V. Hall, S. Eriksson, B. E. Sauer and E. A. Hinds, "Bose-Einstein Condensation on a permanent-magnet atom chip", *Phys. Rev. A* **72**, 03160(R) (2005)
[8] S. Knappe, P. D. D. Schwindt, V. Shah, L. Hollberg, J. Kitching, L. Liew, and J. Moreland, "A chip-scale atomic clock based on Rb-87 with improved frequency stability", *Opt. Expr.* **13**, pp. 1249-1253, (2005).
[9] Y. Shin, C. Sanner, G.-B. Jo, T. A Pasquini, M. Saba, W. Ketterle, D. E. Pritchard, M. Vengalattore and M. Prentiss, "Interference of Bose-Einstein condensates split with an atom chip", *Phys. Rev. A* **72**, 2 (2005).
[10] T. Schumm, S. Hofferberth, L. M. Andersson, S. Wildermuth, S. Groth, I. Bar-Joseph, J. Schmiedmayer and P. Krüger, "Matter-wave interferometry in a double well on an atom chip", *Nat. Phys.* **1**, pp 57 - 62 (2005).
[11] M. Trupke, J. Metz, A. Beige, and E. A. Hinds, "Towards quantum computing with single atoms and optical cavities on atom chips", *J. Mod. Opt.* **54**, pp. 1639-1655, (2007).
[12] J. Schmiedmayer, R. Folman, T. Calarco, "Quantum information processing with neutral atoms on an atom chip", *J. Mod. Opt.* **49**, 8, pp.1375-1388 (2002).
[13] M. Trupke, F. Ramirez-Martinez, E. A. Curtis, J. P. Ashmore, S. Eriksson, E. A. Hinds, Z. Moktadir, C. Gollasch, M. Kraft, G. V. Prakash, and J. J. Baumberg, "Pyramidal micromirrors for microsystems and atom chips", *Appl. Phys. Lett.* **88**, 071116, (2006).
[14] K. I. Lee, J. A. Kim, H. R. Noh, and W. Jhe, "Single-beam atom trap in a pyramidal and conical hollow mirror", *Opt. Lett.* **21**, pp. 1177-1179, (1996).
[15] K. Lindquist, M. Stephens, and C. Wieman , "Experimental and theoretical study of the vapour-cell-Zeeman optical trap", *Phys. Rev. A* **46**, pp. 4082-4090 (1992).
[16] Z. Moktadir and H. Camon, "Monte Carlo simulation of anisotropic etching of silicon: investigation of [111] surface properties", *Modell. Simul. Mater. Sci. Eng.* **5**, pp. 481-488, (1997).
[17] E. Koukharenko, Z. Moktadir, M. Kraft, M. E. Abdelsalam, D. M. Bagnall, C. Vale, M. P. A. Jones and E. A. Hinds, "Microfabrication of gold wires for atom guides", *Sens. Actuators A* **115** 2-3, pp 600-607 (2004).
[18] H. J. Metcalf and P. van der Straten, "Laser Cooling and Trapping", Springer-Verlag New York. (1999).
[19] M. Trupke, J. Goldwin, B. Darquie, G. Dutier, S. Eriksson, J. Ashmore, and E. A. Hinds, "Atom detection and photon production in a scalable, open, microcavity", *Phys. Rev. Lett.* **99**, 063601, (2007).

Appendix E

Micron-sized atom traps made from magneto-optical thin films

Appl. Phys. B (2004)
DOI: 10.1007/s00340-004-1655-7

Applied Physics B
Lasers and Optics

S. ERIKSSON[1,✉]
F. RAMIREZ-MARTINEZ[1]
E.A. CURTIS[1]
B.E. SAUER[1]
P.W. NUTTER[2]
E.W. HILL[2]
E.A. HINDS[1]

Micron-sized atom traps made from magneto-optical thin films

[1] Blackett Laboratory, Imperial College, London SW7 2BW, UK
[2] Department of Computer Science, University of Manchester, Manchester M13 9PL, UK

Received: 24 June 2004/Revised version: 17 August 2004
Published online: 29 September 2004 •

ABSTRACT We have produced magnetic patterns suitable for trapping and manipulating neutral atoms on a 1-μm length scale. The required patterns are made in Co/Pt thin films on a silicon substrate, using the heat from a focused laser beam to induce controlled domain reversal. In this way we draw lines and 'paint' shaped areas of reversed magnetisation with sub-micron resolution. These structures produce magnetic microtraps above the surface that are suitable for holding rubidium atoms with trap frequencies as high as ∼ 1 MHz.

PACS 39.25.+k; 03.75.Be; 75.50.Ss; 75.70.-i

1 Introduction

The study of cold-atom clouds in microscopic magnetic traps and waveguides has recently become a vigorous field of research [1, 2]. In particular, the ability to confine and manipulate atoms above microstructured surfaces – known as atom chips – holds great promise for integrated atom optics and the realisation of new quantum devices. Examples include miniature atom interferometers [3, 4] and quantum information processors [5].

Most atom-chip experiments to date have produced the trapping fields by passing current through integrated wires. This approach has two undesirable features. First, magnetic field noise is generated by thermal fluctuation of the charges in the wires [6, 7]. This can change the internal state of the atoms through magnetic dipole spin-flip transitions [8, 9], causing decoherence and trap loss. Second, the current does not flow as intended within the wires, but wanders from side to side [10], resulting in traps of uneven depth. An atom cloud cooled in such a trap breaks into fragments when the available energy becomes comparable with the amplitude of the noise in the trap depth [10–12]. These imperfections are detrimental for many practical applications.

As an alternative, our group has been working on microscopic patterns of permanent magnetisation [1], which offer a way around the problems discussed above by avoiding currents and by keeping the metal layers thin [7, 8]. Previous experiments used videotape [8, 13], on which patterns with spatial periods as small as 10 μm are conveniently written. Future experiments will aim at controlled tunnelling of atoms between one trap and another as a powerful way to prepare quantum states of the atomic motion [14]. This will require magnetic structures of the order of 1 μm in size, prompting us to investigate Co/Pt thin films. Small structures also make traps so strong that atom clouds can be compressed down to one dimension for new experiments in the physics of quantum gases [15, 16].

In this paper, we describe the fabrication of atomic microtraps based on magneto-optically (MO) patterned Co/Pt thin films. When combined with a suitable uniform external field, the magnetic field above the patterned surface of the film creates local minima where alkali atoms prepared in a weak-field-seeking state can be confined [1]. The first attempt to do this was by the group of P. Hannaford using TbFeCo films, but with these it did not seem possible to achieve the desired control over the domain boundaries [17]. Here we show by contrast that Co/Pt films are suitable for writing well-defined structures on the required 1-μm size scale. The strong magnetisation of the cobalt in conjunction with the small scale of the structures produces large magnetic field gradients of the order of 10^4 T/m. The magnetic field noise will be low because the metal film is thin. This will allow trapped rubidium atoms to be held at micron distances from the surface where the strong field gradient gives trapping frequencies in excess of 1 MHz, corresponding to exceedingly tight atom confinement.

The magnetisation of the film is normal to the surface, providing the freedom to create arbitrary two-dimensional patterns in the plane of the film. This is a key difference between in-plane and perpendicular magnetic media. The writing technique used in this work is based on a standard method used in data-storage applications and has a similar aim, i.e. to produce small-scale patterns. However, high-density data storage aims at achieving small isolated spots on the film, whereas our aim is to produce larger, uniformly magnetised regions with high contrast and small feature sizes along the boundary. MO techniques have not previously been used for this purpose. Here we present the writing of two patterns that are fundamental building blocks for atom trapping and manipulation. The writing process is fully reversible: any pattern can be erased and rewritten, and in principle this could even be done in the pres-

✉ Fax: +44-20-7594-1466, E-mail: stefan.eriksson@imperial.ac.uk

ence of trapped atoms. This offers an advantage in comparison with lithographically prepared atom chips, which cannot be reconfigured.

In Sect. 2 we describe the preparation of Co/Pt multilayer thin films and we summarise their magnetic properties. Section 3 describes the experimental apparatus and the procedure for writing. Section 4 is devoted to analysis of the patterns that were written and a discussion of their application to atom chips. We conclude with a summary of our results.

2 The Co/Pt multilayer thin films

Magneto-optical films have been much studied for their application to data storage [18]. Recently, Co/Pt films such as we are using here have attracted interest because they give a strong optical Kerr rotation to blue light, which can have a small spot size. High resolution makes Co/Pt attractive for writing microscopic atom traps and guides as well as for data storage. Other relevant properties are a strong saturation magnetisation and a large perpendicular anisotropy, leading to a large coercivity and a very square hysteresis loop [19]. The perpendicular anisotropy depends strongly on the crystallographic orientation of the layers: a thick Pt base layer increases the coercivity dramatically by establishing good {111} texture on which to deposit the multilayer. The squareness of the hysteresis loop is optimised by having control over the layer thicknesses: 0.2–0.4 nm for the Co, corresponding to 1–2 monolayers, and $\sim$ 1 nm for the Pt layers [20].

The specific layer structure that we use is shown in Fig. 1. First, the silicon substrate has a 55-nm-thick silicon nitride layer, which seems necessary to achieve MO recording. In our first attempts on silicon we did not have this insulating layer and we found that the 180 mW of laser power available for writing was not enough to make any observable change in the film, either physical or magnetic. This problem is rectified by the silicon nitride layer, which lowers the laser power required for writing, presumably because it increases the thermal resistance between the magnetic layers that must be heated and the silicon wafer that acts as a heat sink.

The Pt and Co layers are laid down by vacuum deposition using an electron-beam source to evaporate the metals. The base pressure before evaporation is 2×10^{-7} Torr and the average pressure during deposition rises to $3–4 \times 10^{-7}$ Torr. We heat the substrate to a temperature of 200 °C in order to establish adequate {111} texture with a platinum base layer that is only 5-nm thick [19]. A thicker layer gives better texture, but inhibits the MO writing by allowing the heat to flow too

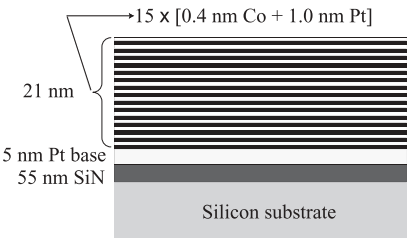

FIGURE 1 Layer structure used for the Co/Pt thin films (not to scale)

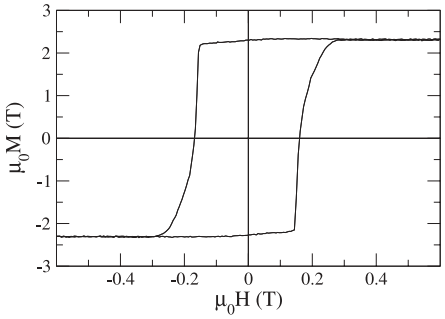

FIGURE 2 Alternating gradient force magnetometer measurement of the hysteresis curve. Here the magnetic moment of the film is expressed as an effective magnetisation within the 6-nm thickness of the Co layers

quickly away from the laser spot. The magneto-optical film itself consists of 15 bi-layers of alternating Co (0.4 nm) and Pt (1.0 nm). The evaporation rates are kept low at 10 pm/s to ensure a good control of the layer thicknesses.

The magnetic properties were determined using an alternating gradient force magnetometer, which yielded the hysteresis curve shown in Fig. 2. The measured coercivity is given by $\mu_0 H_c = 0.16$ T. The measured magnetic moment can be converted to an effective average magnetisation within the net 6-nm thickness of the cobalt. Expressed in this way, the magnetisation at saturation is given by $\mu_0 M_s = 2.3$ T, some 30% higher than that of bulk cobalt. This enhancement can be attributed to additional magnetisation coming from polarised Pt atoms near the Co layers [19].

3 Writing on the films

The writing procedure depends upon the reduction of the coercivity with increasing temperature [21]. The film is initially driven into saturation in one direction normal to the surface by a strong external magnetic field. This field is then reduced below the room-temperature coercivity and reversed. By illuminating the sample locally with a focused laser beam, very small areas of the film can be selectively heated and, with an appropriate movement of either the film or the laser beam, patterns of reversed magnetisation are created.

3.1 *Apparatus*

After using a permanent magnet to saturate it, the film is placed between the pole faces of an electromagnet as shown schematically in Fig. 3. This provides a reverse field of the order of 100 mT for the purpose of writing patterns on the film. The laser used for writing is a frequency-doubled Nd:YVO laser operating at 532 nm in the TM_{00} transverse mode. The first lens L focuses the light to a waist, where a mechanical shutter S is used to switch the beam on and off. A second identical lens recollimates it. Two mirrors M steer the beam to an aspheric lens AL with 0.55 numerical aperture and 4.4-mm focal length that focuses the light to a (calculated) waist of 0.6 μm, i.e. this is the radius at which the intensity drops to $1/e^2$ of its peak value. The Co/Pt film sits horizontally in a tray attached to a three-point kinematic mount KM, which is connected in turn to an xyz translation stage.

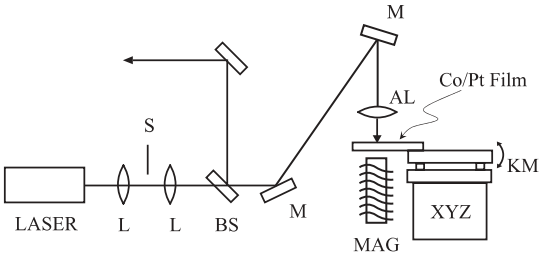

FIGURE 3 Experimental setup for thermomagnetic writing. Abbreviations: L, lenses; S, programmable shutter; BS, beam splitter; M, mirrors; AL, aspheric lens; MAG, electromagnet; KM, kinematic mount; XYZ, translation stages

Approximately 54% of the light is reflected, allowing us to position the film in the focal plane by translating it along the vertical z direction until the retro-reflected beam is collimated. A beam splitter BS picks off the back reflection for this purpose. Since the Rayleigh length of the focused light is only 2 μm, this requires delicate adjustment, for which we use a differential micrometer.

In order to write magnetic patterns, the film is moved horizontally by a translation stage under computer control. Initially, the plane of this xy translation does not coincide exactly with the surface of the film but, through iterative adjustments of the kinematic mount, we make the two planes coincide so that the spot is always focused on the surface. The next two subsections describe how we use this setup to write patterns suitable for atom trapping.

3.2 *Writing an array of lines*

Our first pattern is a set of parallel lines, as shown in Fig. 4. With the reversed magnetic field set at 50 mT and the laser power at 75 mW, the sample is translated at 250 μm/s along the x axis. This produces a line of reverse magnetisation 1-μm wide, which can be as long as the size of the film. At the end of each line, the shutter is closed and the sample is moved back to the start before making a step of 2 μm along y to the start of the next line.

The particular array shown in Fig. 4 covered a 200-μm square area. The figure shows a typical small section of the array imaged by a magnetic force microscope. The dark regions indicate areas magnetised in the original direction whilst the bright regions have reverse magnetisation. Such images give quantitative information about the positions and widths of the lines. They also allow us to see when a region is magnetically saturated. If the film is demagnetised, the domains are mixed, with some magnetised up and others down as shown inset in the top right hand corner of Fig. 4. By contrast, the uniformity of the lines in Fig. 4 shows that their magnetisation is saturated. Along the boundaries between lines, one can see small irregularities: the lines waver by approximately 250 nm peak-to-peak. The period of this noise is typically 300 nm but the spectral distribution is broad. We have not been able to achieve straighter boundaries and we presume that lines written in this way have a fundamental noise level imposed by the domain size.

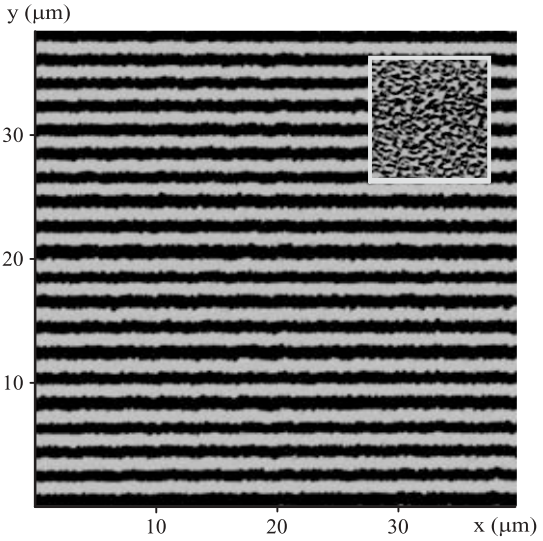

FIGURE 4 Magnetic force microscope image showing part of a pattern of parallel lines written on the film. The dark regions are unchanged from the original magnetisation, whereas the bright regions show where the magnetisation is reversed. *Inset*: a nearly demagnetised piece of the Co/Pt film, showing the size of the domains

This method of writing only works for a relatively narrow range of parameters. For example, if the laser power is lowered to 70 mW, there is hardly any magnetic response to the writing procedure. However, if the scanning speed is reduced at the same time, the film responds once again. This seems reasonable as it must surely be the temperature reached in the magnetic film that is the essential parameter. If instead we increase the laser power to 80 mW, we start to see physical damage to the surface of the film. Atomic force microscope measurements show a 2-nm-high ridge along the line drawn by the laser at this power. This can be avoided by making a compensating change to a higher scan rate. There are also constraints on the strength of the reverse magnetic field bias. Below 50 mT, we start to see domain structure in the body of the lines, indicating that the remagnetisation is not saturated. Above 100 mT the domain irregularities along the boundary lines begin to grow. For this reason, we operate at the lowest reverse field that still saturates the body of the lines.

3.3 *Painting an area*

Our second pattern involves 'painting' an area of reversed magnetisation in the shape of a 40-μm square with a piece missing from the top left, as shown in Fig. 5. The motivation for making this particular shape is discussed in Sect. 4. Once again the pattern is made by drawing a series of lines at 250 μm/s along the x direction, but in this case the step along y is 0.5 μm, which makes successive lines overlap. In order to achieve full overlap of the lines we used a higher laser power of 79 mW and increased the reverse-bias field to 0.1 T.

The edges parallel to the x axis have a similar level of noise to that seen in Fig. 4. However, the transverse deviations can be as large as 1 μm peak-to-peak on the edges parallel to y.

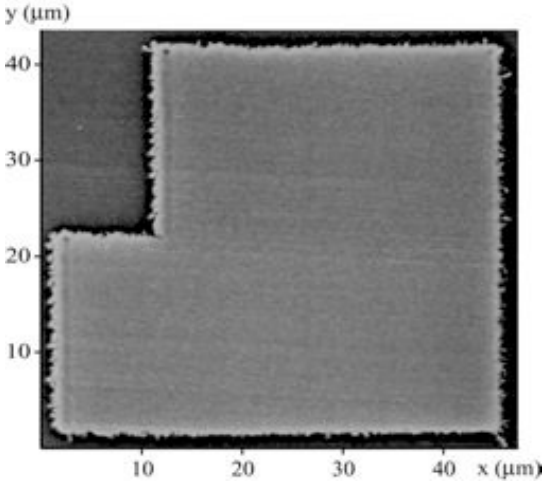

FIGURE 5 Magnetic force microscope scan of a Z-trap pattern. The grey scale in this image is identical to that in Fig. 4

Here the translation stage has decelerated as it approaches the end of the line, resulting in an excess deposition of energy. In combination with the larger reverse bias, this promotes domain growth, leading to the protuberances seen in the picture. We anticipate that this can be remedied by more precise control over the shutter timing, which would allow us to start and end the lines while the stage is still moving at constant velocity. Further, improved actuation along the y direction would allow us to use a shorter step size, so that the pattern could be written with a lower bias field and less laser power. We believe that the noise along the edges of the pattern can be reduced at least to the same level as seen for the array of lines with these modifications of the apparatus.

4 Application to atom microtraps

In thinking about the kinds of fields that could be made above the surface, it is useful to replace the magnetisation by an equivalent current density $\nabla \times M$ [22]. Along a boundary where the magnetisation reverses, going from M to $-M$, this current density results in an equivalent current of $2Mt$, where t is the thickness of the magnetised material. Taking our value of $2.3\ \mathrm{T}/\mu_0$ for the cobalt magnetisation and 6 nm for the thickness of the cobalt, we obtain an equivalent current of 22 mA along boundaries where the magnetisation reverses. Thus, the structures we can make in this magnetic film are equivalent to any network of 22-mA current loops in a plane.

Viewed in this way, the pattern shown in Fig. 4 is equivalent to lines of current parallel to the x axis, spaced by 1 μm and alternating in direction. The magnetic field they produce is easily calculated using the Biot–Savart law. A similar pattern with 3-μm period was recently fabricated by etching a hard-disk drive [23]. Larger structures of this kind have previously been fabricated on videotape and used as atom mirrors [1] and gratings [13]. Here, however, we are primarily interested in the application to trapping because of the unusually high trap frequencies that can be reached in small-scale structures. To be specific, let us consider adding a uniform bias field of 2.6 mT along the y direction to interfere with the field created by the film. Figure 6a shows the resulting contours of constant field strength. The circles in the contour plot enclose lines of zero magnetic field that are formed by destructive interference at a height z of 0.75 μm in a 2-μm-period array. Weak-field-seeking atoms may be trapped on these lines. An atom held in one of these traps will lose its spin orientation if the field is allowed to go strictly to zero, so we include here a small uniform field $B_0 = 0.1$ mT along the x direction to maintain the quantisation.

Figure 6b and c show the field strength versus y and z. In both cases this varies linearly in the vicinity of the trap with a gradient of $B' = 8.5 \times 10^3\ \mathrm{T/m}$, except in the central 10–20 nm, where the bias B_0 is significant. There the field strength grows quadratically, leading to a transverse oscillation frequency for the trapped atom given approximately by

$$f = \frac{1}{2\pi}\sqrt{\frac{\mu}{m}\frac{B'^2}{B_0}}\,, \tag{1}$$

where μ and m are the magnetic moment and the mass of the atom. For ^{87}Rb atoms in the $F = 2$, $m_F = 2$ state, the trap in this example has a very high oscillation frequency of $f = 1.1$ MHz.

We turn now to the x direction, along the axis of the trap. There is no trapping force in this direction, but axial confinement can be achieved if necessary by additional current-carrying wires underneath the chip. For example, two wires positioned at $x = \pm 1000\ \mu\mathrm{m}$, $z = -750\ \mu\mathrm{m}$, each carrying 10 A along y, will confine rubidium atoms in the axial direction with an oscillation frequency of 82 Hz. This is the type of arrangement normally used in our group [10].

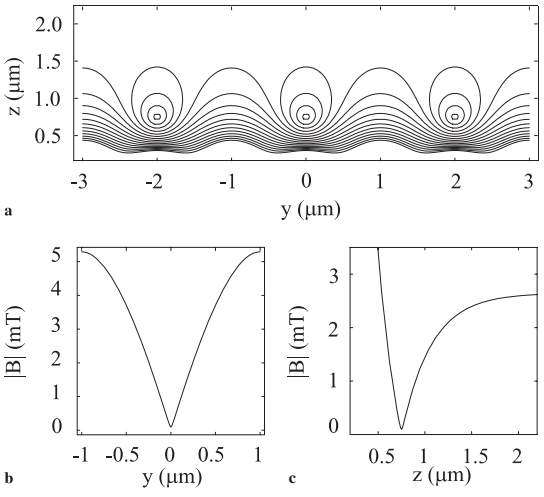

FIGURE 6 Calculated magnetic field magnitude above an array of lines (see Fig. 4) with a 2.6-mT bias along y to form the traps and 0.1 mT along x to preserve the atomic spin orientation. **a** Contours of constant field strength. **b** Field strength versus y through the centre of a trap at $z = 0.75$ μm. **c** Field strength versus z through the centre of a trap at $y = 0$

A more accurate description of the field above the film must take into account the domain structure seen in Fig. 4. Thus, the equivalent currents do not really flow along the x direction but oscillate from side to side in the xy plane. The typical amplitude is $a = 125$ nm and the typical wavelength is $\lambda = 300$ nm. At height $z \gg a$ above such a wire, the main field component is

$$B_y \simeq \mu_0 I/2\pi z\,, \tag{2}$$

whilst the transverse oscillations produce an oscillating field along the wire given by [10]

$$B_x \simeq \frac{\mu_0 I}{2\pi} k^2 a K_1(kz)\cos(kx)\,, \tag{3}$$

where $k = 2\pi/\lambda$ and K_1 is the modified Bessel function. It is this latter field component that makes the traps uneven and causes atom clouds to break up above current-carrying wires. In the present case of Rb atoms 750 nm above the film, this field has an amplitude of ~ 10 nT, corresponding to an undulating potential of ~ 10 nK.

For many applications using trapped atoms this amount of roughness is perfectly acceptable, but for the most sensitive experiments on quantum gases and quantum information processing it is not. We believe that further improvement would be worthwhile and could be achieved by having smaller domain sizes. It is known that the domain sizes are smaller than 100 nm when the films are deposited at higher temperature [24]. However, such films may be less suitable for thermomagnetic writing because the resulting hysteresis loops are less square. Alternative writing procedures are also under investigation.

For the magnetic pattern shown in Fig. 5, the equivalent current is a single loop encircling the region of reversed magnetisation. The Z-shaped edge on the left is the region of interest for atom-trapping purposes. The short central section along x is the 'wire' above which atoms are to be trapped, whilst the longer legs serve as the end wires, providing both axial confinement [25] and a suitable bias of 0.12 mT along x for avoiding spin-flip transitions. For a 22-mA current flowing in this way, we calculate that a bias field of 5.8 mT along y makes a trap lying 0.75 μm above the film. Figure 7a shows the contours of constant magnetic field strength in the xy plane 0.75 μm above the film, with the origin defined to be at the centre of the trap. Figure 7b and c show cuts through the trap in the y and z directions. The transverse oscillation frequency along y or z is 0.9 MHz. In the axial direction along x it is 19 kHz and in this case no auxiliary wires are needed. If a more anisotropic trap is required, one simply has to make the central section of the Z-shaped boundary longer.

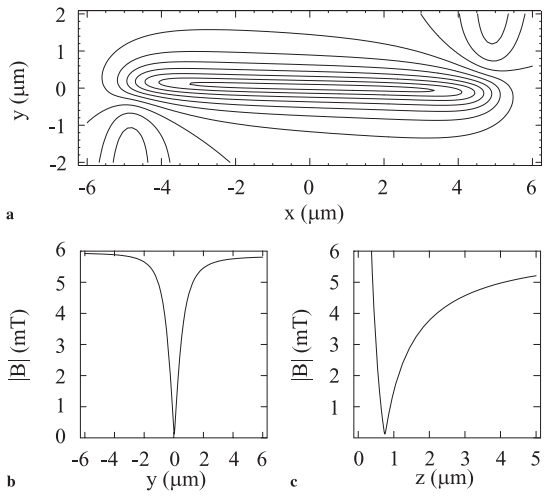

FIGURE 7 Calculated magnetic field strength near the Z-trap of Fig. 5 with 5.8-mT bias along y to form the trap. **a** Contours of constant field strength. **b** Field strength versus y through the centre of a trap at $z = 0.75$ μm. **c** Field strength through trap centre versus z

5 Summary

We have shown that areas and lines of saturated magnetisation can be written thermomagnetically on Co/Pt thin films. We have illustrated the method with two patterns that are relevant for producing high-frequency neutral-atom traps: the long wire and the Z-trap. With these drawing and painting tools any pattern of interest can be made at a resolution down to approximately 1 μm. This small scale gives access to extremely tight traps with MHz frequencies for rubidium atoms, making the method promising for studies of one-dimensional quantum gases and for small atom-trap arrays that could be suitable for quantum information processing.

In atom chips based on current-carrying wires, the magnetic field close to a wire suffers from rf interference and thermal noise, which cause atom loss through vibrational excitations and spin flips. These effects should be avoided with the use of the Co/Pt thin films. A further problem with current-carrying wires is that the current wanders from side to side, leading to uneven traps. A similar effect is found in the Co/Pt thin films due to the domain structure. However the amplitude and period of these excursions are small compared with a micron, making the effect negligible in all but the tightest traps, i.e. those that are closest to the surface.

ACKNOWLEDGEMENTS We are indebted to J. Dyne for expert technical assistance. We also thank D. Lau and B. Vodungbo for their contributions to the early stages of the project. This work was supported by the UK Engineering and Physical Sciences Research Council and by the FASTNET and Cold Quantum Gases networks of the European Union.

REFERENCES

1 E.A. Hinds, I.G. Hughes: J. Phys. D: Appl. Phys. **32**, R119 (1999)
2 R. Folman, P. Krüger, J. Schmiedmayer, J. Denschlag, C. Henkel: Adv. At. Mol. Opt. Phys. **48**, 263 (2002)
3 E.A. Hinds, C.J. Vale, M.G. Boshier: Phys. Rev. Lett. **86**, 1462 (2001)
4 W. Hänsel, J. Reichel, P. Hommelhoff, T.W. Hänsch: Phys. Rev. A **64**, 063 607 (2001)
5 T. Calarco, E.A. Hinds, D. Jaksch, J. Schmiedmayer, J.I. Cirac, P. Zoller: Phys. Rev. A **61**, 022 304 (2000)
6 C. Henkel, S. Pötting, M. Wilkens: Appl. Phys. B **69**, 379 (1999); C. Henkel, M. Wilkens: Europhys. Lett. **47**, 414 (1999)
7 P.K. Rekdal, S. Scheel, P.L. Knight, E.A. Hinds: Phys. Rev. A **70**, 013 811 (2004)
8 M.P.A. Jones, C.J. Vale, D. Sahagun, B.V. Hall, E.A. Hinds: Phys. Rev. Lett. **91**, 080 401 (2003)
9 D.M. Harber, J.M. McGuirk, J.M. Obrecht, E.A. Cornell: J. Low Temp. Phys. **133**, 229 (2003)

10 M.P.A. Jones, C.J. Vale, D. Sahagun, B.V. Hall, C.C. Eberlein, B.E. Sauer, K. Furusawa, D. Richardson, E.A. Hinds: J. Phys. B **37**, L15 (2004)
11 J. Fortágh, H. Ott, S. Kraft, A. Günter, C. Zimmermann: Phys. Rev. A **66**, 041 604(R) (2002)
12 A.E. Leanhardt, Y. Shin, A.P. Chikkatur, D. Kielpinski, W. Ketterle, D. Pritchard: Phys. Rev. Lett. **90**, 100 404 (2003)
13 P. Rosenbusch, B.V. Hall, I.G. Hughes, C.V. Saba, E.A. Hinds: Appl. Phys. B **70**, 709 (2000)
14 M. Greiner, O. Mandel, T. Esslinger, T.W. Hänsch, I. Bloch: Nature **415**, 39 (2002)
15 U. Al Khawaja, J.O. Andersen, N.P. Proukakis, H.T.C. Stoof: Phys. Rev. A **66**, 013 615 (2002)
16 V. Dunjko, V. Lorent, M. Olshanii: Phys. Rev. Lett. **86**, 5413 (2001)
17 D.C. Lau, R.J. McLean, A.I. Sidorov, D.S. Gough, J. Koperski, W.J. Rowlands, B.A. Sexton, G.I. Opat, P. Hannaford: J. Opt. B: Quantum Semiclass. Opt. **1**, 371 (1999)
18 M. Mansuripur: *The physical principles of magneto-optical recording* (Cambridge University Press 1998)
19 C.J. Lin, G.L. Gorman, C.H. Lee, R.F.C. Farrow, E.E. Marinero, H.V. Do, H. Notarys: J. Magn. Magn. Mater. **93**, 194 (1991)
20 W.B. Zeper, F.J.A.M. Greidanus, P.F. Carcia: IEEE Trans. Magn. **25**, 3764 (1989); W.B. Zeper, H.W. van Kesteren, B.A.J. Jacobs, J.H.M. Spruit: J. Appl. Phys. **70**, 2264 (1991)
21 W.W. Clegg, N.A.E. Heyes, E.W. Hill, C.D. Wright: J. Magn. Magn. Mater. **95**, 49 (1991); C.D. Wright, W.W. Clegg, A. Boudjemline, N.A.E. Heyes: Jpn. J. Appl. Phys. **33**, 2058 (1994)
22 J.D. Jackson: *Classical Electrodynamics*, 3rd edn. (Wiley, New York 1998)
23 B. Lev, Y. Lassailly, C. Lee, A. Scherer, H. Mabuchi: Appl. Phys. Lett. **83**, 395 (2003)
24 D. Weller, L. Folks, M. Best, E.E. Fullerton, B.D. Terris, G.J. Kusinski, K.M. Krishnan, B. Thomas: J. Appl. Phys. **89**, 7527 (2001)
25 J. Reichel, W. Hänsel, T.W. Hänsch: Phys. Rev. Lett. **83**, 3398 (1999)